Marie-Albane de Milhe de Saint Victor
Pembroke College

Supervised by
Eleanor Stride and Constantin-C. Coussios

INVESTIGATING MAGNETICALLY TARGETED MICROBUBBLES FOR ULTRASOUND-ENHANCED THROMBOLYSIS

A thesis submitted for the degree of Doctor of Philosophy
Hilary 2016

Abstract

Despite therapeutic advances, ischaemic stroke remains one of the leading causes of mortality and disability worldwide. Microbubble-enhanced sonothrombolysis is an advantageous method to accelerate the reopening of occluded arteries, but further improvements in safety and efficacy are required to attain widespread clinical implementation. This thesis investigates the potential of magnetically targeted microbubbles to enhance sonothrombolysis.

First, a computational and experimental model of a thrombosed vascular network was developed. It showed that magnetic targeting considerably increases the number of microbubbles delivered to the thrombus, a key element for effective sonothrombolysis.

The effect of these magnetically targeted microbubbles on rates of thrombus breakdown was then investigated *in vitro*, first with ultrasound and microbubbles alone (mechanical sonothrombolysis), then with the addition of fibrinolytic drugs (enzymatic sonothrombolysis). Magnetic targeting was not found to affect mechanical treatment, and mechanical lysis rates were highly variable. On the other hand, magnetic targeting significantly accelerated enzymatic treatment, even with low concentrations of fibrinolytic drugs. The mechanisms underlying both treatments were discussed.

In addition, treatment safety was examined. Specifically, the risk of secondary embolism and the feasibility of real-time treatment monitoring were assessed. Neither treatment increased the risk of downstream vascular embolism with large clot fragments. Acoustic monitoring of enzymatic sonothrombolysis was feasible, as a strong correlation was found between lysis rates and the energy of acoustic emissions near the clot surface. There was no strong correlation in mechanical sonothrombolysis.

Magnetic targeting may therefore be regarded as a promising adjuvant to enzymatic sonothrombolysis, improving microbubble delivery to the clot, accelerating its breakdown, and reducing injected drug doses. It is hoped that targeted treatment and real-time monitoring will enhance safety and efficacy in the management of acute and chronic thrombosis, and ultimately improve patient outcomes.

Table of contents

Abstract ..... **ii**

Table of contents ..... **iii**

List of figures ..... **xi**

List of tables ..... **xvi**

List of symbols ..... **xvii**

List of acronyms ..... **xix**

Statement of originality ..... **xxi**

Dissemination ..... **xxii**

Acknowledgements ..... **xxiv**

Chapter 1 . Introduction, aims and objectives **1**

1.1. Introduction to sonothrombolysis 2

1.1.1. Principle of sonothrombolysis 3

1.1.2. Scope of application 4

1.1.3. Microbubble-enhanced sonothrombolysis 4

1.1.4. Statement of the problem 5

1.2. Outline of the thesis 6

1.2.1. Objectives of the work 6

1.2.2. Structure of the thesis 7

Chapter 2 . Microbubbles in sonothrombolysis: a review of the literature **8**

2.1. Role of microbubbles in restoring vessel patency *in vitro* and *in vivo* 9

2.1.1. Clot size reduction: *in vitro* evidence 9

2.1.2. Improving microperfusion 11

2.2. Clinical evidence 13
2.3. Mechanisms of microbubble-enhanced sonothrombolysis 16
2.3.1. Cavitational mechanisms 16
2.3.2. Non-inertial cavitation 18
2.3.3. Inertial cavitation 19
2.3.4. Thermal mechanisms 20
2.3.5. Other mechanisms 22
2.4. Clinical challenges 23
2.4.1. Ultrasound attenuation in bone and tissue 23
2.4.2. Therapeutic agent delivery to the thrombus 25
2.4.3. Effects of an underlying pathology 26
2.4.4. Safety 27
2.5. Optimizing treatment protocols 30
2.5.1. Influence of Ultrasound Parameters 30
2.5.2. Influence of Microbubble Characteristics 33
2.6. Microbubble engineering for sonothrombolysis 37
2.6.1. Targeted microbubbles 37
2.6.2. Drug loaded microbubbles 40
2.6.3. Targeted and loaded microbubbles 43
2.6.4. Microdroplets 44
2.7. Conclusion 45

Chapter 3 . Magnetic targeting to enhance microbubble delivery in occluded microvascular networks 46

3.1. Introduction 47

3.1.1. Motivation 47

3.1.2. Targeted therapeutic agent delivery in obstructed vascular networks 48

3.1.3. Objectives of the investigation 48

3.2. Methods 49

3.2.1. Geometry 49

3.2.2. 2D numerical model 52

3.2.3. Experiments 64

3.3. Results 71

3.3.1. Preliminary studies 71

3.3.2. Flow dynamics 76

3.3.3. Drug delivery 80

3.3.4. Microbubble delivery 84

3.4. Discussion 92

3.4.1. Experimental findings 92

3.4.2. Relevance to *in vivo* mechanisms 95

3.4.3. Clinical implications 97

3.4.4. Future work 98

3.5. Conclusion 98

Chapter 4 . Mechanical sonothrombolysis with magnetically targeted microbubbles .. 99

4.1. Introduction 100

4.1.1. Motivation 100

4.1.2. Structure of the study 101

4.2. Methods 102

4.2.1. Flow phantom 102

4.2.2. *In vitro* clot model 103

4.2.3. Magnetic microbubble preparation 104

4.2.4. Magnetic targeting setup 105

4.2.5. US exposure parameters 107

4.2.6. Image acquisition and processing for lysis monitoring 108

4.2.7. Image acquisition and processing for magnetic targeting evaluation 109

4.2.8. Acoustic data acquisition and processing for cavitation monitoring 111

4.2.9. Debris analysis 113

4.2.10. Histological analysis 113

4.2.11. Statistical analysis 113

4.3. Results and discussion 114

4.3.1. Characterisation of the experimental setup 114

4.3.2. Effect of microbubble concentration on thrombolysis rates 120

4.3.3. Effect of magnetic targeting on microbubble concentration 123

4.3.4. Effect of magnetic targeting on thrombolysis rates: preliminary experiments 126

4.3.5. Experimental variability 130

4.3.6. Effect of magnetic targeting on thrombolysis rates: improved magnetic targeting system 137

4.3.7. Consequences for the design of the magnetic targeting setup 148

4.3.8. Effect of a new magnetic targeting setup on sonothrombolysis..... 152

4.3.9. Clinical implications 159

4.3.10. Limitations of the study 162

4.4. Conclusion 163

Chapter 5 . Enzymatic sonothrombolysis with magnetically targeted microbubbles .. 164

5.1. Introduction..... 165

5.1.1. Motivation 165

5.1.2. Structure of the study 166

5.2. Methods 166

5.2.1. Materials..... 166

5.2.2. Experimental arrangement 167

5.2.3. Flow setup 167

5.2.4. Ultrasound exposure..... 168

5.2.5. Magnetic targeting 168

5.2.6. Data acquisition and processing..... 170

5.2.7. Statistical analysis 172

5.3. Results and discussion 173

5.3.1. Ultrasound field characterisation 173
5.3.2. Magnetic field characterisation 174
5.3.3. Microbubble retention 176
5.3.4. Lysis rates 178
5.3.5. Acoustic emissions 182
5.3.6. Lysis monitoring 184
5.3.7. Safety 186
5.3.8. Histological analysis 187
5.3.9. Limitations 188
5.3.10. Clinical implications 190
5.4. Insights into the mechanisms of sonothrombolysis 193
5.4.1. Mechanical effects 193
5.4.2. Temperature 202
5.5. Conclusion 203

Chapter 6 . Conclusions and future work 204
6.1. Thesis overview 204
6.2. Summary of experimental findings 206
6.3. Clinical significance of the findings 211
6.4. Future work 212

Appendix A . Observing the mechanisms of sonothrombolysis in an acousto-fluidic chamber ……...216

A.1. Introduction 217

A.1.1. Objective 217

A.1.2. Structure of the study 217

A.2. Methods 218

A.2.1. Materials 218

A.2.2. Acoustic chamber 218

A.2.3. Chamber characterization 219

A.2.4. Clot preparation 219

A.2.5. Experimental protocol 220

A.2.6. Image acquisition 221

A.2.7. Image processing 222

A.3. Results 222

A.3.1. Characterising the system 223

A.3.2. Effect of tPA concentration 224

A.3.3. Effect of ultrasound and microbubbles 225

A.3.4. Mechanisms 226

Appendix B . Effect of ultrasound on the structure of fibrin: fluorescence lifetime imaging ……...230

B.1. Rationale 230

B.1.1. Objectives 230

B.1.2. Study design 231

B.2. Methods 232
B.2.1. Clot models 232
B.2.2. Imaging protocol 232
B.2.3. Molecular rotors 233
B.2.4. Experimental groups 233
B.3. Results 234
B.3.1. Preliminary experiments 234
B.3.2. Free dye 234
B.3.3. Labelled fibrinogen monomers 235
B.4. Conclusion 236
Appendix C . Effect of ultrasound on the structure of fibrin: spectral imaging 237
C.1. Rationale 237
C.2. Protocol 238
C.2.1. Materials 238
C.2.2. Methods 238
Appendix D . Transcranial sound field characterisation 240
D.1. Objectives 240
D.2. Methods 240
D.2.1. Experimental methods 240
D.2.2. Numerical simulation 241
D.3. Results and discussion 242
D.4. Conclusion 242

List of figures

Figure 2-1: Example of clot diameter reduction with sonothrombolysis 11

Figure 2-2: Murine brain microvasculature after sonothrombolysis 12

Figure 2-3: Representative frequency spectra for microbubble response 18

Figure 2-4: Localisation of tPA and plasminogen in clots after sonothrombolysis 22

Figure 2-5: Representation of possible drug loading modalities on microbubbles 43

Figure 3-1: Geometry of the bifurcation model 51

Figure 3-2: Lines and points of interest in the bifurcation model 51

Figure 3-3: Relative positions of the magnet and the bifurcation plane 58

Figure 3-4: Microfluidic device fabrication process 65

Figure 3-5: Schematic of the experimental setup 66

Figure 3-6: Sketch of the microfluidic damping device 66

Figure 3-7: Mesh independence study 73

Figure 3-8: Flow rate validation experiments 74

Figure 3-9: Entrance length 75

Figure 3-10: Fluid velocity profile computed along the occluded branch 77

Figure 3-11: Influence of mean inlet velocity on the velocity in the occluded branch. 78

Figure 3-12: Influence of occlusion distance on the velocity in the occluded branch 78

Figure 3-13: Flow pattern in the occluded branch 79

Figure 3-14: Drug distribution in the bifurcation at t=1h 81

Figure 3-15: Simulated half concentration distance during continuous tPA infusion 81

Figure 3-16: Simulated effect of mean inlet velocity on half concentration distance 82

Figure 3-17: Distribution of a fluorescent drug model in the bifurcation at t = 1h 83

Figure 3-18: Experimental half concentration distance during tPA infusion 83

Figure 3-19: Possible delivery outcome for an individual microbubble 84

Figure 3-20: Example of simulated microbubble delivery 86

Figure 3-21: Effect of mean inlet velocity and magnetic targeting on delivery..... 87

Figure 3-22: Effect of mean microbubble diameter and magnetic targeting 88

Figure 3-23: Final state of a microbubble as a function of starting position at the inlet and of microbubble diameter..... 89

Figure 3-24: Experimental microbubble delivery at 5 mm/s inlet velocity..... 90

Figure 3-25: Experimental microbubble delivery at 50 mm/s inlet velocity..... 91

Figure 3-26: Preferential erythrocyte distribution in high-flow branches 94

Figure 4-1: Setup overview..... 103

Figure 4-2: Cross-section of the magnetic targeting setup with Halbach array..... 106

Figure 4-3: Graphical User Interface for clot image processing 109

Figure 4-4: Image processing algorithm for magnetic targeting evaluation 111

Figure 4-5: Signal processing algorithm for quantification of acoustic emissions..... 112

Figure 4-6: Size distribution for magnetic microbubbles..... 115

Figure 4-7: Microbubble response to a magnetic field 115

Figure 4-8: Simulations of magnetic field in the initial setup 117

Figure 4-9: Map of the sound field in the initial setup..... 119

Figure 4-10: Rate of lysis in the microbubble concentration study..... 122

Figure 4-11: Total cavitation dose in the microbubble concentration study..... 122

Figure 4-12: Deflection by the magnet in the initial setup 123

Figure 4-13: Retention by the magnet in the initial setup 125

Figure 4-14: Lytic rates in the preliminary sonothrombolysis study 127

Figure 4-15: Lytic rates in the replicated sonothrombolysis study 129

Figure 4-16: Effect of clot origin on sonothrombolysis..... 130

Figure 4-17: Effect of clot age on sonothrombolysis 131

Figure 4-18: Effect of clot gas content on sonothrombolysis..... 133

Figure 4-19: Total cavitation dose in the 2-5 MHz frequency range in the replicated experiments 134

Figure 4-20: Bivariate representation of lysis rates and total acoustic emissions in the replicated experiments..... 136

Figure 4-21: Simulations of magnetic field in modified setup with closer magnet 138

Figure 4-22: Microbubble deflection in modified setup with reduced magnet distance 139

Figure 4-23: Microbubble retention in modified setup with reduced magnet distance 140

Figure 4-24: Lytic rates with reduced magnet distance..... 142

Figure 4-25: Cavitation dose in the 2-5 MHz range with reduced magnet distance..... 142

Figure 4-26: Microbubble deflection in setup with closer magnet and slower flow 144

Figure 4-27: Microbubble retention in setup with closer magnet and slower flow 145

Figure 4-28: Lytic rates in the magnetic targeting setup with closer magnet and slower flow 147

Figure 4-29: Cavitation dose in the magnetic targeting setup with closer magnet and slower flow 147

Figure 4-30: Layout of the new magnetic targeting system 153

Figure 4-31: Deflection and retention in the new magnetic targeting setup..... 154

Figure 4-32: Lytic rates in the new magnetic targeting setup..... 156

Figure 4-33: Histological analysis after mechanical sonothrombolysis 158

Figure 5-1: Overview of the experimental setup 170

Figure 5-2: Map of the sound field in the focal region..... 173

Figure 5-3: Simulations of the magnetic conditions in the flow chamber..... 175

Figure 5-4: Evidence of magnetic microbubble retention in the experimental setup.... 177

Figure 5-5: accumulation of magnetic material in the focal region..... 177

Figure 5-6: Lytic rates in enzymatic sonothrombolysis with magnetically targeted microbubbles 178

Figure 5-7: Cavitation dose detected during enzymatic sonothrombolysis 183

Figure 5-8: Bivariate representation of the lysis rates and the cavitation dose in enzymatic sonothrombolysis 185

Figure 5-9: Concentration of particles in effluent during enzymatic sonothrombolysis186

Figure 5-10: Histological analysis after enzymatic sonothrombolysis 188

Figure 5-11: Confocal spectral micrographs of fibrin-bound polarity-sensitive probes after sonication 200

Figure A-1: Schematic of the acousto-fluidic chamber..... 219

Figure A-2 : Clot imaging with confocal microscopy in the acousto-fluidic chamber... 222

Figure A-3: Acoustic characterisation of the acousto-fluidic chamber..... 223

Figure A-4: Temperature rise in the absence of flow during ultrasound exposure..... 224

Figure A-5: Effect of tPA concentration on thrombolysis (no US)..... 224

Figure A-6: Effect of ultrasound and microbubbles on clot lysis 225

Figure A-7: Spectral content of the acoustic emissions in the channel 226

Figure A-8: Example of microbubble behaviour under acoustic radiation forces 228

Figure A-9: Example of microstreaming in the channel 228

Figure A-10: Example of model drug penetration into the clot..... 229

Figure B-1: Confocal images of fibrin network with conjugated dyes..... 235

Figure B-2 : Phasor plot of fibrin-conjugated dyes in plasma 236

Figure B-3: Phasor plot of fibrin-conjugated dyes in whole blood..... 236

Figure D-1: Experimental setup for transcranial sound field calibration 241

Figure D-2: Experimental and numerical alignment of the transducer 242

Figure D-3: Experimental and numerical characterisation of the transcranial ultrasound field 243

List of tables

Table 2-1: Safety and efficacy of clinical trials 21

Table 2-2: Summary of sonothrombolysis studies. 36

Table 3-1: Dimensions of the bifurcation phantom 50

Table 3-2: Summary of variable names and values in the numerical model 53

Table 3-3: Values of the parameters and physical constantsin the numerical model 53

Table 3-4: Mesh properties for mesh-independence study 63

Table 4-1: Experimental conditions in the microbubble concentration study 120

Table 4-2: Experimental conditions in the preliminary sonothrombolyiss study 127

Table 4-3: Experimental conditions in the replicated sonothrombolysis study 128

Table 4-4: Experimental conditions in the investigation of the effect of entrapped gas 132

Table 4-5: Experimental conditions in the investigation sonothrombolysis at reduced magnet distance 141

Table 4-6: Experimental conditions in the investigation sonothrombolysis with closer magnet and slower flow 146

Table 4-7: Values used in calculation of magnetophoretic and primary acoustic radiation forces 150

Table 4-8: Experimental conditions in the investigation of sonothrombolysis in new targeting system 155

Table 4-9: Debris sizing after mechanical sonothrombolysis 157

Table 5-1: Proportion of large particles produced by enzymatic sonothrombolysis 187

Table B-1: Characteristics of molecular rotors 233

Table B-2: Experimental groups 233

List of symbols

α	angle between branches in bifurcation
$\boldsymbol{B}$	magnetic flux density
β_{shell}	volume fraction of iron oxide in the ferrofluid
β_{tot}	volume fraction of iron oxide in the microbubble
C_d	tPA concentration in bifurcation
c	speed of sound in water
χ_p	magnetic susceptibility of the material
D	duration of ultrasound pulse
D_c	diffusion coefficient of tPA
D_h	hydraulic diameter of inlet in bifurcation
$d_{p,f,o}$	depth of parent, free and occluded branch in bifurcation
$\boldsymbol{F_{arf}}$	acoustic radiation force on a microbubble
$\boldsymbol{F_d}$	drag force on a microbubble
$\boldsymbol{F_m}$	magnetophoretic force on a microbubble
$\boldsymbol{F_{norm}}$	normalised magnetophoretic force on a microbubble
g	gravitational acceleration
η	dynamic viscosity of water
$\boldsymbol{H}$	magnetic field intensity
k_B	Boltzman's constant
L_{entry}	hydrodynamic entrance length
$l_{p,f,o}$	length of parent, free and occluded branch in bifurcation
$\boldsymbol{M}$	remanent magnetisation vector of the magnet
$\boldsymbol{m_{eff}}$	effective dipole moment

M_{NdFeB} remanent magnetisation of NdFeB

M_p magnetisation of iron oxide particles

M_s saturation magnetisation of particles

μ_0 permeability of vacuum

μ_m relative permittivity of the medium

N_R Normalised Retention

p hydrodynamic pressure in bifurcation

Pa Peak acoustic pressure

R microbubble radius

$r_{0,1,2}$ radius of parent and 2 daughter branches in Murray's law

R_e Reynold's number

R_s thickness of ferrofluid layer on microbubble shell

ρ_a density of air

ρ density of water

$1/T$ pulse repetition frequency

$\boldsymbol{u}$ fluid velocity in bifurcation

$\boldsymbol{v}$ microbubble velocity

V_m magnetic scalar potential

$w_{p,f,o}$ width of parent, free and occluded branch in bifurcation

δ damping coefficient

ω_0 excitation frequency

List of acronyms

B++	Bodipy-based rotor 2 (with 2 positive charges on the hydrocarbon tail)
BC10	Bodipy-based rotor 1
BSA	Bovine Serum Albumin
CLOTBUST	Combined Lysis Of Thrombus in Brain ischaemia using transcranial Ultrasound and Systemic tPA (clinical trial [1])
CT	Computerised Tomography
Cy3	Sulfo-Cyanine3
DDFP	Dodecafluoropentane
DiI	1,1'-dioctadecyl-3,3,3',3'-tetramethylindocarbocyanine perchlorate
DiSC2(3)	3,3′-Diethylthiacarbocyanine iodide
DMSO	Dimethyl sulfoxide
DSPC	Distearoyl-sn-glycero-3-phosphocholine
FDA	American Food and Drug Administration
FE	Di-4-AN(F)EPPTEA (polarity-sensitive dye)
FITC	Fluorescein isothiocyanate
FLIM	Fluorescence Lifetime Imaging Microscopy
HIFU	High Intensity Focused Ultrasound
HSD	Honest Significant Difference (in Tukey's test)
KR	Kiton Red
MB	Microbubble
MRI	Magnetic Resonance Imaging
mRS	modified Rankin Scale
NHS ester	N-hydroxysuccinimide esters
NIHSS	National Institute of Health Stroke Scale

PAM	Passive Acoustic Mapping
PBS	Phosphate-Buffered Saline
PCD	Passive Cavitation Detector
PDMS	Polydimethylsiloxane
PEG	Polyethylene Glycol
PESDA	Perfluorocarbon-Exposed Sonicated Dextrose Albumin (microbubbles)
PH	Parenchymal Haemorrhage
PMMA	Poly(methyl 200) methacrylate
PN	Peak Negative
RGB	Red Green Blue (image)
ROI	Region Of Interest
(s)ICH	(symptomatic)Intracranial Haemorrhage
Sq5	Squaraine 5
(t)ELIP	(tPA-loaded) Echogenic LIPosome
TCCD	Transcranial Color-Coded Duplex
TCD	Transcranial Doppler
ThT	Thioflavin T
(r)tPA	(recombinant) Tissue Plasminogen Activator
TRITC	Tetramethylrhodamine
TUCSON	Transcranial Ultrasound in Clinical SONothrombolysis (clinical trial [2])
US	Ultrasound

Statement of originality

I hereby declare that this submission is my own work and to the best of my knowledge it contains no materials previously published or written by another person, or substantial proportions of material which have been accepted for the award of any other degree or diploma at the University of Oxford or any other educational institution, except where due acknowledgement is made in the thesis.

Any contribution made to the research by others, with whom I have worked at the University of Oxford or elsewhere, is explicitly acknowledged in the thesis and in the joint authorship declaration attached. I also declare that the intellectual content of this thesis is the product of my own work, except to the extent that assistance from others in the project's design and conception or in style, presentation and linguistic expression is acknowledged.

Marie de Saint Victor

April 12th, 2016

Dissemination

Peer-reviewed publications

M. de Saint Victor, D. Carugo, L. Barnsley, C.-C. Coussios, E. Stride, "Magnetic targeting to enhance microbubble delivery in an occluded microarterial bifurcation", *in preparation*

M. de Saint Victor, L. Barnsley, C.-C. Coussios, E. Stride "Sonothrombolysis with magnetically targeted microbubbles", *in preparation*

M. de Saint Victor, C.-C. Coussios, E. Stride "Fibrinolytic drugs and mechanisms of sonothrombolysis: histological observations", *technical note in preparation*

M. de Saint Victor, C. Crake, C.-C. Coussios, and E. Stride, "Properties, characteristics and applications of microbubbles for sonothrombolysis.," *Expert Opin. Drug Deliv.*, vol. 11, no. 2, pp. 187–209, 2014.

Conferences

M. de Saint Victor, D. Carugo, L. Barnsley, C.-C. Coussios, and E. Stride, "Theoretical and experimental investigation of magnetic targeting to enhance microbubble delivery in an occluded microarterial bifurcation", poster presented at the 21st European symposium on Ultrasound Contrast Imaging, Rotterdam, the Netherlands, 21 – 22 January 2016.

M. de Saint Victor, D. Carugo, C.-C. Coussios, and E. Stride, "Ultrasound-enhanced thrombolysis: mechanistic observations", paper presented at the Fall 2015 Meeting of the Acoustical Society of America, Jacksonville, FL, USA, 2 – 6 November 2015.

M. de Saint Victor, D. Carugo, J.Kwan, C.-C. Coussios, and E. Stride, “Mechanisms of ultrasound-enhanced thrombolysis: observations at the microscopic scale”, paper presented at the 15th International Symposium on Therapeutic Ultrasound, Utrecht, the Netherlands, 15 - 18 April 2015.

M. de Saint Victor, C. Crake, C.-C. Coussios, and E. Stride, “Targeted sonothrombolysis with magnetically targeted microbubbles”, paper presented at the 14th International Symposium on Therapeutic Ultrasound, Las Vegas, NV, USA, 2 – 5 April 2014.

Acknowledgements

First and foremost, I would like to express my gratitude to my supervisors for their exceptional support and advice throughout my DPhil: Eleanor Stride who guided me while leaving me the freedom to explore, and always made time for me in her busy schedule; Constantin-C. Coussios who has always supported and challenged me, making me grow as a researcher.

In the BUBBL lab, I am very thankful to Dario Carugo and Lester Barnsley for teaching me microfluidics and magnetism; to David Holroyd for mentoring me throughout my first year and for sharing his medical expertise with me; to Richard Browning for his advice and dry humour in the final months of my thesis; to Paul Lyon for his expert and invariably kind help with phlebotomy. I can't thank enough Jim Fisk and David Salisbury in the workshop for helping me turn blue-sky designs into reality. I am also indebted to Tracey King, Jo Armitage and Daphne Cunningham for making all aspects of life in the lab smoother. I thank the UK Engineering Sciences Research Council (EPSRC) for supporting this work financially.

I am very grateful to the BUBBL and IBME members who made my time in the lab so enjoyable, and who taught me to handle chilli (almost) gracefully: Joshua Owen, Caroline Hartfield, Christophoros Mannaris, Boon Teo, Anjali Seth, Calum Crake, Paul Rademeyer, Ale Guazzi.

Beyond BUBBL, I would like to thank Marketa Kubankova and Erdinc Segzin for their enthusiasm and dedication in our collaborations; Richard Stillion for being so helpful with the preparation of histological samples; Cathy Gray, Murali Somasundaram, and Reena Ravikumar for making my early mornings in the operating theatre pleasant and productive.

I am also truly grateful for the friendships that have been such an important part of my life in Oxford: all at 253 Magdalen Road for making every minute so full and enjoyable; Anthony Bradley for bravely trying to keep me sane; Enrichetta Frezzato and Saulo de Oliveira for making me smile always; Julian Sempill, Julia Costa Lopez and Clara Smith for our mind-opening debates and shared love of music.

And last but certainly not least, my wonderful family and friends in Paris for their trust and encouragements: merci. This thesis is dedicated to Thérèse de David-Beauregard and Marie de Saint Victor (the other one), who are always in my thoughts.

CHAPTER 1

Introduction, aims and objectives

This chapter introduces the research problem addressed in this work. The objectives and scope of the study are defined and the structure of the thesis is outlined.

1.1. Introduction to sonothrombolysis

Microbubbles have long been used in the clinic as contrast agents for ultrasound imaging. They consist of gas-filled microspheres with a phospholipid, polymer, albumin or other biocompatible surfactant shell. On account of their size – typically 2-8μm, the same order of magnitude as a red blood cell – they are confined to the vasculature and are widely used to visualize blood circulation. In echocardiography, they improve endocardial border delineation [3]; they allow visualization of blood perfusion in small blood vessels in the myocardium and in focal liver lesions; they also facilitate the assessment of larger blood vessels, particularly when examining vascular abnormalities by Doppler imaging [4]. Beyond their routine diagnostic use as contrast agents, there is growing interest in the therapeutic potential of microbubbles. For instance, they constitute a promising method of delivering drugs or genes within the body. When oscillating under ultrasound exposure, microbubbles can induce changes in cell membrane permeability, permitting a molecule to enter the cytoplasm. They can also alter vessel wall permeability and enable drug extravasation into surrounding tissue, for instance in a tumour [5]. Another emerging application with major clinical potential is the use of microbubbles in ultrasound-mediated clot lysis, particularly in the context of ischaemic stroke.

1.1.1. Principle of sonothrombolysis

Stroke is a disturbance in the blood supply to the brain, causing rapid damage to brain tissue. It is estimated to be a leading cause of disability and the second highest cause of adult mortality worldwide, accounting for 5.5 million deaths every year [6], [7]. Around 80% of strokes are ischaemic, i.e. caused by an occlusion to a blood vessel which deprives the surrounding tissue of the necessary nutrients [6]. In these cases, there is strong evidence that thrombolysis (i.e. breaking down the blood clot) helps salvage affected tissue and improves clinical outcome [8]. At present, intravenous tissue-plasminogen activator (tPA)[1] is the only thrombolytic drug recommended by the British National Institute of Health and Care Excellence (NICE)[9], as well as the only one approved by the U.S. Food and Drug Administration (FDA) [10]. However, it carries the risk of potentially fatal side effects including intracranial haemorrhage. As a result, intravenous tPA administration is subject to rigid exclusion criteria [11], [12]. Among the most limiting of these criteria is the therapeutic time frame [13]: intravenous administration of the drug is only recommended within the first 3 hours following onset of stroke. In a study conducted at the California Acute Stroke Pilot Registry, only 4.3% of all ischaemic stroke patients arrived in the Emergency Department within this 3-hour window and were eligible for tPA. Of equal concern is the fact that even if all patients had arrived within the required time frame, only 28.6% of them would have been eligible for thrombolytic treatment [14]. Against this background, there is a clear need for an adjuvant therapy that improves the safety and efficacy of tPA treatment. The use of ultrasound (US) and injected microbubble agents is an attractive option. In particular, potentiating thrombolysis locally with ultrasound and microbubbles may allow a reduction in administered drug dose and could limit systemic side-effects, enabling thrombolytic treatment to become available to a larger

[1] Also commonly known as recombinant tissue plasminogen activator (rt-PA) reflecting its method of manufacture, or by specific chemical names of tPAs such as alteplase, reteplase and tenecteplase.

patient population. The echogenicity of microbubbles may also improve patient safety by enabling continuous treatment monitoring [15].

1.1.2. Scope of application

Given its prevalence and the high mortality rate associated with it, stroke is the primary focus of sonothrombolysis research. However, microbubble-enhanced sonothrombolysis has the potential to benefit other thrombotic conditions also. Occluded catheters [16] and dialysis grafts [17] tend to involve large blood clots, which are particularly difficult to dissolve with tPA. Conversely, in acute myocardial infarction, a major issue with current therapies is the phenomenon of "no-reflow", where the myocardial microvasculature is poorly reperfused after the coronary artery is recanalised. In both cases, ultrasound and microbubbles have the potential to address the shortcomings of existing thrombolytic therapies.

1.1.3. Microbubble-enhanced sonothrombolysis

In the 1970s, Trübestein, Sobbe *et al*. first suggested using ultrasound to destroy and remove thrombi [18]. Microbubbles as adjuvants to ultrasound were introduced by Tachibana *et al*. [19]: artificial human blood clots were exposed to 170 kHz ultrasound and urokinase; accelerated thrombolysis was noted when albumin microbubbles were present. Multiple *in vitro* and *in vivo* studies have subsequently shown that microbubbles improve clot breakdown with or without a thrombolytic drug, in addition to reperfusing the surrounding microvasculature (see Chapter 2) [20]–[23]. Several clinical trials have demonstrated accelerated recanalization of occluded vessels [24], [25]. However, real-time treatment monitoring methods need to be further developed and more work is required to improve treatment safety and efficacy.

1.1.4. Statement of the problem

The hydrodynamic conditions in occluded vessels represent one of the major challenges in developing effective sonothrombolysis protocols since they severely limit the number of microbubbles that can be delivered to and retained at the site of a thrombus. Amongst emerging approaches, microbubble targeting is a promising method for increasing the proximity between microbubbles and the thrombus surface, thereby enhancing their lytic effect and potentially enabling a reduction in the systemically administered tPA dose. "Biological" methods of antibody conjugation to the microbubble surface have been investigated [26]–[28]; they ensure thrombus specificity [28]–[30], but still rely on passive accumulation by limited flow. Magnetic targeting of the microbubbles is expected to overcome the restrictions posed by low flow rates by promoting active accumulation. To the best of the author's knowledge, this thesis is the first report to assess magnetic targeting as a method to enhance microbubble delivery in occluded vasculature and accelerate sonothrombolysis.

1.2. Outline of the thesis

1.2.1. Objectives of the work

The overall objective of this thesis is to investigate *in vitro* the potential of magnetic targeting to accelerate microbubble-enhanced sonothrombolysis.

The specific aims are as follows:

- To review the experimental evidence for microbubble-enhanced sonothrombolysis and to identify areas requiring further research.
- To identify the obstacles to drug and microbubble delivery in occluded microvessels and to investigate the potential of magnetic targeting to overcome them.
- To investigate the effect of magnetically targeted microbubbles on sonothrombolysis, both in the absence and in the presence of fibrinolytic drugs.
- To assess the utility of acoustic emission detection as a method of non-invasive treatment monitoring.
- To examine the effect of ultrasound with targeted and non-targeted microbubbles on clot microstructure.
- To identify and discuss possible mechanisms for sonothrombolysis.

1.2.2. Structure of the thesis

In Chapter 2, the published literature on microbubble-enhanced sonothrombolysis is reviewed, and the current challenges to clinical applications are discussed, together with recent approaches for overcoming them.

Among the most significant unresolved challenges is the difficulty of transporting sufficient numbers of microbubbles to the site of a clot in a region of obstructed flow. In Chapter 3, a model of a fully occluded arteriolar bifurcation is developed and drug/microbubble delivery in thrombosed vasculature is investigated both numerically and experimentally. Magnetic targeting is then evaluated as a method to improve microbubble delivery to the clot.

The consequence of this improvement on sonothrombolysis is then studied. Sonothrombolysis can either be performed as a standalone treatment for patients not eligible for conventional fibrinolytic drugs (mechanical sonothrombolysis), or as an adjuvant therapy, in conjunction with tPA (enzymatic sonothrombolysis).

In Chapter 4, the effect of magnetic targeting on mechanical sonothrombolysis is investigated, and various designs for an *in vitro* magnetic targeting system are tested.

In Chapter 5, the effect of magnetic microbubbles on enzymatic sonothrombolysis is examined. Treatment safety and lysis mechanisms are also discussed.

In the final chapter, conclusions for this study are presented and proposals for future work are outlined.

CHAPTER 2

Microbubbles in sonothrombolysis: a review of the literature

Sonothrombolysis can be enhanced by administration of acoustically-active microbubbles and this has the potential to be developed into a powerful adjuvant therapy for the treatment of occlusive conditions such as ischaemic stroke.

In this chapter, the role of microbubbles in sonothrombolysis is evaluated based on published in vitro and in vivo evidence and on a critical review of clinical trials to date. Mechanisms of microbubble-enhanced sonothrombolysis are discussed, with a special focus on acoustic cavitation and thermal effects. A number of challenges to widespread clinical adoption are identified. Key factors for future optimisation of treatment and microbubble design are proposed. Against this background, the rationale for investigating magnetically targeted microbubbles is presented.

A modified version of this review was published in Expert Opinion on Drug Delivery [31] and the contributions of Dr. Calum Crake to sections 2.5. and 2.6.1.c), and to Tables 2-1 and 2-2 are gratefully acknowledged.

2.1. Role of microbubbles in restoring vessel patency *in vitro* and *in vivo*

2.1.1. Clot size reduction: *in vitro* evidence

There is now a considerable body of literature supporting the potential of microbubbles to enhance sonothrombolysis. *In vitro*, various quantitative methods have been used to assess treatment success. From the early *in vitro* studies in the 1990s, clot mass loss has been used to evaluate the outcome of microbubble-enhanced thrombolysis[2]. Both at high [32], [33] and low excitation frequencies [23], [34], treatments combining ultrasound, microbubbles and tPA achieved greater mass loss than tPA alone or tPA with ultrasound. For instance, Datta *et al.* exposed human blood clots to various combinations of rt-PA, perflutren phospholipid microbubbles and 120 kHz ultrasound at a peak-to-peak pressure amplitude of 0.32 MPa [23]. The greatest clot mass loss was observed for clots treated with ultrasound, rt-PA and microbubbles (26.2%, $p = 0.001$). A significantly lower mass loss was achieved (16.0%) with ultrasound and rt-PA in the absence of microbubbles. In the clot mass measurement process, the clot is briefly blotted and placed on a scale. Though straightforward in theory, ensuring reliable and repeatable measurements is challenging, because clot mass is highly dependent on the water content, which is extremely sensitive to the weighing protocol used. A further difficulty in comparing results across studies is the significant variability in the clot models themselves, with a recent study suggesting that the degree of clot retraction is a major determinant of the extent of sonothrombolysis [35].

In addition to clot mass, Kondo *et al*. used diagnostic ultrasound to assess clot cross section during treatment [36]. Both methods showed that lysis was increased when

[2] Thrombolysis refers to the process of thrombus breakdown, while fibrinolysis refers more specfically to the degradation of the fibrin network within the thrombus.

microbubbles were used. Optical monitoring of clot size variation has also been carried out by placing thrombi in acoustically and optically transparent tubing [37], [38]. A study by Petit *et al*. using 1.6 MHz ultrasound reported significant reduction in clot diameter when microbubbles were present, with the magnitude depending on the acoustic pressure and with the location confined to the region exposed to the acoustic beam [37]. The study also showed that microbubbles have the potential to considerably reduce the required tPA dose, though withholding the drug altogether and using only ultrasound with microbubbles led to a visible but only relatively small change in clot diameter (Figure 2-1). This was in contrast with an earlier demonstration that a significant reduction in clot cross section could be achieved without the use of drugs when treating venous blood clots with microbubbles and low-pressure ultrasound at both 1 MHz and 40 kHz [38].

Generally, while the efficiency of microbubbles has been robustly established *in vitro* for sonothrombolysis in the presence of fibrinolytic drugs, evidence of microbubble-enhanced sonothrombolysis in the absence of drugs is mixed. The former treatment has been shown to be more efficient than ultrasound alone, although depending on experimental conditions, the extent of lysis achieved may vary considerably. On the other hand, while clots treated with ultrasound and microbubbles but without fibrinolytic drugs constitute a control group in several sonothrombolysis studies [23], [32]–[34], [37], there is a rather limited body of literature investigating this strategy as a standalone treatment option *in vitro* [38], [39]. This is attributable to the fact that drug-mediated thrombolysis is the gold standard in clinical practice, and that ultrasound and microbubbles are often considered as adjuvant therapies with a clear potential to reduce the quantity of drugs required [23], [37], [40] but not to replace them. In addition, the endogenous tPA found in the *in vivo* setting may be adequate to lyse small clots when combined with microbubbles and ultrasound [21], which

makes comparison with a drug-free *in vitro* model difficult. However, since a substantial proportion of the ischaemic stroke patient population is ineligible for drug-based treatment [14], further investigation of ultrasound and microbubbles as an alternative therapy is warranted.

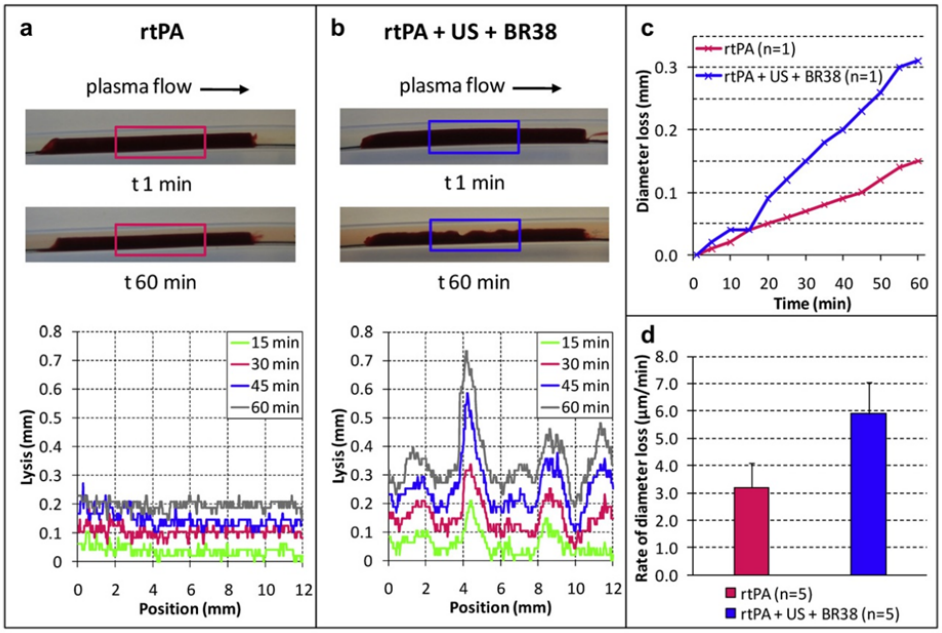


Figure 2-1: Example of clot diameter reduction under flow conditions with 1.6 MHz ultrasound and microbubbles (BR38, Bracco Suisse S.A., Geneva, Switzerland), in the presence of fibrinolytic drugs. (a) rt-PA 0.3 mg/mL and (b) rt-PA 0.3 mg/mL + US 1000 kPa + BR38 (23106 MB/5 min): every 5 min during 60 min, clot lysis profiles and diameter over 12 mm were measured (red and blue rectangles) with a MATLAB program; (c) the diameter loss (mm) was plotted as a function of treatment time (min) for each tested clot; (d) the rate of diameter loss (mm/min) was calculated and averaged for each condition. Reproduced from [37] ***with permission of Elsevier.***

2.1.2. Improving microperfusion

The use of microbubbles has been shown to be beneficial not only in lysing large thrombi that would cause main stem vessel occlusions, but also in reperfusing surrounding microvessels, which is critical to the recovery of ischaemic tissue. This effect was demonstrated in an *in vitro* flow model of partially occluded microvasculature [22]. The upstream pressure burden decreased progressively with the use of 1-MHz ultrasound, tPA and microbubbles. Interestingly, however, the authors found that similar lytic efficacy could be achieved without fibrinolytic drugs if higher acoustic pressures were used.

The first *in vivo* confirmation of the effect was provided by Nedelmann *et al.* in a murine stroke model where a temporary occlusion was created in a middle cerebral artery and removed after 90 minutes, leaving a persistent impairment of microcirculation after the main stem vessel was reopened [41]. Computerised tomography scans of brain microvasculature (Figure 2-2) revealed that only the group treated with a combination of ultrasound, microbubbles and tPA showed a fully reperfused microcirculation in the affected hemisphere, while standard tPA treatment or tPA with ultrasound resulted in only partial flow restoration. Pacella *et al.* also reported improvements to tissue perfusion with ultrasound and microbubbles in a model simulating the distal microvascular thrombosis that occurs after primary percutaneous coronary intervention [42].With robust evidence of clot lysis acceleration in the presence of ultrasound and microbubbles, clinical studies were carried out and are described below.

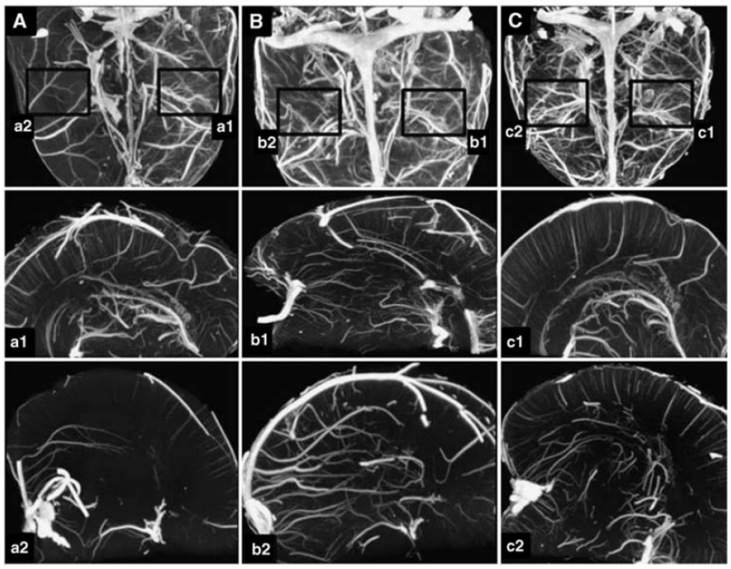


Figure 2-2: sample micro- and nano- computed tomography images of murine brain microvasculature after treatment with ultrasound alone (column A), with ultrasound and microbubbles only (column B), with ultrasound and rt-PA only (column C). The first row demonstrates whole brain scans; the second and third rows respectively show details of the contralateral hemisphere and of the treated hemisphere. This case illustrates persistent impairment of the microcirculation after treatment with ultrasound only. It was partially restored after treatment with ultrasound and microbubbles, and after treatment with ultrasound and rt-PA. Reproduced from [41] ***with permission of SAGE publications.***

2.2. Clinical evidence

Clinical trials of microbubble-enhanced sonothrombolysis have reported promising results (Table 2-1). However, the treatment has yet to fully realize its potential because the critical factors for therapeutic success remain poorly understood. In the hospital setting, microbubble-enhanced sonothrombolytic therapy can be delivered by ultrasound systems commonly used for diagnostic applications. To date, such therapies have been performed with two distinct types of systems, both emitting at frequencies around 2 MHz: Transcranial Doppler (TCD) ultrasound transducers, and Transcranial Color-Coded Duplex (TCCD) transducers. The latter provides simultaneous imaging of the brain structure and assessment of blood flow by superimposing a greyscale B-mode image of the brain with colour-coded flow velocity data. In the past, TCD has been used more frequently than TCCD in randomized controlled trials and case-control studies of sonothrombolysis and sonolysis [43]. However, to the best of the author's knowledge, no conclusive difference in efficacy has been established to date between the two technologies [43]. These systems serve both as therapeutic transducers and monitoring devices throughout treatment, which typically lasts from 30 to 120 minutes.

TCD was used in the seminal sonothrombolysis study CLOTBUST (Combined Lysis Of Thrombus in Brain ischaemia using transcranial Ultrasound and Systemic tPA), a multicentre phase II randomized trial conducted by Alexandrov *et al.* In this trial, all 126 patients received a standard dose of r-tPA, and patients in the treatment arm were continuously monitored using TCD without microbubbles. These patients experienced a higher rate of either complete recanalization or of dramatic clinical recovery after 2h (49% in the target group against 30% in the control group, $p = 0.03$); functional outcome at 3 months was also improved, but without statistical significance (42% against 29%, $p = 0.20$). In fact, based on these preliminary findings, the authors estimated that a pivotal

study on the efficacy of US enhanced thrombolysis would require 600 patients [1], which is far from being realistic in the short term. In order to reduce this number, microbubbles have subsequently been investigated as a method to accelerate the effects of sonothrombolysis. Viguier *et al.* suggested the use of commercially available, galactose-based microbubbles (Levovist®, Schering AG, Berlin, Germany) [44]. In a retrospective feasibility study involving 8 patients, 4 experienced complete recanalization during insonation with 2-MHz TCCD, and 6 manifested significant clinical improvement at 24h. On a larger scale, a non-randomized extension of the CLOTBUST trial by Molina *et al.* further established that microbubbles may enable faster and more complete recanalization [25]. As in CLOTBUST, however, improvement at 24 hours and 3 months was on average higher in the treatment group but without statistical significance. Following this promising evidence, sonothrombolysis with newer generations of bubbles was clinically evaluated and provided similarly encouraging results in terms of time and completeness of recanalization [2], [24], [45], with the further demonstration that early recanalization was sustained at the end of treatment [2], [24] and at 24 hours [24].

Vessel recanalization is a widely accepted marker for therapeutic efficacy, since accelerated flow restoration increases tissue salvage in the ischaemic region. In stroke therapy, it is therefore usually associated with improved neurological outcomes [8]. In the case of microbubble-potentiated sonothrombolysis, with clear indications that the treatment does indeed improve recanalization in cerebral arteries, a trend towards better neurological recovery emerges, but its statistical significance still remains to be demonstrated both *in vivo* and in the clinic.

In laboratory studies *in vivo*, neurological assessment has been performed at 24 hours after microbubble-enhanced sonothrombolysis at 1-3 MHz in a rabbit [21] and a murine [41] stroke model; in both cases, no significant difference in functional outcome was observed.

Clinical investigations have been more encouraging, though comparing published clinical evidence of microbubble-enhanced sonothrombolysis is made difficult by the wide range of treatment protocols, by the choice of different endpoints, as well as by limited population sizes. Clear trends towards better outcomes at 24h [25] and 3 months [2], [25] were nevertheless identified by two studies evaluating microbubble-enhanced sonothrombolytic treatment against tPA alone, with a two-fold increase in functional independence rates at 3 months in one case [2], but improvements did not reach statistical significance. In addition, two studies comparing sonothrombolysis with and without microbubbles demonstrated a benefit with microbubbles [24], [45], though only one reached statistical significance [24]. The small sample size may explain the lack of conclusive evidence in the other study (n= 15) [45]. Further clinical investigation should consider recent evidence that the benefit afforded by sonothrombolysis on functional outcomes depends on the affected vessel: M1 occlusion patients have been shown to benefit more from ultrasound treatment than carotid T occlusion patients [46].

With encouraging evidence of early recanalization, and the possibility of improved neurological outcomes, additional large-scale investigations are needed to confirm the potential of microbubble-enhanced sonothrombolysis to restore neurological function. A large-scale (n = 276) randomised controlled trial is currently underway, with expected results in 2017. It investigates the efficacy of microbubble-enhanced sonothrombolysis in acute ischaemic stroke, in the presence and in the absence of fibrinolytic drugs [47]. As clinical implementation of microbubble-enhanced sonothrombolysis is gaining impetus, effective translation will require improved understanding and control of the underlying mechanisms.

2.3. Mechanisms of microbubble-enhanced sonothrombolysis

The mechanisms of ultrasound-mediated clot lysis and the role of microbubbles in this process remain to be fully elucidated. A number of physical phenomena may be involved, including acoustic cavitation and heating.

2.3.1. Cavitational mechanisms

Acoustic cavitation describes the formation and activity of vapour- and/or gas-filled bubbles in a liquid under the influence of an acoustic field, and there is considerable evidence that it plays an important role in sonothrombolysis. At low acoustic excitation pressures, bubbles oscillate volumetrically, radiating energy predominantly at the frequency of excitation. As the driving pressure increases, the amplitude of the bubble oscillation increases and becomes increasingly non-symmetrical. The frequency spectrum of the acoustic emissions produced by this so called non-inertial cavitation will contain higher harmonics of the driving frequency, as well as sub- and ultra- harmonics of that frequency (Figure 2-3a). Above a certain excitation level, the periodic nature of the oscillations disappears as bubbles expand unstably over the rarefactional half-cycle and proceed to collapse extremely violently, emitting signals over a wide range of frequencies (broadband noise, Figure 2-3b): this is known as inertial cavitation [48] since the bubble collapse is dominated by the inertia of the surrounding fluid. The precise definition inertial cavitation varies according to the theoretical framework used to describe bubble dynamics and indeed has been the subject of some controversy. For the purposes of this review the onset of inertial cavitation is deemed to coincide with the appearance of broadband noise in the acoustic emissions since this can be detected experimentally and has the potential to be used for clinical treatment monitoring.

Supporting evidence for the role of cavitation in sonothrombolysis was first provided by Everbach and Francis in a cavitation suppression experiment carried out in a hyperbaric chamber in the absence of added microbubbles [49]: the authors observed a decrease in clot lysis when the static pressure in the chamber was increased. In this experiment, however, a 1 MHz ultrasound excitation was used in conjunction with a 20 MHz combined active/passive cavitation detector, making the setup exclusively sensitive to acoustic emissions from inertial cavitation. A detailed mechanistic study on the role of both stable and inertial cavitation was first carried out by Datta *et al.* [50] who employed a 120 kHz excitation frequency without added microbubbles and broadband passive cavitation detectors to demonstrate that stable cavitation events were associated with significantly greater lytic success, whilst inertial cavitation slightly reduced ultrasound-mediated enhancement of sonothrombolysis.

Microbubble contrast agents are known to reduce the acoustic pressure needed to observe cavitation by providing a pre-existing bubble that is more readily cavitated than the surrounding medium [51]. This could provide an explanation for the improvements in lysis observed in the presence of microbubbles.

Among the frequency components emitted by cavitating microbubbles, subharmonic and ultraharmonic emissions as well as broadband noise have already been correlated with thrombolysis [23], [33], [52], [53]. With sub- and ultra-harmonic components as hallmarks for stable cavitation as opposed to broadband noise for inertial cavitation, these studies have investigated the most effective cavitational regime.

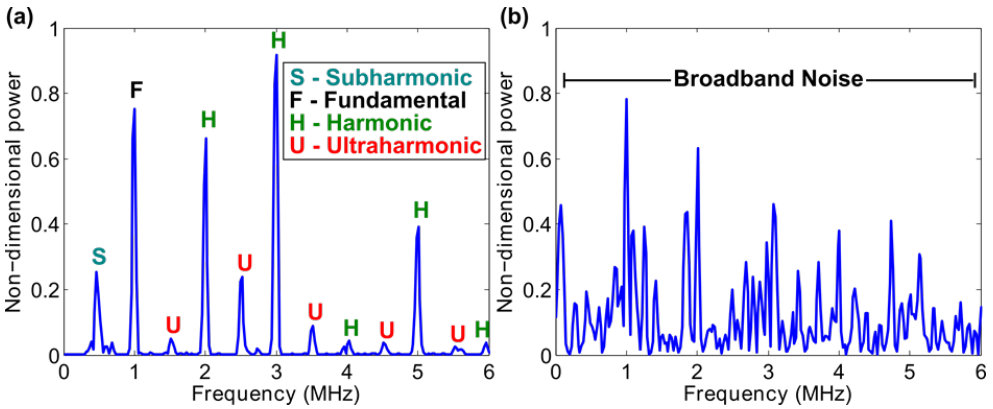


Figure 2-3: Representative frequency spectra for microbubble response at an excitation frequency (f_0) of 1MHz, showing (a) fundamental (f_0), subharmonic ($f_0/2$), harmonic ($2f_0, 3f_0, 4f_0$…) and ultraharmonic ($3f_0/2, 5f_0/2, 7f_0/2$…) peaks; and (b) broadband noise with superimposed harmonics.

2.3.2. Non-inertial cavitation

When undergoing non-inertial cavitation, microbubbles oscillate in a regular, sustained fashion and transfer momentum to the surrounding fluid, causing localized eddying motion. This microstreaming effect may encourage thrombus surface erosion. It may also increase transport of therapeutic agent to the clot site [49], which contributes to increased lytic success [54]. Additionally, gas bubbles embedded into the fibrin network may damage the fibres directly as they expand and contract [55].

In support of the hypothesis that cavitation plays a major role, sustained sub- and ultraharmonic emissions over the whole duration of tPA-facilitated sonothrombolysis have been linked to improved clot lysis in the presence of microbubbles both *in vitro* [33], [56] and ex vivo [52]. In these cases, sonothrombolysis without fibrinolytic drugs did not result in improved clot lysis, which is also consistent with the hypothesis that microbubbles increase drug transport to the clot. Datta *et al*. provided further evidence of microbubble-enhanced drug transport in a study employing Definity® where fluorescently labelled rt-PA penetrated deep into clots treated with 120 kHz ultrasound, rt-PA and microbubbles, whilst penetration was only superficial in clots treated with rt-PA only or with rt-PA and ultrasound [56] (

Figure 2-4). Moreover, the authors exposed clots to increasing acoustic pressures and only observed significant mass loss at pressures above the ultraharmonic emission threshold.

2.3.3. Inertial cavitation

As a microbubble collapses during inertial cavitation, it may produce a high speed jet of fluid that can cause damage to the fibrin network [57]. At high excitation pressures, it may also collapse with such violence that a shock wave is released, directly deteriorating the clot surface [48].

Inertial cavitation events have also been correlated with higher thrombolysis relative to rt-PA alone, (although not relative to stable cavitation alone). In a small scale feasibility study using optical coherence tomography, Kim *et al*. observed the effect of lipid microbubbles on sonothrombolysis with tPA at 1 MHz *in vitro* and found that the presence of microbubbles was associated with increased broadband noise emissions and a trend in decreased clot volume [53]. Simultaneously, formation of irregular patterns was observed on the clot surface facing the ultrasound transducer in the target group.

In diagnostic use, however, inertial cavitation is conventionally avoided, as collapsing microbubbles may disrupt the endothelium [58]. In microbubble-enhanced sonothrombolysis, the benefits associated with these events must therefore be weighed against possible safety concerns and the opportunity to achieve similar or greater levels of sonothrombolysis in a stable cavitation regime.

It should also be noted that cavitational response at the clot site is affected by bubble replenishment patterns: inertial cavitation events often lead to microbubble destruction, whereas stable cavitation is typically sustained for longer periods [33].

The exact impact of each type of cavitation and their relative contribution to clot lysis is unclear. It is probable that both coexist, with varying weight depending on the excitation conditions.

2.3.4. Thermal mechanisms

The contribution of thermal elevation to microbubble-enhanced sonothrombolysis has also been studied, since a rise in temperature in the clinically relevant range (25 - 41°C) is also associated with higher enzymatic lysis [59].

In the absence of microbubbles in the medium, there is a wide consensus that thermal mechanisms can only account for a very small proportion of the lytic effect; although mild heating due to ultrasound absorption by the clot and the surrounding fluid has been recorded in several studies [20], [60]. Microbubble oscillations in a fluid may cause an additional increase in local temperature due to the absorption of energy from the radiated sound field. Repeated oscillations create further heating through viscous friction in the fluid. Heat conduction from microbubbles in the compression phase is also a contributing factor [48]. In diagnostic applications, such temperature elevations are a safety concern, as surrounding tissue may incur damage; in therapeutic applications of ultrasound, they must be balanced with the expected therapeutic benefit.

There is a limited amount of literature documenting the impact of thermal mechanisms on microbubble-enhanced sonothrombolysis, but available evidence shows that resulting temperature elevations are slight *in vivo* [41].

Trial or Study	Complete Rec 1-2 hours	Complete Rec 24 h	3 months mRS	sICH	Definition of sICH
Sonothrombolysis trials					
Alexandrov *et al.* 2004 [1]	T:29/63 C:11/63	T: NA C: NA	mRS (0-1) T: 22/53 C: 14/49	T:3/63 C:3/63	ICH with clinical worsening (indicated by an NIHSS score of ≥4) within 72 hours of stroke's onset
Eggers *et al.* 2008 [61]	T: 3/19 C: 2/18 Partial Rec: T:8/19 C: 2/18	T: 14/19 C: 8/18 Partial Rec: T:2/19 C: 6/18	mRS (0-1) T:4/19 C: 0/18 mRS (0-2) T:5/19 C: 1/18 BI (> = 95) T: 8/19 C:0/18	T:3/19 C: 1/18	ICH on CT within 72 hours from symptom onset associated with an increase in NIHSS ≥ 4 points
Skoloudik *et al.* 2008 [62]	T: 7 /15 (46%) C: NA	T: 12 (80%) C: 10 (67%)	mRS (0-1) T: 8 (53%) C: 4 (26.6%) mRS (0-2) T: 8 (53%) C: 4 (26.6%)	T: 1 (6.6%) C: 1 (6.6%)	ICH on CT/MRI within 24 hours from symptom onset associated with an increase in NIHSS ≥ 4
Sonothrombolysis + MB trials					
Molina *et al.* 2006 [25]	T: (MB): 21/38 (US): 15 /37 C: 9 /36 Partial Rec: T: (MB): 6/38 (US): 10 /37 C: 5 /36	T: unavailable C: unavailable	mRS (0-2) T: (MB):21/38 (US) 17/37 C: 12/36	T: (MB) 1 (US) 1 C: 2	ICH on CT within 72 hours from symptom onset associated with an increase in NIHSS-score of ≥ 4 points
Alexandrov *et al.* 2008 [45]	T:6/12 C:0/3 Partial Rec: T:4/12 C: 2/3	T: unavailable C: unavailable	mRS (0-1) T: 2/5 C:0/1	T: 0 C: 0	ICH on CT within 72 hours from symptom onset associated with an increase in NIHSS-score of ≥ 4 points
Perren *et al.* 2008 [24]	T:7/11 C:8/15	T:NA C: NA	T:NA C:NA 24-hour NIHSS > = 4 points T:9/11 C:6/15	T:1/11 C:1/15	ICH on CT within 72 hours from symptom onset associated with an increase in NIHSS score of ≥ 4 points
Molina *et al.* 2009 [2]	T: 13/23 C: 4/12 Partial Rec: T:2/23 C:3/12	T: unavailable C: unavailable	mRS (0-1) T: 14/22 C: 4/11	T: 3/23 C: 0/12	PH type 2 or type 2 remote (PH2/PH2r) on a repeat CT within 24-36 hours after the treatment period that in the opinion of the treating physician is causally related to neurological deterioration (≥ 4 NIHSS points)

Table 2-1: Safety and efficacy of clinical trials, adapted from [43]***. US = Ultrasound; MB = microbubbles; T= Treatment ; C = Control; mRS = Modified Rankin Scale; BI = Barthel Index; NIHSS = National Institute of Health Stroke Scale; ICH = Intracranial Haemorrhage; PH = Parenchymal Haemorrhage.***

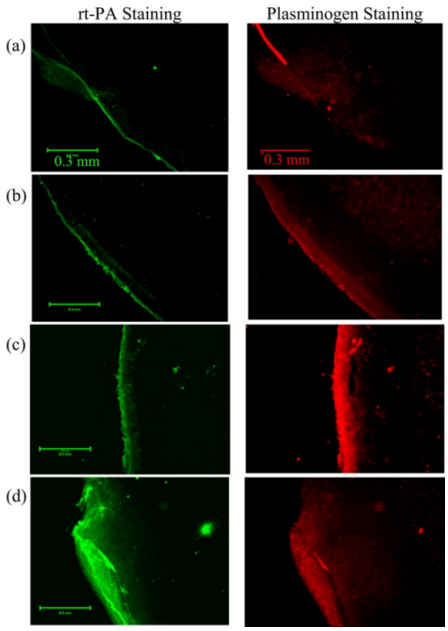


Figure 2-4: dual-fluorescence imaging of blood clots after exposure to 120-kHz ultrasound, rt-PA and Definity® microbubbles. In the left column, rt-PA is stained by fluorescein isothiocyanate (FITC) – conjugated secondary antibody. For the same section, the right column shows plasminogen stained with Texas red (TRITC)–conjugated secondary antibody. Clots were treated with (a) no rt-PA, Definity® or US (control); (b) rt-PA alone treatment; (c) rt-PA, PBS infusions and US (0.32 MPa peak-to-peak amplitude); and (d) rt-PA, Definity® infusions and US (0.32 MPa peak-to-peak amplitude). All scale bars represent 0.3mm. Reproduced from [23] ***with permission of Elsevier.***

2.3.5. Other mechanisms

In certain cases, authors have reported sonothrombolytic success in the absence of either thermal elevation or cavitation [33], [63], suggesting the existence of additional mechanisms. Hypotheses include radiation force – mediated percolation of microbubbles through the thrombus, where the microbubbles are pushed by the propagating ultrasound wave into the thrombus [64]. An *in vitro* study by Acconcia *et al*. provided supporting evidence on the role of radiation forces [65]. The authors used a high frame rate camera to observe the interaction between microbubbles and the surface of fibrin clots under 1 MHz ultrasound. The presence of microbubbles was shown to enhance local deformation of the clot surface: boundary displacement reaches 80 ± 24 μm at 1.6 MPa with microbubbles,

against no detectible displacement in the absence of microbubbles. Microbubbles were also observed to penetrate the clot, forming patent tunnels in the fibrin matrix.

Stimulations of the microcirculation through changes in the release of vasoactive compounds by endothelial cells have also been considered, as they would enhance drug transport to the clot [66], [67].

Acoustic cavitation appears to be the leading mechanism underlying sonothrombolysis, though it is not necessarily the only one. Gaining a deeper understanding of these mechanisms would not only be instrumental in optimizing treatment efficacy, it is also critical in ensuring patient safety. In particular, it is essential to safeguard vessel wall integrity and to prevent clot fragmentation into large pieces liable to cause downstream embolisation.

2.4. Clinical challenges

In order to ensure successful clinical implementation, a number of challenges must be addressed, such as ultrasound wave attenuation in biological tissue, therapeutic agent delivery, as well as patient safety concerns.

2.4.1. Ultrasound attenuation in bone and tissue

A major advantage of sonothrombolysis is that it can be performed non-invasively. For use in the treatment of stroke however, this requires the issue of ultrasound attenuation by prefocal bone and tissue to be addressed.

As ultrasound propagates through the body, it is reflected/scattered and absorbed by tissue and dissipated as thermal or mechanical energy. As a consequence, achievable treatment depth is reduced and higher acoustic pressures are needed to achieve a therapeutic effect at the clot site, which may compromise safety.

This is of particular concern in stroke treatment, as the cranium is a highly attenuating structure. A thinner portion of the skull, the temporal bone window, is routinely used for transcranial diagnostic ultrasound, if needed in conjunction with microbubbles as echo-contrast agents. In a substantial proportion of patients, however, this acoustic window is insufficient for imaging. The population affected is difficult to estimate, because reporting is not generalized, but available data suggests a range of 15-20% [44], [68].

Even with the existence of the temporal bone window, insonation through the skull results in a dramatic drop in peak negative pressures of up to 80% at 1 MHz [38]. Reduced yet still significant lysis can be achieved through attenuating material at reasonable acoustic pressures even in the absence of fibrinolytic drugs, as evidenced *in vitro* trough a cranium by Porter *et al.* at 1 MHz and 40 kHz [38] and *in vivo* through a tissue mimicking phantom by Xie *et al.* at 1.5 MHz [69].

As attenuation increases with frequency in bone and tissue, low-frequency ultrasound is an option to increase penetration depth. Yet in the clinic, this effect must be balanced against safety considerations: low-frequency ultrasound is associated with an increased risk of intracranial haemorrhage (see Optimizing Treatment paragraph below).

Another consequence of ultrasound attenuation in the cranial bone is the risk of thermal damage to the skull. Thermal elevation arises from a combination of high energy attenuation and poor heat convection, since blood perfusion in the bone is limited. This is however highly dependent upon the exposure conditions. A theoretical model by Nahirnyak *et al.* predicted a maximal temperature rise of 1°C when the cranium is exposed to 1 MHz pulsed ultrasound with a spatial peak temporal average intensity of 0.4 W/cm^2 [70].

Finally, the curvature and the uneven thickness/composition of cranial bone create phase aberrations that distort the intracranial ultrasound field [71]. Broad beams that encompass

a larger portion of the brain may be used to ensure that the region of interest is isonated despite the distortions [72]. Various beamforming methods have also been suggested, including element phasing [73], or time-reversal acoustics [74].

2.4.2. Therapeutic agent delivery to the thrombus

The choice of microbubble dose and administration method is largely a balance between treatment improvement and safety. Clot lysis has been shown to improve with microbubble concentration up to a point [75]. However, at higher levels this carries increased risk of 'shielding' target tissue and/or further microbubbles from ultrasound exposure, or embolism due to the gas contained within the bubbles [76]. Additionally, the delivery method (infusion or bolus) may place a limit on total treatment duration – microbubbles are conventionally injected by bolus which provides strong imaging contrast enhancement for a short time [68], [77]; continuous infusion has been shown to increase the useful duration of ultrasound contrast enhancement while still providing adequate enhancement [78]–[80] and has been used clinically in some trials of sonothrombolysis [24]. Bubble replenishment patterns at the clot site also potentially affect acoustic response and lytic mechanisms, as outlined above in the Mechanisms section.

Another concern in microbubble-enhanced sonothrombolysis is the delivery of drugs and microbubbles through the blood stream to an area of reduced flow. The difficulty of achieving microbubble transport to the clot was highlighted by Culp *et al.*'s study of canine arteriovenous grafts with low-frequency ultrasound, where direct intragraft injections of microbubbles tended to lead to more successful recanalization than intravenous delivery (8/8 with direct injections, against 4/10 with IV delivery and 0/8 for direct saline injection) [17]. In a later study with a similar animal model, Xie *et al.* investigated "image-guided" ultrasound therapy, where the clot is continuously imaged with diagnostic ultrasound, and higher intensity therapeutic pulses are triggered only when

microbubbles are detected in the ischaemic region [15]. With this strategy, high rates of recanalization were achieved in the absence of any fibrinolytic drugs (79% angiographic success after 45 min of treatment). This intermittent approach maximizes the efficiency of microbubbles by allowing their complete replenishment at the clot site, whereas more regular ultrasound exposures may destroy the microbubbles before they reach the region of interest. It also enables continuous treatment monitoring and limits unnecessary exposure to high intensity ultrasound [15].

2.4.3. Effects of an underlying pathology

Most *in vivo* studies have been conducted in healthy animals. However, in the clinic, occlusive events are due to a variety of pathologies which might interfere with the success of microbubble-enhanced sonothrombolysis. In particular, cholesterol levels in the thrombus may affect lysis rates . An *in vivo* investigation of atherosclerosis, a major cause of myocardial infarction and stroke, indicated that this was not the case: both atherosclerotic and healthy pigs with acute myocardial infarction experienced a significant decrease in perfusion defect size after treatment with intermittent 1.6 MHz ultrasound, fibrinolytic drugs and microbubbles [81].

2.4.4. Safety

Though microbubble contrast agents are widely recognized as safe and are in routine use in the clinic, rare adverse effects have been reported, such as headaches, nausea and chest pain [82]. They are usually mild and rapidly self-resolving [83], [84]. The present discussion will focus on safety concerns specifically associated with microbubble-enhanced sonothrombolysis

2.4.4.a) Microembolisation

Disruption of a thrombus by ultrasound and microbubbles may result in its fragmentation [38], which carries the risk of secondary embolisation in the microvasculature if clot debris are larger than downstream capillaries (~ 10μm). The size distribution of resulting clot fragments depends greatly on the ultrasound exposure conditions [85], [86]. Ariani *et al.* observed that 99% of clot fragments were under 10 μm in size after *in vitro* sonication of human thrombi at 20 kHz in pulsed mode, in the absence of microbubbles of fibrinolytic drugs [87].

To the authors' best knowledge, no case of pulmonary or systemic embolisation has been reported to date in clinical trials of microbubble-enhanced sonothrombolysis. In order to further increase safety, a study by Molina *et al.* excluded patients with a history of right-to-left cardiac shunt [2], a condition known to increase the risk of re-embolisation.

2.4.4.b) Intracranial haemorrhage

In the case of ischaemic stroke, the main safety concern associated with existing therapies is the risk of intracranial bleeding. Occasionally, intracranial haemorrhage is accompanied by detectable clinical symptoms, often very serious. In most cases, though, the transformation is asymptomatic, i.e. it does not have neurological manifestations. Debate is currently ongoing regarding the clinical significance of asymptomatic bleeding, in order to determine whether it is part of the natural course of reperfusion or whether it is associated with worse outcomes [88]. While stroke therapy research endeavours to limit all types of bleeding, particular emphasis is laid on avoiding symptomatic events, which are clinically catastrophic.

Treatment of ischaemic stroke with tPA is known to increase the risk of both asymptomatic and symptomatic intracranial haemorrhage [89], [90], and the use of ultrasound in conjunction with tPA can increase symptomatic bleeding, particularly at low frequencies [91]. The introduction of microbubbles into the treatment strategy could decrease bleeding rates by lowering cavitation thresholds, thereby allowing thrombolytic effect with reduced damage to surrounding tissue. In addition, using microbubbles and ultrasound to accelerate recanalization may decrease the incidence of symptomatic events, since late revascularisation is associated with an increased risk of symptomatic transformations [92]. However, inappropriate exposure conditions may lead to endothelial damage.

In this case, as previously, it is difficult to draw conclusions from the available data due to the wide variety of experimental conditions reported. A slight trend in increased asymptomatic haemorrhages could nonetheless be noted in two studies comparing microbubble and tPA-enhanced sonothrombolysis with tPA alone [2], [25]. However, the addition of microbubbles may not be the main cause of haemorrhagic transformation, as

similar bleeding rates were observed in studies comparing ultrasound as an adjuvant to tPA with and without microbubbles [24], [25].

Reports of symptomatic transformations were rare and differences in occurrence rates between experimental groups were inconclusive in several studies [24], [25], [45]. A prominent exception was found in the TUCSON trial (Transcranial Ultrasound in Clinical SONothrombolysis), a multicentre phase I-II dose escalation, randomized, single-blinded investigation led by Molina *et al.* [2]. In this study, all patients received intravenous tPA, and the target group also underwent TCD monitoring for 90 min with simultaneous microbubble infusion. Initially, four dose tiers of microbubbles (MRX-801, ImaRx Therapeutics Inc.) were to be evaluated, all of which well below the anticipated safety limit on bubble concentration. The first cohort received half of the dose used in the pilot safety study [45] and confirmed previous findings with shortened time to recanalization, improved sustained complete recanalization, a trend towards better outcomes at 3 months, and no symptomatic haemorrhage. On the other hand, in the second cohort, who received the microbubble dose deemed safe in the pilot study, 3 of 11 patients developed symptomatic haemorrhage, 2 of which were fatal. The study was therefore terminated prematurely. The reasons for such events are unclear, since patients had already been subjected to the same conditions without adverse events. It is postulated that unregulated blood pressure played a role in both fatal events, though the mechanisms of symptomatic and asymptomatic haemorrhage under ultrasound exposure are yet to be fully elucidated. It is critical to gain further understanding into the impact of ultrasound and microbubbles on haemorrhagic transformations, for clinical use of microbubble-enhanced sonothrombolysis to become widespread.

2.5. Optimizing treatment protocols

The acoustic response of microbubbles and hence their effect on thrombolysis depends on a number of factors relating to the microbubbles themselves, the ultrasound exposure regime and their mode of administration.

2.5.1. Influence of Ultrasound Parameters

The ultrasound exposure conditions used in microbubble-enhanced sonothrombolysis are defined by a number of parameters which are largely a balance between lytic efficiency and treatment safety.

2.5.1.a) Pressure

Ultrasound-enhancement of thrombolysis has been shown only to occur above threshold pressure levels sufficient to induce cavitation. Microbubbles may be used to lower this threshold. Previous mechanistic studies on cavitation-enhanced sonothrombolysis have employed widely different frequencies, clot models and exposure regimes, making it difficult to draw general conclusions about the optimal acoustic pressure, which varies greatly between studies (Table 2-2). In addition, the thresholds for cavitation are highly dependent on ultrasound frequency, material parameters and presence of artificial cavitation nuclei. This is further confounded by issues in reporting: cavitation activity is not conventionally monitored in clinical practice, and the pressure output of diagnostic probes is frequently not reported.

2.5.1.b) Frequency

The choice of ultrasound frequency for microbubble-enhanced thrombolysis is largely governed by three factors: the size of the microbubbles, which affects their resonant frequency [48], the increase in attenuation with frequency, which limits the depth of

treatment at higher frequencies, and the increased opportunity for standing waves to form in the cerebral cavity at lower frequencies [72]. The cavitation threshold of microbubbles has also been shown to increase with frequency [93], [94].

Previous studies have generally employed either a 'low' (20-500 kHz) or a 'high' (MHz) frequency range [23] (Table 2-2). The majority of clinical and *in vivo* studies to date have used higher frequency ultrasound, most commonly in the 1-2 MHz range conventionally used by Transcranial Doppler devices. The use of lower frequency ultrasound has advantages of improved skull penetration and positioning tolerance due to insonation of a larger volume. However, the exposure parameters must be carefully chosen to ensure safety: a prominent clinical trial using 300 kHz ultrasound (without microbubbles) was terminated early due to high incidence of intracranial haemorrhage [91]. Follow-up work has suggested this may have involved disruption of the blood-brain barrier [95] due to multi-reflection interference of the long, wide-beamed pulses used [96] or formation of standing waves resulting in pressures above the cavitation threshold [74], both of which could be remedied by changes to the exposure parameters [97].

2.5.1.c) Pulse Length

At pressures exceeding the inertial cavitation threshold a microbubble is likely to be destroyed within a few cycles of ultrasound exposure [98]. However, *in vitro* studies have shown improved lysis (up to a plateau) with longer pulses [99] of tens to hundreds of cycles [22], [100], possibly due to activation of additional bubbles and fragmentation into 'daughter' bubbles [101], or to formation of larger oscillating bubble clusters [102]. Conversely, other studies found only a limited direct effect of pulse length [103] suggesting that shorter pulses preserve microbubbles for longer and result in emissions over a broader frequency range [75].

Clinically, optimisation of pulse length must be balanced against safety concerns, with longer pulses depositing a larger amount of energy within the brain, and with care to avoid standing waves encountered in previous studies [91]. The conventional Mechanical Index metric used to quantify the likelihood of adverse biological effects by diagnostic ultrasound machines is based only on pressure and frequency and assumes a single cycle pulse, however cavitation thresholds of both tissue [74] and microbubbles [104] have been shown to decrease with pulse length, increasing the potential for bioeffects [105] under conditions which would normally be regarded as safe.

2.5.1.d) Pulse Repetition Frequency (PRF)

The ratio of the pulse length to pulse repetition period is known as the duty cycle [106]. Increasing the duty cycle by either increasing PRF or pulse length has been shown to reduce the cavitation threshold [107] in water. Diagnostic imaging duty cycles are typically very low (~0.1%), compared to 10% in pulsed Doppler [93]. Various pulse repetition frequencies and pulse sequences have been employed in sonothrombolysis studies, using Doppler modes [45] or higher duty cycles such as 20%[26], 80% [23], intermittent pulses of several seconds [52] or 100% (continuous wave) over minutes [108]. Increasing duty cycle by varying PRF at a given pulse length has been shown to improve clot lysis [75], possibly due to the shorter pulses improving microbubble survival or allowing greater replenishment. Conversely, increasing PRF may also reduce the destruction thresholds of microbubbles [109], which would be expected to reduce their effect on lysis. *In vivo*, safety must be considered: high duty cycles may allow growth of microbubbles by rectified diffusion [110] increasing the likelihood of bioeffects [93], hence the proposition of a modified mechanical index which includes the PRF and pulse length [111].

2.5.2. Influence of Microbubble Characteristics

The performance of microbubbles *in vivo* is influenced by their structure, size and stability in the bloodstream, which are determined in turn by a number of parameters including the gas contained within the bubble, shell material and size distribution.

The gas contained within microbubbles is known to affect their stability: air-filled microbubbles are generally less stable than those filled with higher molecular weight gases [112]. However, the results of trials comparing performance of the two categories are mixed, and may be influenced by differences in protocol between the *in vitro* and clinical setting. Mizushige *et al.* [113] compared the effects of albumin-air, Levovist® (galactose-air) and dodecafluoropentane (DDFP) microbubbles in combination with tPA in an *in vitro* stirred-beaker model: DDFP microbubbles showed the slowest decay in imaging intensity and were associated with the greatest clot mass loss, suggesting that their greater stability led to improved thrombolytic efficiency. A further *in vitro* study in which clots were treated in an unstirred syringe showed similar results for air-filled versus perfluorocarbon-filled polymer biospheres [114]. This is in contrast to the clinical study of Rubiera *et al.* [68], which compared Levovist® and SonoVue® (sulphur hexafluoride-phospholipid) microbubbles in combination with tPA in 138 patients with middle cerebral artery occlusion and found no significant difference in clinical outcome. The authors hypothesised that the use of bolus injections for microbubble administration in the clinical environment may override the effect of microbubble lifetime by resulting in a similar concentration of microbubbles arriving at the clot per bolus, as opposed to the more constant microbubble concentrations of the above *in vitro* studies. Due to the limited number of commercial contrast agents used in the majority of studies it is difficult to decouple the effects of the gas contained from the shell material, as typically both will

change between agents. In addition, the exposure conditions used between the *in vitro* and clinical setting may differ significantly as discussed below.

The properties of the microbubble shell may affect their response to ultrasound and subsequent destruction. Microbubbles with protein or polymer shells have been shown to exhibit sonic "cracking" which results in rapid dissolution after an ultrasound pulse [115]. Polymer shells also dampen oscillation of the gas core, reducing echogenicity; phospholipid-shelled microbubbles do not exhibit these effects [116]. Borden *et al.* studied the response of single microbubbles made from a range of saturated phospholipids and found that longer chain length materials decreased the rate of acoustic dissolution and fragmentation propensity, albeit in an single-bubble *in vitro* setting without testing of thrombolytic effect [116]. Borrelli *et al.* compared the thrombolytic effect of varying composition and sonication time during bubble fabrication in order to change shell stiffness and found that increasing Young's modulus reduced the rate of microbubble destruction, at the cost of a lower maximum clot mass loss [75]. The authors hypothesised this procedure may have changed the resonant frequency of the microbubbles, which is known to depend on shell parameters [48], but this was not investigated.

The size of microbubbles may also affect their enhancement of thrombolysis, but it is difficult to decouple this from ultrasound parameters: whether a microbubble undergoes cavitation (and if this is stable or inertial in nature) is largely a function of its size, the driving frequency and pressure. Borrelli *et al.* found that 3µm perfluorobutane-BSA-dextrose microbubbles achieved greater thrombolytic effect at 1 MHz than similar 1µm microbubbles in an *in vitro* model. With the larger microbubbles mass loss increased with acoustic intensity up to a point, before falling off due to greater microbubble destruction; the smaller bubbles required greater acoustic intensity before affecting lysis by which point microbubble destruction was already significant [75].

Microbubble properties have been shown decisive in shaping microbubble response during sonothrombolysis. Application-specific microbubbles are therefore a compelling approach to address the challenges of clinical implementation.

Ref	Model	Microbubble Type	US Frequency	US Pressure/Intensity/ MI	Thrombolytic Drug
[117]	Clinical	Galactose-based	2 MHz	<750 mW (TCD)	tPA
[25]	Clinical	Levovist®	2 MHz	n.s. (TCD)	tPA
[118]	Clinical	Levovist®	2 MHz	n.s. (TCD)	tPA
[112]	Clinical	Levovist®	2 MHz	<750mW (TCD)	tPA
[44]	Clinical	Levovist®	2 MHz	471 mW/cm² I_{spta}	tPA
[62]	Clinical	Levovist®/Optison® (for imaging)	2-4 MHz	2.2 MPa PN	tPA/aspirin/ heparin
[68]	Clinical	Levovist®/SonoVue®	2 MHz	385 mW/cm² I_{sptp}	tPA
[119]	Clinical	Luminity®	1.6 MHz	1.5 MPa PN, 26 mW/cm²	tPA/aspirin/ heparin
[2]	Clinical	MRX801 perfluorocarbon lipid	2 MHz	n.s. (TCD)	tPA
[62]	Clinical	Optison® (for imaging)	2 MHz	MI 1.3/TI 1.9	tPA
[120]	Clinical	Optison® (for imaging)	2 MHz	2.2 MPa PN	tPA/aspirin/ heparin
[45]	Clinical	Perflutren lipid	2 MHz	<720 mW (TCD)	tPA
[24]	Clinical	SonoVue®	2 MHz	189 mW/cm²	tPA
[26]	*In vivo* – rat (human blood)	Abciximab phospholipid	2 MHz	1.56 MPa PN, MI 1.3	None
[121]	*In vivo* - rabbit/*in vitro*	DDFP	20 kHz	1.5-2.9 W/cm²	None
[15]	*In vivo* - dog	Definity®	1.5-2 MHz	0.2-2 MPa PN, 0.4-10 W/cm²	None
[69]	*In vivo* - dog	Definity®	1 MHz	0.1-0.8 MPa PN, MI 0.5-1.9	None
[122]	*In vivo* - rabbit	Definity®	1 MHz	0.8 W/cm²	tPA
[40]	*In vivo* - rabbit	Definity®/albumin	1 MHz	0.1 W/cm²	tPA
[21]	*In vivo* - rabbit	Definity®/albumin/eptifibatide	1 MHz	0.16 MPa PN, 0.8 W/cm²	tPA control
[28]	*In vivo* - dog/*in vitro*	MRX-408 (targeted phospholipid)	20 kHz/ 1 MHz	420 kPa PN / 1-5 W/cm²	uPA
[81]	*In vivo* - pig	MRX801 perfluorocarbon lipid	1.6 MHz	MI 1.2	tPA
[123]	*In vivo* - dog	MRX815 perfluorocarbon lipid	1 MHz	1MPa PN, 1-10 W/cm²	None
[27]	*In vivo* - pig	MRX835, MRX802	1.5 MHz	MI 0.2-1.9	uPA/aspirin/ heparin
[124]	*In vivo* - dog	Optison®	n.s.	1.2-2.0 W/cm²	None
[125]	*In vivo* - pig	PESDA[3]	1 MHz	2 W/cm²	Eptifibatide/ heparin

[3] PESDA: Perfluorocarbon-exposed sonicated dextrose albumin microbubbles

Ref	Model	Microbubble Type	US Frequency	US Pressure/Intensity/ MI	Thrombolytic Drug
[126]	*In vivo* - rabbit	PESDA	37 kHz	103 kPa PN	Heparin
[38]	*In vivo* - pig/*in vitro*	PESDA	40 kHz/ 1 MHz	2-400 kPa PN	None
[17]	*In vivo* - dog	PESDA	n.s.	0.6 W/cm², 500kPa PN	Heparin
[127]	*In vivo* - dog	Platelet targeted DPPG	800 kHz	2.4 W/cm²	None
[41]	*In vivo* - rat	SonoVue®	1-3 MHz	MI 1.7	tPA
[128]	*In vivo* - rat	SonoVue®	2 MHz	1.05 MPa PN, MI 1.3	None
[129]	*In vivo* - rat	SonoVue®	2 MHz	1.1MPa, 37.3 W/cm² I_{sptp}	None
[130]	*In vivo* - rat	SonoVue®	2 MHz	2 MPa, 500 mW/cm²	tPA
[131]	*In vivo* - rabbit	SonoVue®	2 MHz	252 mW/m² [cm²?]	uPA
[132]	*In vivo* - rabbit	tPA loaded liposomes	6 MHz	0.75-1.5 MPa PN	tPA
[52]	Ex vivo	Definity®	120 kHz	0.1-0.5 MPa PP	tPA
[113]	*In vitro*	Albumin/SH-U508A/DDFP	10 MHz	0.33 MPa PN, 1W/cm²	tPA
[19]	*In vitro*	Albunex®	170 kHz	0.5 W/cm²	uPA
[37]	*In vitro*	BR38	1.6 MHz	0.15-1 MPa PN	tPA
[133]	*In vitro*	Definity®	1.6 MHz	0.6 MPa PN, MI > 1.0	None
[134]	*In vitro*	Definity®	1-2 MHz	n.s. (Doppler)	tPA
[56]	*In vitro*	Definity®	120 kHz	0.12-0.32 MPa PP	tPA
[32]	*In vitro*	Levovist®	2 MHz	455 mW/cm² Ispta	tPA
[53]	*In vitro*	Lipid	1 MHz	1 MPa	tPA
[135]	*In vitro*	Magnetic PLA-PEG	20 kHz	140 kPa, 6.5W/cm²	tPA
[39]	*In vitro*	MP1950 lipid	1 MHz	MI 1.6	None
[136]	*In vitro*	Optison®	1.1 MHz	0.5-2 MPa PN	None
[137]	*In vitro*	Optison®/SonoVue®	1.7 MHz	1.3-2.1 MPa PN	tPA
[75]	*In vitro*	Perfluorobutane BSA dextrose	1-3 MHz	< 2 W/cm²	None
[22]	*In vitro*	Perfluorobutane lipid	1 MHz	0.2-1.5 MPa PN	tPA
[34]	*In vitro*	PESDA	20 kHz	0.85 MPa PN	uPA
[138]	*In vitro*	Phospholipid/SonoVue	1.4 MHz	MI 0.4/ TIC 1.3	None
[114]	*In vitro*	Polymer-air/PFC	20 kHz	n.s.	None
[36]	*In vitro*	SH-U508A	10 MHz	0.5-1 W/cm²	tPA
[139]	*In vitro*	SonoVue®/albumin	1 MHz	0.5-1.3 MPa	Streptokinase
[140]	*In vitro*	Tirofiban targeted albumin	1 MHz	MI 1.2	None
[141]	*In vitro*	tPA loaded ELIP	120 kHz	0.35MPa PP	tPA
[108]	*In vitro*	tPA loaded ELIP	1 MHz	0.12MPa PN, 2 W/cm²	tPA
[142]	*In vitro*	tPA loaded phospholipid	2 MHz	1.8 W/cm²	tPA
[143]	*In vitro*	uPA loaded nanogel	2 MHz	530 mW/cm²	uPA
[144]	*In vitro*	uPA loaded phospholipid	0.8 MHz	2.8 W/cm²	uPA

Table 2-2: Summary of sonothrombolysis studies.

2.6. Microbubble engineering for sonothrombolysis

The majority of *in vivo* and clinical trials of sonothrombolysis to date have employed commercial echo-contrast agents that were originally developed for use in ultrasound imaging (Table 2-2). The agents used include first-generation stabilised air bubbles (e.g. Levovist® [145]) as well as second-generation products containing higher molecular weight gases (e.g. Optison® [146], SonoVue® [147], Definity® [148]), which are typically administered systemically by intravenous injection. Application-specific engineering of microbubbles has the potential to improve their effect on sonothrombolysis.

2.6.1. Targeted microbubbles

Targeting of microbubbles may be used to maximise their effect on thrombolysis by increasing the concentration of microbubbles at the site of the clot, as well as bringing the bubbles closer to the clot and improving their retention. This may allow lower ultrasound power and microbubble doses to be used, reducing the risk of side effects and improving the safety of treatment. Targeting methods include 'biological' (e.g. antibody-based) means, as well as 'physical' methods such as radiation force and magnetic targeting.

2.6.1.a) Biological targeting

Thrombus formation is typically caused by the rupture of an atherosclerotic plaque which results in adhesion of platelets [149], [150]; the most abundant receptor on the platelet surface is the glycoprotein IIb/IIIa complex, which mediates their aggregation and increases in affinity on platelet activation, making it an ideal candidate for thrombus targeting [149]. Various molecules may be used to target this receptor including abciximab which has been shown to improve both imaging contrast [29], [150] and lysis of thrombi [26] compared to non-targeted microbubbles. However, abciximab has a strong affinity for

platelets and may be detected weeks after treatment [26], increasing the risk of haemorrhage. Other agents which have been used to target the glycoprotein receptor for improved thrombolysis include the antiplatelet drugs tirofiban [140] and eptifibatide [125], while single-chain antibody targeting methods which preserve glycoprotein binding may be used to reduce the risk of haemorrhage compared to conventional drug-based targeting [149]. Alternative ligand targeting methods include the use of peptide sequences (e.g. KQAGDV or RGD) found within fibrinogen [151] which is used in the contrast agent MRX-408 [28], [152].

Binding of biologically-targeted microbubbles to thrombi has been demonstrated both *in vitro* in flow models [30], [151] and *in vivo* [29], [149], [153], leading to improved lytic efficiency compared to non-targeted microbubbles [26]–[28]. An additional benefit of the method is that the location of the clot need not be known a priori, and thus could be used for improved imaging [29], to distinguish between new and old thrombi (such as to distinguish between acute and chronic deep vein thrombosis) [152] or to identify microthrombi before rupture [149]. The primary limitations of biological targeting for use in thrombolysis are dependence on flow, which will be reduced due to the occlusion [29], and a short working distance: microbubbles must already be close to the clot in order to bind. In addition, use of biotin-avidin binding in some conjugation methods may cause an immunogenic response in humans, limiting clinical applicability [149].

2.6.1.b) Acoustic radiation force targeting

The acoustic radiation force can be used to increase the accumulation efficacy of biologically targeted microbubbles. Exposure to a propagating sound wave causes microbubbles translation in the direction of propagation; it can therefore bring greater numbers of targeted agents into direct contact with the target tissue [154]–[156].

This approach has been shown to improve molecular imaging *in vitro* and *in vivo*. It requires however precise alignment of the beam with the target vessel, which may be challenging with more complex *in vivo* geometries. Of equal concern for therapeutic applications is the effect of the targeting ultrasound pulse on the microbubbles: Rademeyer *et al.* have demonstrated that exposure to ultrasound, even at very low amplitudes, may destroy or substantially alter the properties of single microbubbles [157].

2.6.1.c) Magnetic targeting

Magnetic targeting of drug-carrying microspheres was first demonstrated in the late 1970s [158], while magnetic ferrofluid was used in human drug-targeting trials in the 1990s [159]. The potential for magnetic fluids to enhance thrombolysis was also outlined in the 1990s [160]. In other fields, magnetic targeting of microbubbles has improved gene transfection [161], [162] with greater selectivity [163], and may be combined with ultrasound-induced opening of cell membranes (sonoporation) [161] to increase drug uptake at the cellular level, known as magnetofection [164][125, 126]. Magnetic microbubbles may also be also retained against flow near a vascular target using a magnetic field and simultaneously imaged using conventional B-mode ultrasound [165], however the effects on their response of their increased proximity under the influence of the magnetic field remains to be fully explored [166].

A major challenge for translation of magnetic targeting to the clinic is scale-up of the magnet system to allow targeting deep within the human body. Particular issues include the strength of magnetic field and gradient required to counteract blood flow; accumulation of targeted particles between the intended site and magnet, and trapping of particles due to bends in blood vessel geometry [167]. Superconducting magnets [168]

may be used to increase the depth at which magnetic targeting is effective, however, for deep targeting further refinements are necessary to reduce the proportion of material accumulating between the intended site and the magnet. Such methods may include biodegradable stents [169] which can create a local region of high field gradient but require invasive placement within the body; novel electromagnet pole design (in which fringe regions of the magnetic field are overlapped) to create localised regions of higher magnetic field away from the magnet surface [170], or time-variant magnetic fields including physical movement of the magnets [171], on-off [172] or oscillating designs [173].

2.6.2. Drug loaded microbubbles

Recently, the possibility of using microbubbles as fibrinolytic drug carriers has been investigated. In this approach, the drug is loaded onto the bubble and its release at the clot site is triggered by focused ultrasound. The chief advantage of this method is to obtain co-location of cavitational activity and drug release, which may increase drug efficiency. Also, encapsulating the drug will limit its systemic bioavailability, reducing harmful systemic side effects. Conversely, it will temporarily protect it from clearance in the liver; this is of particular interest in the case of tPA, which has a short half-life in the free form [174]. Finally, loaded microbubbles retain their contrast-enhancing capability for ultrasound imaging, which makes it possible to localize tPA in the body and to monitor drug delivery [175].

There are various possible methods of loading microbubbles, as illustrated in Figure 2-5: drugs can be embedded into the shell, attached to the shell electrostatically or with ligands, dissolved in an oil layer beneath the shell, incorporated inside the bubble, or encapsulated within nanocarriers bound to the shell [175], [176]. The choice of the method of loading

depends on the chemical properties of the drug to load as well as on the desired exposure parameters. In the case of tPA, the protein is hydrophilic, which excludes the oil layer option. An added difficulty lies in the fact that it is very large (around 65 000 in relative molecular mass [177]). Choice of exposure parameters influences the mode of drug release, so the method of loading must be chosen accordingly. For instance, if stable cavitation is preferred, the microbubble must be designed to release tPA without incurring destruction. Gene- and drug-loaded microbubbles have been widely investigated in the past fifteen years, but fibrinolytic drug-carrying microbubbles are still in their infancy. Two methods of incorporating thrombolytic agents (tPA [142] or urokinase [144], [178]) into lipid-shell microbubbles were documented: drugs were either included in the lipid mixture at the outset of microbubble preparation [142], [144], or added to the freeze-dried powder of a commercial contrast agent just before reconstitution [178]. These methods preserved drug function, and Mu *et al.* as well as Hua *et al.* demonstrated that the fluorescently labelled drug was located in or directly on the shell of the microbubbles [142], [178]. Ren *et al.*'s group reported high levels of urokinase encapsulation (57 to 78%), and found that the urokinase-loaded microbubbles achieved greater clot mass loss at 0.8 MHz than either urokinase alone or ultrasound and normal microbubbles [144]. These drug-encapsulated bubbles weren't however compared to traditional microbubbles with free urokinase, and further research is warranted to evaluate the impact of drug encapsulation on lytic efficiency. A substantial drawback of direct loading of drugs in microbubbles is the limited area or volume available for attachment, which reduces the amount of drugs it is possible to administer. A possible solution is to attach fibrinolytic-carrying nanoparticles on the microbubble surface. To the best of the authors' knowledge, there is no report of such vehicles to date, but this area is expected to develop: tPA-loaded

liposomes have been successfully prepared [179], and liposome-loaded microbubbles have already been investigated in cancer therapy [180].

A promising alternative for increasing drug loading is the use of tPA-loaded echogenic liposomes (tELIPS). tELIPs are liposomes, i.e. bilayer lipid spheres, which entrap a tPA-containing aqueous phase alongside a gaseous phase that provides it with echogenic properties. Thiukinhoy-Laing *et al.* thus report manufacturing tELIPS with 50% drug entrapment efficiency, 15% of which were fully encapsulated within the liposome, and 35% associated with the shell [108]. These vehicles were stable enough to be imaged with B-mode ultrasound, but could be easily fragmented by colour Doppler ultrasound [132], [141]. This was confirmed *in vivo* in a rabbit model: sonothrombolysis with colour Doppler achieved similar success with encapsulated tPA as with free tPA[132]. Interestingly, these tELIPs were shown to perform even better than Optison® microbubbles and free tPA after a brief 2-minute *in vitro* insonation at 1 MHz [108]. Significant lysis by tELIPS can however be observed without ultrasound exposure, indicating permeability of the lipid bilayer [108], [141].

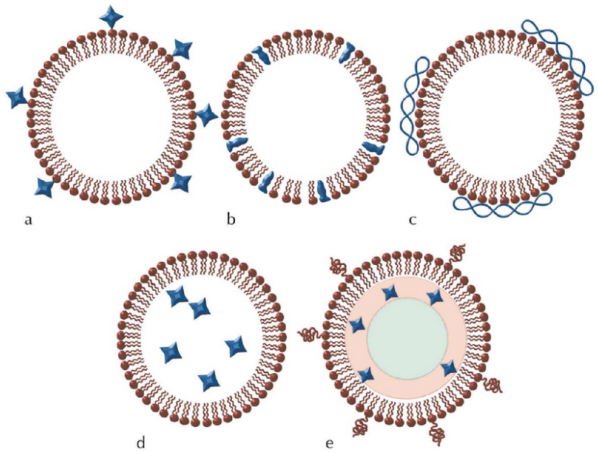


Figure 2-5: Representation of possible drug loading modalities on microbubbles. Drugs may be (a) attached to the membrane surrounding the microbubble; (b) embedded into the membrane itself; (c) bound non covalently to the surface of the bubble (e.g. DNA); (d) formulated to load the interior; (e) hydrophobic drugs can be incorporated into a layer of oily material that forms a film around the microbubble, which is then surrounded by a stabilizing membrane. In this example a targeting ligand is incorporated on the membrane allowing targeted delivery of the drug. Note that in these examples the stabilizing materials are shown as lipids, but could also be polymeric materials. Reproduced from [176] ***with permission of Elsevier.***

2.6.3. Targeted and loaded microbubbles

In order to combine the advantages of both approaches, microbubbles incorporating both drugs and targeting species can be designed.

Biological targeting of drug-loaded microbubbles was achieved with the Arg-Gly-Asp-Ser tetrapeptide (RGDS) as a targeting ligand [142], [178]. Successful thrombus targeting was demonstrated *in vivo* [178]. Hua *et al.*'s group also compared their engineered microbubbles to co-injected tPA and regular microbubbles exposed to 5 MHz; they found a comparable change in clot mass loss with a five times lower dose of tPA [142]. In fact, there is evidence that biological targeting of tPA-loaded microbubbles may not require an additional ligand. tPA itself carries two fibrin-binding domains, and encapsulated tELIPS retain a strong affinity for fibrin [181].

Though magnetically targeted, fibrinolytic-loaded microbubbles have not been investigated to date, alternative options have been suggested, for example non-echogenic vehicles such as ultrasound-sensitive copolymers. Drug release from these rough-surfaced

nanocarriers can be triggered by very low-frequency ultrasound (20 kHz) [182], and they achieve significantly better clot lysis than ultrasound with free tPA [135].

Microbubble engineering for sonothrombolysis is a recent field which is expected to grow rapidly given the potential of such strategies to increase the safety and efficacy of thrombolytic therapies.

2.6.4. Microdroplets

Recently, ultrasound-sensitive perfluorocarbon droplets have been investigated as cavitation nucleation agents in sonothrombolysis: they vaporise into microbubbles upon ultrasound application, and also enhance thrombus breakdown [183]. Because of their lower solubility, the circulation half-life of droplets is higher [184]. Like microbubbles, these particles can be loaded and targeted for therapeutic purposes. For instance, Lee *et al.* have developed magnetically responsive polymer nanodroplets encapsulating Paclitaxel, a chemotherapeutic; *in vitro* studies demonstrated a 40% improvement in cytotoxicity compared with free drug [185].

2.7. Conclusion

Conventionally used in the clinic as diagnostic contrast agents, microbubbles are also promising agents for a range of therapies, including thrombolysis. Exposure to ultrasound and microbubbles has been shown to accelerate both thrombus break-up and restoration of flow to ischaemic regions. Although the mechanisms for thrombus break-up have not been fully clarified, acoustic cavitation has been found to play a major role in this process. In the clinic, microbubble-enhanced sonothrombolysis is a minimally-invasive method with the potential to drastically improve safety by reducing the required dose of thrombolytic drugs or indeed removing the need for them entirely. Microbubbles can further improve patient safety by providing real-time feedback for patient monitoring. Efficacy has yet to be demonstrated however in large scale clinical trials. In order to optimize treatment and to control side-effects, application-specific microbubbles can be engineered, for example by providing a means of drug encapsulation and targeting. In particular, magnetic targeting is an attractive option, promoting active accumulation of large numbers of microbubbles near the thrombus. This thesis is the first investigation to date into the efficacy of magnetic microbubbles in sonothrombolysis.

CHAPTER 3

Magnetic targeting to enhance microbubble delivery in occluded microvascular networks

Ultrasound in combination with microbubbles has emerged as a promising method to accelerate the breakdown of blood clots compared to conventional pharmaceutical treatments. However, its clinical translation is still limited in part by ineffective microbubble delivery to the thrombus. Notably, formation of laminar vortices and abrupt reduction of blood flow within occluded vessels make it difficult to deliver sufficient numbers of microbubbles to the target vascular region.

This study investigates the delivery of thrombolytic drugs and microbubbles in a model of an arteriolar bifurcation with an occluded branch, using both computational and experimental methods. It then examines whether magnetic targeting could be used to overcome the limitations imposed by the fluid dynamic conditions and improve microbubble delivery to the clot.

3.1. Introduction

3.1.1. Motivation

Non-invasive treatments for thrombosis rely on the bloodstream to deliver agents to a region where circulation is severely impaired. When delivering microbubbles, the ischaemic region is often characterized by a marked depletion in microbubbles [186], [187]. In some cases, this perfusion defect even persists in the microvasculature after the main vessel occlusion is relieved [187].

Such ineffective delivery of therapeutic agents can be detrimental to treatment efficacy in the management of all occlusive conditions, whether acute or chronic. In the case of pharmacological thrombolysis for myocardial infarctions, disrupted circulation to and about the clot has been identified as one of the primary causes of treatment failure [188]. Similarly, in the case of ultrasound-enhanced peripheral thrombolysis, Culp *et al.* highlighted the importance of microbubble delivery when investigating albumin microbubbles and low frequency ultrasound in thrombosed canine arteriovenous grafts. Complete recanalization was achieved in all animals that received direct microbubble injections into the occluded grafts (8/8), and only in 4 out of 10 that were treated with a systemic, intravenous injection [17]. In the same way, poor delivery is expected to affect stroke treatment.

Despite these reports, previous studies of drug and microbubble delivery in obstructed vasculature are limited. On the other hand, the wider field of fluid mechanics in diseased vessels has been the subject of much investigation. For instance, the shear stresses in stenosed and occluded vessels have been thoroughly characterised, along with their effects on the endothelium, on the clot, and on platelet activation [189],[190]. Drawing on this large body of work, there is a clear need to investigate therapeutic agent transport in obstructed vasculature.

3.1.2. Targeted therapeutic agent delivery in obstructed vascular networks

Magnetic targeting is a promising approach to overcome these obstacles. Recent work has shown the potential of this targeting method to improve drug delivery in non-occluded vascular networks. Tehrani *et al*. demonstrated *in silico* the feasibility of steering magnetic nanoparticles into a specific branch of a Y-shaped bifurcation [191]. Cherry *et al*. reached a similar conclusion with a more complete physical model and larger magnetic particles [192].

Magnetic targeting has not been investigated so far as a method to deliver therapeutic agents in a fully occluded vascular network. It is hypothesised that an inexpensive permanent magnet system can aid microbubble steering through an idealized vessel network, and that it has the potential to enhance microbubble delivery for sonothrombolysis in the clinic.

Furthermore, suitable magnetic vehicles have already been developed. Torno *et al*. have produced tPA-loaded magnetic polymer microparticles and shown that, in conjunction with ultrasound, they accelerate recanalization in a single, straight vessel [135]. Owen *et al.* have loaded lipid-coated microbubbles with iron oxide nanoparticles and shown that they can be retained with a magnet against clinically relevant flow conditions [193].

3.1.3. Objectives of the investigation

The present study examines the issue of delivering therapeutic agents (tPA and microbubbles) to a fully occluded vessel. The first aim of the study was to investigate the influence of vessel geometry, blood flow velocity and microbubble properties upon the concentration of microbubbles in the occluded branch of a bifurcating vessel. The second objective was to evaluate the effect of magnetic targeting on microbubble delivery in occluded vessels, and to identify the physical parameters that affect the concentration of

microbubbles successfully delivered. This was carried out using both computational fluid dynamic and physical models of an occluded bifurcation.

3.2. Methods

The contribution of Dr. Carugo to the computational fluid dynamics model and the experimental device is gratefully acknowledged, as is the input of Dr. Barnsley for the simulation of the magnetic field.

3.2.1. Geometry

In this study, we consider the simple case of a rigid, Y-shaped arteriolar bifurcation in which one of the daughter branches is fully occluded. Such complete occlusions constitute the majority of ST-elevation myocardial infarction cases [194].

Table 3-1and Figure 3-1 summarize the geometry of the system. The width of the parent branch was based on arteriolar diameters [195]. The daughter branches form a 60° angle with each other. Their width was selected according to Murray's law, which predicts daughter branch radii in a biological vessel network by computing minimal energy expenditure [196]:

$$r_0^3 = r_1^3 + r_2^3 \qquad (3\text{-}1)$$

where r_0 is the radius of the parent branch and $r_{1,2}$ are the respective radii of the daughter branches.

The inlet velocity and the distance from the bifurcation position (point Y on Figure 3-2) to the occlusion (point X) are variable. The inlet velocities are within the range of clinically relevant flow rates for vessels of this size, from 1 to 100 mm/s [195]. The occluded branch

length ranges from 2 to 8 mm, which is within the clinically observed lengths for such vessels [195].

To aid in the investigation, three lines of interest were defined (see Figure 3-2). Line K is a cross-section of the parent branch 1 mm before the bifurcation. Line L runs from the centre of the bifurcation along the middle of the free branch. Line M is symmetrical to line L in the occluded branch. The magnet is represented by a half-inch square element, placed with its magnetisation vector parallel to line M and its surface 10 mm from the centre of the bifurcation (point Y).

Table 3-1: Dimensions of the arteriolar bifurcation phantom used in the numerical model and in the in vitro experiments. The dimensions of the experimental bifurcation were adjusted to the size of the closest available milling tools.

Simulations (2D)	
Parent branch	Width w_p = 250 µm. Length l_p = 11 mm.
Free daughter branch	Width w_f = 180 µm. Length l_f = 8 mm.
Occluded daughter branch	Width w_o =180 µm. Length l_o = [2 to 8] mm.
Angle between daughter branches	$\alpha = 60°$
Experiments	
Parent branch	Width w_p = 250 µm. Depth d_p= 200µm. Length l_p = 10 mm.
Free daughter branch	Width w_f = 178 µm. Depth d_f = 200µm. Length l_f = 8 mm.
Occluded daughter branch	Width w_o =178 µm. Depth d_o = 200µm. Length l_o = 8 mm.
Angle between daughter branches	$\alpha = 60°$

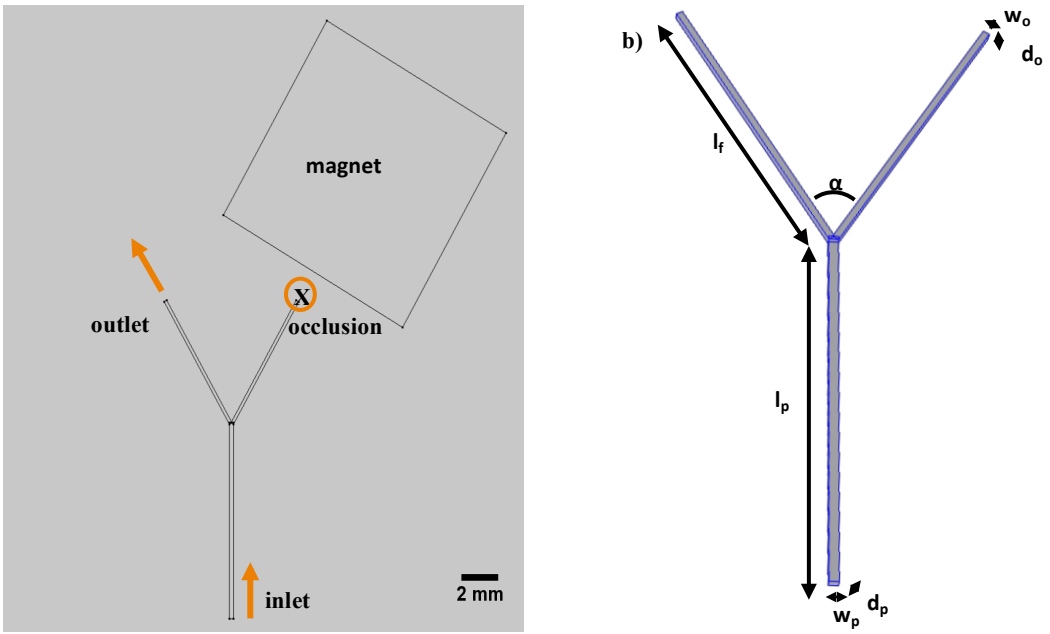


Figure 3-1: Geometry of the bifurcation: a) layout of the bifurcation; b) dimensions (see Table 3-1).

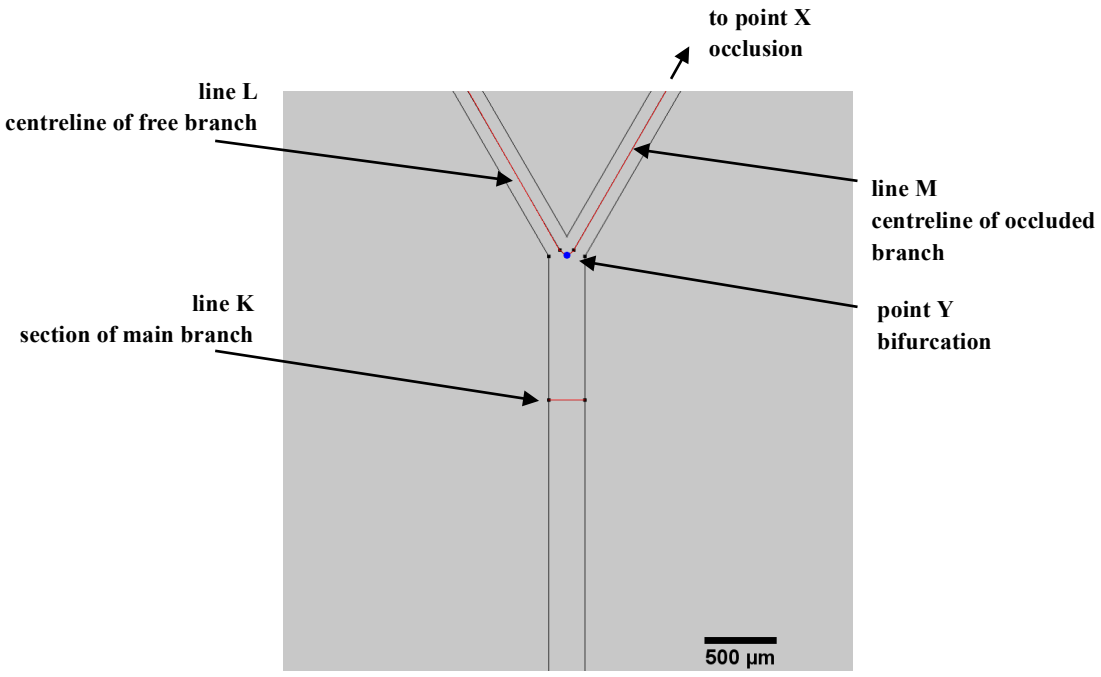


Figure 3-2: Lines and points of interest in the bifurcation model.

3.2.2. 2D numerical model

This section outlines the theoretical basis of the bifurcation simulations and specifies the choices that were made in building the model with the COMSOL Multiphysics® 5.0 software (COMSOL Ltd., Cambridge, UK).

The two-dimensional model was used to simulate successively:

- fluid velocity and the magnetic field in the bifurcation in the steady-state (described in sections 3.2.2.a) and 3.2.2.b))
- tPA concentration in the bifurcation in the first hour after a bolus injection (described in section 3.2.2.c))
- magnetic microbubble distribution in the bifurcation in the first 150 s after a bolus injection (described in section 3.2.2.d))

Table 3-2 summarizes the variable names used in the study. Table 3-3 contains the values that were chosen for various parameters and physical constants.

Independent variables		
Variable	Name	Value at bifurcation inlet
Fluid velocity	$\boldsymbol{u}$	1-100 mm/s
tPA concentration	c_d	6.2 x 10^{-5} mol/m^3
Microbubble radius	R	0.3 – 2.5 μm
Dependent variables		
Variable	Name	
Pressure	p	
Magnetic flux density	$\boldsymbol{B}$	
Microbubble velocity	$\boldsymbol{v}$	

Table 3-2: Summary of variable names and values in the numerical model

Parameter / constant	Name	Value
Density of air	ρ_a	1.2754 kg/m^3
Density of water	ρ	1000 kg/m^3
Dynamic viscosity of water	η	0.00089 Pa.s
Permeability of vacuum	μ_0	4π x 10^{-7} H/m
Relative permittivity of the medium (water)	μ_m	1
Remanent magnetisation of NdFeB	M_{NdFeB}	1.14 x 10^6 A/m
Saturation magnetisation of particles	M_s	4.7 x 10^5 A/m [197]
Diffusion coefficient of tPA	D_c	6 x 10^{-11} m^2/s [198]
Volumetric fraction of iron oxide nanoparticles in microbubble shell	β_{shell}	10 %
Microbubble shell thickness	R_b	5 x 10^{-5} m

Table 3-3: Values of the parameters and physical constants used in the numerical model.

NdFeB magnetisation value given by manufacturer.

3.2.2.a) Hydrodynamics

Flow regime

With the geometry described above, the hydraulic diameter of the channel inlet is

$$D_h = \frac{2\, w_p\ d_p}{w_p + d_p} = 0.22 \text{ mm} \tag{3-2}$$

Using this value as the characteristic dimension of the system, we define the Reynolds number

$$Re = \frac{\rho\, u\, D_h}{\eta} \tag{3-3}$$

where ρ is the fluid density, u is the mean inlet velocity and η is the dynamic viscosity of water.

In the range of mean inlet velocities investigated, $Re \in [0.25\ 25]$. This clearly indicates that the flow is in a laminar regime.

Governing equations

Fluid flow in the bifurcation is governed by mass conservation (continuity) and momentum conservation. For a compressible flow, the continuity equation is:

$$\nabla . (\rho \boldsymbol{u}) = 0 \tag{3-4}$$

where $\boldsymbol{u}$ is the fluid velocity vector.

In the steady state, momentum conservation of this compressible flow is given by:

$$\rho(\boldsymbol{u}.\nabla)\boldsymbol{u} = -\nabla p\, \mathbf{I} + \nabla . \left[\eta(\nabla \boldsymbol{u} + \nabla \boldsymbol{u}^{\mathrm{T}}) - \frac{2}{3}\eta(\nabla . \boldsymbol{u})\mathbf{I} \right] \tag{3-5}$$

where p is the pressure, $\mathbf{I}$ is the identity matrix, and $\boldsymbol{g}$ is the gravitational acceleration vector.

Boundary conditions

At the vessel wall, a no slip boundary condition is applied. Past the bifurcation, the right-hand daughter branch is fully occluded (solid wall, no slip condition at the surface of the occlusion), while the left-hand branch is the outlet (pressure release condition at the extremity).

Injection point

As a consequence of the no slip boundary condition and of fluid viscosity, a parabolic velocity profile develops across the section of the channel. We define the distance between the inlet and a fully developed velocity profile as the hydrodynamic entrance length. In a laminar flow, it is given by:

$$L_{entry} = 0.05\, R_e D_h = 275\ \mu\text{m} \qquad (3\text{-}6)$$

In order to mimic the physiological conditions of intravascular injections, where therapeutic agents are injected systemically at a large distance from the target vessel, the injection point for microbubbles was separated from the fluid inlet by a distance greater than L_{entry}. To reduce computational time, it was placed at a distance of 1 mm from the bifurcation.

3.2.2.b) Magnetic field

In the experiments, a permanent magnet was used to target iron-oxide loaded microbubbles (see section 3.2.2.d)). It was positioned as described in section 3.2.1.

In the numerical simulations, the magnetic field was computed in Comsol® within two distinct regions: the inside of the magnet (internal field) and the rest of the system (external field). The inside of the magnet has permanent magnetic dipole moments. In this region, the magnetic properties of the medium are therefore characterized by the constitutive relation:

$$\boldsymbol{B_{int}} = \mu_0 \, (\boldsymbol{H} + \boldsymbol{M}) \qquad (3\text{-}7)$$

where $\boldsymbol{B_{int}}$ is the magnetic flux density inside the magnet, $\boldsymbol{H}$ is the magnetic field intensity, and $\boldsymbol{M}$ is the remanent magnetisation vector of the magnet.

The external region (the channel and its surrounding elements) is composed of non-magnetic materials such as glass, polymer and water in the *in vitro* study, or tissue and blood in physiological conditions. No magnetic dipole moments are induced, and there is no remanent magnetic field. In this region, the constitutive relation becomes:

$$\boldsymbol{B_{ext}} = \mu_0 \, \mu_m \boldsymbol{H} \qquad (3\text{-}8)$$

where $\boldsymbol{B_{ext}}$ is the magnetic flux density outside the magnet, and μ_m is the relative permeability of the medium (water), which is set to 1.

The magnetic field is in fact described in terms of the magnetic scalar potential V_m. In a system with no electrical currents, the magnetic scalar potential $V_m$is defined by $\boldsymbol{H} = -\boldsymbol{\nabla} V_m$. In addition, the magnet is considered to be homogeneously magnetised, so $\nabla \boldsymbol{M} = 0$.

Thus equations (3-7) and (3-8), combined with Maxwell's equation $\nabla \boldsymbol{B} = 0$ both yield

$$\nabla^2 V_m = 0 \qquad (3\text{-}9)$$

i.e. the Laplace equation.

Boundary conditions

In each region, this equation is solved numerically, using the following boundary conditions. At the interface between the two regions (the surface of the magnet), the normal component of **B** is continuous, so the boundary condition is:

$$\mathbf{n} \cdot (\boldsymbol{B_{ext}} - \boldsymbol{B_{int}}) = 0 \qquad (3\text{-}10)$$

An additional boundary condition is imposed on the perimeter of the system (magnetic insulation):

$$\mathbf{n} \cdot \boldsymbol{B_{ext}} = 0 \qquad (3\text{-}11)$$

Magnetisation correction

A correction factor was applied to the magnetisation of the magnet to account for the three-dimensional geometry of the experimental system: the two-dimensional simulation of the magnetic field assumes that the plane of interest is the mid-plane of the magnet (Figure 3-3a.) , but the bifurcation is situated in the base-plane of magnet, as described in Figure 3-3b. The correction factor was calculated by computing the magnet field produced at point Y (defined in Figure 3-2) in two ways: a) in the symmetrical configuration with Comsol; b) in the more realistic, asymmetrical configuration with a previously published 3-dimensional model [199]. The ratio of the two values yields a correction factor of 0.706. This high value confirms the necessity of correcting the magnetisation vector.

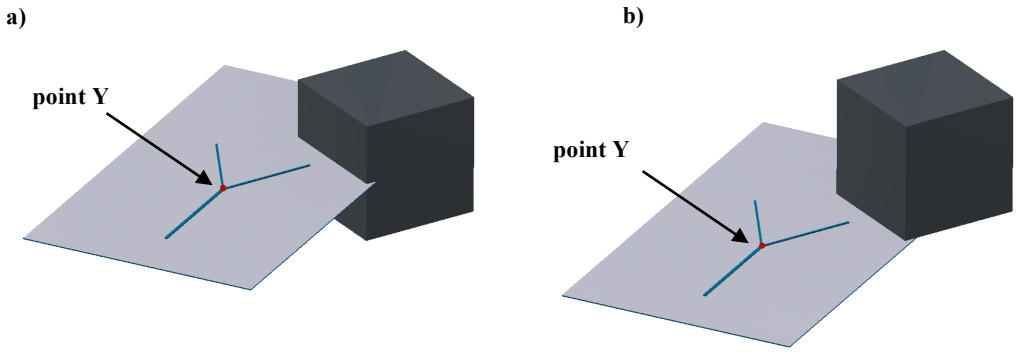


Figure 3-3: Relative positions of the magnet (coloured in black) and the bifurcation plane (grey).
a) in the 2D numerical simulations, the bifurcation is by default in the mid-plane of the magnet;
b) in the 3D experimental setup, the bifurcation is in the base-plane of the magnet.
The bifurcation is coloured in blue. It is not drawn to scale.

Numerical solver

The fluid velocity field and the magnetic field in the steady-state were computed simultaneously in Comsol® Multiphysics using the "Laminar Flow" interface of the "CFD Module" and the "Magnetostatics, No Currents" interface of the "AC/DC Module" respectively. The nonlinear problem was solved numerically for 477027 degrees of freedom with a MUltifrontal Massively Parallel Sparse (MUMPS) direct solver in a fully coupled approach. The relative tolerance was set to 0.001.

3.2.2.c) Drug delivery

The model for drug transport was setup as a time-dependent study over the course of an hour, a clinically relevant timeframe for stroke therapy. Prior to drug injection at the fluid inlet, there is no drug in the network and the flow in the channel has reached a steady state. tPA is injected for 60 minutes at a constant concentration on the order of the clinical guidelines for stroke treatment.

There are no chemical reactions in this system. Mass conservation is given by:

$$\frac{\partial c_d}{\partial t} + \nabla . N = 0 \tag{3-12}$$

where N is the flux of solute.

Two factors contribute to drug transport through the bifurcation: drug advection with fluid flow, and drug diffusion following gradients of concentration. The flux of solute due to diffusion follows Fick's law, so:

$$\frac{\partial c_d}{\partial t} + \nabla . \left(\underbrace{-D_c \nabla c_d}_{\text{diffusion}} + \underbrace{c_d \boldsymbol{u}}_{\text{convection}} \right) = 0 \tag{3-13}$$

The diffusion coefficient D_c for tPA was approximated with values from the literature for bovine serum albumin, a globular protein of similar molecular weight to tPA (66.5 kDa for BSA, 65 kDa for tPA) [198], [200].

tPA transport dynamics were computed in Comsol® using the "Transport of diluted species" interface of the "Chemical Species Transport" module. The transient phase was studied in time steps of 60 seconds over one hour. The tPA concentration was solved for 42882 degrees of freedom with a PARallel Sparse DIrect SOlver (PARDISO) in a fully coupled approach. The relative tolerance was set to 10^{-2} and the absolute tolerance to 10^{-3}.

3.2.2.d) Microbubble delivery

The computational model for microbubble transport was setup as a time-dependent study over the course of 150 seconds, which is on the order of the expected half-life of a bolus injection *in vivo* [201]. Microbubbles were modelled as individual, spherical, incompressible, air-filled particles. At t=0s, 300 microbubbles are injected simultaneously into a steady-state flow[4]. The microbubbles are injected with a uniform distribution along line K (see Figure 3-2).

Each bubble is subjected to a drag force $\boldsymbol{F_d}$ from the fluid and to a magnetophoretic force $\boldsymbol{F_m}$ from the magnetic field. In this two-dimensional model placed in the horizontal plane, gravity and buoyancy are assumed to act orthogonally to the plane of the bifurcation and are ignored.

The balance of forces on a microbubble is therefore given by:

$$\frac{\mathrm{d}m_p\boldsymbol{v}}{\mathrm{d}t} = \boldsymbol{F_d} + \boldsymbol{F_m} \qquad (3\text{-}14)$$

where m_p is the mass of the microbubble and **v** its velocity.

In a regime where inertial forces are small compared to viscous forces, the frictional force on a smooth, spherical bubble moving in a Newtonian fluid is given by Stokes' law:

$$\boldsymbol{F_d} = 6\,\pi\,\eta\,R\,(\boldsymbol{u} - \boldsymbol{v}) \qquad (3\text{-}15)$$

where R is the particle radius.

[4] The number of microbubbles was chosen to provide a high density of microbubbles in the cross-section of the main branch (1.2 microbubbles/µm).

When a particle is suspended in a dielectric fluid and exposed to an external magnetic field H, the magnetophoretic force exerted on the particle is given by:

$$\boldsymbol{F_m} = \boldsymbol{m_{eff}} \,.\, \boldsymbol{\nabla}(\mu_0\, \mu_m \boldsymbol{H}) \tag{3-16}$$

where $\mathbf{m_{eff}}$ is the effective magnetic dipole moment induced by $\boldsymbol{H}$.

It can be shown that in the case of a spherical particle in a medium, where both the particle and the medium are lossless dielectrics of respective permeabilities μ_p and μ_m [202], [203]:

$$\boldsymbol{m_{eff}} = 4\,\pi\, R^3 \frac{\mu_p - \mu_m}{\mu_p + 2\,\mu_m}\, \boldsymbol{H} \tag{3-17}$$

Associating equations (3-16) and (3-17), the magnetophoretic force on the particle becomes:

$$\boldsymbol{F_m} = 2\,\pi\, R^3 \mu_0 \mu_m K\, \nabla|\boldsymbol{H}|^2 \tag{3-18}$$

where $K = \frac{\mu_p - \mu_m}{\mu_p + 2\,\mu_m}$ is known as the Clausius-Mossotti factor.

The relative magnetic permeability of the particle is

$$\mu_p = 1 + \chi_p \tag{3-19}$$

where χ_p is the magnetic susceptibility of the material, characterised by:

$$\chi_p \boldsymbol{H} = \boldsymbol{M_p} \tag{3-20}$$

As the microbubbles are superparamagnetic, their magnetisation $\boldsymbol{M_p}$ can be described using a Langevin function, $\mathcal{L}(y) = \coth y - {}^1/_y$.

$$|\boldsymbol{M_p}| = \beta_{tot} M_s\, \mathcal{L}\left(\frac{M_s V\, \mu_0\, |\boldsymbol{H}|}{k_B T}\right) \tag{3-21}$$

where β_{tot} is the volumetric ratio of superparamagnetic nanoparticles in a microbubble, M_s is the saturation magnetization of the superparamagnetic nanoparticles, V is the effective

volume of a superparamagnetic nanoparticle, and k_BT is the product of the Boltzmann constant and the temperature [204].

Combining equations (3-19) –(3-21) at each point provides a value for μ_p and hence for the Clausius-Mossotti factor K.

Boundary conditions

It was assumed that when a microbubble strikes the vessel wall, it bounces off elastically. Immediately after a collision, the particle velocity is:

$$\boldsymbol{v} = \boldsymbol{v_c} - 2(\mathbf{n}.\boldsymbol{v_c})\mathbf{n} \qquad (3\text{-}22)$$

where $\boldsymbol{v_c}$ is the velocity before striking the wall and $\mathbf{n}$ is the unit vector normal to the wall, pointing into the channel.

Mathematical solver

The trajectories of 300 microbubbles were computed in Comsol® using the "Particle Tracing Module". The transient phase was studied over 150 s, in time steps of 6 ms. The trajectories were solved for 600 degrees of freedom with a Generalised Minimal RESidual iterative algorithm (GMRES) in a fully coupled approach. The relative tolerance was set to 10^{-5} and the absolute tolerance to 10^{-6}.

3.2.2.e) Finite element mesh

A baseline finite element mesh was constructed to resolve the computational model. It comprises two distinct regions: the space inside the channel (fine mesh), and the space outside the channel (coarser mesh). Further mesh refinements were applied at the edges of the channel (boundary layer meshing). In each region, element size in the baseline mesh was chosen to be much smaller than the characteristic length of variation for the fluid velocity field and/or the magnetic field.

In order to reduce mesh-induced error, a mesh-independence study was carried out. A steady-state model of the fluid flow was solved with five different mesh densities: a baseline mesh, two finer meshes, and two coarser meshes. The properties of each mesh are described in Table ***3-4***.

The impact of mesh density on the solution was assessed for four variables. These variables were chosen for their physical relevance to the transport problem: fluid velocity just before the bifurcation (line K on Figure 3-2), fluid velocity along the midline of the occluded branch (line M), magnetic field along the same line, pressure along the midline of the free branch (line L).

The maximum and minimum element sizes remain proportional in the different mesh densities: the sizes in the baseline mesh were multiplied by a number, the "mesh factor", to yield the different mesh densities. A lower mesh factor thus corresponds to a finer mesh. To reduce computational time, the element size outside the channel was not modified. This is due to the fact that in this region, the magnetic field is the only physically relevant field. Recent studies simulating the magnetic field in similar geometries have shown that the mesh density used here is suitable for modelling the magnetic field [205].

Mesh factor	Min element size (m)	Max element size (m)	Number of domain elements	Number of boundary elements
0.5	5.00E-08	1.20E-05	3.9E+05	1.3E+04
0.75	7.50E-08	1.80E-05	2.3E+05	8.5E+03
1	1.00E-07	2.40E-05	1.6E+05	6.5E+03
2	2.00E-07	4.80E-05	7.1E+04	3.3E+03
5	5.00E-07	1.20E-04	2.7E+04	1.5E+03

***Table** 3-4: Mesh properties for mesh-independence study. The study compares the effect of 5 meshes on the numerical solutions for: fluid velocity just before the bifurcation (line K) , fluid velocity along the midline of the occluded branch (line M), magnetic field along the same line, pressure along the midline of the free branch (line L).*

3.2.3. Experiments

A PDMS-glass microfluidic device was used to mimic an arteriolar bifurcation with the same dimensions as the numerical model. To reflect the simulations, three types of experiments were carried out: flow visualisation, drug delivery, and microbubble delivery.

3.2.3.a) Materials

Poly(dimethyl-siloxane) (PDMS) was purchased from Dow Corning Corporation (Auburn, MI, USA). Epoxy adhesive (Yellow Dual Cartridge) was obtained from RS Components Ltd (Northants, UK).

Polyethylene glycol (40) stearate (PEG40S), glycerol, propylene glycol, chloroform and dimethyl sulfoxide (DMSO) were purchased from Sigma Aldrich (Gillingham, UK). 1,2-Distearoyl-sn-glycero-3-phosphocholine (DSPC) was obtained from Avanti Polar Lipids (Alabaster, AL, USA), and sulphur hexafluoride (SF6) from the BOC Group (Guildford, UK). Phosphate-buffered saline (PBS) and the lipophilic dye DiI (1,1'-dioctadecyl-3,3,3',3'-tetramethylindocarbocyanine perchlorate) were acquired from Thermo Fisher Scientific Inc. (Paisley, UK).

3.2.3.b) Experimental setup

The PDMS-glass microfluidic device was manufactured following Carugo *et al.*'s protocol [206], described in Figure 3-4. A poly(methyl 200 methacrylate) (PMMA) block was milled into a negative mould of the bifurcation. Liquid epoxy adhesive was poured over the PMMA, degassed in a vacuum chamber for 5 minutes, and cured at ambient temperature for ~100 min, creating a positive mould. The PDMS device was cast in the epoxy mould with a curing agent:monomer ratio of 1:10 w/w. The magnet was placed on the epoxy mould prior to PDMS casting. The system was degassed in a vacuum chamber for 20 minutes and cured overnight at room temperature. The PDMS layer was then

bonded to a 1-mm thick glass layer (Corning® microscope slides, Sigma Aldrich) by plasma treatment (plasma cleaner ATTO, Diener electronic GmbH, Ebhausen, Germany).

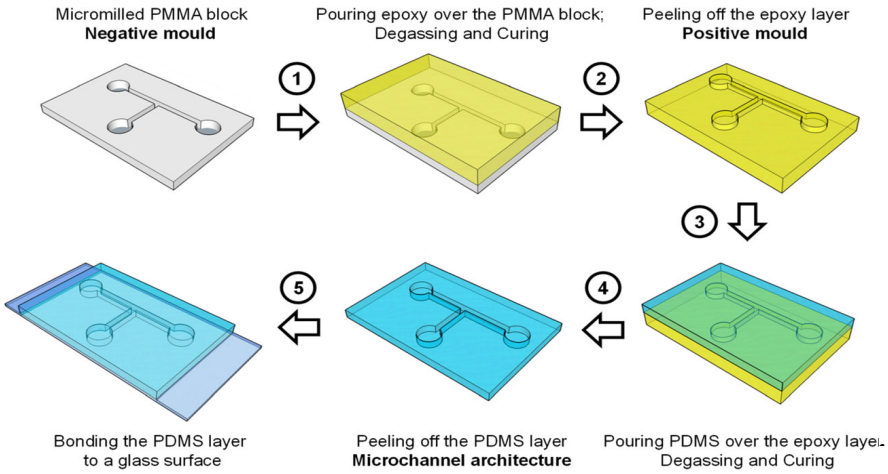


Figure 3-4: Microfluidic device fabrication process. Reproduced from Carugo et al.[206] ***with permission of Springer.***

The dimensions of the device are shown in Table 3-1 and Figure 3-5 illustrates the experimental setup. A syringe pump (World Precision Instruments, Hitchin, UK) fitted with a 3 mL syringe (Beckton Dickinson, Oxford, UK) controlled the flow in the device. At low injection rates, the performance the syringe pump is limited by its motor step. When approaching this limit, the flow delivered by the pump becomes unstable and partially pulsatile [207]. In order to compare with the simulations, which did not take pulsatility into account, these oscillations in the experimental model were dampened with a custom-built flow damping reservoir placed between the pump and the device. Figure 3-6 shows a sketch of the damper.

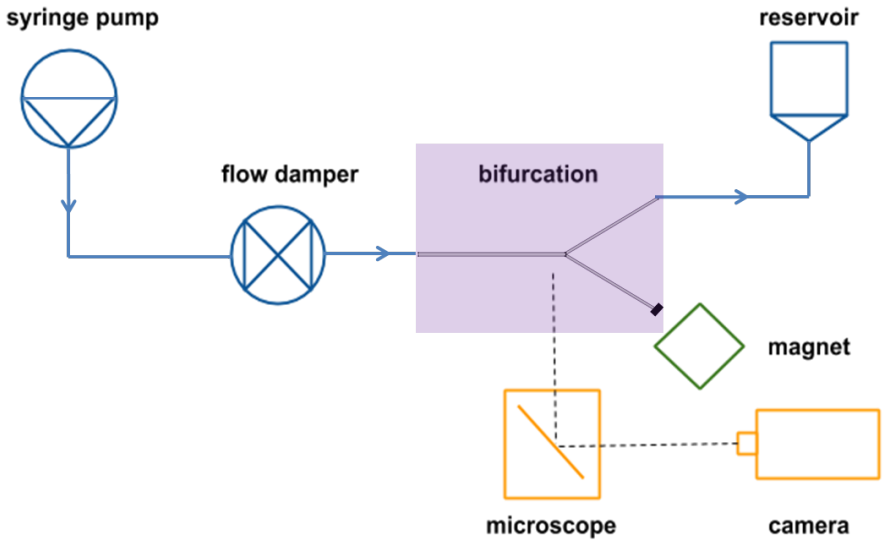


Figure 3-5: Schematic of the experimental setup. A syringe pump controlled flow rates into a microfluidic bifurcation with a fully occluded branch. A single-element permanent magnet provided the magnetic field. A fluorescence microscope enabled real-time imaging of FITC-labelled beads (in the flow visualisation study), TRITC-tagged bovine serum albumin (in the drug delivery study), and DiI-labelled magnetic microbubbles (in the microbubble delivery study).

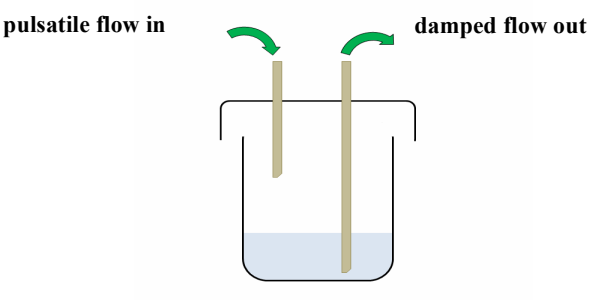


Figure 3-6: Sketch of the custom-made microfluidic flow damping device for use with a syringe pump at low flow rates. The device reduces flow rate oscillations from the syringe pump to ensure a constant flow velocity into the microfluidic bifurcation.

The magnetic field was applied using a single 12.7 mm cubic permanent magnet element (N52 grade NdFeB, with a measured magnetisation value of 1.09×10^6 A/m [199]). The magnet was placed in the same position as in the simulation, with its magnetisation vector parallel to line M and its surface 10 mm from the centre of the bifurcation (point Y). The base of the magnet was flush with the glass slide.

3.2.3.c) Flow visualisation

In the flow visualisation experiments, 2-µm diameter fluorescently-labelled polystyrene beads (Sigma Aldrich) were added to deionised water in the syringe at a 5×10^{-3} % volume/volume. The low volume fraction and the small bead diameter were chosen to ensure that the microbeads do affect the flow. Both branches of the bifurcation were primed with the fluid. Prior to each experiment, an interval of at least 30 seconds was maintained between flow initiation and data acquisition, so as to allow the pressure to stabilise in the microfluidic system.

Images of the bifurcation region were acquired on a fluorescence microscope (Ti Eclipse, Nikon Instruments Inc., NY, USA) with a ×10 objective (Plan Fluor Ph1 DLL, Nikon) and a digital camera (Digital Sight Qi1Mc-U2, Nikon). The excitation and acquisition wavelengths were 470 nm and 510 to 550 nm respectively, the frame rate was set to 14 frames/s, and the camera exposure time ranged from 2 to 67 ms/frame.

3.2.3.d) Drug delivery

In the drug delivery experiments, fluorescent bovine serum albumin was used as a model for tPA (TRITC-BSA, Thermo Fisher Scientific), as it is a globular protein with a similar molecular weight (see 3.2.2.c). The model drug was injected at a final concentration of 6.2×10^{-8} mol/L in deionised water.

Microscopic data acquisition began immediately after flow initiation, with $\lambda_{excitation}$= 470 nm, $\lambda_{acquisition}$= 510 to 550 nm, and a ×10 objective on the fluorescence microscope. A scan of the whole occluded branch was performed every 30 seconds to monitor drug diffusion, with an exposure time of 333ms/frame.

Microscope images were processed with a custom-built code written in Matlab (The MathWorks Inc., Natick, MA, USA). Briefly, greyscale intensity was averaged over the thickness of a 10-pixel thick line with the same coordinates as line M. As luminosity varied slightly in the room over the course of one hour, image brightness was adjusted so that mean greyscale intensity remained constant in a region of interest in the parent branch.

3.2.3.e) Microbubble delivery

In the microbubble delivery experiments, lipid-shelled microbubbles loaded with 10-nm iron oxide nanoparticles were labelled with DiI for visualisation and tracking.

Microbubble preparation

The microbubble formulation protocol was adapted from Owen *et al.*[208]. DSPC and PEG 40 stearate dissolved in chloroform were mixed in a glass vial at a 9:1 molar ratio. The lipid solution was made fluorescent by adding 50 µg of the lipid analogue dye DiI dissolved in DMSO. The solvent was then allowed to evaporate at 50 °C for 12 hours. A solution of PBS, glycerol and propylene glycol was prepared at volume ratios of 8:1:1 and

the lipid film was re-suspended in 2 mL of this solution for over 1 hour at 75 °C under constant stirring. The preparation was then sonicated for 90 s using a 22.5 kHz ultrasonic cell disruptor (Microson XL, Misonix Inc., Farmingdale, NY, USA) operating at level 4, corresponding to an output power of 8 WRMS. During sonication, the tip of the sonicating probe was fully immersed in the solution. In order to obtain magnetic microbubbles, 15 µl of an aqueous suspension of lipid coated magnetic particles (FluidMAG-Lipid, Chemicell Gmbh, Berlin, Germany, 25 mg/ml) were added for the final 30 s of sonication. It was followed by a second sonication step under positive pressure of SF_6 at level 19 for 20 s, with the tip at the gas water interface to entrain gas. The microbubble solution was then cooled in an ice bath for approximately 10 minutes.

Microbubble characterisation

Microbubble size and concentration were assessed as previously described by Sennoga *et al.* [209]. A 10 µl sample was placed in the chamber of a haemocytometer and 30 brightfield images were acquired with an optical microscope (DM 500, Leica Microsystems Ltd., Milton Keynes, UK) fitted with a x40 objective (HI Plan 40x/0.65, Leica). The images were analysed using purpose written software in MATLAB. The experiments were carried out with a concentration of 2.9×10^8 microbubbles/mL diluted in phosphate buffered saline. To limit variations in the delivered microbubble concentration, the syringe was shaken prior to each experiment, and the solution was changed every hour.

Microbubble delivery visualisation

Image acquisition was performed on the fluorescence microscope with a ×10 objective at $\lambda_{excitation}$= 525 nm, $\lambda_{acquisition}$ = 575 to 625nm, and an exposure time of 50 ms/frame. Final microbubble distribution was investigated with scans of the whole occluded branch acquired after 10 minutes, with the focus in the mid-plane of the channel. Therefore at each inlet velocity, two images were acquired: one in the presence of the magnet, and one in the absence of the magnet. These images where processed with purpose-written code in Matlab. After background subtraction, the two images were registered by detection of a circular fiducial marker located at the centre of the bifurcation (Hough transform). Image brightness was normalised in both images by computing the mean brightness in a 50 ×100 pixel region near the centre of the bifurcation. The edges of the occluded channel were then detected by greyscale thresholding. Image brightness was averaged in the cross-section of the channel to yield a brightness profile along the occluded branch.

3.3. Results

3.3.1. Preliminary studies

Before conducting the investigation, preliminary assessments were carried out to validate the *in silico* and the *in vitro* models.

3.3.1.a) Mesh independence study

The simulations were validated by a mesh independence study. Figure 3-7 a-d. superimposes the values of selected variables for five mesh densities. In Figure 3-7 a., the fluid velocity magnitude along lines K and M computed at mesh factors at factors 0.5, 0.75 and 1 were identical within a ±0.8% interval. On the other hand, velocity solutions computed at mesh factors 2 and 5 (orange and dark blue) differed visibly, with a maximum difference on the order of 7.6% at mesh factor 2 and 12.1% at mesh factor 5. In Figure 3-7 d. also shows that mesh densities 2 and 5 affect the position of the local minima.

In Figure 3-7 b., all pressure solutions remained within with a ±1.7% interval from pressures computed at mesh density 1. In Figure 3-7 c., all magnetic field solutions were identical to within ± 1 x 10^{-6} T (<0.1%).

These preliminary simulations indicate that velocity was sensitive to changes in the mesh, while the pressure and magnetic field were hardly affected. They also show that a mesh factor of 1 was the maximum allowable mesh size. Larger mesh elements, obtained with mesh factors 2 and 5, had noticeable effects on the computed velocity field. On the other hand, further refinements in the mesh (factors 0.5 and 0.75) increased computational time without affecting the solution. In the rest of the study, a mesh factor of 1 was therefore applied.

3.3.1.b) Flow rate validation

The flow rates provided by the syringe pump were confirmed experimentally. For each flow rate (the same as in the *in silico* model), multiple images of mid-plane of the mother branch were acquired in the presence of the FITC-labelled polystyrene beads. Custom-built Matlab software computed the velocity profile in the branch from the length of the visible streaks in the fluorescence microscopy images. Figure 3-8 plots these profiles against their theoretical equivalent and shows good agreement in cases c-f., for mean inlet velocity rates greater than 10 mm/s. It was noted that the number of streaks sampled at the highest flow rate (100 mm/s, case f.) was low because at this velocity, the flow markers were moving rapidly through the bifurcation and only a few streaks were visible on the acquired images.

On the other hand, slow flow rates came close to the limits of stability of the syringe pump and the observations did not match the theoretical profiles. In case b., at 5 mm/s mean inlet velocity, the profile was still parabolic but the velocity was slightly higher than expected. In case a., at 1 mm/s, the profile was no longer parabolic and the flow was visibly unstable.

As a result of these preliminary observations, only mean inlet velocities between 5 and 50 mm/s were investigated in the rest of the study.

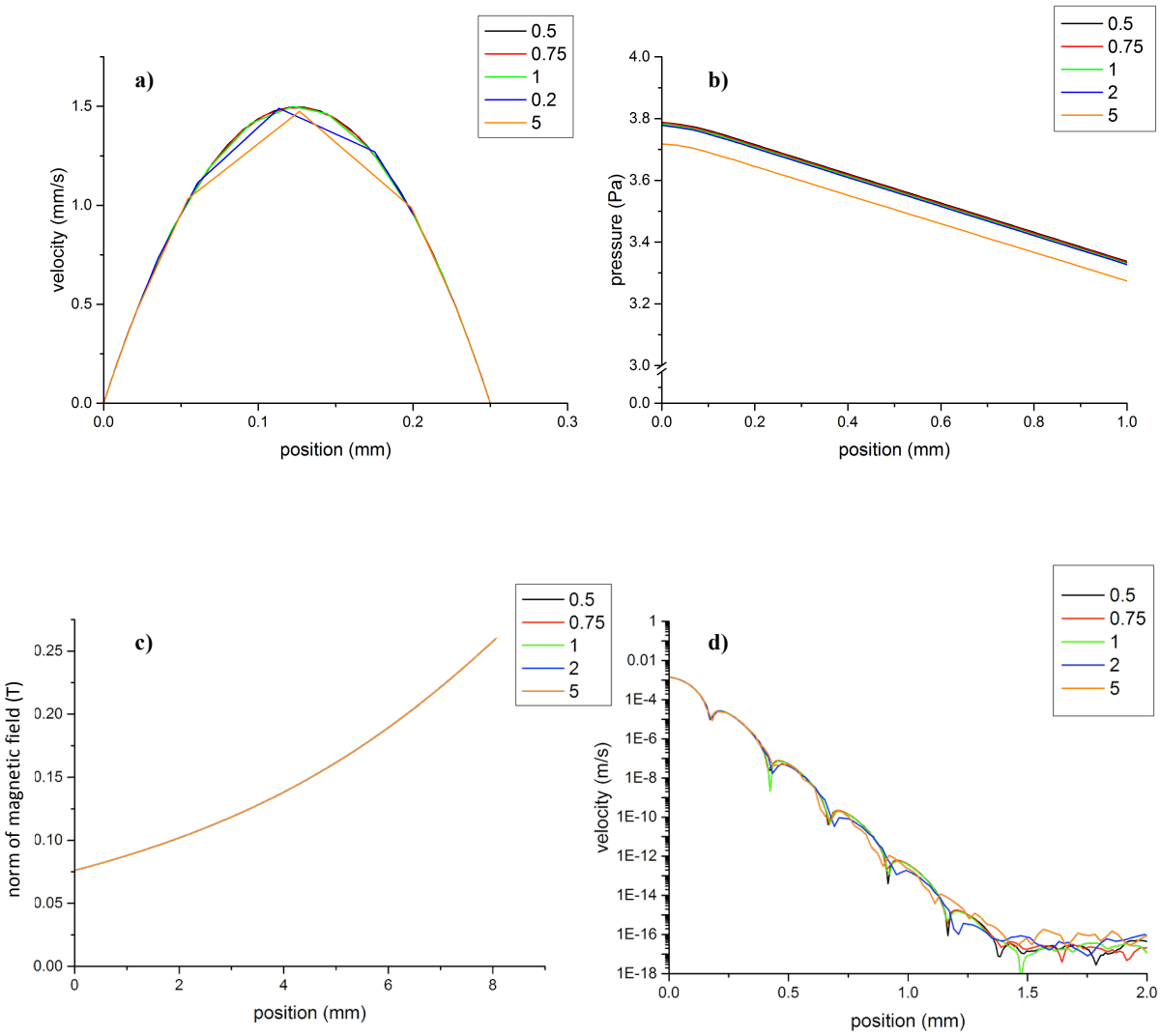


Figure 3-7: Mesh independence study. Selected parameters are plotted along line of interest for five different mesh densities:

a) fluid velocity along the cross section of the main branch (line K in Figure 3-2)

b) pressure along the axis the free branch (line L)

c) norm of magnetic field along the axis of the occluded branch (line M)

d) fluid velocity along the main axis of the occluded branch (line M)

The legend indicates the mesh factor.

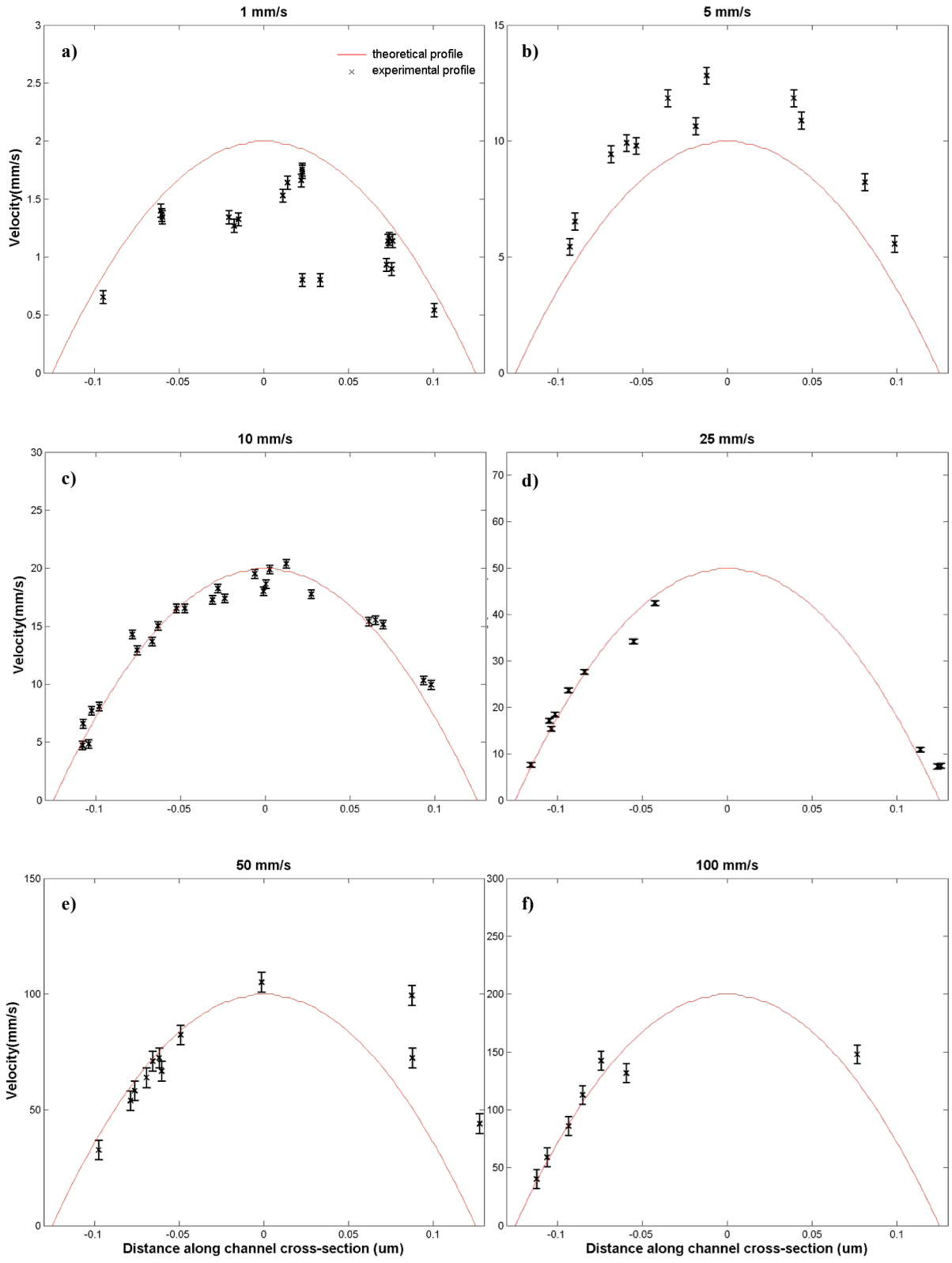


Figure 3-8: Flow rate validation experiments. Experimental observation of the flow profile in the cross section of the main branch. Comparison to theoretical values for different mean inlet velocity settings:
a) 1 mm/s; b) 5 mm/s; c) 10 mm/s; d) 25 mm/s; e) 50 mm/s; f) 100 mm/s.
Error bars represent estimated experimental uncertainty.

3.3.1.c) Entrance length

In order to highlight the necessity of taking entrance length into account (see 3.2.2.a)) and of separating the fluid inlet from the microbubble injection point, Figure 3-9 shows the trajectories of 30 microbubbles uniformly injected into the system at the fluid inlet. The microbubbles moved away from the vessel wall immediately after injection. The trajectories became parallel within a short distance comparable to the computed value of 275 µm, and a region depleted of microbubbles appeared near the walls.

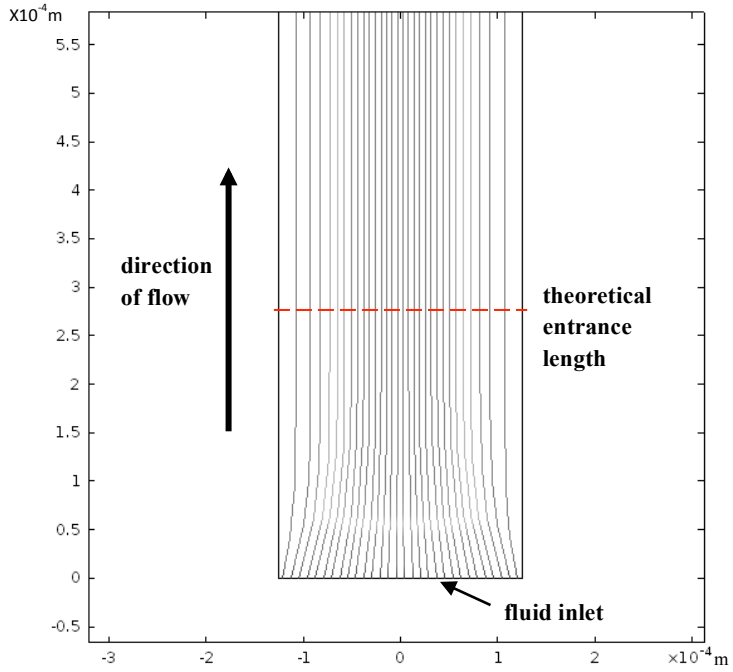


Figure 3-9: Initial trajectories of 30 microbubbles injected uniformly at the fluid inlet (zoom on the inlet region). The trajectories were simulated numerically in Comsol®.

3.3.2. Flow dynamics

The first stage of the investigation explored the general fluid mechanics phenomena that develop in the occluded branch.

3.3.2.a) Simulations

In the COMSOL model, the general flow pattern was computed and the influence of inlet velocity was studied, as well as the effect of clot position along the occluded branch (branch length). Figure 3-10 shows an example of the flow pattern in the occluded branch. Multiple vortices formed and velocity dropped rapidly (- 94 % in velocity magnitude within 150 μm of the bifurcation point). Figure 3-11 and Figure 3-12 show the influence of mean inlet velocity and of occluded branch length on the velocity field in the occluded branch. The fluid velocity along the midline of the branch increased with inlet velocity but wasn't affected by branch length. As a result, the effect of inlet velocity was further examined in this study. The effect of branch length was no longer considered. In addition, it is noted that neither parameter affected the position and size of the vortices.

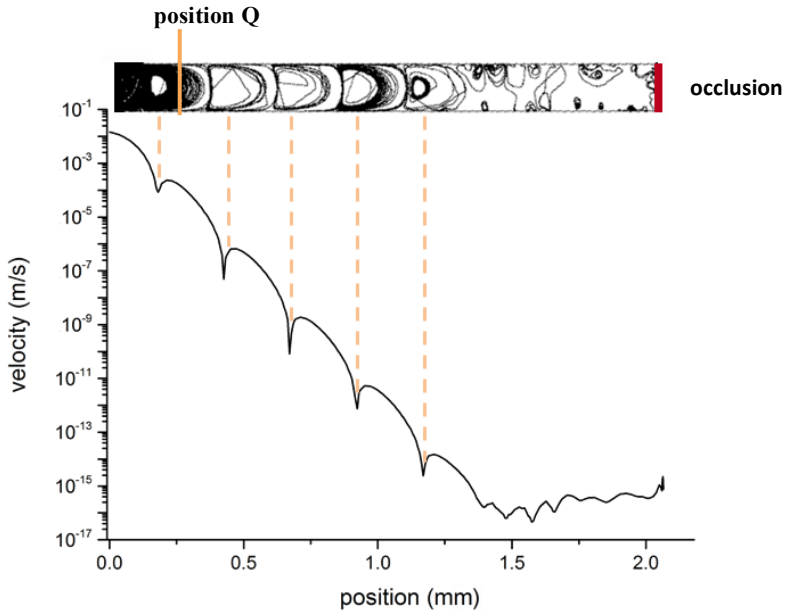


Figure 3-10: Example of fluid velocity profile computed along the axis of the occluded branch (line M).
Fluid velocity is plotted as a function of position along line M.
Inset: streamlines in the occluded branch at corresponding positions. At the centre of each vortex is a local minimum in velocity. Position Q designates the position of interest studied in Figure 3-11.
In this example, mean inlet velocity = 10 mm/s, branch length = 2 mm.

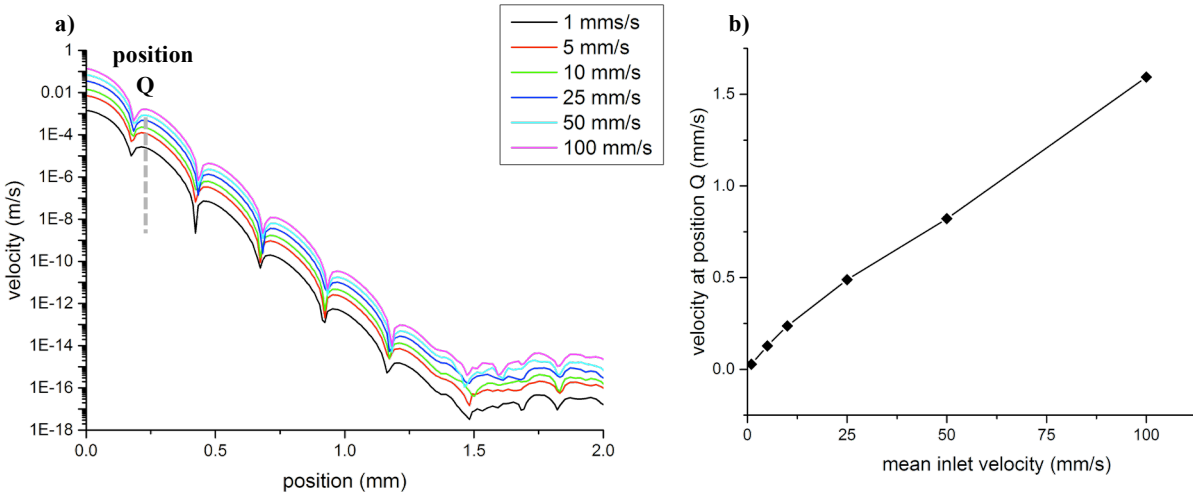


Figure 3-11: Influence of mean inlet velocity on the velocity field in the occluded branch. a) fluid velocity along the axis of the occluded branch (line M) for six mean inlet velocities in the 1-100 mm/s range;
b) velocity at position marked Q in subfigure a.(also see Figure 3-10 for a schematic of position of Q in the occluded branch), as a function of mean inlet velocity.
In this simulation, branch length = 8 mm.

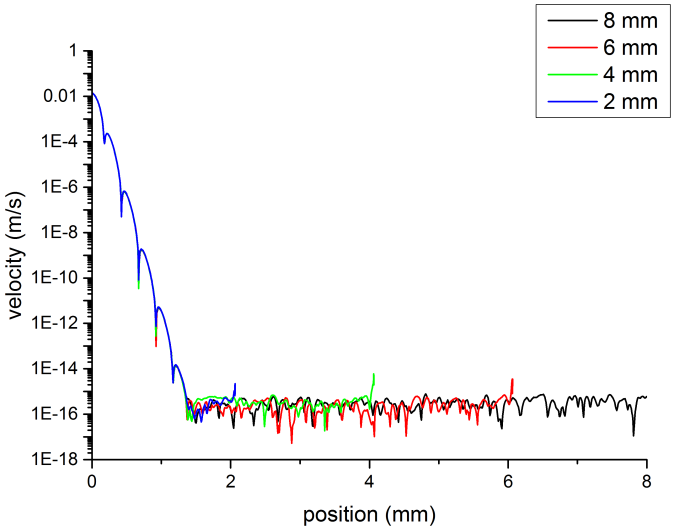


Figure 3-12: Influence of occlusion distance on the velocity field in the occluded branch: fluid velocity along the axis of the occluded branch (line M) for 4 values of branch length: 2 mm (orange), 4 mm (green), 6 mm (red), 8 mm (blue). In this simulation, mean inlet velocity = 10 mm/s.

3.3.2.b) *In vitro* experiments

Figure 3-13 a. shows the flow pattern in the bifurcation, observed by fluorescence microscopy using labelled flow markers. In the parent branch and in the free branch, flow velocity was high and the trajectories of individual markers could not be distinguished. In the occluded branch, the first vortex was clearly visible: flow velocity was lower and individual streaks were seen. Beyond the first vortex, there was no overall movement of the flow markers during data acquisition. The second vortex predicted by the simulations could not be observed. In fact, observing the second vortex would have required a very long exposure time, which would have made the visualisation of the first vortex difficult. The experiment was repeated at all four mean inlet velocities and the pattern was found to be comparable (data not shown).

The predicted flow pattern and the experimental observations were very similar in the first vortex, as shown in Figure 3-13 b.

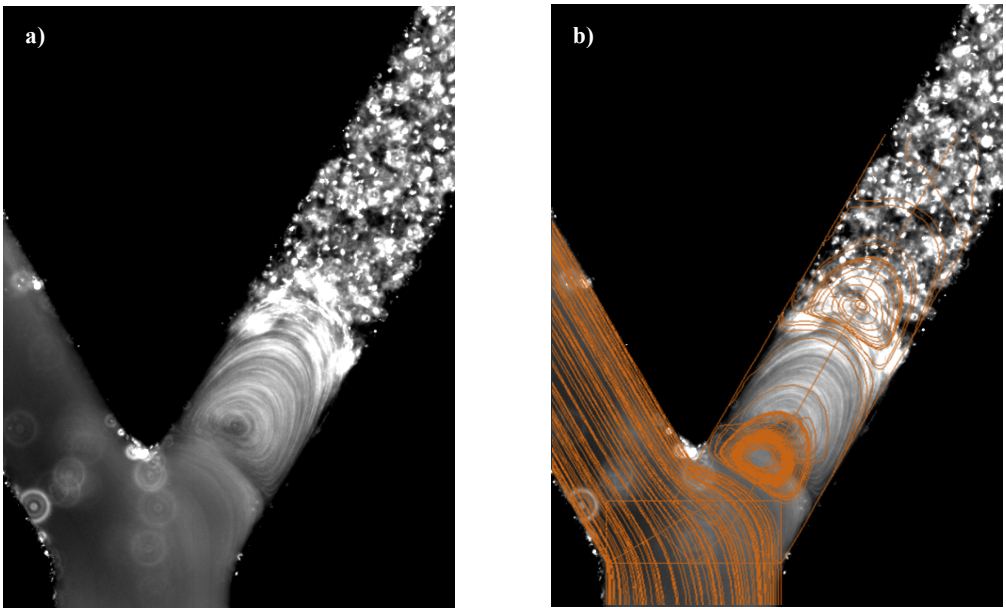


Figure 3-13: Flow pattern in the occluded branch, visualised in fluorescence microscopy using long exposure times (3.4s) and FITC-labelled microbeads as flow markers: a) experimental observations; b) comparison of experimental observations and computed streamlines.
In this example, mean inlet velocity = 10 mm/s, branch length = 8 mm.

3.3.3. Drug delivery

3.3.3.a) Simulations

In silico experiments were carried out to investigate the transient phase of tPA delivery in the bifurcation. Injection of a clinically relevant concentration of tPA was simulated and drug distribution in the following 60 minutes is modelled. Figure 3-14 shows a sharp reduction in drug concentration in the occluded branch (-95% of concentration within 1.7 mm of the centre of the bifurcation at t=1h with a mean inlet velocity of 10 mm/s). This highlights the difficulty of delivering therapeutically relevant drug concentrations at the site of occlusion. It also shows that, as expected, delivery success strongly depends on the location of the clot relative to the bifurcation.

In order to analyse the disparities in concentration, a "half concentration distance" was defined as the distance along line M at which drug concentration reaches half of the injected concentration. Figure 3-15 shows the slow evolution of this distance over time: after an hour, it was only 800 μm. Furthermore, the half concentration distance increased with mean inlet velocity, as indicated in Figure 3-16. However, it was not sensitive to branch length (data not shown).

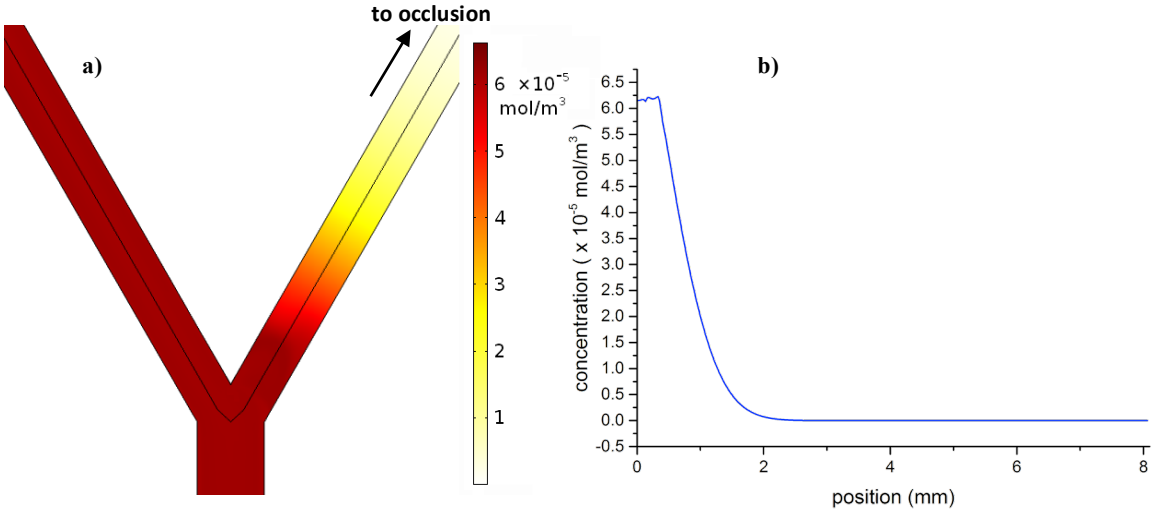


Figure 3-14: Simulated drug distribution in the bifurcation after 1h of continuous tPA infusion at a concentration of 6.2 x 10^2 mol/L: a) heat map of final tPA concentration in both branches; b) final concentration of tPA along line M. In this simulation, mean inlet velocity = 10 mm/s and branch length = 8 mm. In subfigure a), only the bifurcation region is shown. Both branches extend well beyond the first section shown here.

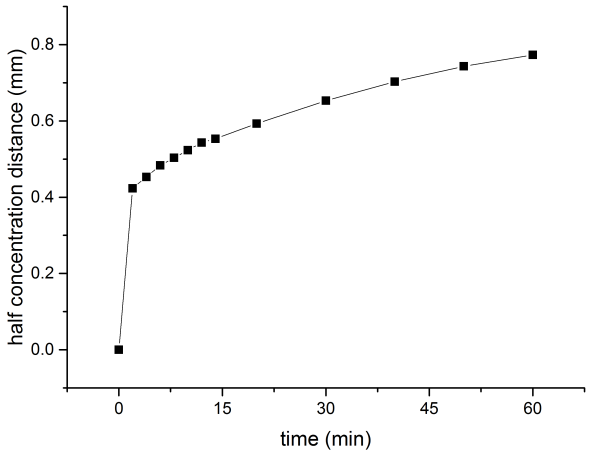


Figure 3-15: Simulated half concentration distance along line M in the first 60 minutes of continuous tPA infusion at a concentration of 6.2 x 10^2 mol/L.
In this simulation, mean inlet velocity = 10 mm/s and branch length = 8 mm.

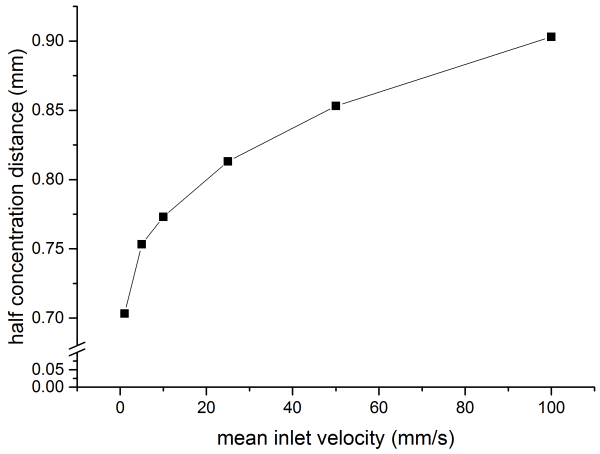


Figure 3-16: Simulated effect of mean inlet velocity on half concentration distance along line M at t=60 minutes during continuous tPA infusion at a concentration of 6.2 x 10^2 mol/L.
In this simulation, branch length = 8 mm.

3.3.3.b) Experiments

tPA delivery was also observed experimentally using a fluorescent drug model (TRITC-labelled BSA) over the course of 60 minutes. The experiments were carried out for a single set of experimental conditions, with a mean inlet velocity of 10 mm/s and a branch length of 8 mm.

Figure 3-17 shows that drug delivery in the occluded branch was indeed limited. After 60 minutes, fluorescence intensity was higher in the first vortex than in the main branch, but it rapidly decreased as the distance from the bifurcation increased and it reached 15% of the main vessel intensity within 750 µm. Unexpectedly, the increase in intensity in the first vortex was much more pronounced in the experiments than in the simulations (+30% greyscale intensity compared to the main branch in the experiments, versus only +1.2% tPA concentration predicted).

Figure 3-18 shows that the evolution of the half concentration distance over time was qualitatively similar to the predicted trends: the distance rapidly increased in the first 15 minutes, then increased more slowly over the next 45 minutes.

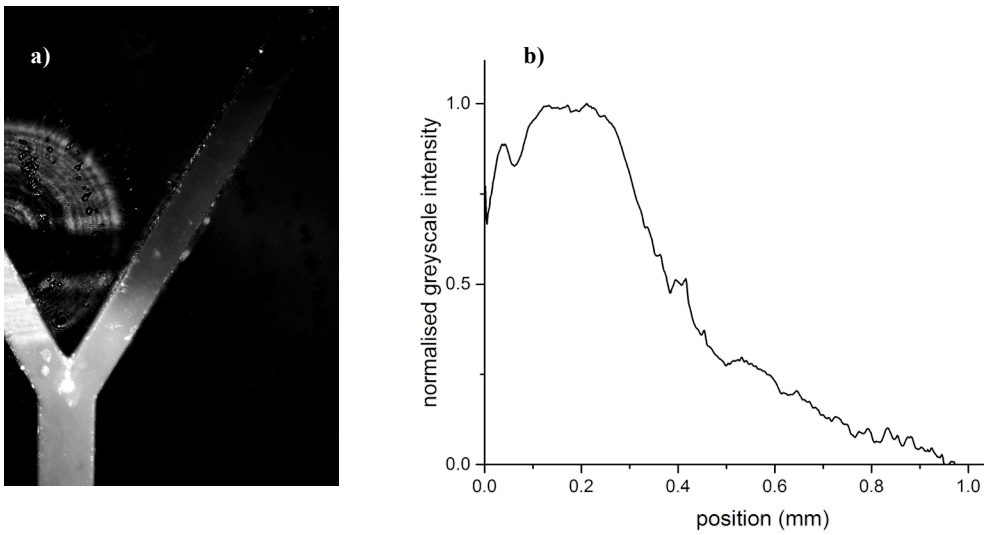


Figure 3-17: Experimental distribution of a fluorescent drug model in the bifurcation at t = 1h after beginning of continuous tPA infusion at a concentration of 6.2 x 10^2 mol/L.
a) fluorescence microscopy image of drug distribution in the occluded branch; b) normalised greyscale intensity along line M.

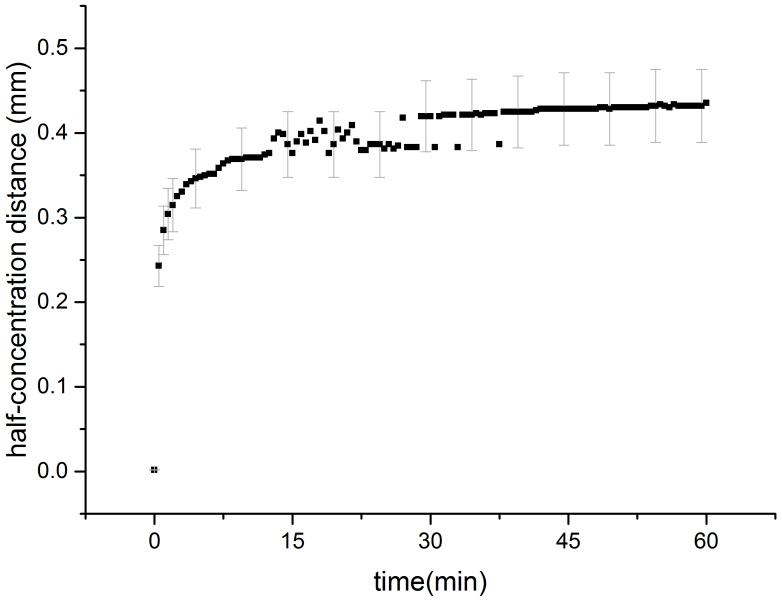


Figure 3-18: Experimental half concentration distance along line M in the first 60 minutes of continuous tPA infusion at a concentration of 6.2 x 10^2 mol/L. Greyscale intensity was computed along line M every 30 s and the half-concentration distance was plotted. The error bars represent experimental error.

3.3.4. Microbubble delivery

3.3.4.a) Simulations

In order to quantify microbubble delivery, 4 possible states were defined for an individual microbubble passing through the bifurcation:

- **undelivered** (the microbubble didn't reached the bifurcation within the experimental time frame, it remained in the region coloured in red in Figure 3-19.
- **bypassed** the occluded branch (it passed into the free branch, marked blue)
- **trapped** in the occluded branch (it was in the regions marked yellow or green)
- **delivered** to the clot (in the green band)

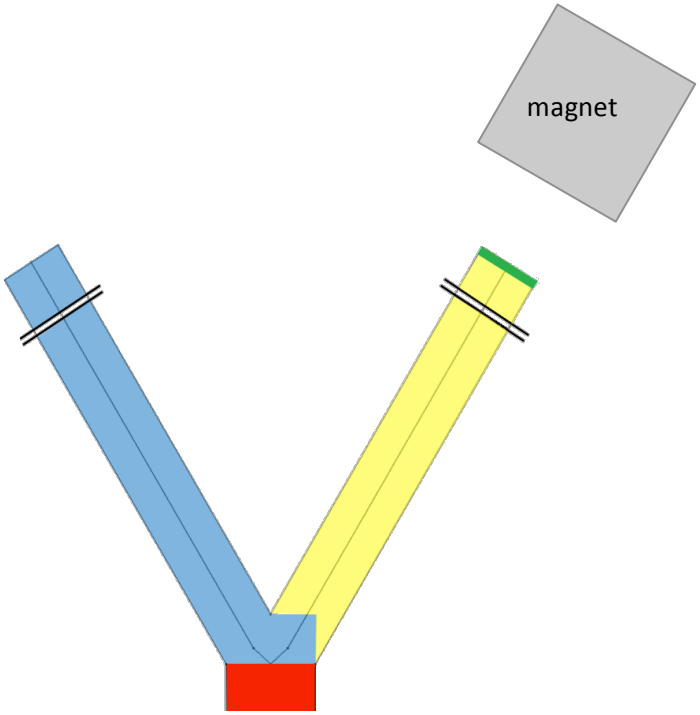


Figure 3-19: Possible delivery outcome for an individual microbubble after 150s: not yet delivered (microbubble in the red region after 150s), bypassed the occluded branch (in the blue), trapped in the occluded branch (yellow + green), delivered to the clot (green). Magnet not drawn to scale.

Challenges to microbubble delivery in the occluded bifurcation

Figure 3-20 a. gives an example of simulated delivery trajectories (black lines) and outcomes (coloured circles) 150 seconds after bubble injection in the absence of a magnetic field. The majority of microbubbles (98.7%) bypassed the occlusion altogether. 1.0% were trapped in the occluded branch, where they all remained trapped in the first fluid vortex, within 350 µm of the bifurcation point. Thus there was no microbubble delivery to the clot.

Effect of magnetic targeting on microbubble delivery

Figure 3-20 b. illustrates microbubble delivery under the same flow conditions, in the presence of a magnetic field. In this case as well, the majority of microbubbles (95.0%) still bypassed the occluded branch, but 2.3% were trapped in the occluded branch, marking a substantial increase in the number of trapped microbubbles. More importantly, all these microbubbles escaped the first fluid vortex and followed a trajectory close to a straight line. Given that these microbubbles were subject only to the magnetophoretic force and to a very low drag force (fluid velocity is negligible past the first vortex), it is to be expected that they reached the clot at a later time point. In this case too, however, no microbubbles were delivered to the clot within the 150 seconds of simulation time.

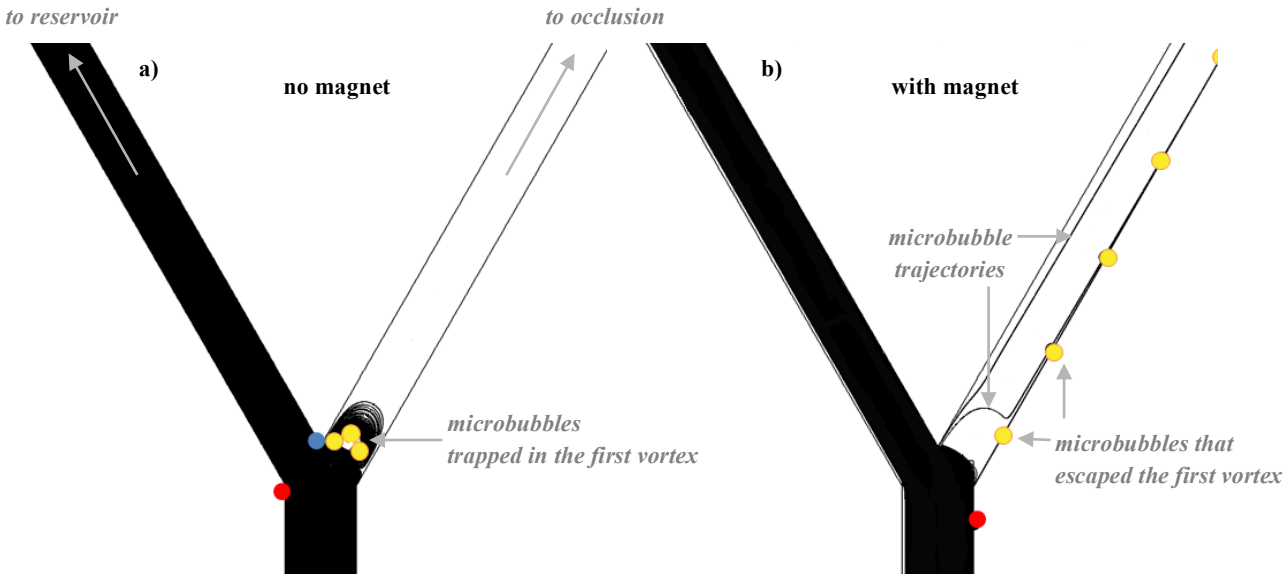


Figure 3-20: Example of simulated microbubble delivery at t = 150 s after injection: a) without magnetic field b) with magnetic field. Black lines trace individual microbubble trajectories, coloured circles show final microbubble position with the colour code defined in Figure 3-19. Both branches extend well beyond the first section shown here. Mean inlet velocity = 10 mm/s, microbubble diameter = 1.2 µm.

Influence of mean inlet velocity on targeted delivery

Since flow conditions vary within vascular networks, the influence of mean inlet velocity on microbubble delivery was investigated with and without magnetic targeting. Figure 3-21 a-b. shows delivery outcomes 150 seconds after injection at mean inlet velocities within the clinically relevant range of 1-100 mm/s, with and without a magnetic field. In the absence of a magnetic field, the proportion of microbubbles trapped in the occluded branch was very low, regardless of the mean inlet velocity (below 2 %). In the presence of a magnetic field, a marked increase in the number of trapped microbubbles was observed at all inlet flow velocities (depending on inlet flow, between 125% to 465% increase, i.e. 4 to 14 additional microbubbles out of 300). The proportion of microbubbles trapped with the magnet was sensitive to mean inlet velocity and, as might be expected, tended to decrease with increasing velocities. Figure 3-21 b. also points to another phenomenon: at low velocities and in the presence of a magnetic field, a large proportion of microbubbles (up to 10% at 1 mm/s) remained undelivered. They were pulled by the magnet close to the

main branch wall, where flow is slower, and they did not reach the bifurcation within the simulation time. This effect decreased rapidly with increasing flow rate. It was also found that no microbubbles of this size (1.2 µm, the mean diameter of the experimental microbubble population [193]) were successfully delivered to the clot within the simulation time, regardless of mean inlet velocity.

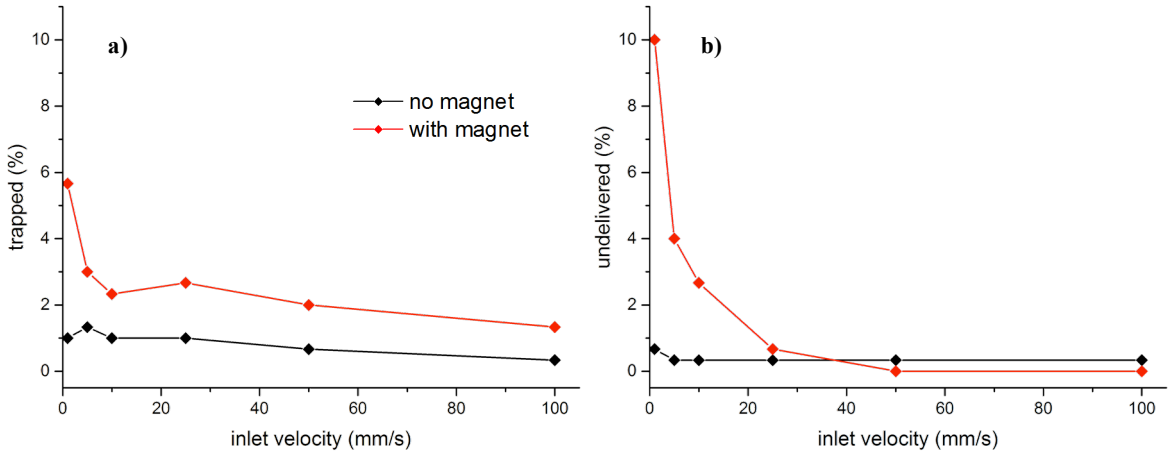


Figure 3-21: Effect of mean inlet velocity and magnetic targeting on microbubble position after 150s simulation time: a) the proportion of microbubbles trapped in the occluded branch; b) the proportion of undelivered microbubbles. In this case, microbubble size = 1.2 µm and branch length = 8 mm.

Influence of microbubble size on targeted delivery

Microbubbles of various sizes experience different drag and magnetophoretic forces, and the formulation can therefore be engineered to optimize bubble size. We therefore investigated the effect of size on delivery outcomes by simulating trajectories for microbubbles within a 0.6-5 µm diameter range, which is comparable to the size range of commercially available contrast agents [210].

Figure 3-22 a-c. shows the outcomes for five different microbubble sizes. In the absence of a magnetic field, size had no effect on delivery outcomes. At all sizes, fewer than 2% of the injected microbubbles were trapped in the occluded branch. On the other hand, in the

presence of a magnetic field, microbubble delivery was considerably enhanced and the outcome was highly sensitive to size due to increased magnetic force. The proportion of microbubbles trapped and delivered increased rapidly with microbubble diameter, from 1% trapped and 1.7% delivered at 0.6µm to 100% trapped and delivered at 5 µm.

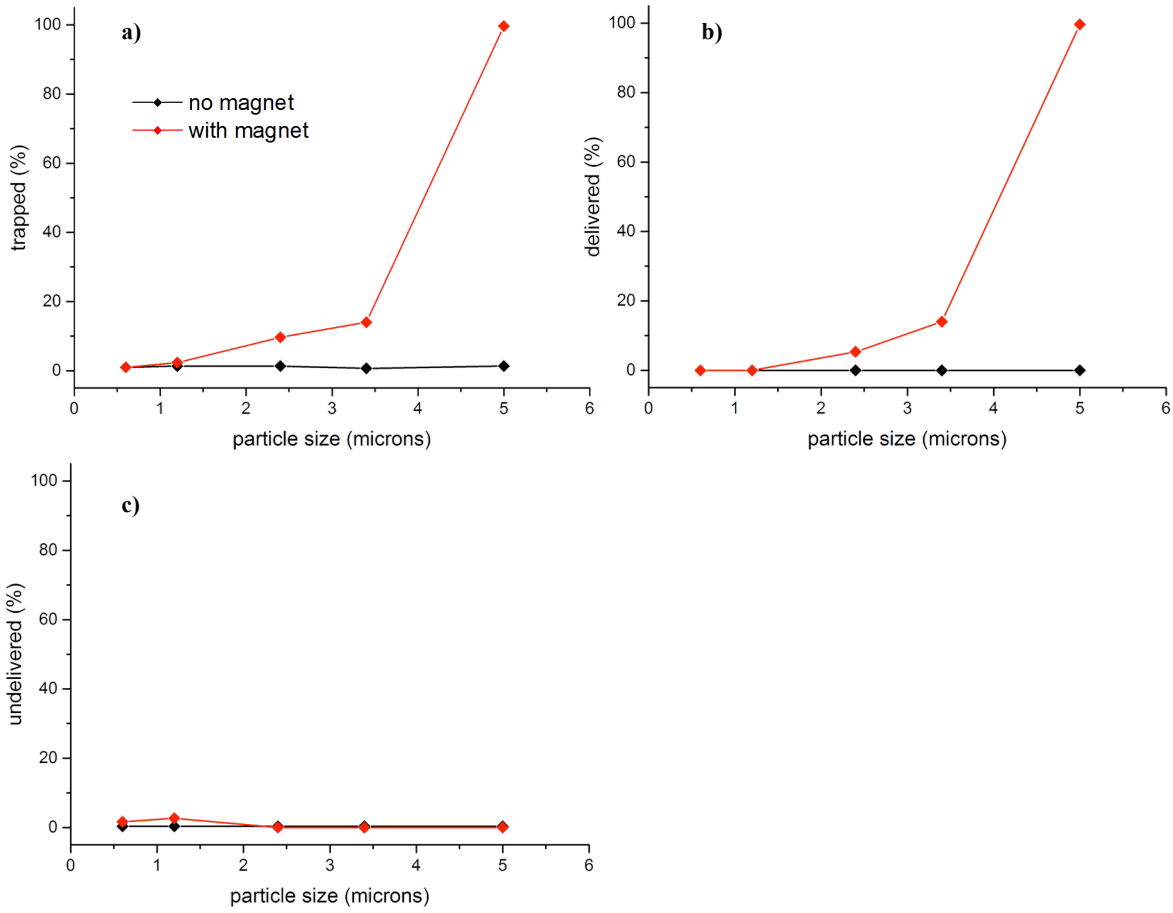


Figure 3-22: Effect of mean microbubble diameter and magnetic targeting on microbubble position after 150 s simulation time: a) the proportion of microbubbles trapped in the occluded branch; b) the proportion of microbubbles delivered to the clot, 8 mm into the occluded branch; c) the proportion of undelivered microbubbles. In this case, mean inlet velocity = 10 mm/s and branch length = 8 mm.

Influence of microbubble size and starting position on delivery outcome

Figure 3-23 clarifies the origin of delivered microbubbles by mapping the final state of microbubbles to their initial positions on the inlet. The microbubbles injected near the side of the channel closest to the magnet were least difficult to deliver.

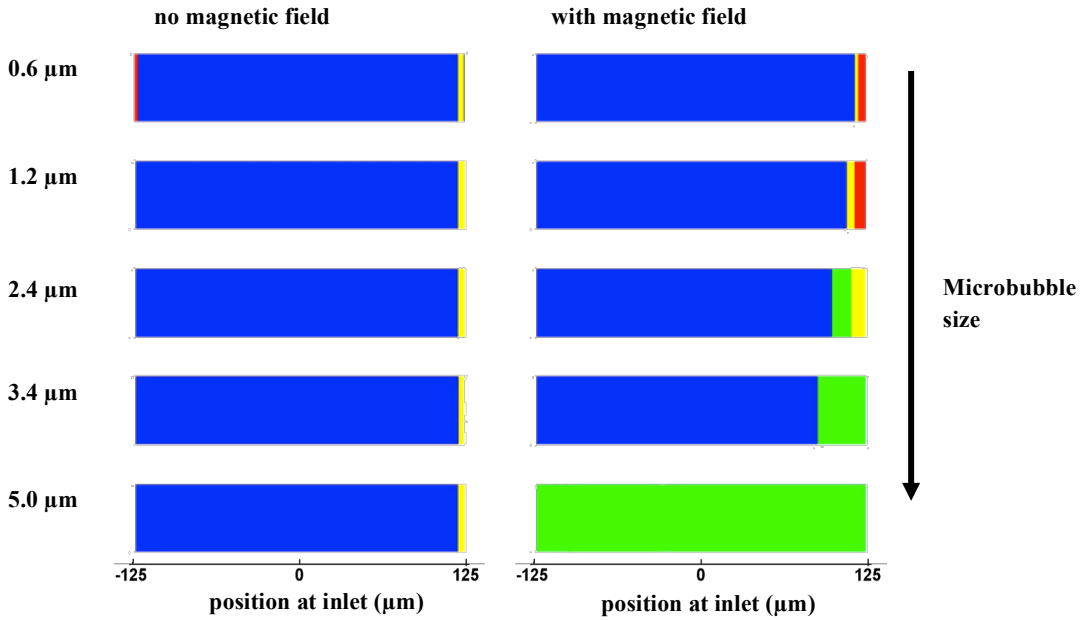


Figure 3-23: Final state of a microbubble as a function of starting position at the inlet and of microbubble diameter. Outcomes are mapped for mean inlet velocity 10 mm/s, in the presence and in the absence of a magnet. Colour indicates delivery outcome as described in Figure 3-19: not yet delivered (red), bypassed the occluded branch (blue), trapped in the occluded branch (yellow + green), delivered to the clot (green).

As the fluid flow profile in the occluded branch was independent of branch length (see Figure 3-12), it can be readily demonstrated that the proportion of microbubbles delivered to the clot at 150 s in the presence of a magnetic field would be greater in a shorter branch, since trapped microbubbles that have escaped the first fluid vortex would reach the clot sooner.

3.3.4.b) Experiments

Effect of magnetic targeting on microbubble delivery

Microbubble distribution was investigated experimentally in the microfluidic bifurcation at various inlet velocities in the presence and in the absence of a magnet. Figure 3-24 shows delivery outcomes in the mid-plane of the occluded branch at a 5 mm/s mean inlet velocity. A marked increase in greyscale intensities was observed in the presence of a magnetic field, up to +159% at 275 µm. The microbubbles were also delivered 175 µm further in the presence of a magnet.

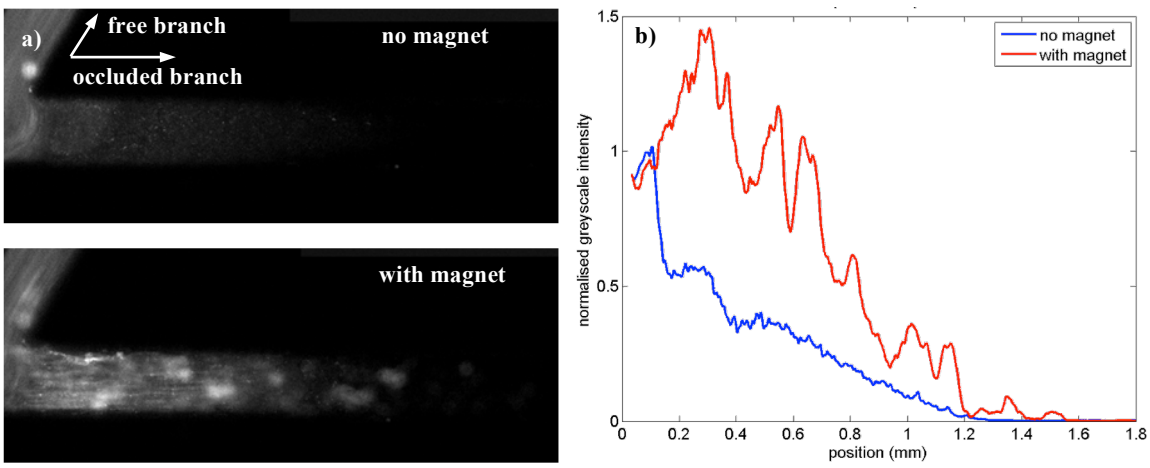


Figure 3-24: Effect of a magnetic field on the delivery of DiI-labelled magnetic microbubbles with 5 mm/s mean inlet velocity; a) fluorescence microscopy image of the mid-plane of the occluded branch at t = 10 minutes; b) normalised greyscale intensity along the occluded branch at t = 10 mm.

Effect of inlet velocity on targeted delivery

Figure 3-25 illustrates microbubble delivery in the mid-plane of the occluded branch at a higher inlet velocity, 50 mm/s. Again, a substantial increase in greyscale intensity was observed in the presence of the magnetic field, though the increase was smaller than at 5 mm/s (up to +21% at 350 µm). In this case as well, the microbubbles were delivered further in the presence of a magnet (+225 µm in 6 minutes).

When the inlet velocity increased from 5 to 50 mm/s, greyscale intensities in the occluded branch in the absence of a magnet maintained similar trends. On the other hand, in the presence of a magnet, microbubble trapping in the first vortex was considerably reduced, which is consistent with the numerical data in section 3.3.4.a). It must however be noted that the shorter experimental time (6 minutes at 50 mm/s, 10 minutes at 5 mm/s) precludes strict comparison.

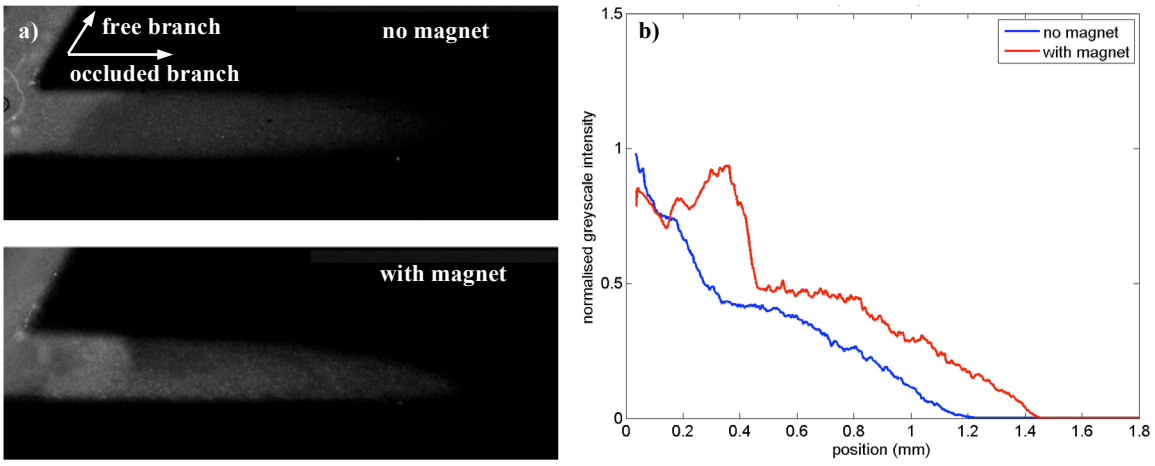


Figure 3-25: Effect of a magnetic field on the delivery of DiI-labelled magnetic microbubbles with 50 mm/s mean inlet velocity; a) fluorescence microscopy image of the mid-plane of the occluded branch at t = 6 minutes; b) greyscale intensity along the occluded branch at t = 6 mm.

3.4. Discussion

3.4.1. Experimental findings

3.4.1.a) Summary of the findings

The present chapter investigates magnetic targeting for enhanced drug delivery in completely occluded vascular bifurcations, using both a computational model and *in vitro* experiments. It was observed that laminar vortices form and that velocity rapidly decreases along the length of the occluded branch. These phenomena were associated with poor transport of therapeutic agents such as microbubbles or thrombolytic drugs towards the clot. During thrombolysis, they would also affect transport of fibrin degradation products away from the clot.

It was demonstrated that a clinically achievable magnetic field greatly improves microbubble transport past the first vortex and beyond, towards the clot. The effect of two physiological parameters on delivery success was studied, and it was shown that microbubble delivery decreases with increasing blood velocity at the inlet of the network, while distance between the bifurcation point and the occlusion does not affect outcomes. Yet it should be noted that the distances investigated were all large (2-8 mm for a 180 μm diameter branch), although they were within the physiological length range for this vessel size [195]. This observation may differ for occlusions placed closer to the bifurcation. Considering microbubble design, delivery efficacy increases with microbubble size and magnetic load.

3.4.1.b) Comparison of experiments and simulations

Moreover, the *in vitro* and *in silico* experiments showed good qualitative agreement. Slight differences between the two may be attributed in part to 3-dimensional effects not taken into account by the 2-D numerical simulations. Discrepancies in the geometry of the experimental device as a result of fabrication also play a role. In addition, residual pulsatility of the pump and Brownian motion contribute to microscopic motion of the fluid particles and of the microbubbles, enabling them to cross streamlines, and modifying delivery outcomes. More significantly, the amount of magnetic material on a microbubble is difficult to measure experimentally and was approximated in the computational model. Two additional limitations are specific to the microbubble delivery experiments. The observations were carried out over 6 to 10 minutes: in this interval, a large number of microbubbles were observed to float upwards and stick to the top plane of the magnet, which affected their motion. The use of greyscale intensities to evaluate delivery outcomes must also be qualified. Though greyscale intensities are appropriate to observe trends in microbubble delivery, they do not translate directly into microbubble numbers, as free DiI may be present in the solution and diffuse into the occluded branch alongside DiI-labelled microbubbles.

3.4.1.c) Links with previously published findings

To the author's best knowledge, this study is the first investigation of magnetic targeting to enhance particle delivery in occluded vasculature. On the other hand, drug diffusion in occluded bifurcations has been previously investigated in other physiological contexts. Carugo *et al*. modelled fluid velocity and doxorubicin distribution in a bifurcation occluded by a drug-eluting chemoembolic bead [211]. Verhaagen *et al*. investigated drug distribution in a fully occluded side-channel during antimicrobial treatment of the root

canal. Numerical and experimental data showed that flow in the main canal induces a cascade of vortices in the lateral microchannel, with rapidly decreasing velocities. The authors also reported that beyond the opening region of the channel, drug transport is slow and diffusion-dominated [212]. These observations are consistent with the findings of the present study.

This study identifies microbubble transport patterns in the occluded branch which closely resemble known observations of red blood cell distribution. A combination of microfluidic effects contribute to haematocrit depletion in vascular branches with lower flow rates than the main branch, a phenomenon known as plasma skimming and illustrated in Figure 3-26 [213]. These effects have been widely used in microfluidic devices to achieve continuous plasma separation [214]–[216]. In a recent computational study, Sinclair *et al*. identified a similar skimming effect on solid microspheres in porcine coronary arteries [217].

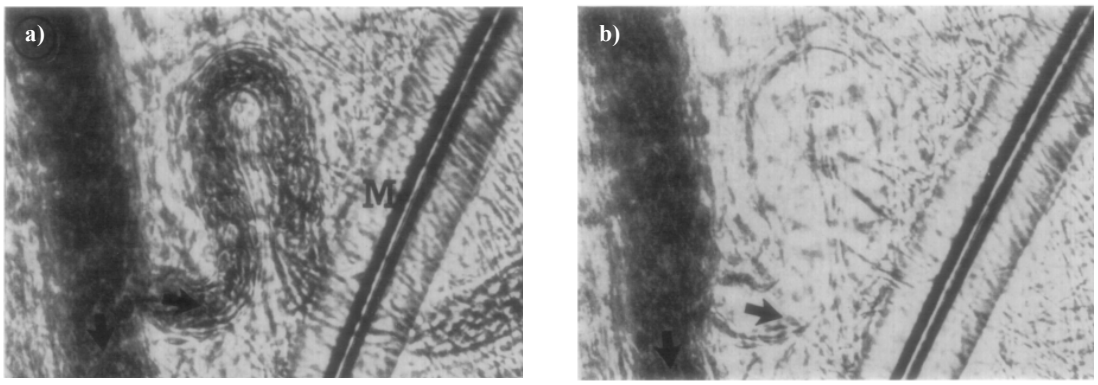


Figure 3-26: Illustration of preferential erythrocyte distribution in high-flow branches. Metarteriole branching from terminal arteriole, with microneedle (M) positioned across metarteriole. a) no compression, rapid flow in both vessels; b) partial compression, slowed flow and haematocrit depletion in the metarteriole. Reproduced from Svanes et al. with permission [213] ***of Elsevier.***

3.4.2. Relevance to *in vivo* mechanisms

The results shown in sections 3.3.3 and 3.3.4 demonstrate that, without targeting, very low concentrations of thrombolytic drugs and microbubbles reached the clot within the treatment timeframe. Nevertheless, thrombolysis and sonothrombolysis are known to be clinically effective treatments, though their effects could be accelerated by increasing microbubble concentration near the thrombus surface [218]. The study therefore presents only a worst-case scenario for drug delivery. *In vivo* occlusions may differ from the chosen model in several ways.

(a) The present study is limited to the case of complete occlusions, though partial occlusions may also lead to acute clinical symptoms. In a multicentre cardiology study by the TIMI study group, a cohort of 147 patients with ST-elevation myocardial infarction was assessed by angiography upon admission. In 65% patients, the angiographic contrast agent did not perfuse the clot and remained in the proximal region (complete occlusion); in a further 14%, the contrast agent perfused the clot without fully opacifying the distal region. In the remaining 21% patients, partial to complete perfusion of the distal vessel was observed [194]. Similarly, a limited degree of microbubble perfusion was observed *in vivo* by Xie *et al*., with microbubbles passing through microchannels present in fully obstructive clots [15].

Though not studied here, therapeutic agent transport is also disrupted by a partially obstructed vasculature, although it is more effective than in fully occluded vasculature. Agent replenishment at the clot site decreases with decreasing flow rates. In addition, partially occluded vessels also experience erythrocyte depletion (see 3.4.1); it is likely that microbubble transport follows similar patterns. In the

case of partial occlusions, magnetic targeting plays a dual role: particle steering and retention against flow.

(b) In this model, the thrombus lies deep within the occluded branch (2-8 mm from the from the bifurcation point). Thrombi positioned closer to the bifurcation are exposed to higher concentrations of therapeutic agents.

(c) The computational and experimental setups do not take pulsatility into account. In arterial occlusions, pulsatility induces mild stirring of the fluid and may accelerate therapeutic agent transport. This effect is however moderate in the microvasculature, as pulsatility is dampened along the vascular system. In microvessels, the Womersley number of blood flow is typically much lower than one, on the order of 0.04 [195]. Viscous forces predominate over transient inertial forces and pulsatility may be ignored. In arteries, however, pulsatility may no longer be neglected, with Womersley numbers on the order of 4 [195].

(d) The magnetic targeting experiments were carried out in water; the model did not take into account the non-Newtonian and particulate characteristics of blood, which are expected to reduce targeting efficacy *in vivo*. Owen *et al*. reported decreasing numbers of magnetic microbubbles retained against flow with increasing haematocrit levels, suggesting that collisions between erythrocytes and microbubbles impede microbubble translation in a magnetic field. This effect is however not limited to magnetically targeted carriers; the authors also reported drastic reduction in retention for biotinylated microbubbles on an avidin-coated surface in the presence of red blood cells [219].

3.4.3. Clinical implications

The present study provides valuable guidance for clinical translation of magnetically targeted sonothrombolysis.

Requirements can be formulated for a clinically relevant magnetic targeting system. Magnetic microbubbles of sufficient size (> 2.4 μm) were successfully delivered to the occluded branch with a magnetic flux density of 7.6×10^{-2} T and a magnetic flux density gradient of 10.90 T/m at the bifurcation point (point Y). To provide a comparison with MRI, similar flux densities can be readily achieved in an MRI scanner, but such flux density gradients are not currently feasible with MRI technology [220], [221]. In addition, treatment time and cost make MRI technology a less than ideal candidate for magnetic drug delivery in stroke therapy. More conveniently, the required flux density and flux density gradient are achievable with permanent magnet arrays at depths up to 40 mm into the body [199]. Another factor to consider for clinical applications is the alignment of the magnetic targeting system. The magnetophoretic force on the microbubbles is parallel to the gradient of the magnetic field. Successful microbubble delivery therefore relies on appropriate positioning of the magnet with respect to the occluded vessel. This can be accomplished clinically with imaging techniques such as power Doppler ultrasound imaging, provided the vessel of interest is wide enough and not too tortuous. Real-time ultrasound imaging would also be beneficial to assess microbubble delivery to the thrombus, and to monitor treatment progress.

As a consequence of the geometrical constraints we have discussed (vessel size, tortuosity, and depth), compelling applications for magnetically targeted sonothrombolysis include ischaemic stroke and myocardial infarction. These conditions usually involve vessels that are larger than the microvessels in this study, on the order of a few millimetres in diameter [222]. The flow is usually assumed to be laminar and the model developed in this study

remains valid, though a larger magnetophoretic force is required to overcome the drag force, which increases linearly with fluid velocity. Owen *et al*. have demonstrated retention of the magnetic microbubbles in laminar conditions with flow rates up to 0.25 $ml.s^{-1}$ and shear rates up to 622 s^{-1} [193]. However, in stenosed and diseased arteries, turbulences may arise [223]. In this case, Stokes' drag no longer applies and adjustments to the model are required.

3.4.4. Future work

In light of this discussion, several improvements to the model could be implemented. A three dimensional numerical model could be setup, with model of the magnetic field separated from the main multiphysics model in order to reduce computational time. It could also be extended to partially occluded vasculature. To increase clinical relevance of the models and prepare *in vivo* validation, flow pulsatility and the non-Newtonian characteristics of blood could be included; application-specific magnets must also be designed, building on the specifications formulated in the previous section. Following this study of magnetically targeted microbubbles, other magnetic drug delivery carriers could be investigated, such as nanodroplets or drug-loaded polymer microparticles.

3.5. Conclusion

In this study, we have examined the challenges involved in of delivering therapeutic agents to thrombosed vessels. We have shown that magnetic targeting has the potential to increase delivery efficacy and that the magnetic field required is clinically achievable. This introduces a promising approach to the treatment of stroke, myocardial infarction and other occlusive conditions. Magnetically targeted sonothrombolysis is a particularly compelling application, as therapeutic efficacy depends on microbubble concentration near the thrombus. This is investigated further in the next chapter.

CHAPTER 4

Mechanical sonothrombolysis with magnetically targeted microbubbles

Magnetic targeting allows non-invasive manipulation of microbubble populations. This opens promising applications in non-invasive therapies that are sensitive to microbubble concentration.

This chapter investigates the effect of magnetically targeted microbubbles on sonothrombolysis in the absence of fibrinolytic drugs. The effect of microbubble concentration on clot lysis rate is studied. Subsequently, the effect of magnetic targeting on microbubble concentration is assessed. Then the effect of magnetic targeting on lysis rate is investigated. The sources of experimental variability are discussed, and improvements to the magnetic targeting system are evaluated.

4.1. Introduction

In the previous chapter, obstacles to microbubble delivery in occluded vascular networks were investigated. It was demonstrated that magnetic targeting can be used to increase microbubble concentration in the region of the thrombus. The objective of the present chapter is to evaluate the use of these magnetically targeted microbubbles in conjunction with ultrasound to accelerate thrombus breakdown, in the absence of thrombolytic drugs. In addition, acoustic emissions are investigated as an indicator of treatment progress.

4.1.1. Motivation

Increased microbubble concentrations have been shown to significantly increase lysis in previous studies [224]. Therefore targeting has the potential to enhance the lytic effect of microbubbles by increasing their concentration at the site of the clot. This in turn could allow use of lower ultrasound power and microbubble systemic doses, thus reducing the risk of harmful side effects and improving treatment safety.

In this context, magnetic microbubbles are a promising option: magnetic targeting involves the use of magnetic field gradients to direct therapeutic agents to the clot and to retain them. Torno *et al*. have demonstrated that magnetically targeted, drug-loaded, ultrasound-sensitive copolymers improve clot lysis over ultrasound and free t-PA [135]. Using magnetically targeted microbubbles brings two additional advantages over the copolymers. Firstly, the microbubbles can be visualized by ultrasound imaging, allowing treatment monitoring and enhancing patient safety. Secondly, microbubbles enhance cavitation, which is thought to play an important role in clot lysis [33], [50], [52], [53] . To date, the therapeutic effect of these magnetic microbubbles has not been investigated in the context of sonothrombolysis. In other fields, they have been used to improve *in vitro* gene transfection; ultrasound-enhanced gene delivery was reported to be more effective with

magnetically active microbubbles than with non-magnetic microbubbles or with non-echogenic magnetic micelles [162].

This chapter focuses exclusively on mechanical thrombolysis, in the absence of fibrinolytic drugs. This approach was chosen because of the high proportion of ischaemic stroke patients who do not comply with the stringent eligibility criteria of tPA treatment [225]. In addition, it is pertinent to investigate mechanical sonothrombolysis and drug-enhanced sonothrombolysis separately because the mechanisms involved are likely to be different.

4.1.2. Structure of the study

After characterising the setup (§ 4.3.1), the first step in the investigation was to confirm that an increase in microbubble concentration is associated with improved mechanical lysis of the clots. Whole porcine blood clots were placed in a model middle cerebral artery and exposed to ultrasound with a range of physiologically relevant microbubble concentrations (§4.3.2). The outcome outlined the sensitivity of the treatment to increased microbubble concentrations, thereby providing specifications for an effective magnetic targeting system. As a second step, the magnetic targeting system was evaluated by quantifying its effect on microbubble trajectories (§ 0).

Combining the previous two experiments, the effect of magnetic targeting on the rate of clot lysis and on acoustic emissions was assessed (§ 4.3.4). As the experiments yielded unexpected results, the possible sources of discrepancy were then explored (§ 4.3.5) and solutions were investigated (§ 4.3.6 to 4.3.8). The effect of mechanical sonothrombolysis on clot fragment size and clot microstructure was also studied (§4.3.8).

4.2. Methods

4.2.1. Flow phantom

The overall arrangement, shown in Figure 4-1, was adapted from the protocol initially described by Petit *et al*. [37]. The experiments were carried out in a 50 x 80 x 55 cm Lucite tank containing approximately 120 litres of filtered, deionized and degassed water which was maintained at 37±1.5°C by a heating circulator (GD100, Grant Instruments, Cambridge, UK). Prior to each experiment, a clot sample was placed in an optically and acoustically transparent polyolefin tube (3.2 mm inner diameter and 0.18 mm wall thickness, Heatshrink-Online Ltd, Huntingdon, UK). The internal diameter of the tube was selected to correspond to the typical dimensions of a middle cerebral artery (MCA) [226]. The MCA is one of the brain vessels most commonly affected by ischaemic stroke: in a clinical study of 109 acute ischaemic stroke patients, 73% cases were identified as MCA occlusions [227].

The assembly was then placed in the tank, with the clot resting at the bottom of the horizontal tube. The tube was connected to a flow loop circulating phosphate-buffered saline (Sigma Aldrich Corporation, St Louis, MO, USA) using a peristaltic pump (Minipuls 2, Gilson Inc., Middleton, WI, USA). The flow velocity was varied between experiments, over a range consistent with the range of blood flows observed in a partially occluded middle cerebral artery [228]. A syringe pump (World Precision Instruments Ltd, Hitchin, UK) delivered the microbubbles into the main PBS flow upstream from the clot.

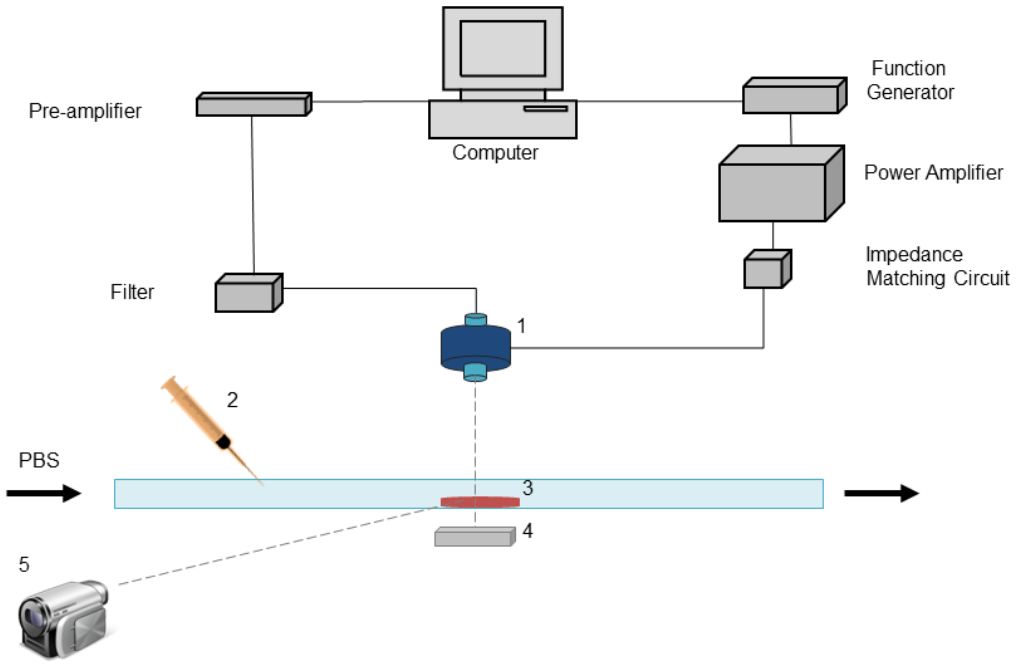


Figure 4-1: Setup overview.
The clot (3) is placed in a flow chamber under PBS flow. Microbubbles are continuously delivered into the flow by an infusion pump (2). A magnet (4) enables magnetic retention of the microbubbles at the clot site. Ultrasound exposure and acoustic monitoring are performed by coaxial HIFU and PCD transducers (1). Lysis progress is monitored using a digital camera (5).

4.2.2. *In vitro* clot model

Fresh whole blood clots were prepared in a manner similar to the protocol described by Meunier *et al.* [99]. Briefly, 4-0 size braided silk sutures (Ethicon US LLC, Somerville, NJ, USA) were threaded through 3.4 mm inner diameter, 60 mm long borosilicate cylinders (Aimer Products Ltd, Enfield, UK). Each cylinder was then placed in an additive-free 13 mm inner diameter Vacutainer tube (BD, Franklin Lakes, NJ, USA). Arterial blood was collected from the carotid artery of a female large white X landrace breed pig. This procedure was carried out in accordance with the animal protection legislation of the United Kingdom and was approved by the ethics committee at the University of Oxford. Blood samples (2 mL) were aliquoted into the Vacutainers and

incubated for 6 hours in a water bath at 37°C. The clots were stored at 4°C to allow retraction. After 24 hours, they were carefully extracted from the borosilicate cylinders and stored for up to 15 days in degassed phosphate-buffered saline at 4°C. The clots were typically of cylindrical shape, with a diameter of ~1.7 mm and a length of ~3 cm.

In two instances (see § 4.3.4.a) and 4.3.5.a)), a human clot model was substituted for the pig model. Whole blood was sampled from the antecubital fossa an adult volunteer who provided written consent. This procedure was approved by the Central University Research Ethics Committee at the University of Oxford. The clot preparation protocol remained otherwise unchanged.

The choice of the clot model (human or porcine) was based on availability. A porcine model is frequently used for *in vitro* and *in vivo studies* of thrombosis and thrombolysis because humans and swine have similar hematologic physiologies [229].

4.2.3. Magnetic microbubble preparation

The protocol for magnetic microbubble preparation was based on the method first described by Stride *et al.* [161]. The microbubbles were prepared by sonication using a 22.5 kHz ultrasonic cell disruptor (Microson XL, Misonix Inc., Farmingdale, NY, USA) operating at level 4, corresponding to an output power of 8 W_{RMS}. Briefly, 15 ml of deionized water were added to 15 mg of the phospholipid DSPC (1,2 distearoyl-sn-glycero-3-phosphocholine, Avanti Polar Lipids Inc., Alabaster, USA). The sonicating probe was first inserted into this solution for 90 seconds to disperse the lipid; then it was placed at the air-liquid interface for 15 seconds to entrain gas. Subsequently, 15 µl of a ferrofluid (10 nm spherical magnetite nanoparticles in isoparaffin, 10% volume fraction, purchased from Liquids Research Ltd, Bangor, UK) were added to the solution. The

microbubble solution was then sonicated again for 30 seconds with the probe tip fully inserted into the fluid, and for 15 seconds with the probe tip at the air-liquid interface. The vial was manually shaken vigorously for 45 seconds.

Microbubble concentration and size were assessed as previously described by Sennoga *et al.* [209]. A 10 µl sample was placed on a microscope slide and 25 pictures were taken with a x40 objective. The images were analysed using purpose written software in MATLAB (The MathWorks Inc., Natick, MA, USA) to count particles of sizes ranging from 0.2 µm (~ 2 pixels) to 15 µm.

4.2.4. Magnetic targeting setup

Magnetic targeting of the microbubbles was provided by a Halbach array constructed from five identical permanent magnets (N52 grade NdFeB, 1.5 T at the surface, from NeoTexx, Berlin, Germany). It was placed below the clot at an angle of 10° from the horizontal plane and covered with a 5 -mm layer of acoustically absorbing material (Aptflex F36, Precision Acoustics, Dorchester, UK) to limit the formation of standing waves. It was positioned so that the HIFU focus was directly above the centre of the array (see Figure 4-2). The distance between the surface of the clot and the surface of the array was adjusted before each experiment using the passive cavitation detection transducer (see section 4.2.5) in pulse-echo mode. During experiments that did not involve magnetic targeting, the Halbach array was replaced by a stainless steel block in order to maintain a comparable sound field. A Halbach array was chosen because it provides a high magnetic field and magnetic gradient in the tube, both of which are necessary to overcome shear forces and retain microbubbles. Owen *et al*. showed in previously published work that the array used in this study effectively enhances microbubble retention against physiologically relevant flows [193].

The magnetic field and the magnetic field gradient in the flow chamber were computed using a numerical model first described by Barnsley *et al.* [199]. The magnetisation value of the magnet, an essential input parameter to the model, was determined experimentally by measuring the field profile of a single NdFeB element using a three-axis Hall probe connected to a 3-channel gaussmeter (Model 460, Lake Shore Cryotronics, Inc.,OH, USA). The field profile was then fitted to an analytical expression for the field generated by a cuboid [230], yielding a magnetisation value of 1.087×10^{6} A.m^{-1}. The contribution of Dr. Lester Barnsley with his numerical model is gratefully acknowledged.

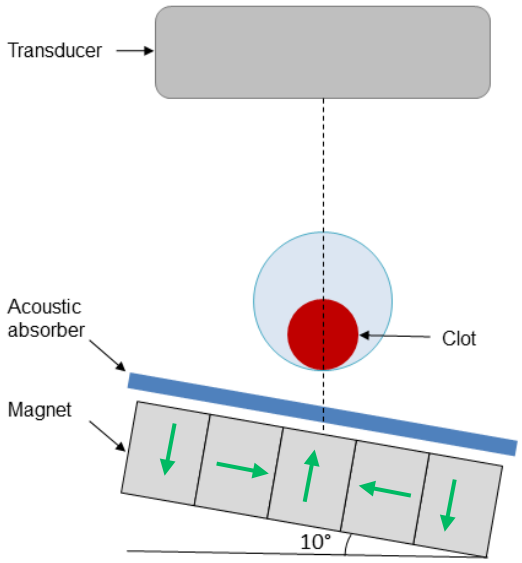


Figure 4-2: Cross-section of the magnetic targeting setup.
A 5-element Halbach array is placed below the clot at an angle of 10°. The orientation of the magnetisation vector is indicated for each element of the array (green arrows). An acoustically absorbing layer limits the formation of standing waves. The centre of the clot and the centre of the Halbach array are aligned with the axis of the HIFU transducer.

4.2.5. US exposure parameters

The acoustic setup is shown in Figure 4-1 and was previously described by Hockham *et al.* [231]. It comprised a high-intensity focussed ultrasound (HIFU) transducer positioned co-axially and confocally with a passive cavitation detection (PCD) transducer.

The ultrasound source was a focused, circular, single element, 500 kHz transducer (Sonic Concepts, Bothell, WA, USA). The transducer centre frequency was chosen to balance considerations of treatment safety and efficacy. Lower frequency ultrasound is more effective at breaking down blood clots [103], [232] and is less attenuated by tissue and bone, but safety concerns have been raised in several studies conducted with low- to mid-frequency transcranial ultrasound (60 to 300 kHz) [91], [233].

This HIFU transducer had a diameter of 64.00 mm and a radius of curvature of 62.64 mm. The measured -6 dB focal dimensions were 4 mm laterally and 37 mm axially [234]. It was driven by a function generator (3325DA, Agilent Technologies Inc., Santa Clara, CA, USA) and connected to a power amplifier (A300, Electronics & Innovation Ltd., Rochester, NY, USA) with a custom-made impedance matching network to maximize power transfer to the transducer (Sonic Concepts). The HIFU transducer was driven in pulsed mode to allow replenishment of microbubbles in the focal region between pulses.

The sound field at the focus of the transducer was measured in absence of the clot and vessel with a calibrated fibre optic hydrophone (Precision Acoustics) mounted on a 3-D translation stage. This type of hydrophone was chosen because its directionality is negligible at 0.5 MHz, which allows it to be placed perpendicularly to the HIFU axis in this geometry without the need for correcting the sensitivity [235]. The pulse length was set to 200 cycles, with a pulse repetition frequency of 50 Hz. This pulse length was chosen

in order to optimize the amount of data acquired while maintaining a similar sound field to the one produced with 5000-cycle pulses (data not shown).

Passive cavitation detection (PCD) of acoustic emissions was carried out using a focused, circular, single-element, 7.5 MHz transducer (Panametrics V320-SU, Olympus Inc., Waltham, MA, USA). This PCD transducer had a focal length of 75 mm, an aperture of 12.5 mm, and a -3 dB beamwidth of 18.7 mm. The signal was acquired using a 2 MHz high-pass filter (Allen Avionics Inc., Mineola, NY, USA) to block signals at the fundamental frequency. The filter was connected to a pre- amplifier for x25 signal amplification (SR445A, Stanford Research Systems, Sunnyvale, CA, USA). The signal was then acquired into a binary file at 10^8 samples per second using a data acquisition card and control software written in LabView (National Instruments, Austin, TX, USA).

Before each experiment, the foci of the HIFU and the PCD transducer were aligned with the surface of the clot using the PCD transducer in pulse-echo mode.

4.2.6. Image acquisition and processing for lysis monitoring

Lytic progress was assessed from the variations in clot diameter throughout treatment. Images of the clot were captured every 30 seconds with a digital camera (Canon EOS 500D, Canon Ltd., Reigate, UK) fitted with a macro lens and placed at a distance of 45 centimetres from the clot, achieving an average resolution of 0.02 millimetres/pixel. The images were processed off-line with purpose-written code in Matlab. The algorithm computed the scale of the frames and the location of the HIFU focus by detecting a red fiducial marker attached to the surface of the absorber (colour thresholding). In each frame, the outline of the clot was then detected by set level thresholding in a 3 millimetre wide window around the HIFU focus. The maximum change in diameter compared to the

first frame was computed. A linear regression on the maximum change in diameter at each time point yielded the rate of lysis.

Figure 4-3 shows an example of the user interface built to facilitate image processing, with an example of clot segmentation (magenta overlays) in the focal region.

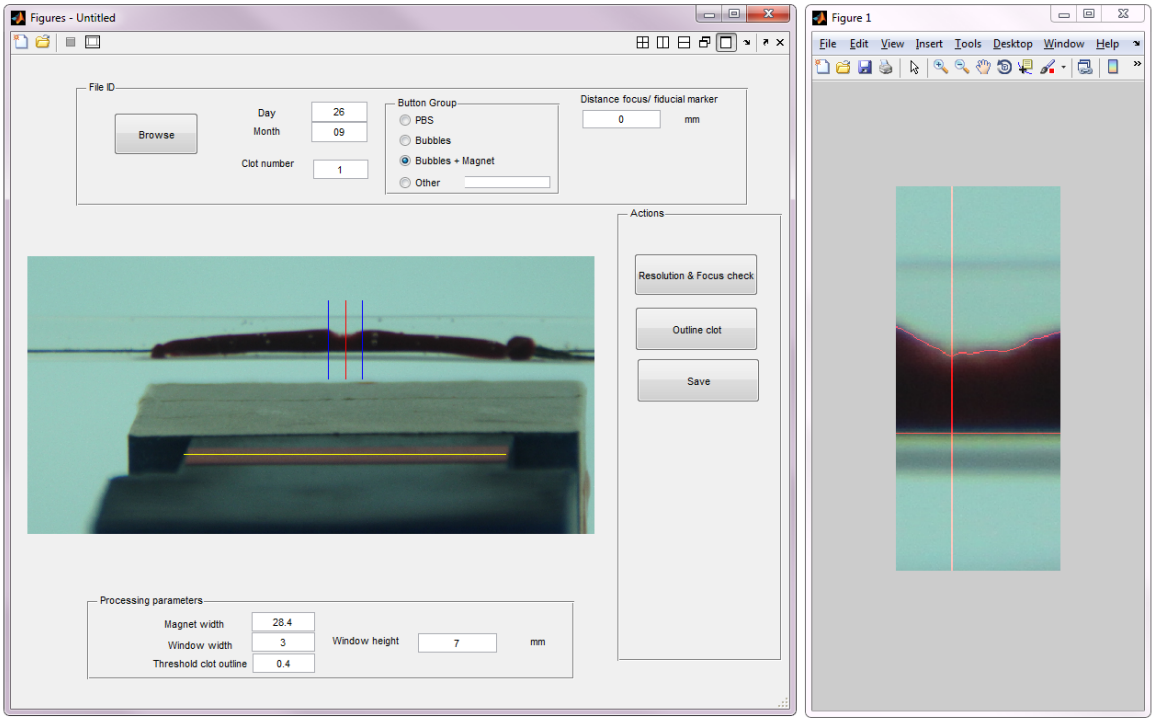


Figure 4-3: Graphical User Interface for clot image processing.
a) general layout of the interface. The yellow line delimits the detected fiducial marker (red rectangle). The vertical blue lines mark the boundaries of the region of interest for image processing. The vertical red line indicates the centre of this region; b) clot outline detection in the region of interest. At each time point, clot boundaries are identified and highlighted in magenta. The point of greatest lysis depth is marked by a vertical magenta line.

4.2.7. Image acquisition and processing for magnetic targeting evaluation

Magnetic targeting increases microbubble concentration in two ways: a) by deflecting microbubble trajectories across streamlines and pulling them closer to the clot; b) by retaining microbubbles against flow. Both effects were evaluated in the present experimental setup by optical methods.

In order to visualise the light brown microbubble solution in the flow chamber while maintaining a similar fluid velocity profile, the blood clot was replaced by a light-coloured clot phantom of similar dimensions. A bolus (1 mL) of the microbubble stock solution was injected by hand into the PBS flow over 5 seconds. Images of the clot were captured with the digital camera at a rate of 30 frames per second for at least 60 seconds, with a resolution of 0.085 mm/pixel.

The images were processed with purpose-written code in Matlab (see Figure 4-4). Image resolution was obtained by detecting the length of a fiducial marker, as described in the previous paragraph. Two regions of interest (ROI) were then defined in the tube, each 3 millimetres wide: a focal ROI centred directly above the middle of the magnet, and an upstream ROI located 25 mm away, well away from strong magnetic gradients.

The total greyscale value in this upstream ROI was computed for each frame of the video, yielding an intensity profile over time that provided time points for bolus start (t_0), peak (t_1) and end (t_2).

The remainder of the image analysis was performed on the focal ROI, using the blue component of the RGB image. Two separate phenomena were quantified:

a) **the shift in the position of the flowing bolus**.

   This effect was assessed from the image taken 2 seconds before bolus peak t_1. This time point was chosen to provide sufficient microbubble concentrations while avoiding greyscale saturation in the focal region. The microbubble bolus was visualised by subtracting from this image the image taken at t_0, before bolus start. The greyscale values were then averaged to provide a concentration profile in the cross-section of the ROI.

b) the quantity of retained magnetic material

This effect was assessed from the image taken immediately after bolus end, at t_2. The magnetic material trapped at the end of the experiment was visualised by subtracting from this image the image taken at t_0. The greyscale values were then added to provide a total retention value in the ROI.

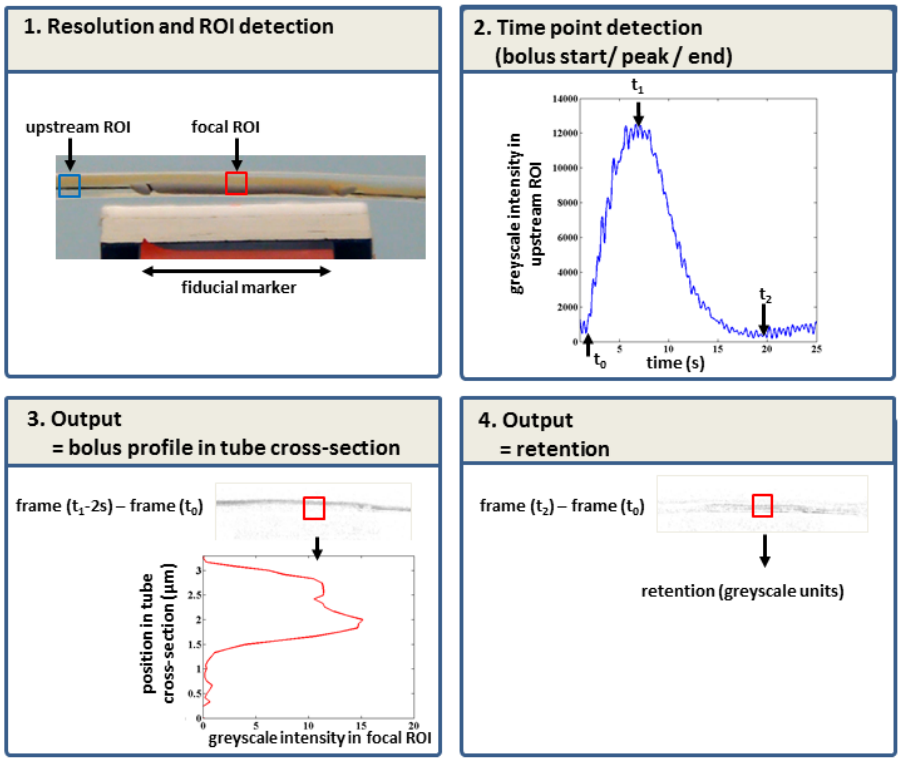


Figure 4-4: Image processing algorithm for magnetic targeting evaluation. The input is a video of the microbubble bolus passing through the flow chamber. The outputs are the bolus profile in the tube cross-section, computed 2 seconds before bolus peak, and a measure of retention after bolus end.

4.2.8. Acoustic data acquisition and processing for cavitation monitoring

Acoustic emissions at the treatment site were recorded using the passive cavitation detection setup. The signal processing methodology was adapted from Datta *et al.* [23]. In order to limit data volume, the emissions were detected for every 10th ultrasound burst, and only the first 2 ms of the 10-ms bursts were recorded. As the microbubbles are

constantly replenished, acoustic cavitation is expected to be consistent enough over time to justify this sampling scheme. Each burst was processed as follows:

a) The first 90 µs of the burst were discarded to account for the acoustic time of flight from the HIFU transducer to the focal region and on to the PCD transducer. The signal was zero padded.

b) The signal was windowed using a Hanning window.

c) Its power spectral density was derived by Fast Fourier Transform.

d) The power spectral density was integrated over the 2-5 MHz frequency range.

Finally, cavitation doses thus computed for each burst were summed over the whole duration of treatment, yielding a total cavitation dose (units V^2) which is proportional to the acoustic energy detected in the focal region of the PCD.

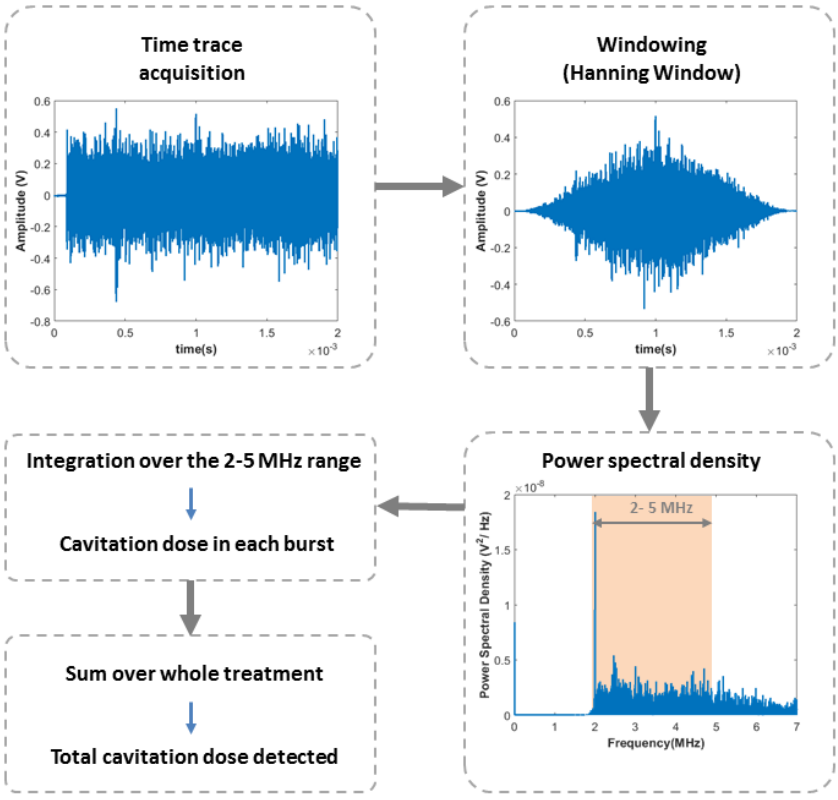


Figure 4-5: Signal processing algorithm for quantification of acoustic emissions. The input is a series of voltage traces acquired with the PCD, the output is a cavitation dose detected in the 2-5 MHz range over the whole duration of treatment.

4.2.9. Debris analysis

In order to assess debris size, 15 mL of effluent were collected halfway through treatment and immediately stored at -20°C. The samples were then defrosted for 12 hours at 4°C. This low temperature was maintained so as to inhibit the enzymatic activity of tPA, limiting further breakdown of the clot debris. 100 µL samples of the solution were analysed with an optical particle sizer (Accusizer 780, Particle Sizing Systems, Santa Barbara, CA, USA). Three samples were analysed for each clot.

4.2.10. Histological analysis

After treatment completion, the clots were immersed in formalin, and fixed in paraffin. 5-µm slices were prepared and stained with eosin and haematoxylin. They were analysed in bright field microscopy (Ti Eclipse, Nikon Instruments Inc., NY, USA) using a x20 objective (S Plan Fluor EWLD, Nikon).

4.2.11. Statistical analysis

In this study, a p-value less than 0.05 (noted *) was considered as a statistically significant difference between two groups. A p-value less than 0.01 was noted **. Depending on the nature of the data and the sample size, various statistical methods were applied:

In § 4.3.1 to 4.3.6: Only two experimental groups have n>5, so a two-sided Student's t-test was applied to compare them in Matlab. Where n<5, the interpretation of the experimental data was confined to general observations about the mean and spread of the data.

In § 4.3.8: All three experimental groups have n>5, so differences among experimental groups were analysed in Matlab using two-way ANOVA, with post hoc Tukey HSD testing for multiple comparisons between groups.

In § 4.3.5: Correlations between variables were analysed by Pearson product-moment correlation.

4.3. Results and discussion

4.3.1. Characterisation of the experimental setup

Prior to the sonothrombolysis experiments, three aspects of the experimental setup required characterisation: the microbubbles, the magnet, and the ultrasound field.

4.3.1.a) Microbubble characterisation

Microbubble concentration in the stock solution was $2.9 \times 10^8 \pm 4.4 \times 10^6$ microbubbles/mL, with a gas concentration of 0.55 ± 0.04 µL/mL (estimated from 6 series of 20 micrographs). The size distribution of the microbubbles is shown in Figure 4-6. Mean microbubble diameter was 1.03 ± 0.73 µm, revealing a markedly polydisperse size distribution. The range of particle sizes was suitable for clinical applications: 0.04% of the particles were larger than 10 µm in diameter. For comparison, the mean diameter of the commercial contrast agent Sonovue is 2.5 µm and the concentration is $2\text{-}5 \times 10^8$ microbubbles/mL, with a gas concentration of 8 µL/mL [210].

Figure 4-7 shows the response of the superparamagnetic microbubble suspension to a weak magnetic field. When a magnet was approached, the microbubbles aligned to form growing chains. When the magnet was removed, the bubbles gradually separated again. It should be noted that a fraction of the particles analysed as microbubbles could in fact be micron-sized droplets of ferrofluid; these droplets cannot reliably be distinguished from microbubbles by optical methods. In addition, the micrographs suggest that a small proportion of the microbubbles are not magnetically active. These microbubbles contribute to sonothrombolysis, but they do not respond to targeting.

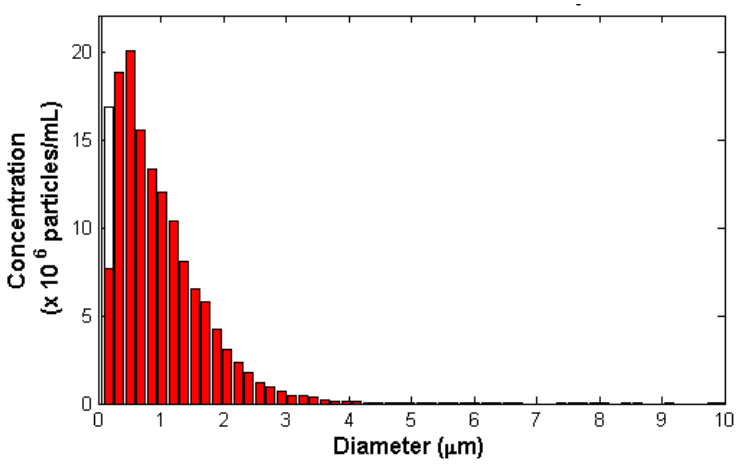


Figure 4-6: Size distribution for magnetic microbubbles determined via optical microscopy for a set of 20 micrographs acquired with a ×10 objective and analysed in Matlab®. The white bar represents particles smaller than 0.2 μm.

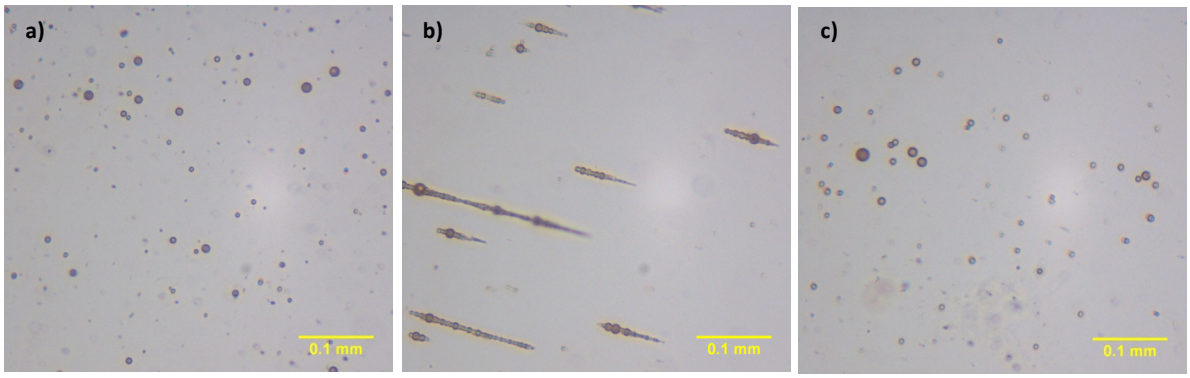


Figure 4-7: Microbubble response to a magnetic field: optical micrograph of the magnetic microbubble stock solution a) before application of a magnetic field; b) during exposure of the microbubbles ta a magnetic field; c) a minute after removal of the magnetic field. The images were acquired with a ×10 objective. The central image was obtained after holding a 1.35 T permanent magnet at the edge of the microscope slide for 30 seconds.

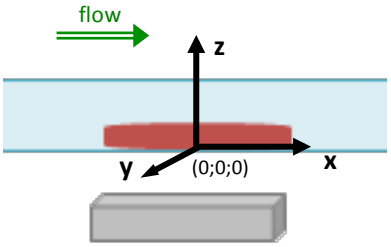
4.3.1.b) Magnet characterisation

A numerical simulation mapped the magnetic conditions created in the flow chamber (3.2 mm diameter) by a magnet placed 15.2 mm below the clot. Figure 4-8 illustrates the resulting magnetic field and magnetic field gradient in the tube.

The magnitude of the magnetic field was in the 3.2-11.0 $\times 10^{-2}$ T range; the magnitude of the field gradient was in the 4.7-17.2 T/m range. This provides a practical comparison of the magnetic targeting system with other known systems. For instance, a clinical MRI scanner can readily achieve magnetic fields of this magnitude, but such gradients are beyond the values typically obtained with MRI [220], [221]. In addition, the values observed in the present system were similar to those achieved in the previous chapter.

As expected, the magnetic field and the magnetic field gradient were symmetrical about the Oxz plane, defined as the xz plane passing through the origin. Both fields varied within the flow chamber, with a global maximum directly above the middle of the magnet (point (0,0), 0.11 T and 17.2 T/m).

The magnetophoretic force on a magnetic particle is proportional to the product of the magnetic field and of the magnetic field gradient. The data therefore indicate that, as the microbubbles flow into the chamber, they are subjected to a substantial magnetophoretic force well before they reach the HIFU focus (defined by $-3 \leq x \leq 3$). The magnetophoretic force increases with microbubble proximity to the bottom of the tube. It also increases over time as the microbubbles progress with the flow towards the focus.



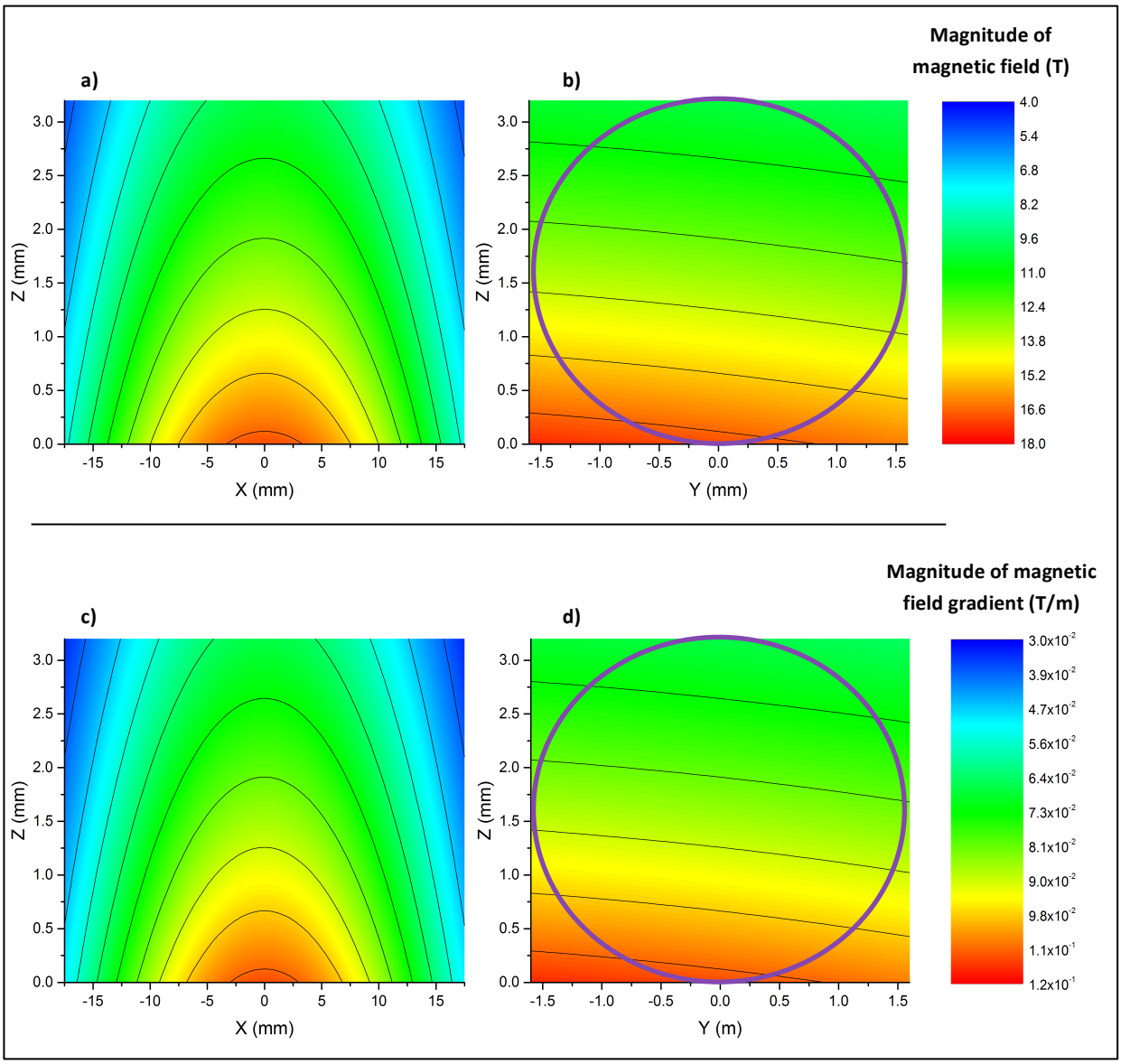


Figure 4-8: Simulations of magnetic field created in the transverse plane of the flow chamber by a linear 5-element Halbach array placed at a distance of 15.2 mm from the surface of the clot; a) magnitude of magnetic field in the Oxz plane; b) magnitude of magnetic field in the Oyz plane; c) magnitude of magnetic field gradient in the Oxz plane; d) magnitude of magnetic field gradient in the Oyz plane. The purple circle in b) and d) shows the location of the vessel. The inset (above) shows the orientation of the axes and origin.

4.3.1.c) Ultrasound field characterisation

In order to construct a map of the sound field in the setup, the HIFU transducer was calibrated in water at 37°C in the presence of the magnet. A region of 64 mm^2 around the focus was scanned with a fibre optic hydrophone in the transaxial plane, with a resolution of 0.25 mm in the Z direction and 1 mm in the X direction; in the transverse plane, a total area of 16 mm^2 was mapped with a resolution of 0.25 mm.

Figure 4-9 shows the sound field measured in the focal region in the presence of the magnet. Figure 4-9a) indicates that despite the magnet angle and the presence of an acoustic absorber, a partial standing wave forms in the system. However, this standing wave only gives rise to limited amplitude variations in the focal region (± 6%). Moreover, Figure 4-9b) suggests that the magnet does not affect the expected shape of the ultrasound field in the transverse plane.

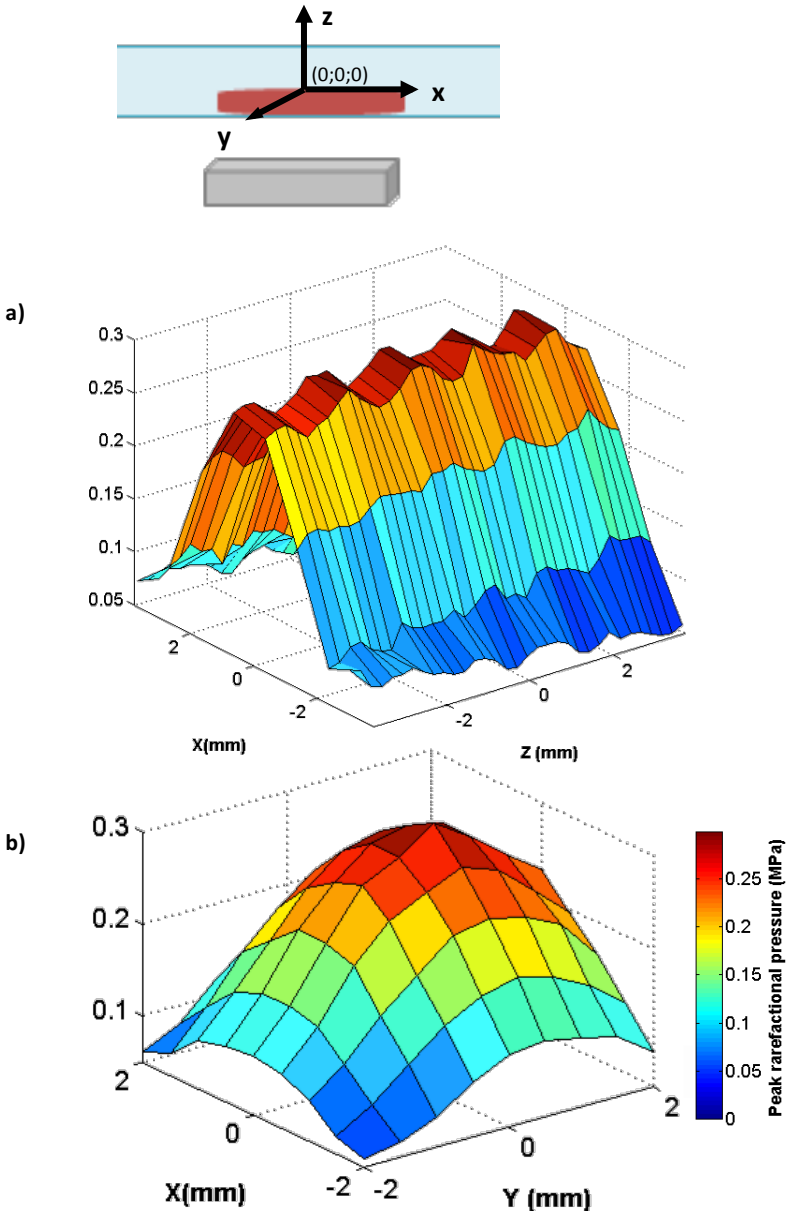


Figure 4-9: Map of the sound field created by the HIFU transducer in the focal region, in the presence of the magnetic targeting system: a) in the transaxial plane; b) in the transverse pane. Calibrations scans were carried out with a fibre optic hydrophone in a water bath maintained at 37°C. Focal pressure was set to 290 kPa. Inset (above): orientation of the axes and origin.

4.3.2. Effect of microbubble concentration on thrombolysis rates

The first step in the investigation of targeted sonothrombolysis was to test the assumption that an increased concentration of microbubbles leads to accelerated sonothrombolysis. Porcine whole blood clots were exposed to ultrasound and a range of clinically relevant microbubble concentrations; lysis rates and acoustic emissions were recorded.

At this stage of the study, no magnetic targeting was required, and the Halbach array was replaced by a stainless steel bar to maintain a comparable sound field. In each experimental group, three to four retracted porcine clots were exposed to ultrasound and microbubbles for 30 minutes. In the control group, the clots were exposed to HIFU and a flow of PBS only. The maximum volume of gas delivered (on the order of 6.4 microliters of air) was well below the maximum dose recommended for cardiovascular imaging with the commercial agent Sonovue (32 microliters of sulphur hexafluoride). The parameters of ultrasound exposure are shown in Table 4-1.

Parameter	Value
PBS flow rate	13 mL/min
Magnet position	upper face of steel bar – surface of clot: 15.2 mm
Microbubble concentration	$0.7 – 2.5 \times 10^6 \pm 3.8 \times 10^4$ microbubbles/mL in PBS flow
Peak Rarefactional Pressure	1.15 MPa
Pulse repetition frequency	4 Hz
Duty cycle	4%
Pulse repetition frequency	20 minutes

Table 4-1: Experimental conditions used for investigating the effect of increasing microbubble concentration on mechanical sonothrombolysis.

Figure 4-10 shows the resulting rates of lysis, obtained from linear regressions of the maximum depths of lysis plotted over time with an R-squared value of 0.87 ± 0.12. No clot lysis was observed in the absence of microbubbles: lysis rates remained within the noise threshold in the negative control group (0.01 mm/min, the equivalent of a 10 pixel difference over the whole treatment). On the other hand, rapid mechanical sonothrombolysis was achieved on these retracted blood clots with the chosen exposure conditions in the presence of sufficient microbubble concentrations (> 1.8 x 10^6 microbubbles/mL). In addition, a clear trend emerged for accelerated lysis with increasing microbubble concentrations. On average, the lytic rates varied rapidly with microbubble concentration. For instance an increase from 1.8 to 2.2 x 10^6 microbubbles/mL was associated with a 20% increase in average lysis rates.

These findings agree with the observations of Borelli *et al*. on mechanical sonothrombolysis of rabbit whole blood clots at 1 MHz with 1-µm microbubbles. The authors noted a sharp increase in clot lysis with microbubble concentrations up to 3 x 10^8 microbubbles/mL, followed by a plateau and a decrease in lysis efficacy from 1.3 x 10^9 microbubbles/mL [218].

In this study, the small sample size precluded further statistical analysis. In addition, variability in lysis rates was high, ranging for instance from 0.0085 to 0.0422 mm/min in the group treated with 2.5 x 10^5 microbubbles/mL.

Figure 4-11 shows the total cavitation dose detected in the 2-5 MHz range during treatment. As expected, presence of microbubbles enhanced cavitation activity, and there was a trend for increased cavitation dose with increasing microbubble concentrations up to 2 x 10^6 microbubbles/mL.

It can be noted that in when increasing the concentration of microbubbles, the group with the highest concentration experienced highly variable lysis rates and a slight decrease in

cavitation doses. This suggests the onset of shielding phenomena, whereby microbubbles present between the source and the target region prevent efficient ultrasound propagation.

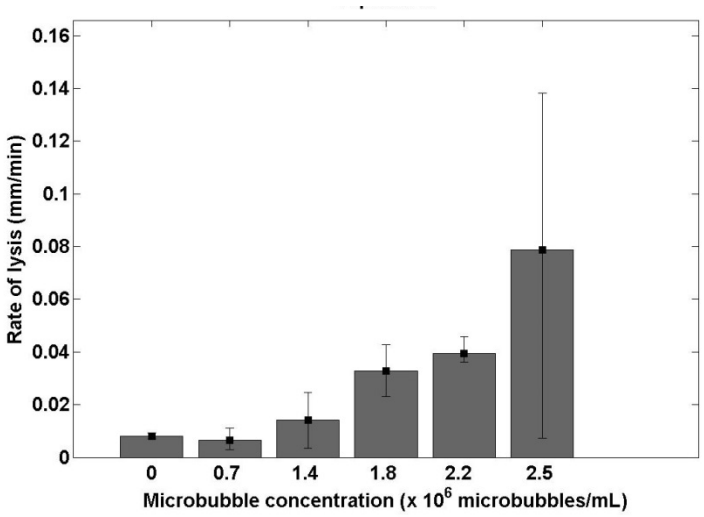


Figure 4-10: Rate of lysis in the first 20 minutes of mechanical sonothrombolysis with increasing microbubble concentrations (n=3). The clots were treateted with 0.5 MHz ultrasound, 1.15 MPa peak rarefactional pressure, a 4 Hz pulse repetition frequency and a 4% duty cycle. Maximum depth of clot lysis was computed on photographs taken every 30 seconds during treatment, yielding the lytic rate. Error bars show the range of lysis rates observed.

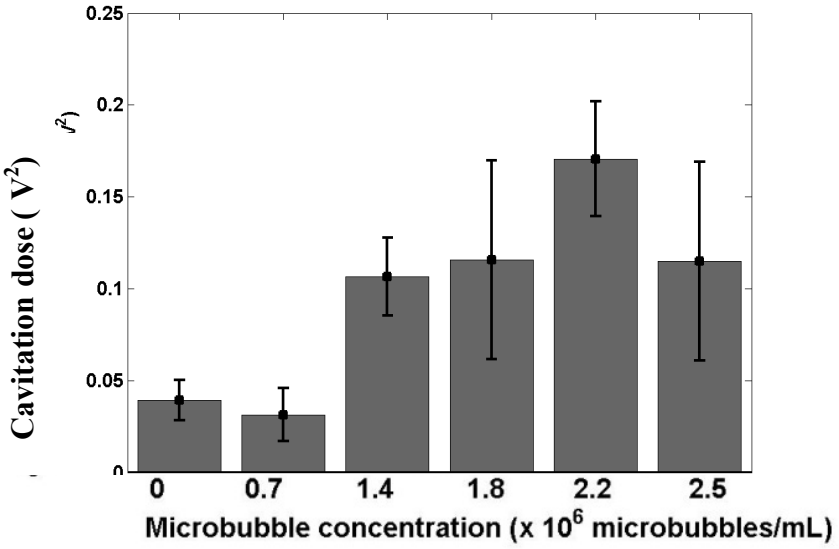


Figure 4-11: Total cavitation dose in the 2-5 MHz range in the study of the effect of microbubble concentration on mechanical sonothrombolysis. The clots were treateted with 0.5 MHz ultrasound, 1.15 MPa peak rarefactional pressure, a 4 Hz pulse repetition frequency and a 4% duty cycle (n=3). The acoustic emissions at the focus were acquired with a 7.5 MHz PCD transducer mounted coaxially with the HIFU transducer. Error bars show the range of lysis rates observed.

4.3.3. Effect of magnetic targeting on microbubble concentration

The effect of the magnetic targeting system on microbubble concentration in the focal region was evaluated by quantifying two phenomena: a) deflected microbubble trajectories that affect the distance between the bubbles and the clot and b) microbubble retention against flow.

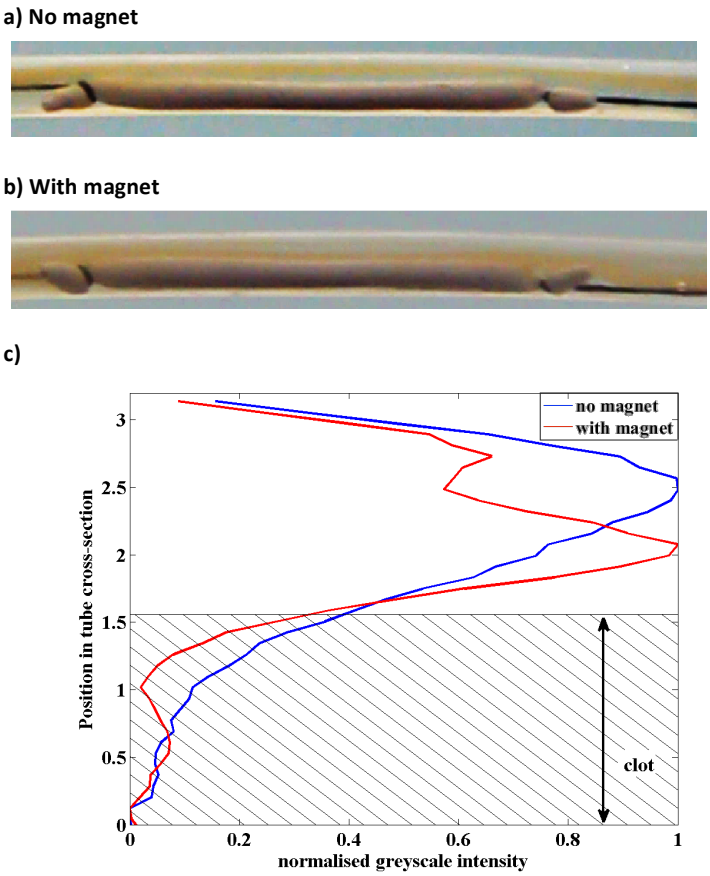


Figure 4-12: effect of the magnetic targeting system on magnetic material position in the cross-section of the flow chamber:
a) Image of the flow chamber just before bolus peak in the absence of a magnetic field. Still from the video at time $t = t_1 - 2s$; b) Image of the flow chamber just before bolus peak in the presence of a magnetic field. Still from the video at time $t = t_1 - 2s$. The images were contrast-enhanced for clarity; c) greyscale profile in the cross-section of the tube in the absence and in the presence of a magnet (blue and red lines respectively). The profiles were normalised to their maximum intensity. The lines represent the average of three experimental runs.

Figure 4-12 a) illustrates the flow of a microbubble bolus past the clot phantom in the absence of a magnetic field. The microbubble stock solution was brown in colour and buoyant in the flow system. This confirms that the lipid microbubbles were associated with magnetic material, and that greyscale intensity was a good optical indicator for locating the magnetic microbubbles. Figure 4-12 b) gives an example of the same experiment carried out in the presence of the Halbach array. The bolus was visibly deflected downwards, towards the magnet. This deflection is quantified in Figure 4-12 c): the point of maximum bolus concentration was moved by 0.4 mm towards the clot in the presence of the magnetic targeting system. However not all magnetic material was affected, and a fraction of the bolus remained buoyant, with a concentration peak at 57% of the main peak in greyscale intensity.

Figure 4-13 illustrates microbubble retention. Figure 4-13 a) and b) provide an example of the flow chamber just after bolus end, in the presence and in the absence of a magnetic field. A small difference in colour can be observed at the base of the two clots, indicating magnetic material retention. Figure 4-13 c) quantifies in each case the change in total greyscale intensity before and after the microbubble bolus. Even in the absence of a magnet, the focal region is very slightly darker after the microbubble bolus has passed (+ 9.3 ± 2.6 greyscale levels). This is due to the impurities present in the microbubble stock solution, including undispersed clusters of powdered lipid. The difference is enhanced in the presence of the Halbach array (+ 16.8 ± 2.0 greyscale levels), indicating that magnetic material was retained. It must however be noted that this type of optical experiment cannot distinguish between magnetic microbubbles and magnetic oil droplets. It is therefore likely that the retained material comprises a mixture of the two types of particles.

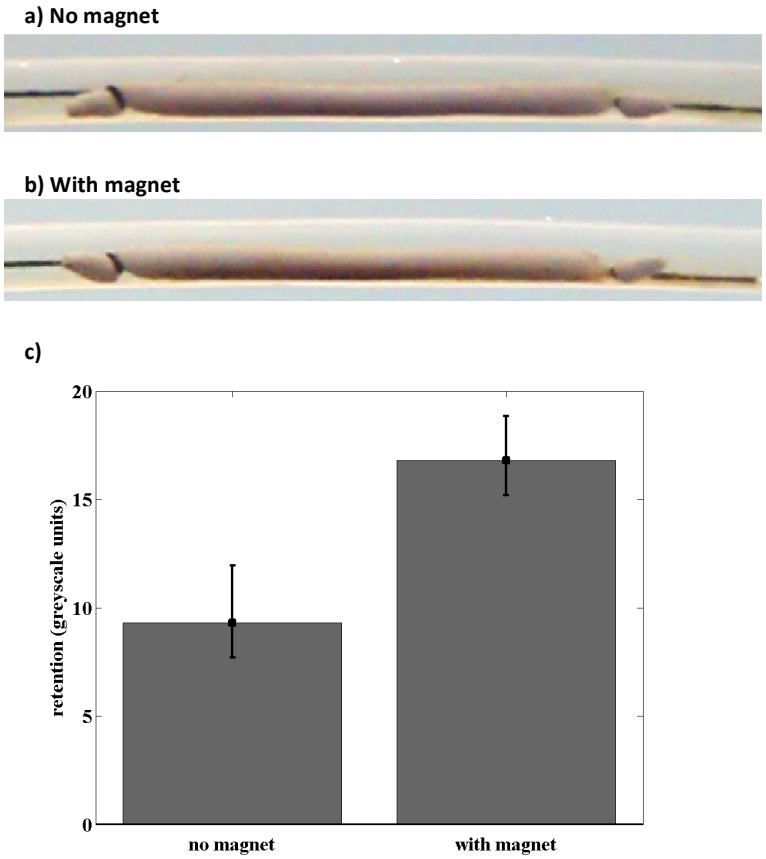


Figure 4-13: effect of the magnetic targeting system on magnetic material retention near the clot: a) image of the flow chamber just after bolus end in the absence of a magnetic field; b) image of the flow chamber just after bolus end in the presence of a magnetic field. The images were contrast-enhanced for clarity; c) quantification of retention: sum of greyscale values in the focal ROI after bolus end in the presence and the absence of a magnetic field. The error bars represent the range of retentions observed in three experimental runs.

4.3.4. Effect of magnetic targeting on thrombolysis rates: preliminary experiments

At this point in the investigation, it has been established that mechanical sonothrombolysis is accelerated by increasing microbubble concentrations. It has also been shown that magnetic targeting with iron-oxide loaded microbubbles and a linear Halbach array increases microbubble concentration in the region of the clot. The subsequent sections investigate the hypothesis that magnetically targeted microbubbles have the potential to accelerate sonothrombolysis.

4.3.4.a) Pilot study

A pilot study was carried out with a limited sample size (n= 3) on a human clot model. The parameters are summarized in Table 4-2. Figure 4-14 shows the clot lysis rates observed in all three experimental groups. Negligible thrombolysis (<0.01 mm/min) was observed in the ultrasound only group. On the other hand, rapid lysis (>0.034 mm/min) was achieved for all the clots treated with microbubbles, in the absence of any fibrinolytic drugs. The average rate of lysis was 4.4 times greater in the group treated with ultrasound and non-targeted microbubbles than in the group treated with ultrasound alone. Magnetic targeting provided an additional 60.1% increase in average lysis rates over non-targeted treatment. In this limited clot population, experimental repeatability was high, with a narrow range of lysis rates in each experimental group.

Parameter	Value
PBS flow rate	12.2 mL/min
Magnet position	upper face of magnet – surface of clot: 15.2 mm
Microbubble concentration	$3.0 \times 10^6 \pm 4.6 \times 10^4$ microbubbles/mL in PBS flow
Peak Rarefactional Pressure	720 kPa
Pulse repetition frequency	4 Hz
Duty cycle	4 %
Treatment time	15 min

Table 4-2: Experimental conditions in the preliminary studyof sonothrombolysis with magnetically targeted microbubbles.

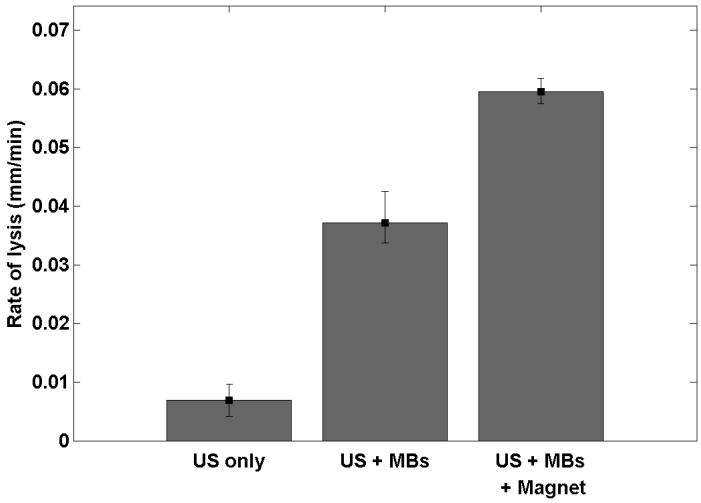


Figure 4-14: Lytic rates in the preliminary study of sonothrombolysis with magnetically targeted microbubbles (n = 2 in the US only group, n = 3 in the other two). The clots were treateted with 0.5 MHz ultrasound, 720 kPa peak rarefactional pressure, a 4 Hz pulse repetition frequency and a 4% duty cycle. Maximum depth of clot lysis was computed on photographs taken every 30 seconds during treatment, yielding the lytic rate. Error bars show the range of lysis rates observed.

4.3.4.b) Replicated experiment

Building on these promising early data, the experiment was replicated with a larger sample size (n = 6) in a porcine clot model. The parameters are summarised in Table 4-3. They are identical to the parameters used in the pilot study, with the exception of the peak rarefactional pressure in the focal region. Preliminary experiments showed that in this particular batch of clots, no lysis could be observed at 720 kPa even in the presence of microbubbles. Adjustments in pressure were therefore necessary to account for batch-to-batch variations in clot properties. In the experiments described in this section and in the rest of the chapter, a preliminary pressure-ramp study was carried out before each series of experiments in order to identify a suitable pressure value, defined by a rate of lysis greater than 0.03 mm/min in the US + microbubbles group (data not shown).

Parameter	Value
PBS flow rate	12.2 mL/min
Magnet position	upper face of magnet – surface of clot: 15.2 mm
Microbubble concentration	$3.0 \times 10^6 \pm 4.6 \times 10^4$ microbubbles/mL in PBS flow
Peak Rarefactional Pressure	1 MPa
Pulse repetition frequency	4 Hz
Duty cycle	4 %
Treatment time	15 min

Table 4-3: Experimental conditions in the replicated study of sonothrombolysis with magnetically targeted microbubbles.

Figure 4-15 reports the lytic rates in this repeated study. As noted in the pilot study, a large increase in average lytic rates was observed in the US+MB group over US only (three-fold increase). However, no significant change in lysis rates was observed with the addition of magnetic targeting ($p = 0.86$).

It was also noted that thrombolytic rates were highly variable. For instance, in the US + MB + Magnet group, lysis rates ranged from 0.02 to 0.09 mm/min.

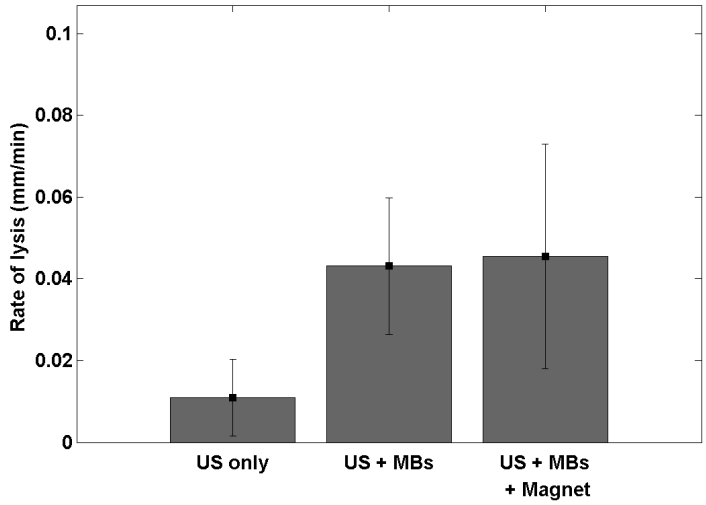


Figure 4-15: Lytic rates in the replicated study of sonothrombolysis with magnetically targeted microbubbles (n = 3 in the US only group, n = 6 in the other two groups). The clots were treateted with 0.5 MHz ultrasound, 1 MPa peak rarefactional pressure, a 4 Hz pulse repetition frequency and a 4% duty cycle. Maximum depth of clot lysis was computed on photographs taken every 30 seconds during treatment, yielding the lytic rate. Error bars represent standard deviations from the mean.

In this series of experiments, the use of magnetic targeting was not found to significantly accelerate sonothrombolysis. These observations were unexpected given the initial investigations on microbubble concentration described in sections 4.3.2 and 0. Two reasons are suggested for the discrepancy: (a) clot lysis rates are highly variable, making it difficult to compare treatment outcomes; (b) the current magnetic retention system does not sufficiently increase microbubble concentration at the clot site. These factors are investigated further in the following sections.

4.3.5. Experimental variability

This section describes the steps taken to investigate the sources of experimental variability when performing sonothrombolysis with magnetic microbubbles. These sources include clot properties as well as microbubble properties.

4.3.5.a) Clot variability

Clot origin

The chemical composition of blood varies from individual to individual, yielding clots with different structures and mechanical properties [236]. A preliminary study was therefore carried out with human blood clots originating from two different volunteers. Figure 4-16 shows the lysis profiles obtained over 15 minutes for a single clot in each group. A high discrepancy was observed between the two individuals. This indicates that variations in clot properties between individuals cannot be ruled out as a source of variability. In order to increase consistency, each subsequent series of experiments was performed with clots originating from a single individual.

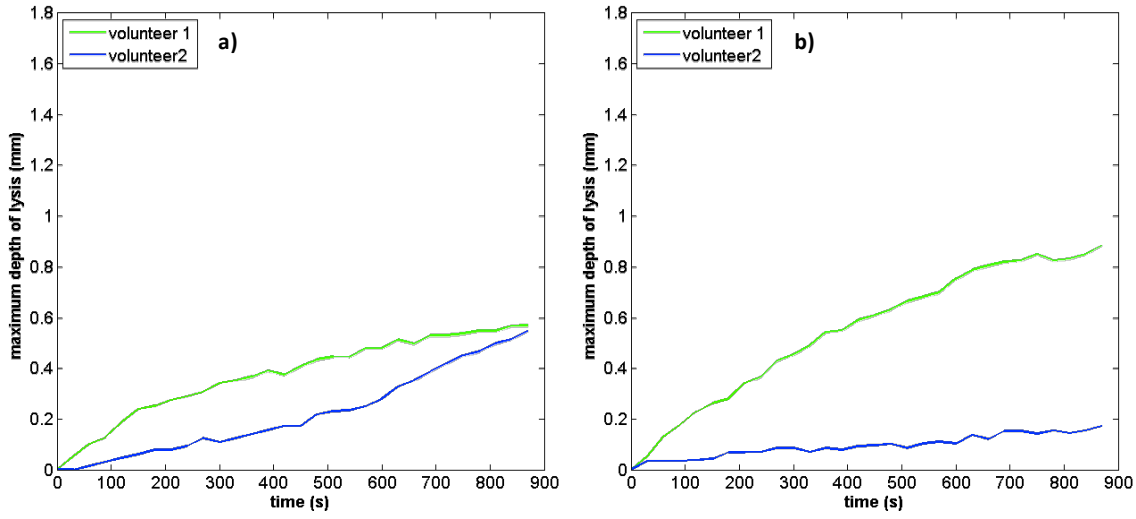


Figure 4-16: Role of clot origin in lysis variability. Maximum lysis depth over time during sonothrombolysis, with whole human blood clots originating from two different volunteers (n = 1). Ultrasound exposure was performed at 0.5 MHz, 720 kPa peak rarefactional pressure, a 4% duty cycle and a 4 Hz pulse repetition frequency. Maximum depth of clot lysis was computed on photographs taken every 30 seconds during treatment.
a) treatment with US and non-targeted microbubbles; b) treatment with US and magnetically targeted microbubbles.

Clot age

Clot properties evolve over time wih the constant rearranging of the fibrin network. In this study, all clots were used in an interval of 4-14 days after formation, which has been shown to be a period of relative stability in clot properties for sonothrombolysis [56]. The rates of lysis collected in paragraph 4.3.4.b) were plotted as a function of clot age (Figure 4-17). No correlation could be found between clot age and lytic rate (Pearson's correlation coefficient r = 0.20, non-significant), ruling out clot age as a main source of variability. These results are in agreement with the findings of Holland *et al.* who showed that clots aged between 2-16 days have similar responses to tPA treatment [56].

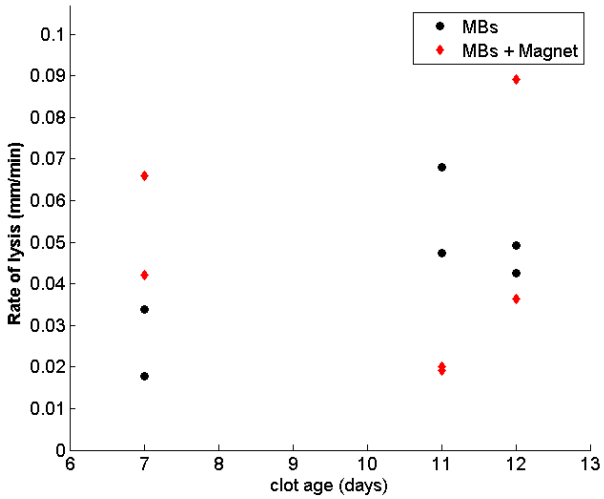


Figure 4-17: Rates of sonothrombolysis as a function of clot age for porcine whole blood clots treated at 0.5MHz, 1 MPa peak rarefactional pressure, a 4% duty cycle and a 4 Hz pulse repetition frequency, in the presence and in the absence of magnetic targeting (red and black markers respectively). Maximum depth of clot lysis was computed on photographs taken every 30 seconds during treatment, yielding the lytic rate.

Clot gas content

Cavitation is widely agreed to play a significant role in sonothrombolysis [49], [50]. The existence of cavitation nuclei in the clots is therefore expected to modify treatment outcomes. Moreover, the presence of gas in the clot would weaken the clinical relevance of the experiments.

As a result, clots were stored in degassed PBS until use; yet the possibility of entrapped gas still remained. A preliminary experiment was thus carried out to ascertain the effect of entrapped gas. Porcine blood clots were degassed for 30 minutes in a vacuum chamber (Nalgene Vacuum Dessicator, Thermo Fischer Scientific Inc., Waltham, MA, USA, connected to a MZ 2 NT diaphragm pump, Vacuubrand GmbH, Wertheim, Germany) and immediately exposed to ultrasound in the absence of magnetic targeting. The parameters of exposure are shown in Table 4-4. Control samples were used as in the previous studies and were not degassed.

Lytic rates are shown in Figure 4-18 for degassed and control samples. Variability remained high with degassed clots, indicating that modifying clot gas content does not resolve the issue of variability in lysis rates. Subsequent experiments were therefore carried out with non-degassed clots.

Parameter	Value
PBS flow rate	20.3 mL/min
Steel bar position	upper face of steel bar – surface of clot: 15.2 mm
Microbubble concentration	$2.5 \times 10^6 \pm 3.8 \times 10^4$ microbubbles/mL in PBS flow
Peak Rarefactional Pressure	810 kPa
Pulse repetition frequency	4 Hz
Duty cycle	4 %
Treatment time	15 min

Table 4-4: Experimental conditions in the investigation of the effect of entrapped gas on microbubble-enhanced sonothrombolysis.

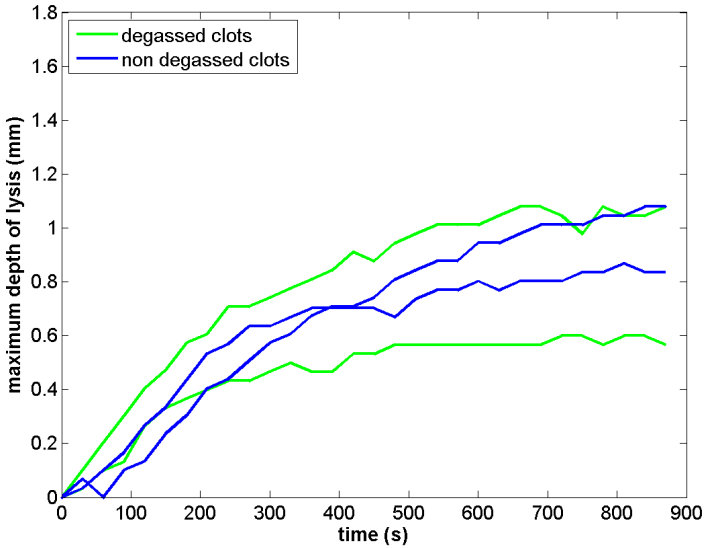


Figure 4-18: Maximum lysis depth over time during sonothrombolysis, with degassed and non-degassed clots (n = 2). Ultrasound exposure was performed at 0.5 MHz, 810 kPa peak rarefactional pressure, a 4% duty cycle and a 4Hz pulse repetition frequency. Maximum depth of clot lysis was computed on photographs taken every 30 seconds during treatment.

4.3.5.b) Microbubble variability

Microbubble size and concentration

Batch-to-batch variability in the physical properties of the microbubble stock solution was assessed from nine vials prepared over 4 consecutive days. Twenty micrographs were analysed for each vial.

Microbubble concentration was consistent between batches, at $2.95 \times 10^8 \pm 5.23 \times 10^6$ microbubbles/mL. As a comparison, Mulvana *et al*. characterised a similar microbubble formulation and found a concentration of $3.7 \times 10^8 \pm 0.9 \times 10^8$ microbubbles/mL across batches. Mean microbubble diameter was also repeatable, at 1.05 µm ± 0.02 µm. This closely agrees with the size variability reported by Mulvana *et al*., at 1.2 ± 0.03 µm. Polydispersity was repeatable as well: the standard deviation of particle diameters in individual batches ranged between 0.71 and 0.76 µm. Lastly, estimated gas content was reasonably consistent, at 0.61 ± 0.10 µg/mL (compared to 0.65 ± 0.18 µg/mL in Mulvana *et al*.).

This analysis indicates that variability in the size and concentration of microbubbles is not a likely cause of variability in lysis rates.

Acoustic response

Consistency in microbubble acoustic response was also examined. Figure 4-19 reports the cavitation dose detected at the treatment site during the replicated experiment (paragraph 4.3.4.b). As expected, acoustic emissions were substantially higher in the groups treated with microbubbles ($1.8 \times 10^{-2} \pm 5.6 \times 10^{-3}$ V^2 on average in the US only group, compared to $4.7 \times 10^{-2} \pm 1.7 \times 10^{-2}$ V^2 in the US + MB group). However, the acoustic emissions in the magnetic targeting group were slightly lower than in the non-targeted group ($4.7 \times 10^{-2} \pm 1.7 \times 10^{-2}$ V^2 and $4.1 \times 10^{-2} \pm 2.3 \times 10^{-2}$ V^2 respectively), however the difference was not significant ($p = 0.63$). In fact, the high variability observed in lysis rates corresponded to a high variability in the acoustic emissions. For instance, in the experimental group treated with ultrasound and non-targeted microbubbles, they ranged from 2.3×10^{-2} V^2 to 6.1×10^{-2} V^2.

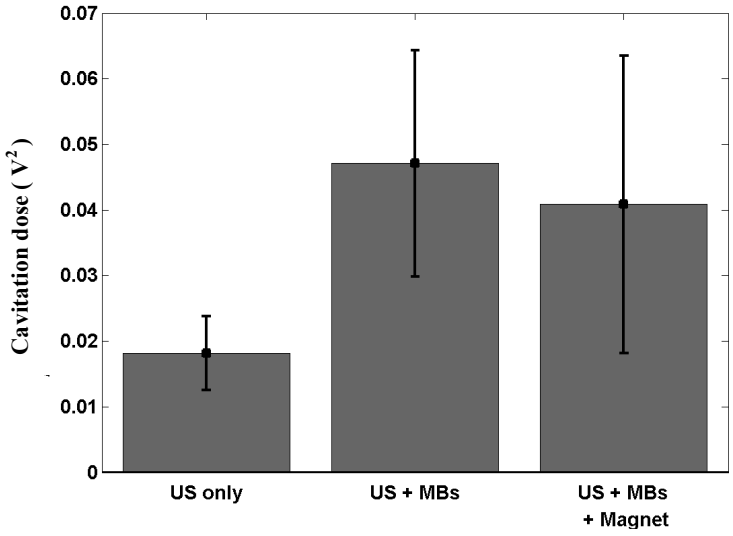


Figure 4-19: Total cavitation dose detected in the 2-5 MHz frequency range during sonothrombolysis of retracted porcine clots. The clots were treateted with 0.5 MHz ultrasound, 1 MPa peak rarefactional pressure, a 4 Hz pulse repetition frequency and a 4% duty cycle (n = 3 in the US only group, n = 6 in the other two groups). The acoustic emissions at the focus were acquired with a 7.5 MHz PCD transducer mounted coaxially with the HIFU transducer. Error bars represent standard deviations from the mean.

In fact, Figure 4-20 provides closer analysis of the data, with a bivariate representation of the lysis rates and acoustic emissions for each sample in the replicated experiments. It reveals the existence of a point in the US + MB + Magnet group with unusually low acoustic emissions (circled in blue). The frequency spectrum of the emissions in this experimental run includes low harmonics and ultraharmonics with a negligible level of broadband emissions. This is very different from the typical response of microbubbles in the conditions of exposure (high broadband emissions combined with high harmonics and ultraharmonics). It suggests a defect in the cavitation detection system, for instance the existence of a large air bubble obstructing the PCD transducer. The data point was subsequently considered as an outlier and excluded.

Importantly, no correlation between lysis rate and acoustic emissions could be found. The correlation graph (Figure 4-20) illustrates the absence of a strong correlation between lysis rates and acoustic emissions. There is a weak but significant positive correlation: Pearson's correlation coefficient $r = 0.548$, while $r_c = 0.532$ is the critical value at $p=0.05$. Therefore the variability in lysis rates cannot be fully assigned to the variability in the acoustic response of the microbubbles.

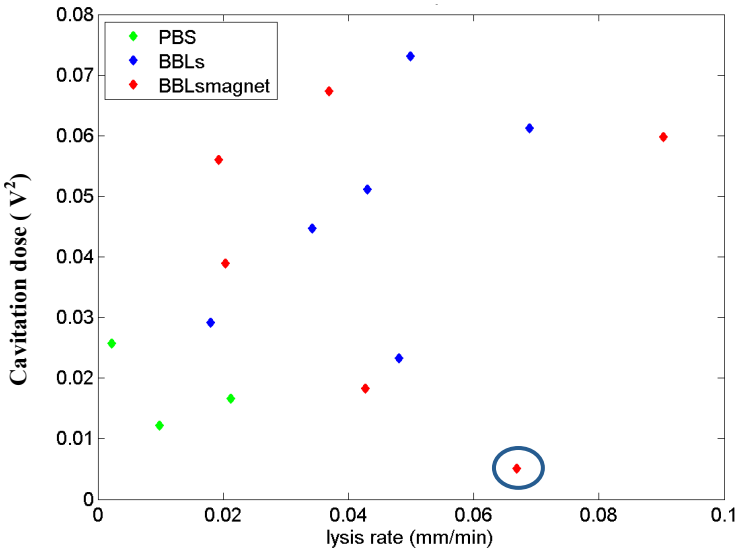


Figure 4-20: Bivariate representation of the lysis rates and the total acoustic emissions (2-5 MHz range) in the replicated experiment. The clots were treateted with 0.5 MHz ultrasound, 1 MPa peak rarefactional pressure, a 4 Hz pulse repetition frequency and a 4% duty cycle (n = 3 in the US only group, n = 6 in the other two groups). Maximum depth of clot lysis was computed on photographs taken every 30 seconds during treatment, yielding the lytic rate. The acoustic emissions at the focus were acquired with a 7.5 MHz PCD transducer mounted coaxially with the HIFU transducer.

Magnetic response variability

During the final sonication step of microbubble preparation, it is expected that the lipid microbubbles will incorporate highly variable amounts of ferrofluid into their coating. This would, in turn create a wide variety of magnetic responses, which could be quantified by magnetic relaxivity [208]. Yet as the lysis rates are highly variable even in the non-targeted group (US + MBs), differences in magnetic response are not the prime source of variability in lysis rates.

4.3.6. Effect of magnetic targeting on thrombolysis rates: improved magnetic targeting system

Magnetic targeting in the initial setup was not found to be associated with a significant acceleration in sonothrombolysis. Yet it was established in paragraph 4.3.2 that lysis rates are sensitive to microbubble concentration, although a substantial increase in concentration is necessary to observe a corresponding increase in lysis rates. The magnetic targeting setup was therefore modified to increase microbubble retention at the clot site.

Owen *et al.* have observed that magnetic microbubble retention against flow depends on the magnitude of the magnetic field gradient, as well as on fluid velocity [193]. Two modifications to the magnetic targeting setup were therefore considered: (a) altering the position of the magnet to increase the field gradient near the clot; (b) reducing the flow rate in the chamber.

4.3.6.a) Modified magnet position

The forces acting on the microbubble population were increased by moving the magnet by a distance of approximately one wavelength (3.1 mm) closer to the clot.

A series of sonothrombolysis experiments was carried out in this modified setup. The parameters are summarized in Table 4-5; they remained the same as in section 4.3.4, again with the exception of the peak rarefactional pressure.

Characterising the modified magnetic targeting system

Figure 4-21 shows maps of the magnitude magnetic field and the magnitude of the magnetic field gradient produced in the flow chamber by the modified magnetic targeting system. As expected, the shapes of both fields are unchanged, but the field values achieved in this setup are markedly higher: the magnetic field was in the 4.7-18.0 $\times 10^{-2}$ T range and

the magnetic field gradient was in the 7.3-28 T/m range (compared to 3.2-11.0 $\times 10^{-2}$ T and 4.7-17.2 T/m respectively in the previous system).

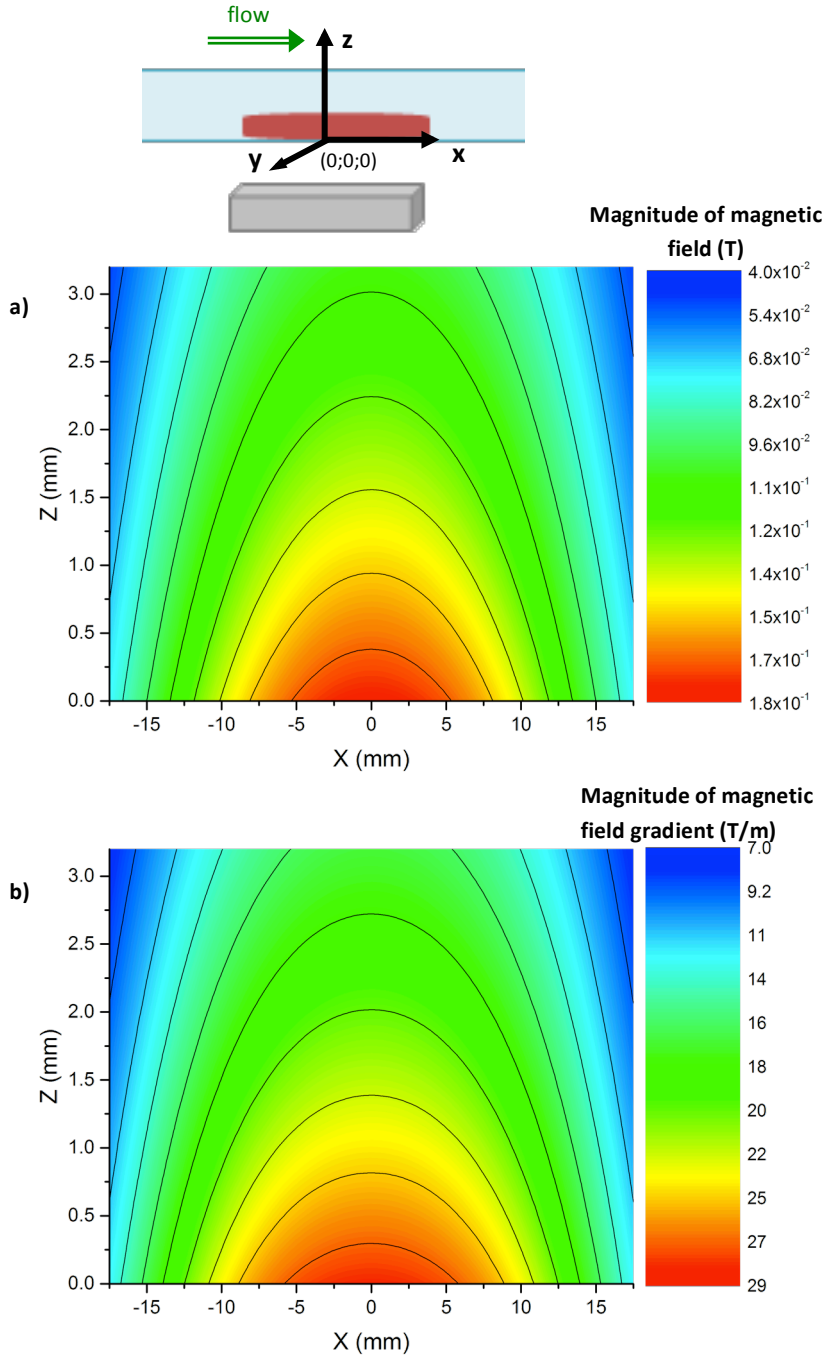


Figure 4-21: Simulations of magnetic field created in the transverse plane of the flow chamber by a linear 5-element Halbach array placed at a distance of 12.1 mm from the surface of the clot.
a) magnitude of magnetic field and ; b) magnitude of magnetic field gradient.
Inset (above): orientation of the axes and origin

Effect of the modified magnetic targeting system on microbubble distribution

As in the previous setup, the magnet deflected the trajectories of the microbubbles, bringing them closer to the clot as illustrated in Figure 4-22 a) and b). Quantitative comparison is shown in Figure 4-22 c). The peak of the bolus was brought 0.33 mm closer to the surface of the clot, approximately the same distance as in the previous setup (± 1 pixel). The difference lies in the fact that in this case, the whole bolus was deflected: no secondary peak of buoyant material was observed. The total proportion of microbubbles brought in contact with the clot was therefore increased.

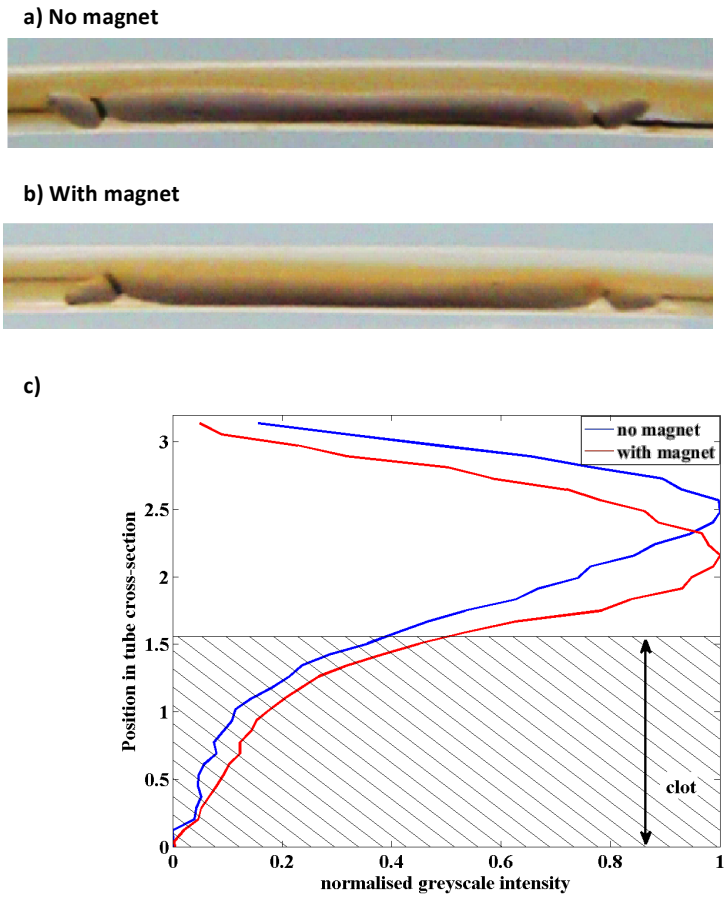


Figure 4-22: Effect of the magnetic system with modified magnet distance on the position of magnetic material in the cross-section of the flow chamber: a) image of the flow chamber just before bolus peak in the absence of a magnetic field. Still from the video at time $t = t_1 - 2s$; b) image of the flow chamber just before bolus peak in the presence of a magnetic field. Still from the video at time $t = t_1 - 2s$. The images were contrast-enhanced for clarity; c) greyscale profile in the cross-section of the tube in the absence and in the presence of a magnet (blue and red lines respectively). The profiles were normalised to their maximum intensity. The lines represent the average of three experimental runs.

Figure 4-23 investigates magnetic material retention in the modified setup. Magnetic retention was found to be very similar to the values previously observed: + 16.9 ± 3.2 greyscale levels, compared with + 16.8 ± 2.0 in the previous iteration of the system.

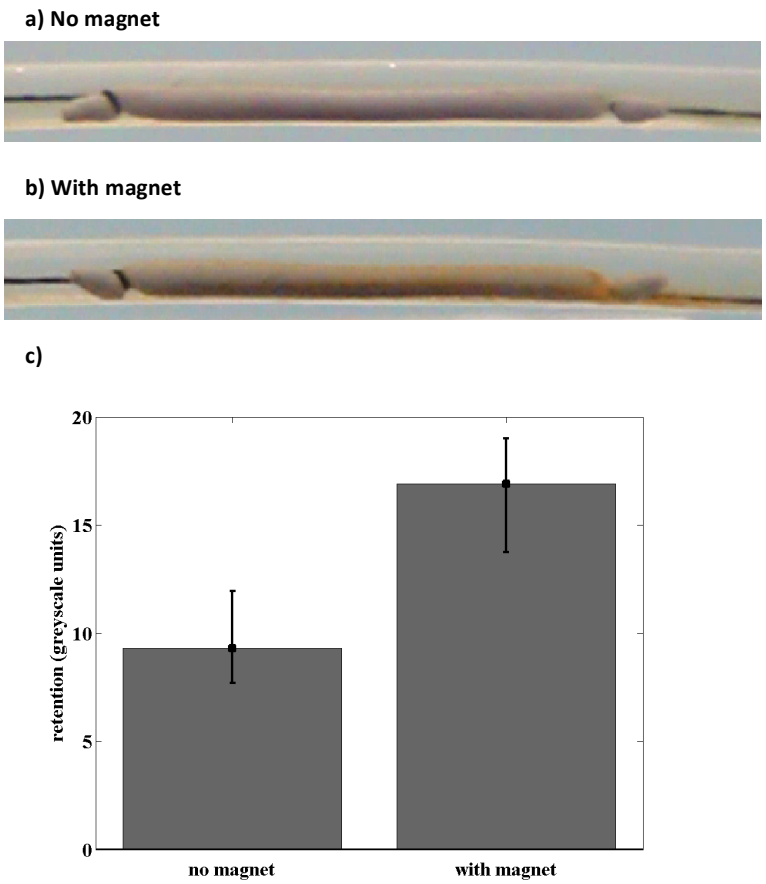


***Figure 4-23:** Effect of the magnetic targeting system with modified magnet distance on the retention of magnetic material near the clot: a) image of the flow chamber just after bolus end in the absence of a magnetic field; b) image of the flow chamber just after bolus end in the presence of a magnetic field. The images were contrast-enhanced for clarity; c) quantification of retention: sum of greyscale values in the focal ROI after bolus end in the presence and the absence of a magnetic field. The error bars represent the range of retentions observed in three experimental runs.*

Effect of the modified magnetic targeting system on sonothrombolysis

Figure 4-24 illustrates the lysis rates in the modified magnetic targeting setup. The lytic rates observed in the magnetic targeting group were slightly lower on average than in the non-targeted group ($3.5 \times 10^{-2} \pm 1.8 \times 10^{-2}$ and $4.1 \times 10^{-2} \pm 1.6 \times 10^{-2}$ mm/min respectively), though there was no significant difference between the two experimental groups ($p = 0.58$). In both cases, the lytic rate was markedly higher in the presence of microbubbles than in the control group treated with ultrasound only ($4.1 \times 10^{-2} \pm 1.6 \times 10^{-2}$ mm/min in the US + MB group compared to $4.6 \times 10^{-3} \pm 3.4 \times 10^{-3}$ mm/min in the US only group).

Figure 4-25 shows the associated acoustic emissions in the 2-5 MHz frequency range. As observed previously, acoustic emissions were substantially higher in the groups treated with microbubbles ($1.8 \times 10^{-3} \pm 1.2 \times 10^{-3}$ mm/min in the US only group, compared to $2.7 \times 10^{-2} \pm 1.1 \times 10^{-2}$ mm/min in the US + MB group). The acoustic emissions were also slightly higher in the targeted group than in the non-targeted group ($3.6 \times 10^{-2} \pm 1.5 \times 10^{-2}$ mm/min and $2.7 \times 10^{-2} \pm 1.1 \times 10^{-2}$ mm/min respectively), however the difference was not statistically significant ($p = 0.39$).

Parameter	Value
PBS flow rate	12.2 mL/min
Magnet position	upper face of magnet – surface of clot: 12.1 mm
Microbubble concentration	$2.4 \times 10^{6} \pm 3.7 \times 10^{4}$ microbubbles/mL in PBS flow
Peak Rarefactional Pressure	895 kPa
Pulse repetition frequency	4 Hz
Duty cycle	4 %
Treatment time	15 minutes

Table 4-5: Experimental conditions in the investigation sonothrombolysis with magnetically targeted microbubbles at a reduced magnet distance.

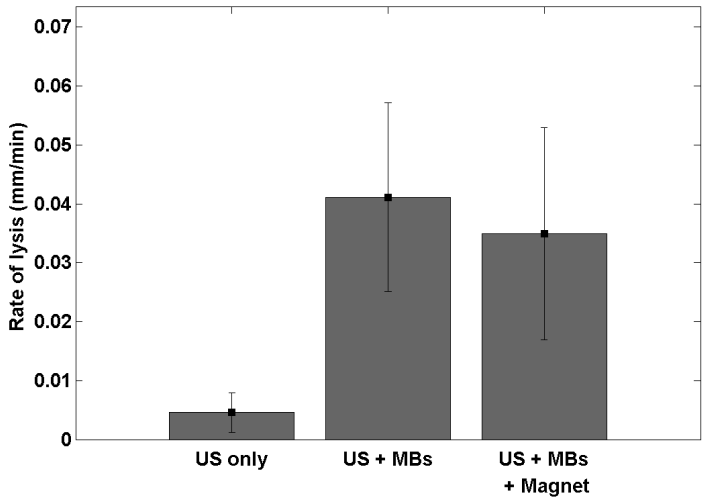


Figure 4-24: Lytic rates in the modified magnetic targeting setup (closer magnet) for the study of sonothrombolysis with magnetically targeted microbubbles (n = 3 in the US only group, n = 5 in the other two groups). The clots were treateted with 0.5 MHz ultrasound, 895 kPa peak rarefactional pressure, a 4 Hz pulse repetition frequency and a 4% duty cycle. Maximum depth of clot lysis was computed on photographs taken every 30 seconds during treatment, yielding the lytic rate. Error bars represent standard deviations from the mean.

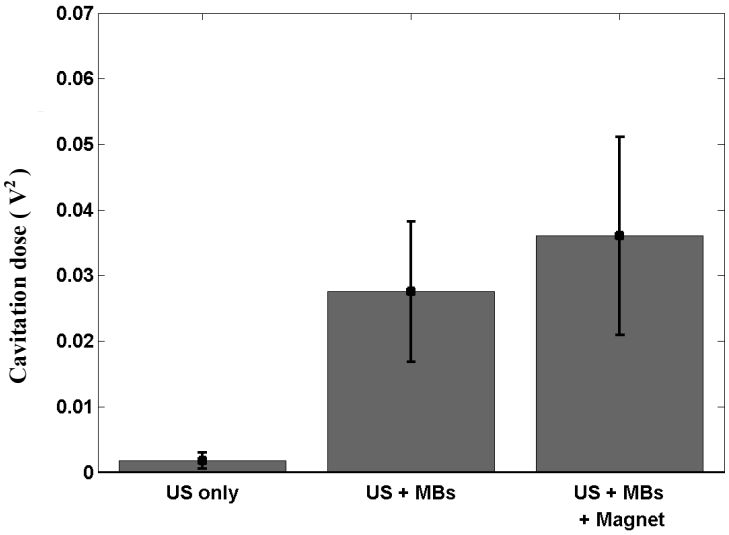


Figure 4-25: Total cavitation dose in the 2-5 MHz frequency range during sonothrombolysis of retracted porcine clots in the modified magnetic targeting setup (closer magnet). The clots were treateted with 0.5 MHz ultrasound, 895 kPa peak rarefactional pressure, a 4 Hz pulse repetition frequency and a 4% duty cycle (n = 3 in the US only group, n = 5 in the other two groups). The acoustic emissions at the focus were acquired with a 7.5 MHz PCD transducer mounted coaxially with the HIFU transducer. Error bars represent standard deviations from the mean.

4.3.6.b) Lower flow and pulse repetition frequency

An additional improvement was considered on the new magnetic setup: the flow rate in the chamber was reduced by 50%. In order to allow microbubble replenishment between ultrasound bursts, the pulse repetition frequency was also reduced by 75%. Burst duration was not modified (10 ms) and the magnet was placed in the same position as in section 4.3.6.a). The parameters used in this part of the study are summarised in Table 4-6.

Effect of the modified magnetic targeting system on microbubble distribution

The effect of the magnet and the modified flow rate on microbubble trajectories is shown in Figure 4-26. The Halbach array was found to deflect the microbubbles more than in the two cases previously investigated with higher flow rates. The greyscale peak of the bolus was brought 0.78 mm closer to the clot by the magnet, compared with 0.32 mm previously. Magnetic retention was also greatly enhanced at this flow rate. It can be readily observed in the examples of Figure 4-27 a) and b). Figure 4-27 confirms this finding: + 35.3 ± 8.9 greyscale levels in the presence of a magnetic field, compared to + 8.5 ± 4.7 without targeting.

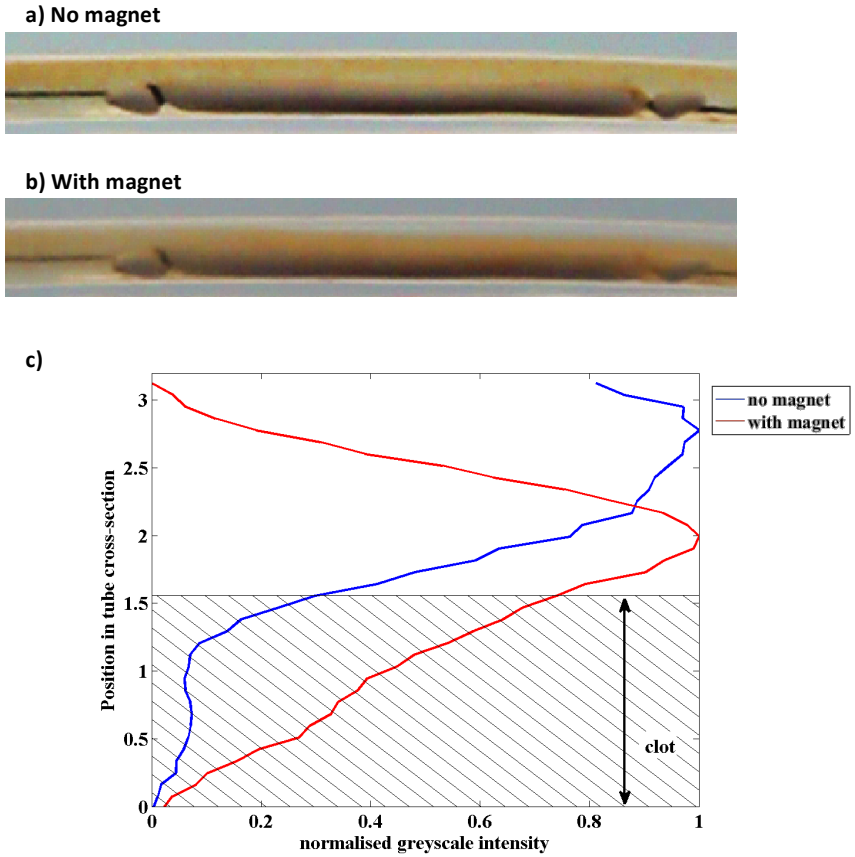


Figure 4-26: effect of the magnetic targeting system with modified magnet position and PBS flow rate on microbubble position in the cross-section of the flow chamber: a) Image of the flow chamber just before bolus peak in the absence of a magnetic field. Still from the video at time $t = t_1 - 2s$; b) Image of the flow chamber just before bolus peak in the presence of a magnetic field. Still from the video at time $t = t_1 - 2s$. The images were contrast-enhanced for clarity; c) greyscale profile in the cross-section of the tube in the absence and in the presence of a magnet (blue and red lines respectively). The profiles were normalised to their maximum intensity. The lines represent the average of three experimental runs.

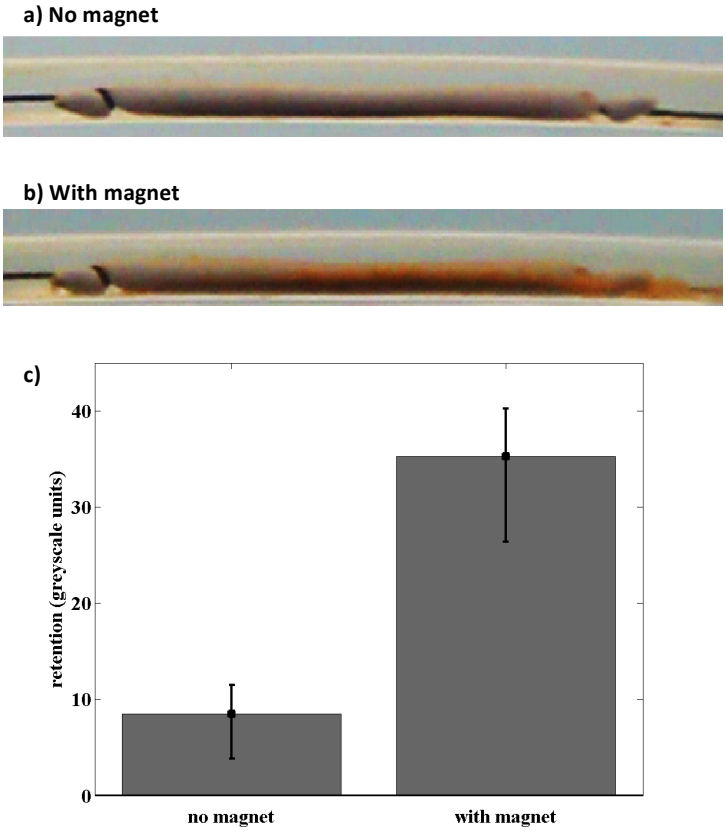


Figure 4-27: effect of the magnetic targeting system with modified magnet distance and PBS flow rate on the retention of magnetic material near the clot: a) image of the flow chamber just after bolus end in the absence of a magnetic field; b) image of the flow chamber just after bolus end in the presence of a magnetic field. The images were contrast-enhanced for clarity; c) quantification of retention: sum of greyscale values in the focal ROI after bolus end in the presence and the absence of a magnetic field. The error bars represent the range of retentions observed in three experimental runs.

Effect of the modified magnetic targeting system on sonothrombolysis

Figure 4-28 shows the lytic rates observed in this series of experiments. As expected, lysis rates with the reduced pulse repetition frequency were much slower than previously (<0.017 mm/min). Despite the longer treatment time, final lysis depths were also very low (<0.046 mm). In all experimental groups, limited and highly variable sonothrombolysis was observed, and no compelling difference between experimental groups was observed ($p = 0.83$ between US + MB group and US + MB + Magnet group).

As in the previous series of experiments, the acoustic emissions (

Figure 4-29) did not significantly differ between the targeted and non-targeted group ($p = 0.46$).

Parameter	Value
PBS flow rate	6.5 mL/min
Magnet position	upper face of magnet – top of clot: 12.1 mm
Microbubble concentration	$2.3 \times 10^6 \pm 3.5 \times 10^4$ microbubbles/mL in PBS flow
Peak Rarefactional Pressure	1.1 MPa
Pulse repetition frequency	1 Hz
Duty cycle	1%
Treatment time	30 minutes

Table 4-6: Experimental conditions in the investigation sonothrombolysis with magnetically targeted microbubbles at a reduced magnet distance and a reduced flow rate.

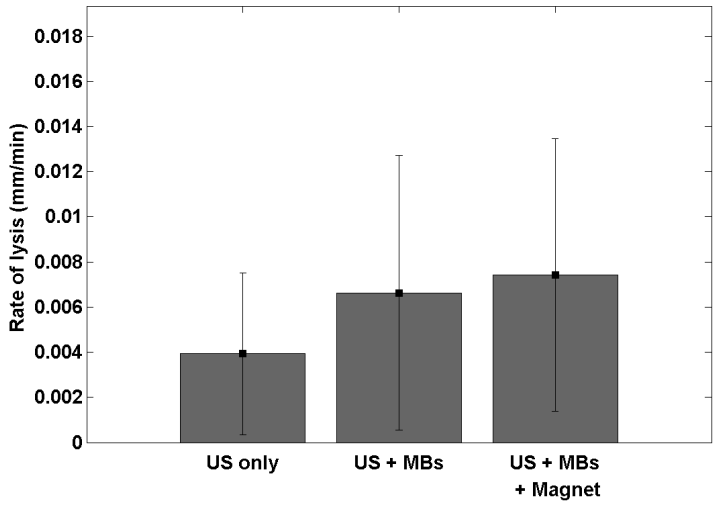


Figure 4-28: Lytic rates in the modified magnetic targeting setup (closer magnet and slower flow) for the study of sonothrombolysis with magnetically targeted microbubbles (n = 3 in the US only group, n = 6 in the other two groups). The clots were treateted with 0.5 MHz ultrasound, 895 kPa peak rarefactional pressure, a 4 Hz pulse repetition frequency and a 4% duty cycle. Maximum depth of clot lysis was computed on photographs taken every 30 seconds during treatment, yielding the lytic rate. Error bars represent standard deviations from the mean.

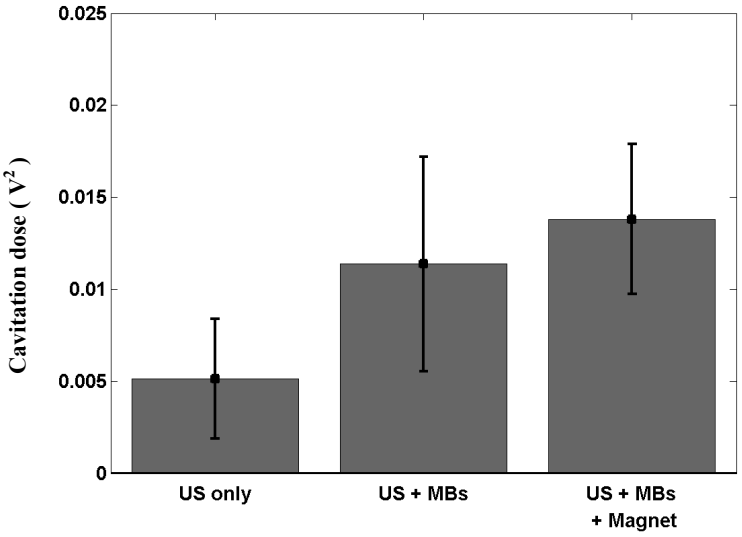


Figure 4-29: Total cavitation dose detected in the 2-5 MHz frequency range during sonothrombolysis of retracted porcine clots in the modified magnetic targeting setup (closer magnet and slower flow). The clots were treateted with 0.5 MHz ultrasound, 895 kPa peak rarefactional pressure, a 4 Hz pulse repetition frequency and a 4% duty cycle (n = 3 in the US only group, n = 6 in the other two groups). The acoustic emissions at the focus were acquired with a 7.5 MHz PCD transducer mounted coaxially with the HIFU transducer. Error bars represent standard deviations from the mean.

4.3.7. Consequences for the design of the magnetic targeting setup

Deflection or retention?

At the onset of this study, it was demonstrated that higher microbubble concentrations are associated with accelerated clot lysis. The magnetic targeting setup increases microbubble concentration in two ways: by bringing the microbubbles closer to the clot (figures 4-16, 26, and 30), and by retaining them against flow on the clot surface (figures 4-17, 27, and 31). The experimental data indicates that while retention does take place, it is limited, and the former effect is expected to be predominant in this setup.

In the absence of a magnetic field, most microbubbles are kept away from the clot surface by buoyancy. The Halbach array deflects the point of maximum microbubble concentration towards the clot by 320 µm to 780 µm, thus increasing the concentration of microbubbles at the surface of the clot.

However in this setup, the primary acoustic radiation force also contributes to microbubble deflection towards the clot. For a microbubble driven at resonant frequency, assuming small-amplitude oscillations, the magnitude of the primary acoustic radiation force is given by:

$$\left|\boldsymbol{F}_{arf}\right| = \frac{2\,\pi\,P_a^2\,R}{\delta\,\omega_0\,\rho\,c}\left[\frac{D}{T}\right] \qquad (23)$$

where P_a is the peak applied acoustic pressure, R is the microbubble resting radius, δ is the total damping coefficient, ρ is the density of the medium, c is the velocity of sound in the medium, and ω_0 is the resonant frequency of the microbubble, D is the pulse duration and 1/T is the pulse repetition frequency [237]. An order of magnitude was computed with the values in Table 4-7. The radius of the microbubble was chosen to approach the diameter of an air-filled microbubble that is resonant at 0.5 MHz [238]. During a pulse, the force on the microbubble is estimated at 66.0 µN. In average over time, it is 2.6 pN.

In comparison, the model of the magnetic field described in paragraph 4.2.4 yields a normalised force $|\boldsymbol{F_{norm}}| = \frac{|\boldsymbol{F_m}|}{M_s V}$ where $\boldsymbol{F_m}$ is the magnetophoretic force acting on the microbubble, M_s is the saturation magnetisation of iron oxide particles, and V is the volume of iron oxide present on a microbubble. In the final iteration of the magnetic targeting system, the maximum value of the normalised force is 26.1 T/m. With the assumptions listed in Table 4-7, the magnitude of the magnetophoretic force is estimated at 0.078 pN.

Therefore the deflection caused by the primary acoustic radiation force cannot be neglected during ultrasound exposure. It pushes the microbubbles in the same direction as the magnetophoretic force, but it is present in both the US + MB group and in the US + MB + Magnet group. It is probably accountable in part for the similar results observed in the two groups.

In contrast to microbubble deflection, microbubble retention occurs over time. The magnet can therefore be used to accumulate larger quantities of microbubbles passively before starting ultrasound exposure, or between ultrasound bursts.

This rapid analysis suggests that microbubble deflection is not sufficient and that an effective magnetic targeting system for sonothrombolysis ideally maximises microbubble retention. It must however be noted that in a clinical context, the geometry of the setup is more complex, and the direction of the primary acoustic radiation force may not be aligned with the magnetophoretic force.

Symbol	Parameter	Value (unit)	Reference
$\boldsymbol{P_a}$	Peak acoustic pressure	1 (MPa)	experimental conditions
$\boldsymbol{R}$	Microbubble radius	10 (μm)	[238]
δ	Damping coefficient	1.27	[237]
$\boldsymbol{\omega_0}$	Excitation frequency	0.5 (MHz)	experimental conditions
ρ	Density of water	1000 (kg/m^3)	[237]
c	Speed of sound in water	1500 (m/s)	[237]
$\boldsymbol{D}$	Pulse duration	1x 10^{-5} (s)	experimental conditions
$\boldsymbol{1/T}$	Pulse repetition frequency	4 (Hz)	experimental conditions
M_s	Saturation magnetisation of particles	4.7 x 10^5 (A/m)	[197]
R_s	Thickness of ferrofluid layer on microbubble shell	5 x 10^{-8} (m)	[193]
$\boldsymbol{\beta}$	Volume fraction of iron oxide in the ferrofluid	0.1	manufacturer documentation

Table 4-7: Values used for parameters in calculation of primary acoustic radiation force and magnetophoretic force.

The role of fluid velocity

In most magnetic targeting systems, the magnetophoretic force is orthogonal to the direction of fluid flow. Therefore the time required for a microbubble to reach its final position doesn't depend on fluid velocity, but the final position does. As a consequence, capture efficiency in the focal region depends on fluid velocity. This was confirmed in Figure 4-23 and Figure 4-27 with a four-fold increase in greyscale intensity in the focal region when the flow rate was reduced by 50%. This finding highlights the importance of taking into account the fluid velocity when designing a magnetic targeting system. Incidentally, the *in vivo* efficacy of magnetic targeting systems is bolstered by the low flow rates in occluded vessels: larger accumulation may be achieved *in vivo* than in the experiments presented here. This makes magnetic targeting a potentially attractive candidate for sonothrombolysis.

Microbubble localisation

A critical aspect in the design of a magnetic targeting setup is to direct the microbubbles to precisely the desired location. This is particularly difficult under flow conditions, where the microbubbles can readily be trapped by the magnet upstream from the treatment site. In the present setup, the Halbach array is much wider than the focal region (30 mm and 3 mm respectively), increasing the risk of inaccurate trapping. A smaller magnet with higher gradients would be desirable to overcome this issue.

In these experiments, the microbubbles are also at risk of being trapped directly against the inner surface of the flow chamber, on either side of the clot (the clot is a small cylinder inserted into a cylinder of larger diameter). This effect contributes to reducing the proportion of microbubbles that come in contact with the clot in the focal region. However, it is inherently associated with the geometry of the setup and it would not apply *in vivo*.

Consequence: application-specific magnets

These considerations underline the growing need to tailor magnetic targeting systems to their chosen application, taking into account the geometry, depth and flow rate of the target vessel [167], [199], [239] . For sonothrombolysis, a magnetic targeting system that maximises microbubble retention at the HIFU focus is an advantageous option.

Against this background, the experiment was repeated in a magnetic targeting setup designed to maximise microbubble retention at the HIFU focus.

4.3.8. Effect of a new magnetic targeting setup on sonothrombolysis

Description and characterisation of the system

The new magnetic targeting system differs markedly from the setup previously used. It was modified to address the limitations of the Halbach array, and in particular the fact that the array's large retention area (~40 mm wide) reduces the proportion of microbubbles retained in the narrow ultrasound focal region (~3 mm wide at 0.5 MHz). In this instance, the magnetic field was applied using a single 12.7 mm cubic permanent magnet element (N52 grade NdFeB), with a measured magnetisation value of 1.09×10^6 A/m. The magnet element was placed below the clot at an angle of 45^0, its upper vertex directly in contact with the flow channel and 7 mm downstream from the axis of HIFU exposure (Figure 4-30 b.). During experiments that did not involve magnetic targeting, the magnet was replaced by a stainless steel block of identical dimensions in order to maintain a comparable sound field.

In addition to maximising total retention in the focal region, the setup was designed to optimise the location of microbuble retention: of particular concern with the Halbach array were microbubbles accumulating on either side of the clot, where their therapeutic efficacy is limited. A PDMS[5] sleeve with a rectangular cutout (Figure 4-30 b.) was therefore added around the flow channel to ensure that the microbubles accumulate directly on the surface of the clot.

[5] Polydimethylsiloxane (PDMS) is an optically transparent polymer with an acoustic impedance close to that of water [300].

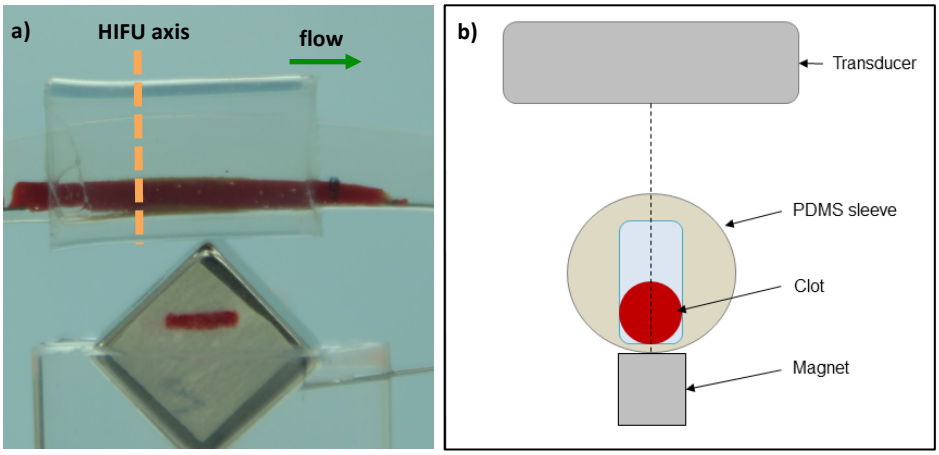


Figure 4-30: Layout of the new magnetic targeting system with PDMS sleeve and single cubic magnet element: a)photograph in front view; b) schematic of cross-section.

Effect of the setup on microbubble distribution

The effect of the new system on the microbubbles was quantified as before, by examining the position of the bolus peak during flow (Figure 4-31 A1-2) and the accumulation of microbubbles after bolus end (Figure 4-31 B1-2).

It is visible from the videos stills in Figure 4-31 A1 that the magnet considerably deflects the microbubbles; quantification in Figure 4-31 A2 indicates that the magnet shifts the concentration peak of the bolus by 3.33 mm towards the surface of the clot, compared to 0.78 mm in the previous setup. Moreover, the video stills in Figure 4-31 B1 show the accumulation of magnetic material on the surface of the clot after bolus end, corresponding to a 5-fold increase in greyscale intensity in the focal region (Figure 4-31 B2).

This analysis confirms that the new magnetic targeting system produces high microbubble retention, and that it is confined to the surface of the clot.

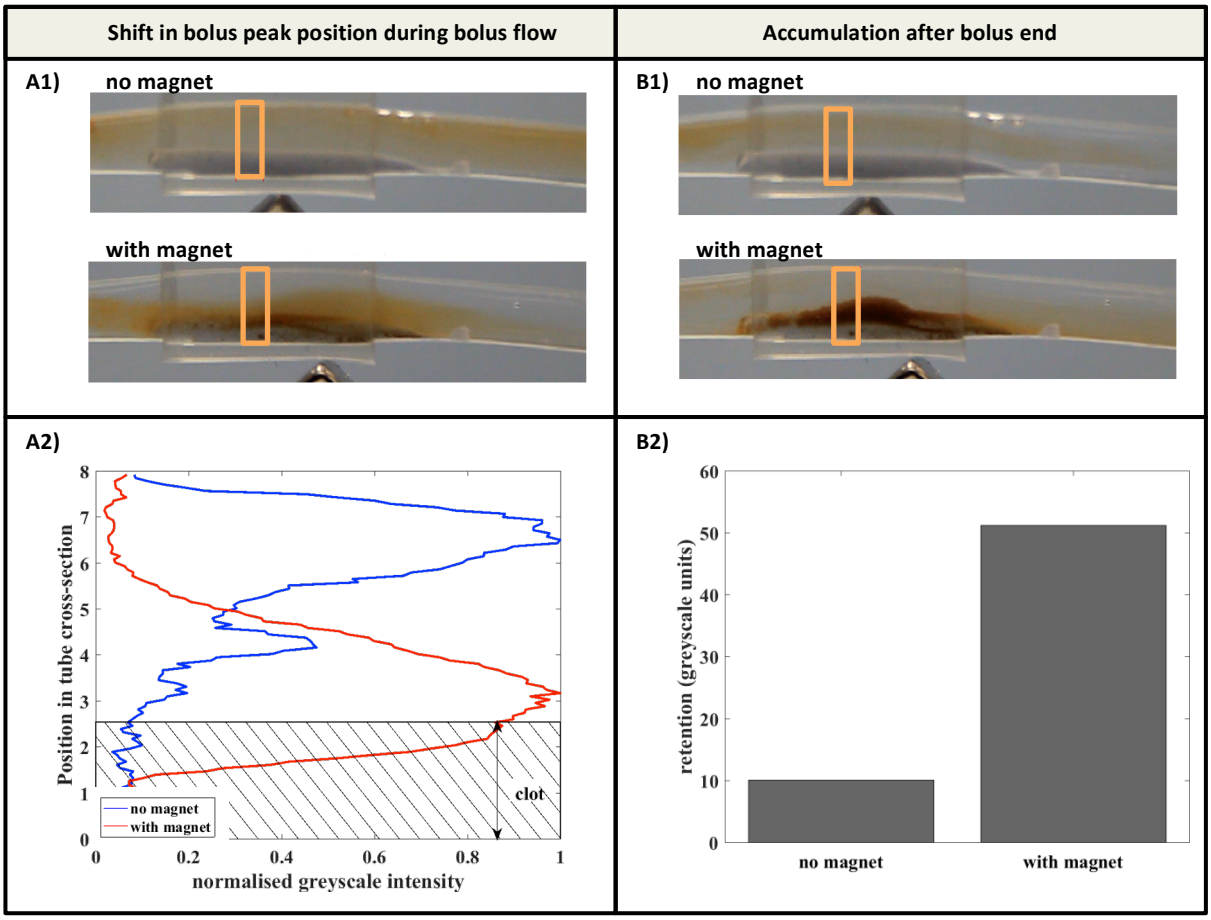


Figure 4-31: Effect of the new magnetic targeting system on microbubble distribution: shift in bolus peak (A) and accumulation (B):

A1) Image of the focal region (orange rectangle) during bolus flow: still from the video at time $t = t_1 - 2s$, in the presence and in the absence of a magnet;

A2) Quantification of deflection: greyscale profile in the cross-section of the tube in the absence and in the presence of a magnet (blue and red lines respectively). The profiles were normalised to their maximum intensity (n = 1);

B1) Image of the focal region (orange rectangle) just after the end of bolus flow, in the presence and in the absence of a magnet;

B2) Quantification of retention: sum of greyscale values in the focal ROI after bolus end (n = 1).

Effect of the new magnetic targeting setup on lysis rates

Mechanical sonothrombolysis was carried out again inthe new magnetic targeting setup, with the parameters shown in Table 4-8. In the presence of microbubbles, there was minimal lysis (Figure 4-32, 1.6 ± 2.0 µm/min); in the presence of microbubbles, lysis was clearly visible, although highly variable and a great deal slower than in the previous experiments (8.4 ± 8.6 µm/min in the US + MBs group, and 7.7 ± 7.9 µm/min in the US + MBs + Magnet). The low rates of lysis may be attributed to the low pulse repetition frequency; it was chosen to maximise microbubble accumulation between ultrasound pulses, but it considerably reduced lysis.

There was no significant difference in lysis rates between the groups. Therefore in this new setup with enhanced microbubble accumulation and confinement to the clot surface, magnetic targeting did not enhance mechanical lysis either.

Parameter	Value
PBS flow rate	5.5 mL/min
Microbubble concentration	$5.9 \times 10^6 \pm 8.9 \times 10^4$ microbubbles/mL in PBS flow
Peak Rarefactional Pressure	1.5 MPa
Pulse repetition frequency	0.4 Hz
Duty cycle	0.4 %
Treatment time	30 minutes

Table 4-8: Experimental conditions in the investigation of sonothrombolysis with magnetically targeted microbubbles in new targeting system.

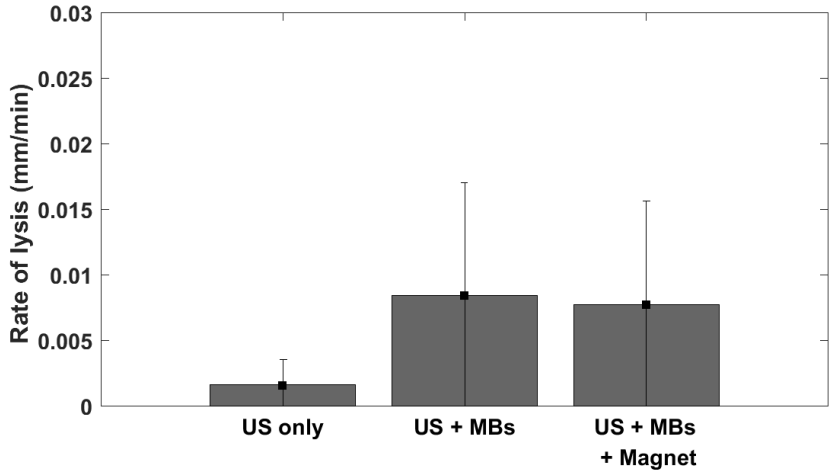


Figure 4-32: Lytic rates in the new magnetic targeting setup (single permanent magnet element) for the study of mechanical sonothrombolysis with magnetically targeted microbubbles (n = 6 in the US only group, n = 8 in the other two groups). The clots were treateted with 0.5 MHz ultrasound, 1.5 MPa peak rarefactional pressure, a 0.4 Hz pulse repetition frequency and a 0.4% duty cycle. Maximum depth of clot lysis was computed on photographs taken every 30 seconds during treatment, yielding the lytic rate. Error bars represent standard deviations from the mean.

Treatment monitoring

A very weak, but significant correlation was found between lysis rates and total cavitation dose in the 2-5 MHz range (Pearson's correlation coefficient $r = 0.45$, $p<0.05$).

Risk of downstream embolism

The particles in the effluent were sized to evaluate the risk of downstream embolism created by clot fragments larger than 10 µm, the diameter of small capillaries (Table ***4-9***). Over 99.18 ± 0.41% of particles was found to be smaller than 10 µm, and there was no statistically significant difference between the experimental groups. This indicates that mechanical sonothrombolysis with the chosen experimental conditions is safe.

Experimental group	Particles < 10 µm
US only	99.18% ± 0.41%
US + MB	99.55% ± 0.23%
US + MB + Magnet	99.69% ± 0.15%

***Table** 4-9: Proportion of particles smaller than 10 µm in effluent during mechanical sonothrombolysis of whole porcine blood clots with magnetically targeted microbubbles. The clots were treated for 30 minutes with 0.5 MHz ultrasound (direction of propagation: black arrows), 1.5 MPa peak rarefactional pressure, a 0.4 Hz pulse repetition frequency and a 0.4% duty cycle. Particles were analysed by a laser diffraction particle sizer.*

Histological analysis

The high variability in macroscopic damage (i.e., lysis depth measured on the digital images) coincides with a wide range of effects on clot microstructure, as illustrated by the histological samples in Figure 4-33. In clots treated with ultrasound and microbubbles, three distinct outcomes were observed:

- no macroscopic damage, associated with minimal pitting of the clot surface (b1)
- some macroscopic lysis, surprisingly accompanied by extensive microscopic damage in the shape of deep channels and cavities below the surface of the clot (b2 and c1). Closer inspection (inset in b2) reveals that these regions are not only depleted in erythrocytes, but that fibrin is also largely absent[6].
- macroscopic lysis, associated with a thick layer of erythrocyte-depleted fibrin matrix , and minimal fibrin breakdown (c2).

Interestingly, the nature of the damage observed in the US + MB group differs slightly from the US + MB + Magnet group: the "tunnels" are smoother and more continuous in the presence of a magnet. The hypothesis that different mechanisms intervene in both groups warrants further investigation. Clots treated with ultrasound only (Figure 4-33 a), on the other hand, did not incur visible damage, and the position of the HIFU focus could not be located with precision.

[6] Fibrin is an acidophilic polymer, stained pink by eosin [301].

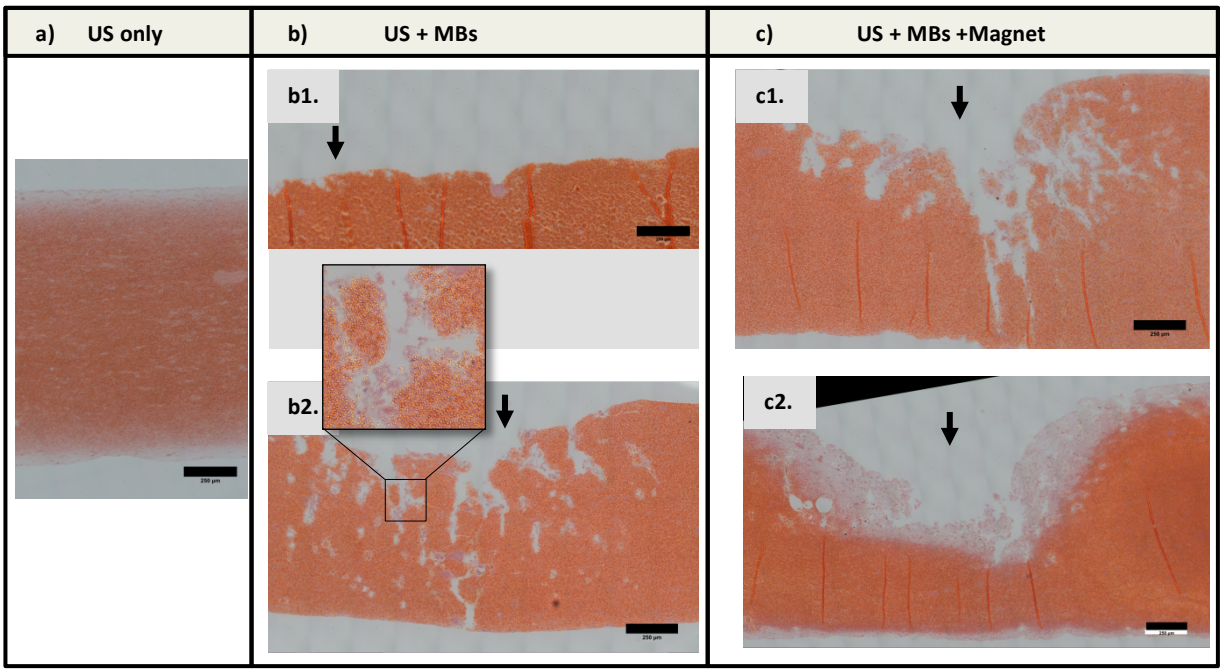


Figure 4-33: Histological samples of porcine clots after magnetically targeted mechanical sonothrombolysis. The clots were treated for 30 minutes with 0.5 MHz ultrasound (direction of propagation: black arrows), 1.5 MPa peak rarefactional pressure, a 0.4 Hz pulse repetition frequency and a 0.4% duty cycle. The clots were fixed in formalin, embedded in paraffin and stained with eosin and haematoxylin. Inset: zoom on a damaged area. Scale bar: 250 µm.

By describing three possible outcomes for clots treated with ultrasound and microbubbles, these observations add new elements to a recent study by Petit *et al.*, who reported erythrocyte depleted regions with a substantial compression of the fibrin mesh, but no lysis of the fibrin strands after sonothrombolysis at 1 MHz and 350 kPa peak-negative pressure [240].

These findings therefore shed light on the microscopic effects of ultrasound and microbubbles on blood clots. Clinically, they indicate that even in the absence of extensive thrombolysis, ultrasound and microbubbles can contribute to vessel recanalisation by enhancing thrombus porosity.

The underlying mechanisms have, however, not been fully clarified. They will be further discussed in Chapter 5, along with possible reasons for the variability in microscopic structures.

4.3.9. Clinical implications

Mechanical sonothrombolysis: feasibility and variability

The experiments in this chapter were carried out in the absence of any fibrinolytic drugs. A high proportion of the acute ischaemic patient population is ineligible for tPA administration [14], warranting the study of purely mechanical sonothrombolysis. Preliminary clinical studies have shown that early arterial recanalisation is on average accelerated with ultrasound and microbubbles, and a randomised controlled trial is currently underway [47]. Yet as this treatment is less effective than enzymatic sonothrombolysis (with tPA) [23], it has been the subject of much fewer *in vitro* and *in vivo* reports.

In vitro studies vary greatly in their assessment of treatment feasibility. There is wide agreement that mechanical sonothrombolysis is more effective on average than controls (no tPA, no ultrasound), but the difference is not significant in all studies [23], [32], [34], [37]. Such discrepancies are possibly due to the range of frequencies used. In this study with mid-frequency ultrasound (0.5 MHz), no lysis was observed with US alone, and a rapid acceleration in lysis was observed with US and microbubbles. This study thus establishes that mechanical sonothrombolysis is feasible at this frequency, and that it leads to rapid clot lysis (on the order of 30 µm/min) in the presence of sufficient microbubble concentrations.

In the absence of microbubbles, mechanical sonothrombolysis has been shown to be possible only at much higher pressures (≥6 MPa at 1 MHz) [86].

It is worth noting that *in vivo* sonothrombolysis without tPA administration may be further aided by the release of endogenous rtPA by the endothelium at the site of thrombosis [241].

Lysis rates were highly variable in all groups treated with microbubbles. Petit *et al.* reported similar observations (±100% variability in lysis rates) in human whole blood clots treated with 1.6 MHz ultrasound and a commercial microbubble agent in the absence of tPA. All other experimental groups had lower variability, both in absolute and in relative terms [37]. The sources of such variability remain unclear. In the discussion in paragraph 4.3.5, clot origin, age, and gas content have been ruled out as the main sources of variability. Variability in microbubble concentration, size and acoustic properties did not account either for the observed variability in lysis rates.

Treatment monitoring

A secondary objective of this study was to assess the acoustic emissions in the 2-5 MHz frequency range as an indicator for monitoring lytic efficacy. As expected, cavitation dose was markedly enhanced when microbubbles were present (Figures 4-23, 29, and 33). However no strong correlation between lysis rates and acoustic emissions could be established (Figure 4-24). Therefore total cavitation dose in the 2-5 MHz range does not appear to be a robust monitoring indicator for mechanical sonothrombolysis. The conclusions were unchanged when quantifying the emissions in specific frequency ranges (data not shown, emissions in the ultraharmonic or broadband frequency range). This important point will be further discussed in the following chapter.

Applicability of the clot model

The clot model used in this study is a retracted blood clot, which best approximates platelet-rich thrombi. These retracted clots have denser fibrin networks than unretracted clots, but the diameter of their fibers are similar. They are also more difficult to lyse with tPA (with or without ultrasound) than unretracted clots [35]. Marder *et al*. performed histological analysis on clots retrieved from the cerebral arteries of acute ischaemic stroke patients and showed that 75% of the clots comprised platelet-rich regions. The clots were however highly heterogeneous in their architecture, unlike the present clot model. The authors also reported that the mean diameter of the clots in the middle cerebral artery (1.8 ± 0.8 mm) was similar to the clots used in this study [242].

The flow chamber reflects a model of a partial arterial occlusion widely used in the literature [37], [53], [99]. As discussed in the previous chapter, such configurations occur frequently, though they are less common than full arterial occlusions [194]. The model provides however a satisfactory setting to compare targeted and non-targeted treatments.

4.3.10. Limitations of the study

Microbubble formulation

During microbubble preparation, the ferrofluid was added in great excess, resulting in the presence of a large quantity of magnetic micro-droplets which are difficult to separate from the microbubbles for sizing and for injection. This limits the reliability of microbubble characterisation techniques. It also implies that the magnetic targeting experiments measure the behaviour of both microbubbles and droplets. On the other hand, the ferrofluid is not expected to nucleate cavitation, as discussed in greater detail in Chapter 5. However, improving the microbubble formulation was beyond the scope of this project. Recently, Owen *et al*. have developed novel lipid-shelled magnetic microbubble formulations that overcome this difficulty by replacing the isoparaffin-based ferrofluid by an aqueous suspension of iron oxide nanoparticles [208].

Statistical significance

For the reasons detailed in paragraph 4.3.5.a), each series of experiment was carried out with blood clots sourced from a single individual. However, the trend of response to sonothrombolysis was consistent across the various experimental series, and with previously published data [23], [32], [37]. Therefore the conclusions drawn from single-individual data are expected to be generally applicable.

A more important limitation is the size of the experimental groups. Statistical evaluation of magnetically targeted versus non-targeted microbubbles was carried out on relatively low sample numbers (n = 5 or 6), though they are in line with most published reports in the field [37], [53], [56]. Due to the limited availability of clot samples, the secondary control groups (US only) include particularly few replicates (n=3). They were however consistent across experimental series, and they were not expected to yield significant clot lysis.

4.4. Conclusion

The present chapter has demonstrated that mechanical sonothrombolysis is achievable at 0.5 MHz in the presence of microbubbles and that its rate is positively correlated with microbubble concentration. It has also confirmed that magnetic microbubbles can be successfully manipulated to increase microbubble concentration at the target site. Despite promising preliminary findings, magnetic targeting in the present system was not found to be associated with a significant acceleration in mechanical sonothrombolysis. This could be attributed to one or several of the following factors: (i) highly variable mechanical lysis rates, which make it difficult to obtain any statistically significant results; (ii) limitations in the design of the magnetic targeting setup, leading to insufficient retention of microbubbles, or to retention away from the region of interest (doesn't apply to section 4.3.8); (iii) microbubble shielding, which disrupts ultrasound propagation in the focal region when high concentrations of microbubble are present.

In addition, acoustic emissions during treatment did not provide a strong indicator of lysis progress. Lytic rates were found to be highly variable in the absence of thrombolytic drugs.

In the next chapter, magnetically targeted microbubbles are investigated in the context of tPA-enhanced sonothrombolysis.

CHAPTER 5

Enzymatic sonothrombolysis with magnetically targeted microbubbles

In the previous chapter it was found that magnetically targeted microbubbles did not consistently accelerate thrombolysis via mechanical erosion. In this chapter the effect of magnetically targeted microbubbles on sonothrombolysis in vitro in the presence of tissue plasminogen activator is investigated. First the effect of a new magnetic targeting system on microbubble distribution is examined. The efficacy of the targeted microbubbles for sonothrombolysis is then evaluated, and the feasibility of non-invasive treatment monitoring is assessed. Finally, treatment safety and lysis mechanisms are discussed.

5.1. Introduction

5.1.1. Motivation

In the previous chapter, it was found that magnetically targeted microbubbles did not significantly enhance mechanical sonothrombolysis, i.e., sonothrombolysis in the absence of fibrinolytic drugs. The next step was therefore to test whether magnetic microbubbles could produce any enhancement in enzymatic sonothrombolysis.

The mechanisms involved in the two treatments are likely to be different. Specifically, there is growing evidence that enzymatic sonothrombolysis is not merely the sum of two distinct processes, mechanical sonothrombolysis and tPA-induced fibrin lysis. Cintas *et al.* exposed human whole blood clots to-2 MHz ultrasound and noted that the lytic effect of galactose-based microbubbles and tPA was greater than the combined effect of each agent, suggesting a synergy between the fibrinolytic drug and the microbubbles [32].

Magnetically targeted enzymatic sonothrombolysis has been investigated with vehicles other than microbubbles. Torno *et al.* investigated ultrasound-sensitive polymer microparticles *in vitro* and demonstrated significant lysis enhancement in thrombi exposed to free tPA and 20 kHz ultrasound [135]. Whilst this report constitutes a valuable proof-of-concept for magnetically targeted enzymatic sonothrombolysis, the very low frequency used and the large diameter of the particles (20 μm on average) preclude safe clinical translation. Subsequently, smaller (< 5 μm) tPA-loaded carriers were developed, although the change in particle size affected their ultrasound sensitivity [182].

The objective of this chapter was therefore to investigate magnetically targeted microbubbles for enzymatic sonothrombolysis. These have the advantages of being biocompatible (both in terms of size and composition), highly ultrasound-sensitive, and well characterised [243]. In addition the feasibility of non-invasive acoustic methods for treatment monitoring is evaluated.

5.1.2. Structure of the study

After characterising the ultrasound field and the magnetic field in the setup (§ 5.3.1 and 5.3.2), microbubble retention at the treatment site was quantified (§5.3.3). The effect of the magnetically targeted microbubbles on lysis rates and acoustic emissions was then investigated (§ 5.3.4 and 5.3.5). Cavitation detection was evaluated as a treatment monitoring technique (§ 5.3.6), and the risk of downstream embolisation was assessed (§5.3.7). In addition, the effect of treatment on clot microstructure was examined (§5.3.8). The limits of the experimental setup (§ 5.3.9) and the clinical implications of the findings were then discussed (§ 5.3.10). Finally, the possible mechanisms involved in sonothrombolysis were reviewed (§5.4.).

5.2. Methods

5.2.1. Materials

All animal work was approved by an animal care and ethics review committee and conformed to the UK Animals (Scientific Procedures) Act 1986. Whole blood for clot preparation was obtained from the carotid artery of a female large white X landrace breed pig.

Fresh frozen plasma for the flow solution was prepared by collecting whole blood from the aortic artery of a female large white X landrace breed pig into citrated blood bags (CPDA-1, Fenwal Inc., Lake Zurich, IL, USA). The sample was then aliquoted into 50 millilitre centrifuge tubes which were spun at 4,400 rotations per minute in a 15 centimetre radius centrifuge for 20 minutes at room temperature to separate blood components. The plasma was stored at -80°C until use. It was defrosted in a 37°C incubation chamber for at least 15 minutes prior to experiments.

Phosphate-buffered saline was sourced from Sigma Aldrich (PBS, Sigma Aldrich Corporation, St Louis, MO, USA). Tissue plasminogen activator (Actilyse, Boehringer Ingelheim Pharma GmbH & Co. KG, Ingelheim am Rhein, Germany) was reconstituted in water to the concentration of 1 mg/mL and stored in 400µL aliquots at -80°C. Under these storage conditions, the enzyme is stable for up to a year [244], [245].

5.2.2. Experimental arrangement

The experimental setup is illustrated in Figure 5-1. It is similar to the arrangement described in the previous chapter, with the exception of the magnetic targeting system. Four experimental groups were considered: exposure to tPA only, US + tPA, US + tPA + non-targeted microbubbles, and US + tPA + targeted microbubbles.

5.2.3. Flow setup

A porcine whole blood clot was formed around a silk suture according to a protocol previously described by Petit *et al.* [37]. It was placed in an acoustically transparent flow chamber (3.2 mm diameter) maintained at 37°C.

A solution of dilute plasma (1.25% v/v fresh frozen plasma in phosphate-buffered saline) was circulated once through the chamber at a rate of 3 mL/min by a peristaltic pump (Minipuls 2, Gilson Inc., Middleton, WI, USA).

Lipid-shelled microbubbles were produced in-house and loaded with iron-oxide nanoparticles following the method reported in the previous chapter. These magnetic microbubbles were infused continuously, along with tPA, into the diluted plasma at a rate of 140 µL/min using a syringe pump (World Precision Instruments Ltd, Hitchin, UK). The final concentrations of tPA and microbubbles in the diluted plasma were 0.75 µg/mL and $8.1 \times 10^6 \pm 1.2 \times 10^5$ microbubbles/mL respectively.

5.2.4. Ultrasound exposure

The experimental apparatus for HIFU exposure is identical to the setup described in the previous chapter.

The clot was exposed for 60 minutes to pulsed high intensity focused ultrasound at 0.5 MHz (0.5 MHz HIFU transducer, Sonic Concepts, Bothell, WA, USA), with 5×10^4 cycle bursts and a 0.2 Hz pulse repetition frequency, corresponding to a 2% duty cycle.

The ultrasound field in the setup was characterised as in the previous chapter. Briefly, a fibre optic hydrophone (Precision Acoustics, Dorchester, UK) was inserted into the setup after removal of the clot and vessel, and a 6 mm x 6 mm x 6 mm volume was scanned. The peak rarefactional pressure at the focus was set to 630 kPa, close to the pressure used by Petit *et al*. in a recent study of enzymatic sonothrombolysis with non-targeted microbubbles with a similar experimental setup [37].

5.2.5. Magnetic targeting

The magnetic retention system used in this study (Figure 5-1) was adapted from the last targeting system investigated in the previous chapter (§4.3.8). Briefly, the magnetic field was applied using a single 12.7 mm cubic permanent magnet element (N52 grade NdFeB), with a measured magnetisation value of 1.09×10^6 A/m. The magnet element was placed below the clot at an angle of 45^0, its upper vertex in contact with the flow channel directly below the HIFU focus. During experiments that did not involve magnetic targeting, the magnet was replaced by a stainless steel block of identical dimensions in order to maintain a comparable sound field.

Two improvements upon the previous system were therefore implemented: the PDMS sleeve was removed and the magnet was translated.

The magnetic field produced in the flow chamber was predicted using the numerical model described in the previous chapter (§4.2.4). The contribution of Dr. Lester Barnsley with this numerical model is gratefully acknowledged.

Accumulation of magnetic material in the flow chamber was also quantified. To facilitate visualisation of the dark brown microbubble solution, the clot was replaced by a light-coloured phantom of the same dimensions. A 1 mL bolus was injected into the PBS flow and images were acquired at 30 frames/s with a digital camera (Canon EOS 500D, Canon Ltd., Reigate, UK). The photographs were processed with purpose-written code in Matlab (The MathWorks Inc., Natick, MA, USA) to quantify retention of magnetic material over 12 seconds. In each frame, the region of interest (ROI) was defined as a 3-mm wide window around the axis of the HIFU transducer. An image of the microbubble solution was obtained by subtracting from each frame a baseline photograph acquired before microbubble injection. NR(t), the "normalised retention" at a given time point t was defined as the total greyscale intensity in the ROI at this time point, divided by the total greyscale intensity in the ROI at t=0:

$$N_R(t) = \frac{I(t)}{I\,(0)} \qquad (24)$$

where I(t) is the total greyscale intensity in the ROI at time t.

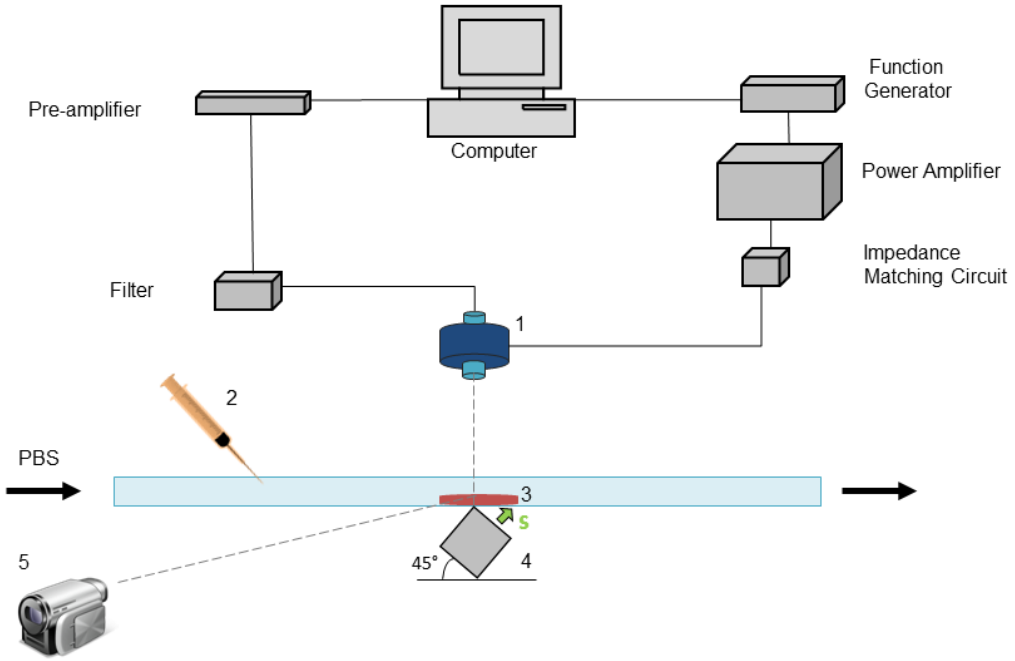


Figure 5-1: Overview of the experimental setup. The clot (3) is placed in a flow chamber under dilute plasma flow (1.25% v/v in PBS). tPA and microbubbles are continuously delivered into the flow by an infusion pump (2). A magnet (4) ensures magnetic retention of the microbubbles at the clot site. Ultrasound exposure and acoustic monitoring are performed by coaxial HIFU and PCD transducers (1). Lysis progress is monitored using a digital camera (5).

5.2.6. Data acquisition and processing

Clot lysis

Lysis progress was assessed from the changes in clot diameter throughout treatment. Images of the clot were captured every 30 seconds using a digital camera. Clot outlines were detected off-line using custom-written code in Matlab, and the maximum depth of clot lysis was computed at each time point. Linear regression on the depth of lysis over the 60 minutes of treatment yielded the overall lytic rate. In the group with magnetic targeting, magnetic material accumulated near the clot until it obstructed the focal region, so the regression was limited to the period before full obstruction. Full details on image processing are provided in the previous chapter.

Cavitation detection

Acoustic emissions in the focal region were monitored using a passive cavitation detection (PCD) setup, comprising a 2 MHz high pass filter (Allen Avionics Inc., Mineola, NY, USA), a x25 pre-amplifier (SR445A, Stanford Research Systems, Sunnyvale, CA, USA), and a focused 7.5 MHz ultrasound transducer mounted coaxially with the HIFU transducer (Panametrics V320-SU, Olympus Inc., Waltham, MA, USA). The first 2 ms of each 100 ms pulse were then acquired at 10^8 samples per second in a binary file using a data acquisition card and control software written in LabView (National Instruments, Austin, TX, USA). As the microbubbles are constantly replenished in the flow chamber, cavitation is expected to be consistent throughout treatment. Signal acquisition was therefore triggered for every 10^{th} burst in order to reduce data volume.

The acoustic emissions recording during each burst were processed in a similar way to Chapter 4 (§ 4.2.8), as follows:

a) The first 90 µs of the burst were discarded to account for the acoustic time of flight from the HIFU transducer to the focal region and back to the PCD transducer.
b) The signal was zero padded and windowed using a Hann window. Its power spectral density was derived by Fast Fourier Transform.
c) The total the power spectral density detected in the 2-5 MHz frequency range was computed.
d) Cavitation dose in the 2-5 MHz range was computed by integrating the power spectral density over the corresponding frequency range.
e) Cavitation dose in the ultraharmonic range was computed by integrating the power spectral density over six consecutive frequency bands containing ultraharmonics (odd multiples of half the driving frequency) with central values ranging from

2.25 MHz to 4.75 MHz and widths of 25 kHz, which is of the order of the -3dB bandwidth of the driving transducer.

f) Similarly, cavitation dose in the broadband range was computed by integrating the power spectral density over six consecutive frequency bands located well away from harmonic and ultraharmonic peaks, with centres in the 2.375-4.875 MHz range and widths of 25 kHz.

Finally, the cavitation doses computed for each burst were summed over the whole duration of treatment. Each cavitation dose (total, ultraharmonic, broadband) has units of V^2 and is proportional to the acoustic energy detected in the corresponding frequency range within the focal region of the PCD.

Debris analysis and histological analysis

Particle sizing and histology were carried out following the protocols described in Chapter 4 (§ 4.2.9 and 4.2.10 respectively).

5.2.7. Statistical analysis

Differences among experimental groups were analysed in Matlab using two-way ANOVA, with post hoc Tukey HSD testing for multiple comparisons between groups. Statistical significance was defined as $p<0.05$ (noted with * in the figures). Data with greater significance ($p<0.01$) was noted with **.

5.3. Results and discussion

5.3.1. Ultrasound field characterisation

The ultrasound field in the vessel was characterised with a fibre optic hydrophone. The transverse ultrasound field, parallel to the upper vertex of the magnet (y direction) has the same shape as in the free field (Figure 5-2 a.). The axial scan (Oxz plane) reveals the formation of partial standing waves (Figure 5-2 b.), with variations of ±25.9% in peak rarefactional pressure along the axial direction.

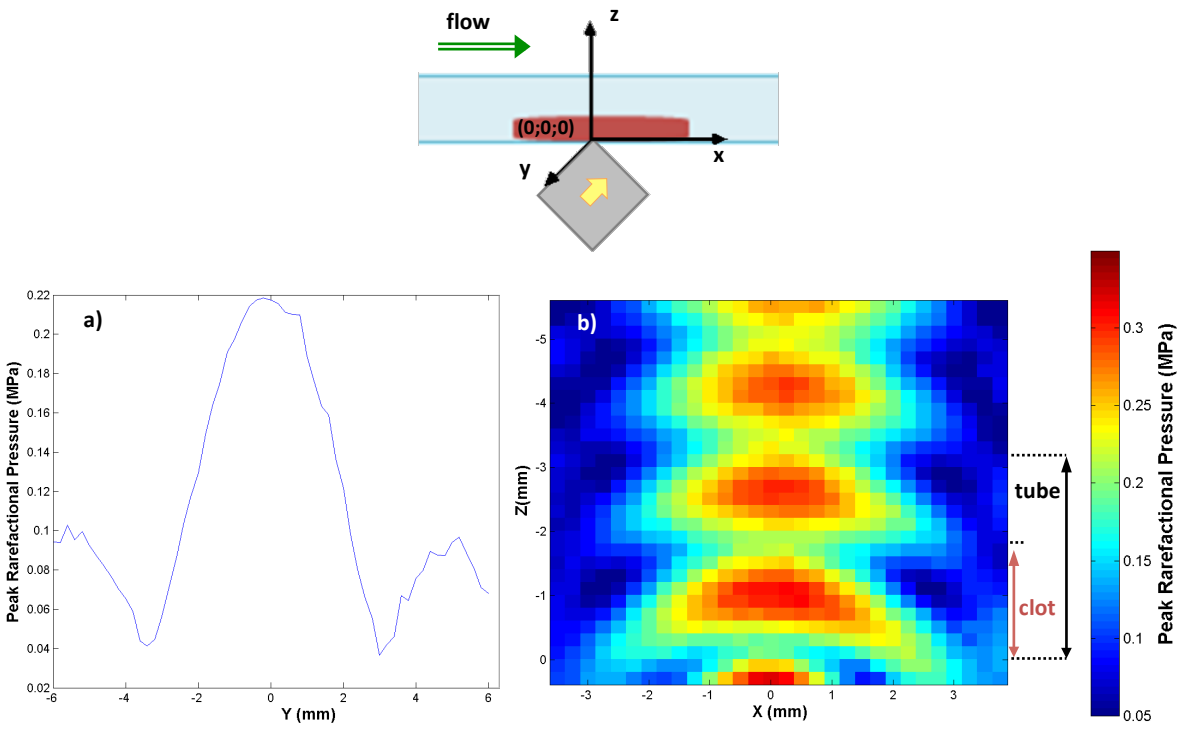


Figure 5-2: Map of the sound field created by the HIFU transducer in the focal region. a) in the transverse direction; b) in the axial plane. Calibrations scans were carried out with a fibre optic hydrophone in a water bath maintained at 37°C. Focal pressure was set to 220 kPa. Inset (above): origin, orientation of the axes, and magnetisation vector (yellow arrow).

5.3.2. Magnetic field characterisation

A numerical simulation was performed to map the magnetic field and the magnetic field gradient in the vessel. As expected, the magnitudes of both fields were symmetrical about the Oxz plane (data not shown) but not about the Oyz plane (Figure 5-3), because of the orientation of the magnetisation vector. The magnet achieved strong fields and steep gradients within the vessel. Both decreased rapidly with increasing distance from the upper vertex of the magnet. In the Oxz plane, the magnitude of the magnetic field was in the 2.5-93 $\times 10^{-2}$ T range; the magnitude of the magnetic field gradient was in the 11-34000 T range. For comparison, the respective ranges for the first iteration of the magnetic targeting system in the previous chapter (with the Halbach array) were 3.2-11.0 $\times 10^{-2}$ T and 4.7-17.2 T/m. It must however be noted that the numerical model breaks down in a region less than about 1 mm away from the magnet surface. This is due to the approximation of the magnetic medium as a lattice of evenly distributed point dipoles, which is no longer valid in short range. In addition, the region of the Oxz plane defined by $Z < 1.7$ mm is occupied by the clot, and no microbubbles can be present. Magnetic targeting takes place in the free space, where the magnetic conditions were less extreme, though the values remained high: 2.5-27 $\times 10^{-2}$ T for the magnetic field and 11-85 T/m for the magnetic field gradient.

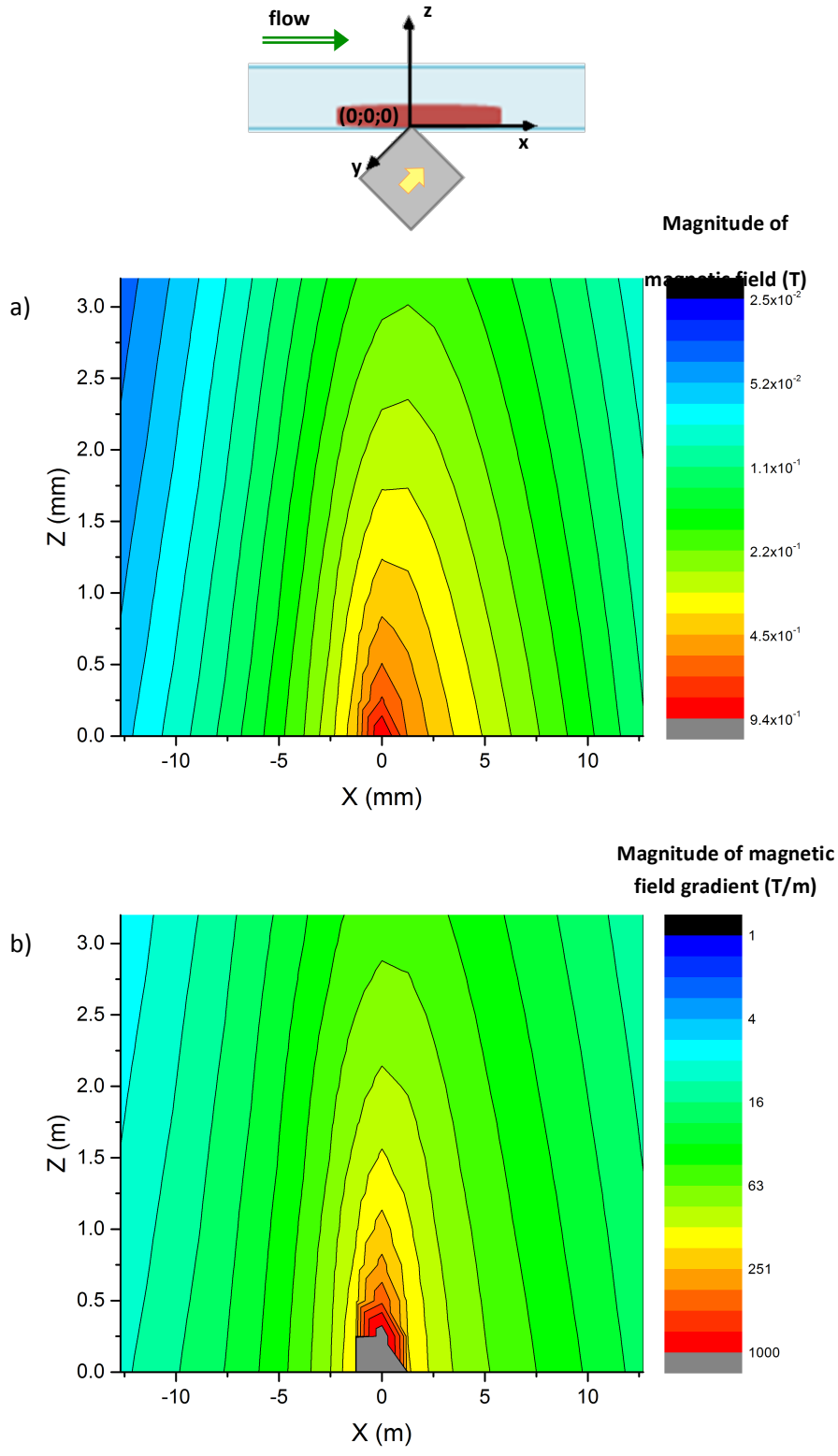


Figure 5-3: Simulations of the magnetic conditions created by the magnet in the axial plane of the flow chamber; a) magnitude of magnetic field; b) magnitude of magnetic field gradient. Inset (above): origin, orientation of the axes, and magnetisation vector (yellow arrow).

5.3.3. Microbubble retention

The new magnetic targeting system provides appreciably improved control over microbubble location. Figure 5-4 shows the experimental setup after injection of a bolus of microbubble stock solution (brown suspension) into the flow, past a clot phantom (blue cylinder). In the absence of a magnet and of ultrasound exposure (Figure 5-4 a.), the microbubbles float to the top of the flow chamber and do not come into contact with the clot phantom. In the presence of a magnet (Figure 5-4 b.), the magnetic material accumulates in a narrow region (~3 mm-wide) that coincides with the focus of the HIFU transducer. As the clot is narrower than the tube, Figure 5-4 c. shows that some magnetic material collects at the bottom of the flow chamber on either side of the clot, where therapeutic efficacy is limited. Despite this, a substantial proportion of the magnetic material accumulates at the target site, directly on top of the clot.

The proportion of microbubbles retained in this system is quantified in Figure 5-5. In the absence of a magnet, the total greyscale intensity remained constant in the focal region over the period of observation, indicating no change in the amount of magnetic material. On the other hand, total greyscale intensity increased rapidly in the presence of a magnetic field (approximately two-fold increase in ten seconds), confirming a large increase in local concentration.

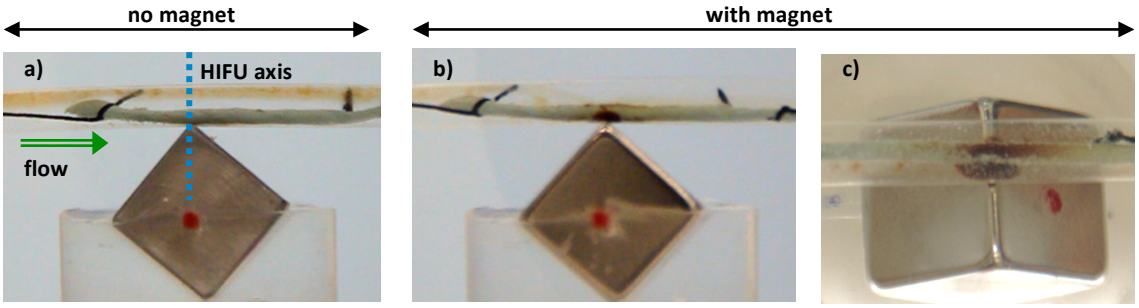


Figure 5-4: Evidence of magnetic microbubble retention in the experimental setup. Magnetic microbubbles (brown suspension) flowing past a model clot (light blue cylinder) in the absence and in the presence of a magnet. a) and b) are front views; c) is a top view.

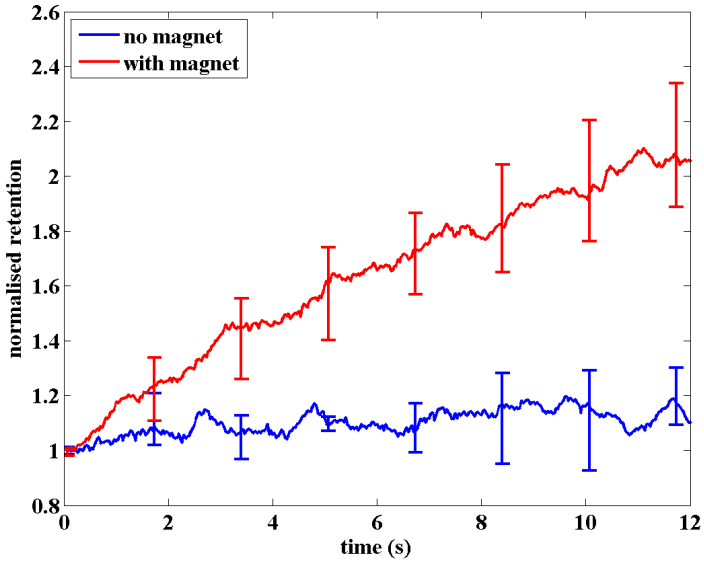


Figure 5-5: Accumulation of magnetic material in the focal region over 12 seconds with (red line) and without (blue line) magnetic targeting (n =3). A 1 mL bolus of the microbubble stock solution was injected into the flow and images were acquired at 30 frames/second. Normalised retention at a given time point t is defined as the total greyscale intensity in the ROI at this time point, divided by the total greyscale intensity at t = 0. Error bars represent the range of values observed.

5.3.4. Lysis rates

Maximum depth of clot lysis was measured every 30 seconds over the 60 minutes of treatment. Linear regression was carried out on the maximum depth of lysis; in the group with magnetic targeting, accumulated magnetic material obstructed the field of view yielded rates of lysis with an acceptable fit ($R^2 = 0.75 \pm 0.3$). In the two experimental groups involving microbubbles, the linear fit was very good ($R^2 = 0.95 \pm 0.04$).

Figure 5-6 shows the rates of lysis in all four experimental groups. Negligible lysis was observed in the clots treated with tPA only or with tPA + US (1.3 ± 1.4 µm/min and 2.9 ± 2.8 µm/min respectively). Lysis rates were substantially increased in the presence of non-targeted microbubbles (11.2 ± 4.1 µm/min, non-significant)[7]; they were further accelerated (x 3.3 on average) with magnetic targeting (36.6 ± 23.4 µm/min, $p<0.05$).

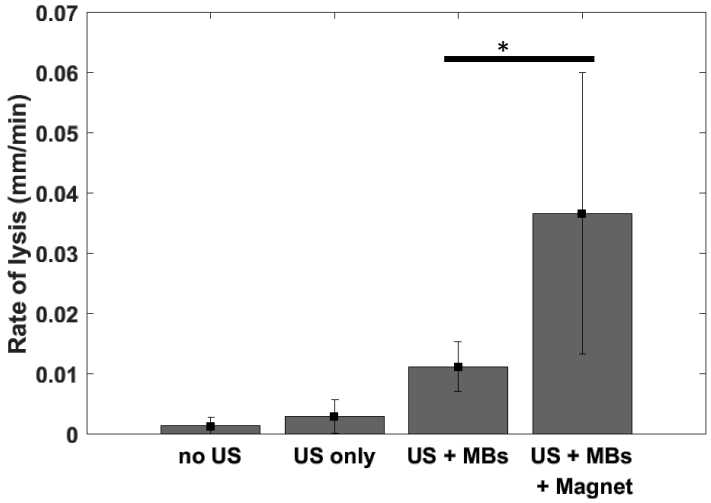


Figure 5-6: Lytic rates in enzymatic sonothrombolysis with magnetically targeted microbubbles (n=6). The clots were treated with tPA (0.75 µg/mL), 0.5 MHz ultrasound, 630 kPa peak rarefactional pressure, a 0.2 Hz pulse repetition frequency and a 2% duty cycle. Maximum depth of clot lysis was computed on photographs taken every 30 seconds during treatment, yielding the lytic rate. Error bars represent standard deviations from the mean. Significance (* = p<0.05) was calculated by ANOVA with Tukey post hoc test.

[7] Despite the considerable difference in lysis rates between the US only and the US + MBs group, it was not statistically significant (p = 0.67). This is attributed to … the variability in the US + MBs + Magnet group. In the Tukey HSD test, the "honestly significant difference" criterion takes into account the mean square within groups value, which is very large.

The fact that the drug alone did not produce significant lysis is attributable to the low concentration of tPA (0.75 µg/mL) compared to clinical doses and the relatively short time frame of the experiment. tPA breaks down fibrin in two stages: it activates the plasminogen present in the clot into plasmin, a fibrinolytic enzyme which then cleaves the fibrin fibres. Both the rate of plasminogen activation and the total rate of lysis increase with tPA concentration [246], [247]. The beginning of fibrinolysis at this tPA concentration were further examined microscopically (see Appendix B). Confocal imaging of the receding lysis front in a fluorescently-labelled plasma clot yielded an average lysis initiation time[8] of 23 minutes at 0.75 µg/mL, compared to 17 minutes at 1.5 µg/mL, and over 43 minutes at 0.25 µg/mL. After lysis initiation, the rate of lysis was also higher at 1.5 µg/mL than at 0.75 µg/mL. These microscopic data, albeit in a different clot model (unretracted clots are more susceptible to enzymatic fibrinolysis than retracted clots [35]), shed light on the observations in the control group (tPA only).

Even at such a low concentrations of tPA, substantial lysis acceleration occurred with ultrasound and non-targeted microbubbles. This is in agreement with previous studies that reported the possibility of lowering administered drug doses with ultrasound and microbubbles [37], [40]. For instance, Brown *et al.* demonstrated *in vitro* that with pulsed 1 MHz ultrasound and albumin/dextrose microbubbles, tPA concentration could be reduced up to five times while maintaining thrombolytic efficacy [40]. Such results are encouraging in terms of patient safety, as lower doses of tPA could reduce the risk of intracranial haemorrhage in acute stroke management.

The results from the magnetically targeted treatment group validate the initial hypothesis of this study and demonstrate the strong potential of magnetically targeted microbubbles to accelerate enzymatic sonothrombolysis.

[8] Defined as the first time point at which lysis is strictly greater than zero.

Other targeting methods

Comparing these promising results to other targeting methods is difficult. Whereas various microbubble targeting strategies have been investigated both *in vitro* and *in vivo* [26]–[28], [125], [140] and have been found to enhance lytic rates compared to tPA alone or tPA + US controls, few published studies have compared targeted and non-targeted microbubbles. Yet when considering clinical translation, this comparison is crucial to justify the use of targeting. This may be due to the fact that, to the author's best knowledge, all studies to date have investigated biological means of microbubble targeting, where non-targeted and targeted microbubbles must have slightly different formulations, and thus possibly different properties. For instance, changes in composition would modify shell viscosity and elasticity, affecting in turn the cavitation behaviour of the microbubbles [116], [248]. Alonso *et al.* compared the lytic efficacy of platelet-specific immunobubbles to non-specific immunobubbles in rats treated with pulsed 2 MHz ultrasound, and noted that plasma D-dimer levels were higher for animals treated with specific immunobubbles than in the non-specific control group. Histological analysis also showed clear disintegration of the clot in four out of five clots in the platelet-specific immunobubble group, compared to one out of five in the non-specific group [26]. Xie *et al.* investigated another type of platelet glycoprotein IIb/IIIa–targeted microbubbles in a porcine model of anterior descending artery thrombosis in the presence of recombinant prourokinase, a fibrinolytic drug. Compared to "nude" microbubbles, targeted microbubbles were associated with significantly greater replenishment of contrast agents in the at-risk area of the myocardium after 15 minutes of treatment [27].

Other (non-microbubble) targeted agents have also been evaluated in enzymatic sonothrombolysis. Holland *et al.* have developed fibrin-targeted, tPA-loaded echogenic liposomes [181]. These liposomes provide targeted contrast enhancement for diagnostic imaging of *in vivo* thrombi [132]; in combination with 120 kHz ultrasound, they have been shown to be more effective at lysing thrombi *in vitro* than free tPA + US. However, recent *in vitro* studies have demonstrated that sonothrombolysis with these liposomes was significantly less effective than with free tPA and commercial perfluorocarbon microbubbles. In order to improve the efficacy of the liposomes, future formulations may encapsulate a high molecular weight gas [249].

As discussed in Chapter 2, the main advantage of magnetically targeted microbubbles over these biological approaches is their long working distance: magnetically targeted microbubbles do not need to be initially in contact with the clot to accumulate at the target site.

5.3.5. Acoustic emissions

The acoustic emissions from the focus were monitored throughout treatment.

Figure 5-7 shows the dose detected in three frequency ranges: in the 2-5 MHz range, the ultraharmonic emissions (odd multiples of half the driving frequency), and broadband emissions.

In all three frequency ranges investigated, the use of microbubbles was associated with a significant increase in acoustic emissions over the US only group ($p<0.01$). In addition, there was a significant increase in acoustic emissions with targeted microbubbles over non-targeted microbubbles ($p<0.01$). This validates the hypothesis that magnetic targeting enhances cavitation energy in the focal region by increasing the concentration of cavitation nuclei.

It must also be noted that the cavitation dose detected is much lower than in the previous chapter (Figures 4-23, 29, *33*), as the pressure and total number of pulses applied are lower.

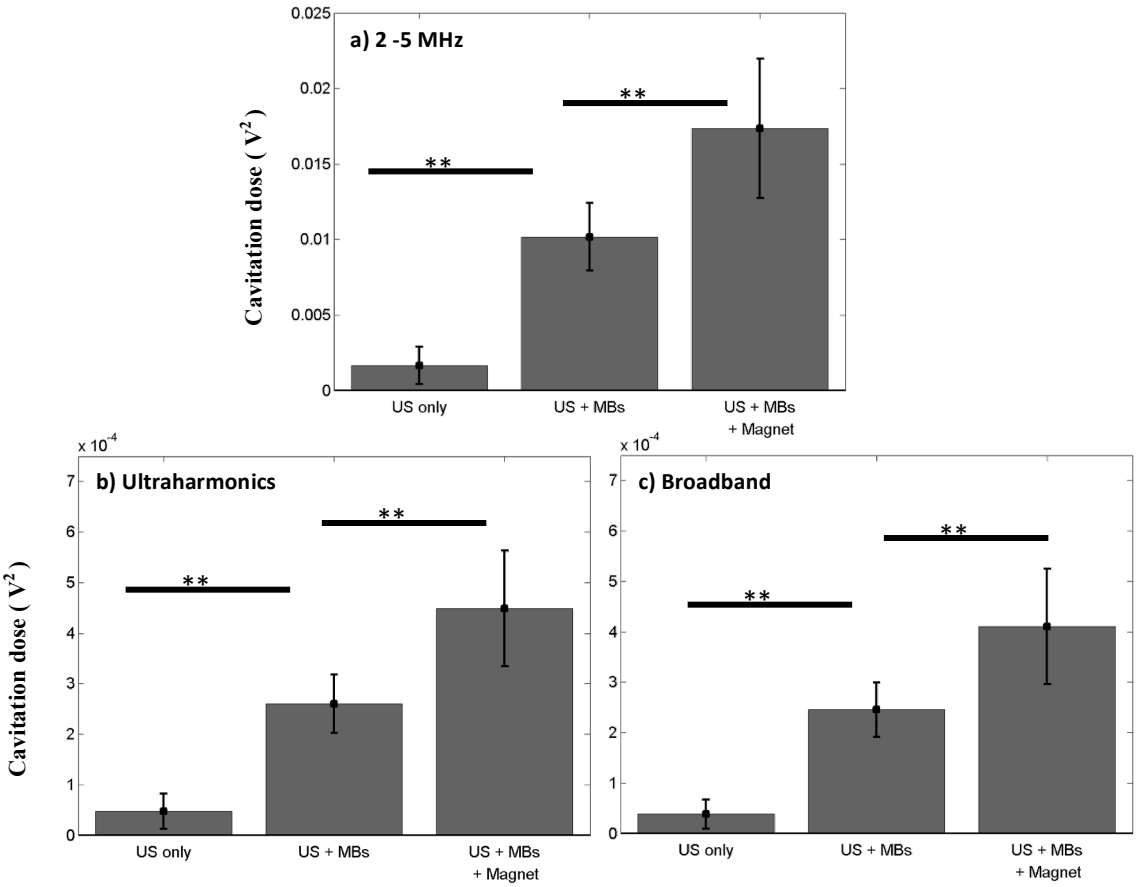


Figure 5-7: Cavitation dose detected during enzymatic sonothrombolysis of retracted porcine clots with magnetically targeted microbubbles (n = 6). The clots were treateted with tPA (0.75 µg/mL), 0.5 MHz ultrasound, 630 kPa peak rarefactional pressure, a 0.2 Hz pulse repetition frequency and a 2% duty cycle. The acoustic emissions at the focus were acquired with a 7.5 MHz PCD transducer mounted coaxially with the HIFU transducer. Error bars represent standard deviations from the mean: a) total dose in the 2 – 5 MHz frequency range; b) ultraharmonic dose in the in the 2 – 5 MHz frequency range; c) broadband dose in the in the 2 – 5 MHz frequency range.
Significance (** = p<0.01) was calculated by two-way ANOVA with Tukey post hoc test.

5.3.6. Lysis monitoring

Acoustic emissions in the focal region were investigated as an indicator for treatment success. Lysis rates were plotted against acoustic emissions in all three frequency bands of interest (Figure 5-8). Acoustic emissions were found to increase with lysis rates in all three cases, with good linear correlation ($R = 0.870$ and $p < 0.01$ in the 2-5 MHz range; $R = 0.866$ and $p < 0.01$ in the ultraharmonic range; $R = 0.873$, $p < 0.01$ in the broadband range).

All three frequency ranges were thus found to be equivalent indicators of lytic success. This contrasts with a previously study by Datta *et al.* The authors reported a strong correlation between final clot lysis and ultraharmonic emissions ($R = 0.83$, $p<0.001$) when exposing whole porcine blood clots to tPA, pulsed 120 kHz ultrasound and lipid-shelled microbubbles. At the pressures employed (320 kPa), however, most of the acoustic emissions occurred in the harmonic and ultraharmonic range, so no correlation was found between lysis and broadband emissions [23]. In the experiments presented here, the acoustic emissions occurred both in the ultraharmonic range and in the broadband range. These findings suggest that the value of broadband emissions as an indicator of lytic success strongly depends on the cavitation regime in the focal region. This is further discussed in §5.4.1, where the role of cavitation in lysis mechanisms is examined.

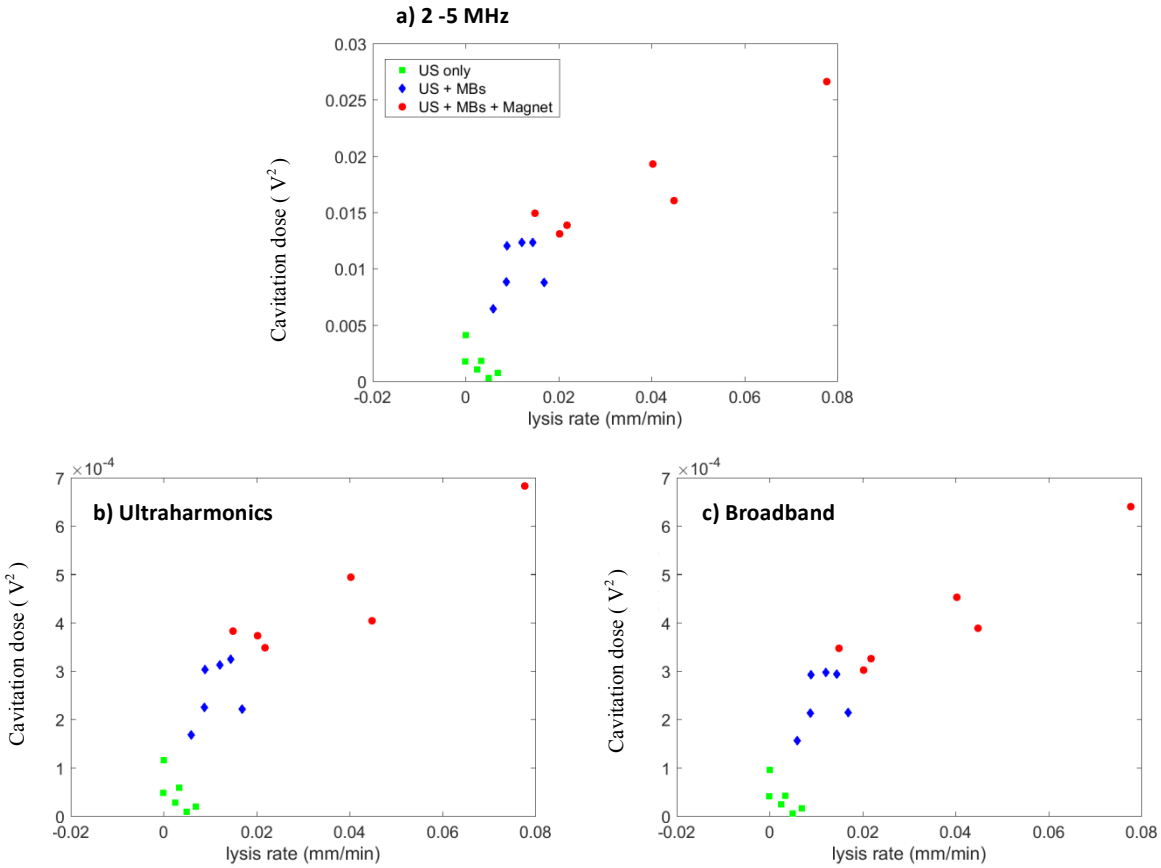


Figure 5-8: Bivariate representation of the lysis rates and the cavitation dose detected in different frequency ranges during enzymatic sonothrombolysis of retracted porcine clots (n=6). The clots were treateted with tPA (0.75 µg/mL), 0.5 MHz ultrasound, 630 kPa peak rarefactional pressure, a 0.2 Hz pulse repetition frequency and a 2% duty cycle. Maximum depth of clot lysis was computed on photographs taken every 30 seconds during treatment, yielding the lytic rate. The acoustic emissions at the focus were acquired with a 7.5 MHz PCD transducer mounted coaxially with the HIFU transducer.

a) total dose in the 2 – 5 MHz frequency range; b) ultraharmonic dose in the in the 2 – 5 MHz frequency range; c) broadband dose in the in the 2 – 5 MHz frequency range.

5.3.7. Safety

In order to assess treatment safety, the effluent was collected during treatment and analysed. Significantly fewer particles were present in the targeted group than in the non-targeted group (Figure 5-9). In the absence of a control with targeted microbubbles and no US, it is not possible to say whether the difference with targeting can be attributed to fewer clot fragments, or simply to the fact that more magnetic material remains trapped in the flow chamber.

Table 5-1 shows the proportion of these particles that were larger than 10 µm, approximately the diameter of a capillary. It did not significantly change between experimental groups, and in all cases, over 99.9% of the particles were smaller than the required size, indicating that the risk of downstream embolisation with this treatment is very low.

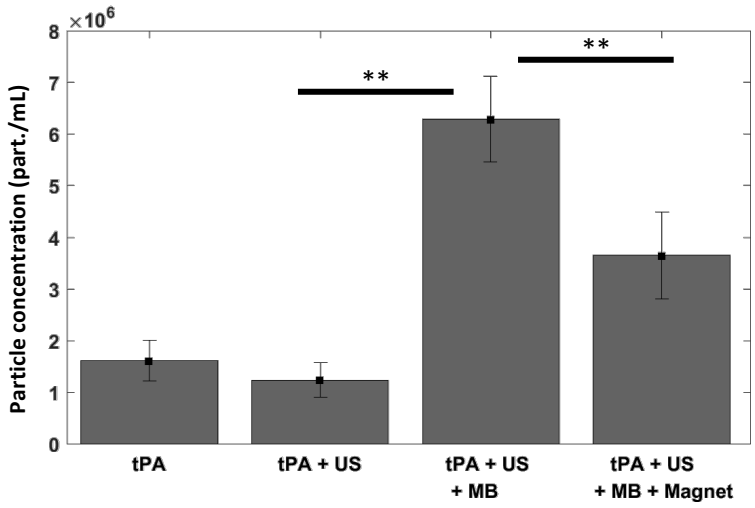


Figure 5-9: Concentration of particles in effluent during enzymatic sonothrombolysis of whole porcine blood clots with magnetically targeted microbubbles. The clots were treated with tPA (0.75 µg/mL), 0.5 MHz ultrasound, 630 kPa peak rarefactional pressure, a 0.2 Hz pulse repetition frequency and a 2% duty cycle. Particles were analysed by a laser diffraction particle sizer. Error bars represent standard deviations from the mean.
Significance (** =p<0.01) was calculated by two-way ANOVA with Tukey post hoc test.

Experimental group	Particles < 10 µm
tPA	99.96% ± 0.005%
tPA + US	99.93% ± 0.02%
tPA + US + MB	99.94% ± 0.02%
tPA + US + MB + Magnet	99.93% ± 0.02%

Table 5-1: Proportion of particles greater than 10 µm in effluent during enzymatic sonothrombolysis of whole porcine blood clots with magnetically targeted microbubbles. The clots were treated with tPA (0.75 µg/mL), 0.5 MHz ultrasound, 630 kPa peak rarefactional pressure, a 0.2 Hz pulse repetition frequency and a 2% duty cycle. Particles were analysed by a laser diffraction particle sizer.

5.3.8. Histological analysis

The effect of treatment on clot structure was investigated on eosin- and haematoxylin-stained clot samples (Figure 5-10). The surface of clots treated without microbubbles (Figure 5-10 a. and b.) was smooth. On the clot treated with tPA with US, it was not possible to identify with precision the focal region. In the samples treated with non-targeted microbubbles, the damaged region is ~2 mm wide, with a smooth surface and several small areas of erythrocyte depletion (Figure 5-10 c., direction of US exposure shown by the black arrow). Closer inspection shows that these cavities still contain fibrin. These observations are in agreement with a recent report by Petit *et al.* [240].

All of the samples treated with targeted microbubbles were entirely lysed at the HIFU focus after 60 minutes of treatment. Figure 5-10 d. shows the remaining clot fragments on either side of the lysed region. Numerous erythrocyte-depleted cavities with accumulation of magnetic material are present throughout the clot.

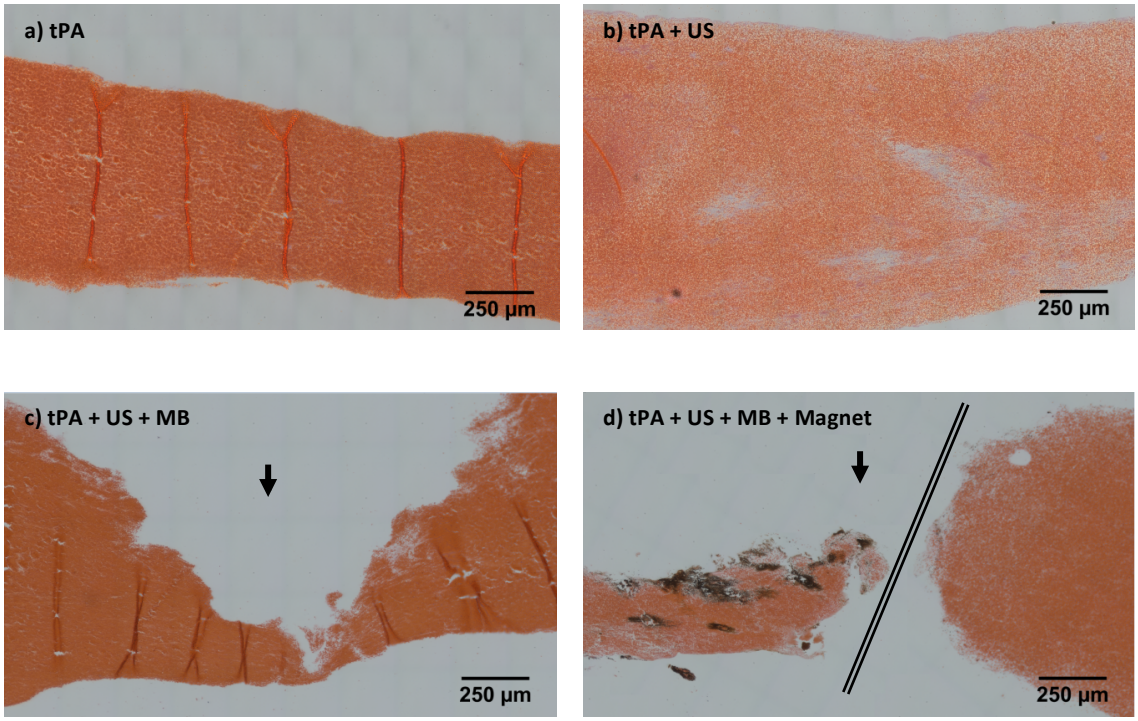


Figure 5-10: Histological samples of porcine clots after magnetically targeted enzymatic sonothrombolysis. The clots were treated for 60 minutes with tPA (0.75 µg/mL), 0.5 MHz ultrasound (direction of propagation: black arrows), 630 kPa peak rarefactional pressure, a 0.2 Hz pulse repetition frequency and a 2% duty cycle. The clots were fixed in formalin, embedded in paraffin and stained with eosin and haematoxylin.

5.3.9. Limitations

The microbubble stock solution contains a large proportion of ferrofluid microdroplets. As discussed in Chapter 4, these microdroplets limit the accuracy of microbubble characterization and of accumulation quantification methods. In addition, the present study did not examine the effect of this ferrofluid emulsion on sonothrombolysis. However, the ferrofluid is not expected to be an effective cavitation agent: when investigating gene transfection with magnetic microbubbles and1 MHz ultrasound, Stride *et al.* did not observe any effect in the controls conducted with ferrofluid micelles only at 1 MPa peak to peak pressure [161]. The ferrofluid is not expected to be a suitable magnetofection agent either: tPA is a largely hydrophilic molecule and it is not expected to associate with the isoparaffin or with the uncoated magnetite nanoparticles in the fluid.

In the image analysis algorithm, lytic rates were obtained after linear regression of lysis depth over time. However, previously published studies have shown that a sigmoidal curve is more appropriate to model thrombolysis and sonothrombolysis progress [99], [249], [250]. In the preliminary experiments detailed in Appendix A, where lysis was slower, the lysis curve was also sigmoidal. However, in this set of experiments where rapid lysis occurred, a simple linear regression yielded a satisfactory fit (see § 5.3.4).

Most published studies use travelling waves when studying sonothrombolysis [27], [37], [50], [251]. Due to the geometrical characteristics of the setup, the ultrasound field used in this study included a partial standing wave. This is not expected to affect microbubble oscillations, as the size of a microbubble (~1-10 μm) is much smaller than half the wavelength at 0.5 MHz ($\frac{\lambda}{2}$=1.5 mm), but it may affect microbubble translation. It must be noted that in clinical applications, standing waves are generally not desirable for patient safety [74], [91]. The partial standing waves observed here are inherent to the geometry of the *in vitro* setup, but standing waves may also form *in vivo* in transcranial applications [74], [252].

Finally, the analysis of the acoustic signals, based on previous publications in the field [56], [253], can be further improved. In particular, the method used to separate ultraharmonic from broadband components relies heavily on the bandwidth of the chosen comb filter (25 kHz) and does not fully distinguish broadband signals from ultraharmonics. Recent studies have sought to address this issue with sum-of-harmonic methods in the time-domain [254].

5.3.10. Clinical implications

This investigation has established that magnetically targeted microbubbles have the potential to significantly accelerate enzymatic sonothrombolysis without increasing the risk of downstream embolism. These findings are particularly promising in the context of ischaemic stroke therapy, where early tissue reperfusion is crucial to salvage brain tissue and improve patient outcomes [8].

Expected clinical benefits

In both microbubble groups, lysis started immediately after treatment initiation, while no substantial damage was achieved in the tPA control group within the treatment timeframe. This finding agrees with Molina *et al.*'s report that 2-MHz ultrasound and non-targeted microbubbles decrease the median time to any recanalisation from 60 minutes (tPA only controls) to 30 minutes in ischemic stroke patients [2]. Therefore microbubble-enhanced sonothrombolysis can start tissue reperfusion earlier, saving precious time for ischemic tissue recovery.

In this chapter, 5/6 clots in the targeted group were fully lysed in less than 60 minutes, whilst there were none in the non-targeted group (although the clots were substantially damaged). This indicates that magnetically targeted sonothrombolysis may considerably reduce total treatment duration, allowing greater tissue salvage and limiting the adverse side-effects associated with prolonged ultrasound exposure.

At the relatively low concentration of tPA used, no substantial clot lysis was observed within the clinical timeframe in the control group. Magnetically targeted microbubbles are therefore expected to considerably reduce the required amounts of fibrinolytic drugs, limiting the potentially fatal side-effects associated with tPA administration.

Transcranial treatment

The main difficulty in stroke applications is the presence of cranial bone, a highly attenuating structure, in the ultrasound path. A common approach is to insonate the cerebral vessels through the thinnest portion of the skull, the temporal bone, although it is insufficient in a substantial minority of patients [44], [68], [72], [251]. Temporal window insufficiency has been attributed to excessive skull thickness [255] and changes in bone density [256].

The choice of mid-frequency ultrasound (0.5 MHz) in the present study is advantageous to overcome these challenges. Ammi *et al.* measured attenuation at 0.12, 1.3 and 2.0 MHz in five *ex vivo* human skull specimens and found that two out of five skulls exhibited an insufficient temporal window at 1.3 and 2.0 MHz (up to 96.6% pressure reduction); at 0.12 MHz, all skulls were suitable and pressure reduction was lower (22.5%). The beam was however more severely distorted at the lower frequency [72].

It is therefore hypothesized that 0.5 MHz is an appropriate frequency for clinical applications of enzymatic sonothrombolysis. In the preliminary experiments described in Appendix D, the ultrasound field was mapped in the hippocampus region during insonation through the temporal bone at 0.5MHz (the hippocampus region is close to the posterior cerebral artery and it is a few centimetres posterior to the middle cerebral artery). A 65% reduction in pressure was observed, as well as some spatial aberrations. The effect of the skull on the ultrasound field could readily be predicted from computed tomograms of the skull using a finite elements method. For acute situations such as ischaemic stroke, however, CT imaging may not be feasible before treatment inception, so accurate information on the acoustic field at the treatment site may not be available.

It must also be noted that clinical success relies on operator skill, as transducer alignment relative to the skull affects greatly ultrasound transmission [72], [257].

Treatment monitoring

This chapter has also shown that acoustic emissions at the site of treatment enable real-time monitoring for magnetically targeted enzymatic sonothrombolysis. In clinical applications, acoustic monitoring can be achieved with a conventional diagnostic imaging probe using passive cavitation mapping methods (PAM) [258], [259]. Crake *et al.* have reported real-time *in vivo* cavitation monitoring with PAM, and shown that both cavitational activity and molecular agent uptake were enhanced by magnetically targeted microbubbles [260].

In ischaemic stroke treatment monitoring, the presence of the skull imposes additional challenges, including a) aberrations in the propagation of the cavitation signals, leading to distortions upon image reconstruction; b) strong attenuation of the acoustic signal in bone. Recent studies have proposed beamforming techniques to address these issues, using CT or MRI imaging [261], [262].

Exposure conditions

Multiple studies have been carried out to determine the effect of exposure conditions (including acoustic pressure, pulse length, duty cycle, see §2.5.1) on treatment success and safety [55], [99], [103], [218], [263]. It is likely that the optimal exposure parameters are application-specific, as the time constraints and safety requirements depend on the type of occlusive event. In this chapter, the parameters were not optimised to a particular application, but a low pulse repetition frequency (0.2 Hz) was chosen to allow microbubble accumulation between ultrasound pulses; it may also be beneficial to limit the adverse bioeffects of ultrasound exposure. Before *in vivo* translation, further work is required to optimise the other ultrasound parameters.

5.4. Insights into the mechanisms of sonothrombolysis

To maximise treatment safety and optimise exposure parameters, an understanding of the mechanisms of sonothrombolysis is necessary. Despite a number of recent studies on the subject, these mechanisms have not been fully clarified [49], [50], [264]–[266]. It is likely that several mechanisms are simultaneously involved in clot breakdown, with different contributions depending on the experimental conditions.

The bioeffects of ultrasound on blood clots fits broadly into two categories: mechanical effects, and thermal effects. The following paragraph discusses the various possible mechanisms in the light of previously published reports and of the results presented in this thesis.

5.4.1. Mechanical effects

The mechanical action of ultrasound and microbubbles has been shown to break down blood clots. These effects include phenomena such as acoustic streaming, acoustic radiation forces, and microbubble activity. The resulting damage to the clot could be a combination of: a) clot erosion through damage to the superficial fibrin fibres, b) enhanced mixing of fibrinolytics near the surface of the clot, affecting tPA availability and the evacuation of fibrin degradation products, c) accelerated drug transport, with deeper penetration of fibrinolytic agents into the clot. The first two effects have not been extensively investigated; on the other hand, the improvement in drug transport has been widely shown to occur in sonothrombolysis [23], [267], [268].

5.4.1.a) Acoustic streaming

Acoustic streaming is the displacement of fluid particles by a propagating ultrasound wave, resulting from the absorption of acoustic energy. This effect could enhance the supply of fibrinolytic enzymes to the clot surface, or increase their penetration into the fibrin matrix.

Sakharov *et al.* have shown that 1-MHz ultrasound has approximately the same effect as mild stirring, producing a two-fold acceleration in lysis compared to tPA alone. When US and mild stirring are applied together, the added effect of ultrasound is much smaller (30% acceleration), suggesting that the two treatments have a similar effect on the clot [54]. At the microscopic level, exposure of clots to ultrasound in the absence of microbubbles has also been shown to enhance total tPA uptake, as well as the depth of tPA penetration into the clot [267], [268].

In the experiments reported in this chapter, however, no significant lysis was observed in the absence of microbubbles, ruling out acoustic streaming of the fluid as the prime mechanism for sonothrombolysis in this case.

In order to further investigate the mechanisms of sonothrombolysis at the microscopic scale, a microscope-compatible acousto-fluidic device was developed. Porcine plasma clots were exposed to 963-kHz ultrasound and lipid-shelled microbubbles in the presence of 0.75 µg/mL tPA. A marked acceleration in thrombolysis was observed over tPA only controls. This was achieved in the absence of acoustic streaming: fluorescent beads present in the fluid near the clot boundary were not significantly displaced in the ultrasound field (§A.3.4.c)).

5.4.1.b) Acoustic radiation forces on the clot

The propagating ultrasound wave can also transfer momentum to the clot, resulting in clot translation. In fact, the force exerted by the ultrasound is much larger on the clot than on the fluid, as the absorption coefficient of sound is two orders of magnitude greater [266], [269], [270]. This phenomenon could increase lysis by creating a "pumping" effect. Bader *et al*. observed that human blood clots exposed to pulsed ultrasound and 120 KHz and 0.44 MPa peak-to-peak translate synchronously with the initiation and cessation of the ultrasound pulses, with a maximum displacement on the order of 225 µm [266]. Translations of this magnitude are however expected to be specific to the experimental setup, as the clots were free to translate along the direction of sound propagation. In the present chapter, however, clot motion was limited, as the clots were resting against the bottom of the chamber. In addition, no significant lysis was observed in the absence of microbubbles. The acoustic radiation force on the clot is therefore not expected to be the main mechanism of lysis in these experiments.

5.4.1.c) Acoustic radiation forces on the microbubbles

Finally, primary radiation forces also apply to the microbubbles: momentum transfer results in rapid microbubble translation towards the clot. In the previous chapter, we have shown that the primary acoustic radiation force on the bubbles is far from negligible with the chosen ultrasound exposure conditions.

Using high speed imaging, Acconcia *et al*. have observed that microbubbles pushing against the surface of a clot during a single burst of ultrasound (1MHz, 0.2 MPa, 1ms burst) create a local deformation of the surface on the order of 80 µm. After the ultrasound burst, the surface bounces back due to the viscoelastic properties of the medium [65]. This effect alone could enhance drug pumping into the clot. The same authors have also shown

that as a result of primary acoustic radiation forces, individual microbubbles can become embedded in the fibrin mesh near the surface of the clot, or penetrate into the clot and translate further with every ultrasound pulse [264]. Both behaviours have the potential to promote thrombolysis. Oscillating, embedded microbubbles could pump fibrinolytic drugs into the clot, as well as damage neighbouring fibrin strands by applying repeated mechanical stresses. Burrowing microbubbles have been shown to promote drug transport into the clot and to break fibrin fibres as they progress [57], [264]. Statistical analysis showed that the outcome (microbubble embedding or burrowing, and subsequent fibrin damage or uptake of model drug) depends on the initial size of the microbubbles and on the local structure of the fibrin matrix. There is also evidence that microbubble coalescence under secondary radiation forces contribute to the process [264], [266].

In a setup closer to the one presented in this chapter, Bader *et al*. have also observed clear evidence of microbubble burrowing and continued oscillations within in the clot [266]. Given the acoustic conditions, similar microbubble behaviour is expected to occur in the present setup. In the previous chapter, histological analysis revealed the presence of deep tunnels into the clot surface, as well as the formation of discrete erythrocyte- and fibrin-depleted cavities of damage below the surface. As this type of damage only occurred in the clots treated with ultrasound and microbubbles, it is likely that they were caused by microbubbles embedded or translating within the clot. Interestingly, this type of damage was not observed in the present chapter, with similar acoustic conditions and the addition of tPA. This finding suggests that the dominant mechanism might be different in enzymatic sonothrombolysis. In the preliminary experiments described in Appendix A, acoustic radiation forces on the microbubbles were clearly observed, but there was no evidence either of microbubble penetration into the clot (§A.3.4.d)).

5.4.1.d) Cavitation activity

As discussed in the introduction, cavitation has been shown to play a crucial role in sonothrombolysis [33], [49], [50], [240], and a combination of microstreaming and micro-jetting has been hypothesised as the primary mechanism for clot breakdown.

Origin of the cavitation activity

In Chapters 4 and 5, substantial lysis only occurred in the presence of microbubbles, i.e. external cavitation nucleation agents. In contrast, endogenous cavitation nucleation agents such as gas entrapped during clot preparation did not play a substantial role in clot breakdown.

Cavitation in mechanical sonothrombolysis

The precise role of cavitation in mechanical sonothrombolysis has not been fully investigated to date. The preliminary pressure-ramp studies in Chapter 4 showed that lysis only occurred within the experimental timeframe when the acoustic pressure was well beyond the threshold for broadband emissions: no substantial lysis was observed with ultraharmonics alone (data not shown).

More importantly, the subsequent experiments showed no strong correlation between lysis rates and cavitation dose, a metric that is proportional to acoustic energy, regardless of the frequency band of interest (total emissions, ultraharmonics, or broadband). In addition, clot lysis rates were highly variable and histological analysis revealed a highly irregular clot surface. These findings lead to the following hypothesis: clot damage may be attributed to a small proportion of microbubbles that penetrate into the clot through acoustic radiation force, and proceed to deplete the red blood cells and damage the neighbouring fibrin fibres by undergoing repeated oscillations or inertial collapse. Because

of the complex structure of the clot, this is a highly variable process, though the number of microbubbles penetrating the matrix is likely to be increased when microbubble concentration increases. This would explain the high variability in lysis rates and the trend for increased rates of lysis with increasing microbubble concentrations. Only a minority of the cavitating microbubbles would play an effective role in clot breakdown, which would justify the absence of apparent strong correlation between lysis and cavitation energy emitted in the focal region. This hypothesis requires further investigation.

Cavitation in enzymatic sonothrombolysis

The role of cavitation in enzymatic sonothrombolysis has been more closely investigated in the literature [23], [50], [139], [240]. In the present chapter, histological analysis showed that the surface of the clots treated with US and non-targeted microbubbles was smoother, suggesting a different mechanism from enzymatic sonothrombolysis. In addition, a high degree of correlation existed between lytic rates and emitted acoustic energy. As opposed to mechanical sonothrombolysis, this suggests a collective effect of the microbubbles in enzymatic sonothrombolysis.

In the experimental conditions of this chapter, the acoustic emissions included a mixture of harmonic, ultraharmonic, and broadband components. All frequency components exhibited a similar relationship with lytic rates. The precise role of each component was however not investigated. In a static *in vitro* model with 120 kHz ultrasound, Datta *et al.* achieved greatest enzymatic sonothrombolysis when ultraharmonic emissions were maximized and broadband emissions were negligible. In their study, microbubble replenishment was episodic, with a bolus injection every 3 minutes. In the conditions maximising ultraharmonic emissions, cavitation activity was sustained for over two minutes between

replenishments; on the other hand, it decreased within a few seconds when broadband emissions were detected [23]. Whilst these findings suggested that sustained, periodic cavitational events are preferable to inertial collapse, this statement must be qualified in the case where microbubbles are continuously replenished. In a flow model similar to the setup in present chapter, Petit *et al*. achieved the greatest depth of lysis with broadband emissions only; the authors also reported significantly more lysis with a combination of broadband and ultraharmonics than with ultraharmonics alone [240]. It is therefore hypothesised that when microbubbles are constantly replenished, their inertial collapse is more effective towards clot breakdown than stable oscillations; on the other hand, when only a fixed number of microbubbles are available without possibility of replenishment, prolonged oscillations are preferable, as inertial collapse depletes the medium of cavitation nuclei too rapidly.

Cavitation activity can enhance enzymatic clot lysis in multiple ways, as discussed in Chapter 2. Oscillating microbubbles create microstreaming fluid patterns [271] that can erode superficial fibrin, increase the availability of fibrinolytic enzymes, and remove degradation products faster [35]. Collapsing microbubbles generate microstreaming and create fluid jets [272] that could erode fibres [57], push tPA into the clot, or increase tPA availability near the fibres by damaging or expelling erythrocytes. In the preliminary experiments described in Appendix A where only ultraharmonic emissions were detected, sonothrombolysis was associated with some microstreaming, but there was no evidence of an increase in model drug penetration. This observation is in contrast with other published studies that report enhanced tPA uptake and penetration into the clot during enzymatic sonothrombolysis [56], [267].

These findings illustrate the complex relationship between cavitation activity and clot lysis in enzymatic sonothrombolysis. Clarifying this relationship is essential in order to optimise treatment safety and efficacy. The ultimate aim is to identify acoustic conditions that maximise lysis rates while limiting potentially harmful inertial cavitation events [58], [273]. Bearing these constraints in mind, the exposure parameters employed in this study could be optimised in further investigations.

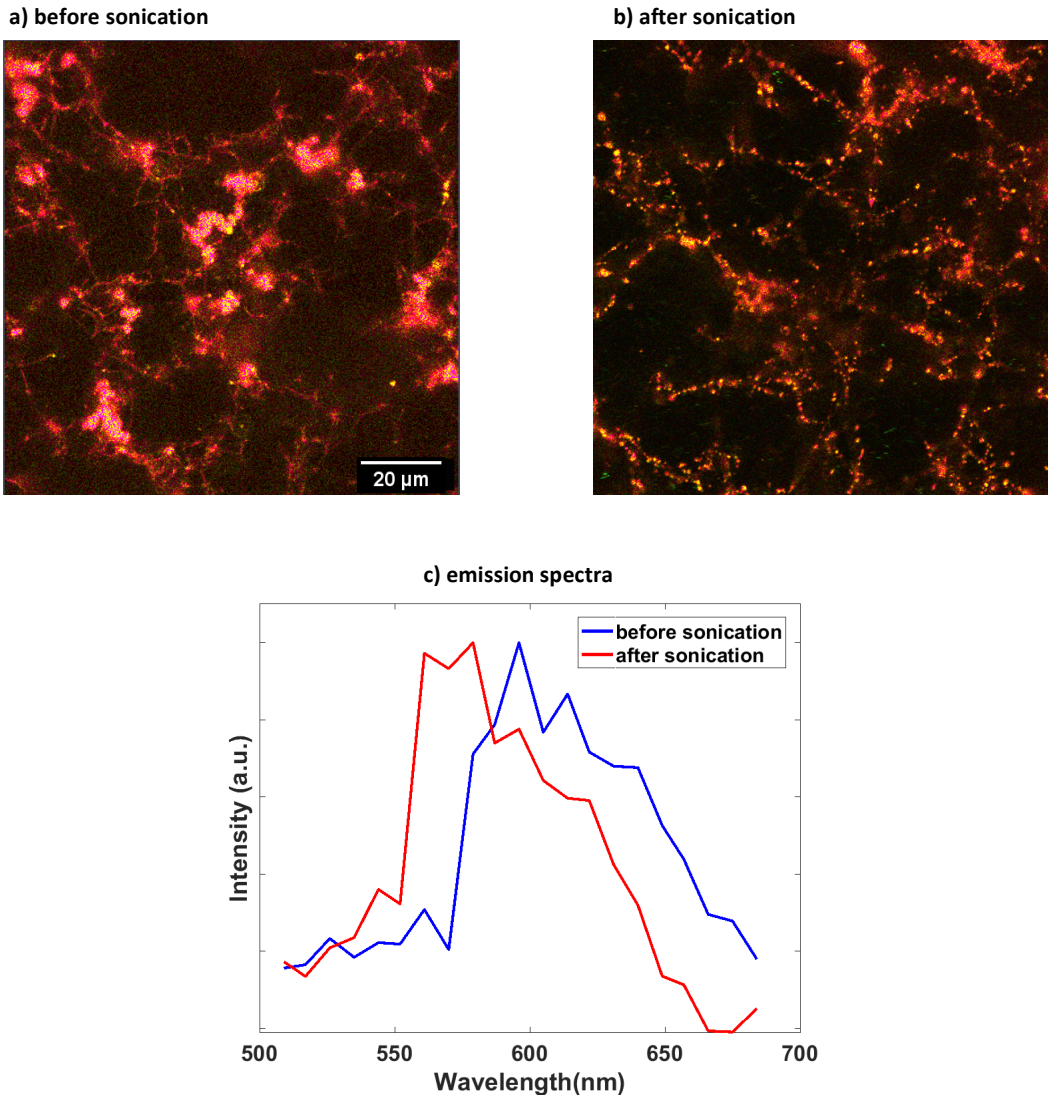


Figure 5-11: Confocal spectral micrographs of fibrin-bound polarity-sensitive probes (FE) after sonication for 135s at 20 kHz (see Appendix D): a) before sonication; b) after sonication; c) emission spectra, indicating a shift in emitted wavelength after sonication (see Appendix D).

5.4.1.e) Mechanical / chemical effects

To date, ultrasound has not been shown to have an effect on the structure and activity of the tPA molecule [274], although there is some evidence for a pressure-dependent effect on streptokinase, another plasminogen activator [274], [275].

On the other hand, the effect of ultrasound on the structure of fibrin networks has been documented. Exposure to pulsed ultrasound alters the flow resistance in fibrin gels [276]. It is associated with a reorganisation of non-cross-linked fibrin, and particularly with a reduction in fibre diameter [265], [277] and an increase in the number of fibres per unit volume, without evidence of fibre breakage [277]. This disaggregation is reversed within 15 minutes of treatment end. No such changes were observed in cross-linked networks. Such changes do not result from thermal elevation, but are possibly cavitation-mediated [276], [277].

These changes in turn affect the interaction of tPA with fibrin: ultrasound accelerates tPA binding to fibrin fibres, increases the maximum binding of tPA, and in some cases alters the binding affinity [278].

Further investigations were considered to clarify the effects of ultrasound on fibrin, with the additional advantage of spatial information offered by advanced microscopy techniques. In the experiments described in Appendix C, fibrin gels were tagged with viscosity-sensitive molecular rotors in order to map local changes in fibrin structure. A suitable rotor could however not be identified. In the preliminary experiments described in Appendix D, a polarity-sensitive dye (Di-4-AN(F)EPPTEA (FE), hitherto used to probe cellular membranes [279], [280]) was used to image a non-cross-linked fibrin gel. A shift in the dye's emission spectrum was observed immediately after exposure to 22.5 kHz ultrasound (Figure 5-11). This promising proof of concept warrants further study.

5.4.1.f) Magnetofection

The added effect of magnetic targeting on sonothrombolysis is most likely attributed to enhanced microbubble activity in the focal region. The effect of magnetofection, though less likely, remains to be studied: the microbubbles and ferrofluid microdroplets in the microbubble stock solution may penetrate into the clot, creating channels and/or entraining fluid into the clot. Histological analysis has indeed shown that some magnetic material becomes embedded into the erythrocyte-depleted cavities of the clot, although there is no evidence that they are responsible for creating the cavities, as similar cavities also observed in the absence of magnetic targeting.

5.4.2. Temperature

The second mechanism candidate is thermal elevation resulting from acoustic energy absorption by the clot or by the surrounding fluid. This phenomenon could contribute to lysis acceleration, as tPA-induced clot mass loss increases with temperature in the 30 to 40°C range [281]. In this chapter, however, heat convection by the diluted plasma flow is expected to prevent significant temperature increase. In the preliminary experiments described in Appendix A, temperature was monitored with a thermocouple and remained unchanged (§A.3.4.a)). Temperature rise is therefore not expected to be an essential mechanism under these experimental conditions. This result is in agreement with previously published findings: although some *in vitro* studies have reported a mild increase in temperature during treatment [20], [54], [60], sonothrombolysis can be achieved without significant temperature rise at the target site [20], [41], [60]. This is encouraging for patient safety, as mild hyperthermia could be harmful to the ischemic brain [282], [283], while neuroprotective effects have been attributed to hypothermia [283], [284].

5.5. Conclusion

The results in the present chapter have demonstrated *in vitro* that magnetically targeted microbubbles can significantly accelerate enzymatic sonothrombolysis at 0.5 MHz, with the potential to reduce administered drug doses and to achieve faster recanalisation of occluded blood vessels. The total energy of acoustic emissions was strongly correlated with lytic rates, providing a valuable technique of real-time treatment monitoring. This indicates that magnetic targeting is a promising method to enhance treatment efficacy and patient safety in the management of occlusive conditions.

CHAPTER 6

Conclusions and future work

6.1. Thesis overview

Sonothrombolysis is emerging as a promising approach to accelerate vessel reopening in acute ischemic stroke. The objective of this work was to investigate the potential of magnetically targeted microbubbles to further enhance sonothrombolysis.

In Chapter 2, a review of the literature on microbubble-enhanced sonothrombolysis was presented. It identified several technical challenges that still need to be overcome in order for sonothrombolysis to become an integral part of clinical practice. These include:

a) obtaining conclusive evidence of significant improvement in long-term functional outcomes for patients,
b) improving the transport of microbubbles to the clot in a region of obstructed flow,
c) overcoming the attenuation of ultrasound by bone and tissue,
d) gaining a better understanding and control of haemorrhagic transformations,
e) developing clinically applicable treatment monitoring strategies.

From the elements highlighted in Chapter 2, it is clear that insufficient microbubble delivery to the occluded vessel is a major hindrance to effective sonothrombolysis

(challenge b). The influence of magnetic targeting on microbubble distribution in occluded vascular bifurcations was therefore investigated in Chapter 3.

Within the occluded vessel itself, the next difficulty lies in obtaining rapid breakdown of the thrombus in order to maximise tissue recovery, and hopefully, achieve successful treatment outcomes (challenge a). The effect of magnetically targeted microbubbles on clot lysis was therefore studied, first in the absence and then in the presence of fibrinolytic drugs (Chapters 4 and 5 respectively). In these two chapters, the feasibility of acoustic treatment monitoring was also examined (challenge e). The findings from this investigation are as follows:

6.2. Summary of experimental findings

Magnetic targeting and microbubble delivery in occluded vascular networks

Therapeutic agent distribution was studied numerically and experimentally in a model of a fully occluded microvascular bifurcation (Chapter 3). With good agreement between the experiments and simulations, it was demonstrated that:

- Laminar vortices and rapidly decreasing fluid velocity along the length of the occluded vessel constituted serious obstacles to drug and microbubble transport towards the thrombus.
- Magnetic targeting considerably improved microbubble delivery to the thrombus (up to 100% delivery of the injected dose with magnetic targeting, compared to 0% without). This effect is influenced by the physiological parameters in the occluded network. In particular, targeting efficacy decreases with increasing blood velocity at the inlet of the network, while the distance between the bifurcation point and the occlusion point does not affect outcomes. The latter was however only investigated in the case where the occlusion distance is very large compared to the vessel diameter.
- Microbubble design also affected targeting outcomes: as expected, delivery efficacy increases with the magnetic particle loading of individual microbubbles.
- The magnetic fields required for effective targeting can readily be obtained with MRI technology, but the magnetic field gradients are not currently achievable; they are, however, feasible with permanent magnets. This study therefore warrants the development of application-specific magnetic targeting systems.

Magnetic targeting and microbubble concentration at the thrombus surface

Within the occluded vessel, magnetic targeting was expected to increase the concentration of microbubbles near the thrombus surface in two ways: i) by deflecting towards the thrombus the trajectory of microbubbles present in the flow, and ii) by pulling microbubbles out of the flow altogether and retaining them on the surface of the thrombus. In the experimental model of a partially occluded middle cerebral artery used in Chapters 4 and 5, mere deflection by the magnet (effect i) was not found to be sufficient for targeted sonothrombolysis, as it was far exceeded by the deflection in the same direction due to the acoustic radiation force. Only microbubble retention (effect ii) was relevant.

Mechanical sonothrombolysis

In this work, mechanical and enzymatic sonothrombolysis were studied separately. While enzymatic treatment (Chapter 5) has been more widely investigated in the literature, mechanical treatment (Chapter 4) is expected to have the greatest clinical benefit, as it provides an alternative therapy for patients who are not eligible to receive tPA.
Separating the two methods yielded valuable findings on mechanical sonothrombolysis with conventional (non-targeted) microbubbles:

- Mechanical sonothrombolysis with microbubbles was feasible as a standalone treatment within a clinically relevant timeframe (15-30 minutes) and with clinically achievable ultrasound exposure parameters.
- An increase in the administered concentration of microbubbles tended to accelerate mechanical sonothrombolysis (for instance an increase by 22% in microbubble concentration from 1.8×10^6 microbubbles/mL was associated with a 20% increase in average lysis rates).

- Rates of mechanical sonothrombolysis were, however, highly variable. This variability could not be attributed to variations in clot origin, age, or gas content, or in the properties of the microbubbles. In contrast, enzymatic sonothrombolysis with non-targeted microbubbles was more consistent.
- Even in clots where no macroscopic lysis was observed with mechanical sonothrombolysis, histological analysis revealed extensive microscopic damage in the clots treated with microbubbles, including red blood cell depletion and sectioned fibrin fibres. In comparison, the surface of clots treated with enzymatic microbubble-enhanced sonothrombolysis was smoother, with only a few areas of red blood cell depletion.

Sonothrombolysis with magnetically targeted microbubbles

The main objective of the study was to investigate the effect of magnetic targeting on microbubble-enhanced sonothrombolysis:

- Magnetic targeting did not consistently enhance mechanical sonothrombolysis, possibly due to high variability in lysis rates.
- On the other hand, magnetic targeting significantly accelerated enzymatic sonothrombolysis (3-fold increase in lysis rate on average over non-targeted controls).

Treatment safety

Sonothrombolysis, whether mechanical or enzymatic, did not increase the risk of downstream embolism by creating large clot fragments.

Treatment monitoring

A key challenge in clinical applications of sonothrombolysis is the provision of real-time feedback to ensure patient safety and adjust treatment protocols to account for patient-to-patient variability. In this work, the feasibility of acoustic treatment monitoring was investigated, and the acoustic emissions at the treatment site were analysed.

In particular, three types of emissions were examined: the total emissions, the ultraharmonic emissions (at odd multiples of half the driving frequency), and the broadband emissions. In all experiments, a combination of ultraharmonics and broadband was detected during treatment.

- In mechanical sonothrombolysis, no strong correlation was observed between lysis rates and emitted acoustic energy (Pearson's correlation coefficient $R=0.548$, $p<0.05$ for the total cavitation dose). Acoustic monitoring may therefore not be suitable for mechanical sonothrombolysis.
- In enzymatic sonothrombolysis, on the other hand, a strong and significant correlation was found between lysis rates and emitted acoustic energy ($R=0.870$, $p< 0.01$ for the total emitted cavitation dose). This correlation was similar in all three types of emissions investigated. Acoustic monitoring may thus be regarded as a promising tool for enzymatic sonothrombolysis.

Mechanisms of sonothrombolysis

Understanding of the mechanisms underlying desirable effects (clot lysis) as well as adverse events (haemorrhage) of sonothrombolysis is needed in order to improve treatment design and increase confidence in patient safety. Possible mechanisms of sonothrombolysis were examined and three hypotheses were formulated:

- clot damage in mechanical sonothrombolysis is due to a small subset of the microbubble population penetrating into the clot through acoustic radiation force, and remaining embedded near the surface or continually burrowing into the fibrin matrix. Through repeated oscillations or inertial collapse, these microbubbles deplete the clot in erythrocytes and damage fibrin fibres.
- in contrast, clot damage in enzymatic sonothrombolysis is due to a collective effect of the microbubble population.
- the microbubble replenishment scheme determines the most effective cavitation regime for enzymatic sonothrombolysis. When microbubbles are constantly replenished, inertial collapse is more effective than stable oscillations; on the other hand, when no replenishment is available, inertial collapse destroys cavitation nuclei too rapidly, and sustained oscillations are preferable.

6.3. Clinical significance of the findings

Expected clinical benefits of targeted sonothrombolysis

Clinical trials for stroke have already demonstrated that microbubble-enhanced enzymatic sonothrombolysis accelerates recanalisation in occluded arteries, while *in vivo* and *in vitro* evidence also show that it restores perfusion in the microvasculature. By incorporating magnetic targeting and acoustic treatment monitoring, it is hoped that future trials will demonstrate an even more significant improvement over fibrinolytic drugs alone, and will provide conclusive evidence of significant improvements in neurological outcomes associated with accelerated recanalisation.

Clinical implementation

For the purposes of clinical acceptance, microbubble-enhanced sonothrombolysis is best deployed as an adjuvant to existing drug-based strategies for the foreseeable future. However, in the longer term, this study has shown that magnetic microbubbles can play a key role in reducing the administered rt-PA dose. With increased confidence in this approach, mechanical sonothrombolysis may become possible, although appropriate treatment monitoring techniques remain elusive.

Area of application

Ischaemic stroke is possibly the condition to which microbubble-enhanced sonothrombolysis would be most beneficial, given the severe side effects of current treatments. As a result, it is the main focus of research in the field. Yet, it is also the application that is associated with the greatest difficulties in terms of US absorption, safety and time constraints. It is expected that sonothrombolysis research would benefit from early experience in less severe conditions such as peripheral thrombosis and occluded

grafts. All these applications are amenable to magnetic targeting, as the vessel of interest is relatively superficial.

6.4. Future work

Improvements to the present studies

The numerical and experimental bifurcation model presented in Chapter 3 has shed light on microbubble delivery in occluded vascular bifurcations. Extending the numerical simulation into a three-dimensional model will provide a valuable opportunity to gain further understanding of microbubble trajectories. In addition, the clinical relevance of the study will be improved by taking into account factors that affect targeting efficacy *in vivo*, such as arterial pulsatility and the particulate nature of blood [219]. Ultimately, the effect of different bifurcation geometries will be considered, including study of partially occluded vessels, shorter occluded branches, and different bifurcation angles [211].

Chapters 4 and 5 have provided insights into a novel treatment approach, sonothrombolysis with magnetically targeted microbubbles. Several improvements to this proof-of-concept investigation are proposed. Firstly, mechanical and enzymatic sonothrombolysis were examined separately, with different ultrasound exposure parameters and magnetic targeting systems. This allowed extensive study of mechanical sonothrombolysis as a standalone therapy, but prevented direct comparison of the two treatments. Further studies of enzymatic sonothrombolysis should therefore include a tPA-free control group. Secondly, each series of experiments was carried out with blood samples from a single individual. This enabled the author of this work to rule out patient-to-patient variability in clot composition as a source of experimental variability. Further

studies however, should include clots from multiple individuals, in order to strengthen their clinical relevance.

Lastly, spectral analysis of the acoustic emissions was implemented using a frequency domain comb filter based on previously published work [23]. As discussed in Chapter 5, this approach cannot fully separate ultraharmonic emissions from broadband signal. Recent developments into time-domain algorithms should be applied in future studies [254].

Further investigation into the mechanisms of sonothrombolysis

In this work, the mechanisms of mechanical and enzymatic sonothrombolysis were discussed, and several hypotheses were raised. Further experiments are therefore suggested.

Specifically, preliminary experiments were carried out in an acousto-fluidic device (Chapter 5 and Appendix A), yielding promising information on the microscopic progress of the lytic front, the lack of temperature rise or acoustic streaming, the presence of microstreaming, and the dynamics of tPA penetration into the clot. More work is required to confirm these observations and extend the investigation to other mechanisms and ultrasound exposure conditions.

Among the possible mechanisms of sonothrombolysis, the chemical and mechanical effects on fibrin have not yet been extensively studied. Associating polarity-sensitive molecules to fibrin provided encouraging preliminary results (Chapter 5, Appendix C), pointing to possible changes in local fibre structure, and warranting additional experiments.

Microbubble formulation

The sonothrombolysis studies presented in this work employed a well-characterised magnetic microbubble formulation with an oil-based ferrofluid [162], [210]. As a result, the microbubble stock solution included a high proportion of ferrofluid microdroplets that are not acoustically responsive. An alternative formulation based on aqueous magnetic suspensions [208], used in Chapter 3, should be employed in all further studies. Eventually the objective should be to develop a tPA-loaded magnetic microbubble, in order to achieve co-location of cavitation activity and drug release.

In vivo translation

The ultimate goal is to translate the findings presented in this report into the clinic. The first step towards implementation is to develop application-specific magnets, tailored to the depth, flow rate and geometry of the target vessel. This thesis has suggested a range of magnetic fields and gradients suitable for delivery to microvascular occlusions (Chapter 3) and for sonothrombolysis in the middle cerebral artery (Chapter 5). Building on this and on recent work by Barnsley *et al.*[205], further research will facilitate the design of magnetic targeting systems for *in vivo* and clinical applications.

Next, *in vivo* validation will need to be carried out. A variety of animal models for thrombosis have been used in the literature, including rats, rabbits, dogs and pigs [285], [286]. Model choice is subject to the occlusive condition of interest (acute or chronic, embolic or thrombotic etc.). For instance, hyperlipidaemic porcine models can simulate coronary atherosclerosis [287]. However, the cost and the logistics of handling large animals do not make this option easily applicable. Rabbit carotid or femoral arteries, on the other hand, provide a well-characterised and more accessible model for embolic stroke

[40], [288]. Thrombotic events can be modelled by stimulating Virchow's triad[9] in rabbit aortas [289], rat middle cerebral arteries [128], or canine arteriovenous grafts [69]. Regardless of the chosen model, particular attention will be paid to treatment safety by performing histological analysis of the endothelium and, if applicable, of cerebral tissue.

Thirdly, the findings on acoustic emissions presented in this work will be instrumental to improve real-time monitoring in future protocols of *in vivo* enzymatic sonothrombolysis. Current monitoring methods such as B-mode and Doppler imaging only provide evidence of the absence or presence of microbubbles, and potentially of the outcome of treatment (recanalisation). These conventional modalities do not provide robust monitoring or localisation of thrombolytic efficacy itself. A recent development capable of addressing these limitations is passive acoustic mapping (PAM), a technique that enables real-time localisation and quantification of cavitation activity. Crake *et al.* have successfully mapped *in vivo* the shift in the spatial distribution of cavitation that occurs with magnetic microbubbles in the presence of magnetic field. They have also observed an increase in the intensity and sustainability of cavitation [290]. Further *in vitro* and *in vivo* work will therefore assess the feasibility of monitoring magnetically targeted sonothrombolysis with PAM.

By improving treatment safety and efficacy, it is hoped that magnetically targeted sonothrombolysis with real-time acoustic monitoring will improve patient outcomes in the management of occlusive conditions.

[9] The three main categories of thrombosis-inducing factors: hypercoagulability, blood stasis, and endothelial injury.

APPENDIX A

Observing the mechanisms of sonothrombolysis in an acousto-fluidic chamber

In this chapter, the mechanisms of sonothrombolysis at the microscopic scale were systematically investigated. A novel acousto-fluidic chamber was presented and characterised for real-time monitoring of sonothrombolysis at the microscopic scale. The feasibility of achieving sonothrombolysis in this system was assessed. The mechanism candidates for lysis in this setup were examined: temperature rise and acoustic radiation force were ruled out, microstreaming and acoustic radiation force were observed. In addition, ultrasound and microbubbles did not enhance penetration of a model drug into the clot. The significance of these preliminary findings is further discussed in Chapter 5.

A.1. Introduction

A.1.1. Objective

In Chapters 4 and 5, clot diameter was used as a measure of treatment success. Reducing clot size, and hence restoring blood flow, is the first objective of stroke therapy in the clinic, and vessel recanalization is the primary endpoint in clinical trials [43], [291]. However, observations at a much finer scale are necessary to elucidate the mechanisms responsible for treatment success. The causes of clot breakdown are to be found at the level of the insoluble fibrin network that makes up the clot and determines its mechanical properties. At present, the mechanisms for sonothrombolysis have not been fully clarified. Yet treatment efficacy and patient outcomes could be greatly improved by further understanding – and harnessing- these mechanisms.

This study investigates the microscopic effects of ultrasound and microbubbles on a blood clot in a novel acousto-fluidic chamber design.

A.1.2. Structure of the study

First, a setup was designed in which sonothrombolysis may, for the first time, be observed in real-time under a conventional microscope. It enabled systematic investigation of the main mechanisms candidates: temperature rise, acoustic radiation force, and cavitation. Further insight into cavitation-related phenomena was also gained by visualising acoustic streaming and bubble-induced clot damage. The impact of these various mechanisms on the clot was then examined: drug penetration and clot surface erosion were examined.

A.2. Methods

The contribution of Dr. Carugo to the design of the acousto-fluidic chamber is gratefully acknowledged.

A.2.1. Materials

Calcium chloride, sodium chloride, agarose, Tris-HCl, bovine fibrin, thrombin from bovine plasma, fluorescein isothiocyanate (FITC), and 2-µm diameter FITC-labelled polystyrene beads were purchased from Sigma Aldrich Company Ltd (St Louis, MO, USA). TRITC-labelled bovine serum albumin and phosphate-buffered saline (PBS) were obtained from Life Technologies (Carlsbad, CA, USA). Tissue plasminogen activator (Actilyse, Boehringer Ingelheim Pharma GmbH & Co. KG, Ingelheim am Rhein, Germany) was reconstituted in water to the concentration of 1 mg/mL and stored in 400µL aliquots at -80°C. Polydimethylsiloxane (PDMS) and epoxy were purchased from Dow Corning Ltd (Midland, MI, USA) and the 1 mm thick piezo-electric transducers from Meggit GmbH (PZ26, Offenbach / Main, Germany). Lipid-coated sulphur-hexafluoride microbubbles (Sonovue®) were obtained from the Bracco Group (Milan, Italy).
Fresh frozen pig plasma was prepared and stored as indicated in Chapter 5.
Fluorescently labelled fibrinogen was prepared in house according to the protocol described by Sakharov *et al.*[292]. Thrombin was diluted in buffer (0.15 mol/L NaCl and 0.01 mol/L Tris-HCl, pH 7.4) to a final concentration of 100 NIH units/mL.

A.2.2. Acoustic chamber

An acoustic system was specifically designed to allow for simultaneous ultrasound exposure and observation of the clot with an inverted microscope (Figure A-1). The 10 x 10 mm piezo-electric element was coupled with a 170 µm thick borosilicate coverslip using a thin layer of epoxy. On the reverse side of the coverslip, a rectangular PDMS mold

contained the clot. A metallic wire was inserted along the base of the clot during preparation, providing upon removal a horizontal channel running 12 mm from the near edge of the piezoelectric element.

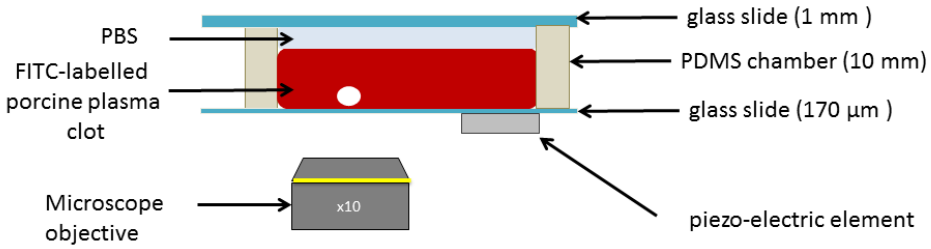


Figure A-1: Schematic of the acousto-fluidic chamber, including the clot (red), the piezo-electric

A.2.3. Chamber characterization

The ultrasound field in the channel was characterized with a fibre optic hydrophone (Precision Acoustics, Dorchester, UK).

As piezo-electric elements are prone to causing heating, temperature rise in the system was monitored under experimental conditions (see below) over 30 minutes using a thermocouple (Omega Technologies, Westlake Village, CA, USA).

A.2.4. Clot preparation

The clot preparation protocol was adapted from Collet *et al*. and Sakharov *et al*.[292], [293]. Briefly, 800 µL of fresh frozen pig plasma were aliquoted into the chamber, with 1µM FITC-labelled fibrinogen and 30 mM $CaCl_2$. Thrombin was added to a final concentration of 0.78 NIH units/mL.

The clot solution was immediately pipetted into the open PDMS chamber and incubated for 1 hour at 37°C. The metallic wire was then removed and the channel was flushed with PBS. The chamber was then filled to the top with PBS and closed with a 1mm-thick glass slide, taking care to remove any air bubbles. The clot was stored at 4°C until use, within 6 hours.

A.2.5. Experimental protocol

A.2.5.a) Clot lysis experiments

At the start of each experiment, a fresh clot chamber was placed onto the stage of a Zeiss 780 confocal microscope (Carl Zeiss AG, Oberkochen, Germany) fitted with an incubator operating at 37°C. A syringe pump (World Precision Instruments Ltd, Hitchin, UK) was used to flow into the channel a PBS solution of fresh frozen plasma, microbubbles (final concentration of 5×10^7 microbubbles/mL) and fibrinolytic agent (tPA, 0.25-1.5 μg/mL) at a rate of 2 mL per hour. Imaging and ultrasound exposure were initiated 15 min after flow started.

Ultrasound exposure was provided by the piezo-electric element driven at 963 kHz with a pulse repetition frequency of 1 Hz and a duty cycle of 0.05%. The frequency was chosen as it minimizes the impedance of the system (data not shown).

A.2.5.b) Penetration experiments

In the experiments investigating drug penetration, the setup was identical but the tPA was replaced with a fluorescent probe of similar molecular weight (TRITC-labelled bovine serum albumin), at a concentration of 2.5 μg/mL. The chosen concentration was higher than in the clot lysis experiments to allow visualisation. Imaging and ultrasound exposure were initiated immediately after flow started.

A.2.5.c) Cavitation measurements

Acoustic emissions near the clot surface were acquired over 30 minutes in a similar setup to the clot lysis experiments, with a fibre optic hydrophone inserted into the channel.

A.2.5.d) Acoustic streaming and microstreaming

Acoustic streaming was investigated in the chamber using a 2% agarose clot phantom, with 5 x 10^{-3}% volume/volume FITC-labelled beads in the channel. Fluorescence images were acquired at 30 frames per second with an inverted microscope (Ti Eclipse, Nikon Instruments Inc., NY, USA) and a x4 objective (PlanFluor, Nikon).

A.2.5.e) Acoustic radiation force

Acoustic radiation force was also investigated in the chamber using a 2% agarose clot phantom, and images were acquired in bright field microscopy at a rate of 30 frames per second.

A.2.6. Image acquisition

A.2.6.a) Clot lysis experiments

The edges of the channel were imaged with a ×10 objective (EC Plan-Neofluar, Carl Zeiss AG). Excitation of the FITC dye was provided by a 488nm laser in combination with a 497-684 nm band pass filter for the emissions. The focal plane was chosen as the mid-plane of the channel, and the area of interest was a 2.45 × 2.45 mm square centred 2 mm from the inlet of the channel. Images were acquired with 8x averaging every 2 minutes for 30 minutes.

A.2.6.b) Penetration experiments

The edges of the channel were imaged with a ×10 objective. Excitation of the FITC dye was provided by a 488nm laser in combination with a 493-553 nm band pass filter for the emissions. Excitation of the TRITC dye was provided by a 543nm laser in combination with a 556-669 nm band pass filter for the emissions. The area of interest was a 7.8 x 0.9 mm rectangle. Images were acquired every 90 seconds for 15 minutes.

A.2.7. Image processing

Image processing was carried out in Matlab (The MathWorks Inc., Natick, MA, USA).

A.2.7.a) Clot lysis experiments

In each frame, the edges of the channel were detected by thresholding, and the average channel diameter was computed. Percentage diameter change at a time point t was given by $L(t) = \frac{d(t)-d(0)}{d(0)}$ where d(t) is the channel diameter at time t.

A.2.7.b) Penetration experiments

As in Chapter 3, the half concentration distance D was chosen as an indicator of drug penetration. It was defined as the distance at which the TRITC intensity is half the average TRITC intensity in the channel.

A.3. Results

The acousto-fluidic chamber enables multiple methods of visualising the clot: images may be acquired of the fluorescently labelled fibrin network (Figure A-2a.), the entire channel (Figure A-2b.), or the mid-plane of the channel (Figure A-2c.). In this preliminary study, the data from the mid-plane of the channel will be exclusively discussed.

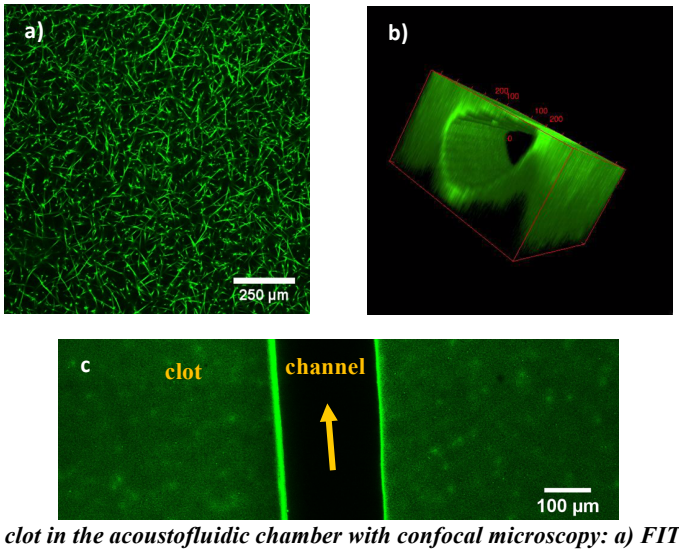


Figure A-2: Imaging the clot in the acoustofluidic chamber with confocal microscopy: a) FITC-labelled fibrin network (x63 objective); b) three-dimensional scan of the channel; c) mid-plane of the channel, with direction of flow (yellow arrow).

A.3.1. Characterising the system

A.3.1.a) Acoustic characterisation

The first step in the investigation was to characterise the acoustic field created by the piezo-electric element in the channel. Pressure varies along the length of the channel, with a maximum peak rarefactional pressure of 250 kPa (Figure A-3). The acoustic field includes a main frequency component at the excitation frequency and two harmonics, two orders of magnitude lower in amplitude.

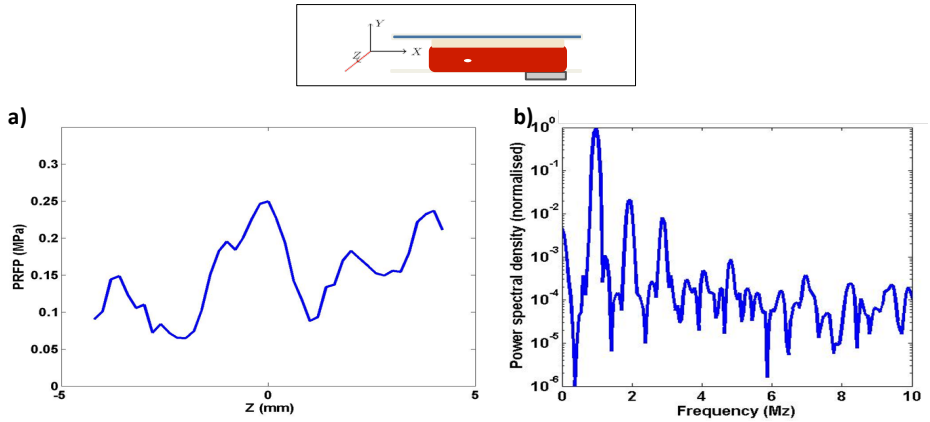


Figure A-3: Acoustic characterisation of the acousto-fluidic chamber, performed with a fibre optic hydrophone in water during exposure to 963 kHz ultrasound with a maximum peak rarefactional pressure of 250 kPa, a pulse repetition frequency of 1 Hz and a duty cycle of 0.05%: a) peak rarefactional pressure along the channel,; b) spectral content of the acoustic field. Inset: schematic of the chamber and orientation of the axes.

A.3.1.b) Temperature

As piezo-electric elements tend to create heating, a preliminary test was carried out to confirm that the chosen ultrasound parameters cause minimal heating in the chamber (Figure A-4). A negligible temperature rise was observed in the water-filled chamber over 30 minutes of exposure in the absence of flow (0.98°C, data not shown).

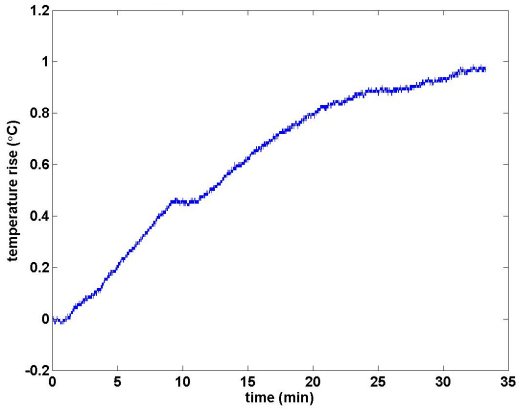


Figure A-4: temperature rise in the chamber in water, in the absence of flow, over 30 minutes of exposure to 963 kHz ultrasound with a maximum peak rarefactional pressure of 250 kPa, a pulse repetition frequency of 1 Hz and a duty cycle of 0.05%.

A.3.2. Effect of tPA concentration

After characterising the chamber, the feasibility of monitoring thrombolysis in real-time was assessed, and the effect of tPA on clot lysis was evaluated in the absence of ultrasound (Figure A-5). As expected, higher concentrations of tPA accelerate clot lysis: at 0.25 µg/mL, diameter change was 4.6 ± 9.3% after 28 minutes; at 0.75 µg/mL it was 121.9 ± 61%; and at 1.5 µg/mL, it was 281.3 ± 152%. It must also be noted that at 1.5 µg/mL, lysis rates were highly variable, although the relatively small sample size precluded further statistical analysis. In the subsequent paragraphs, a concentration of 0.75 µg/mL was chosen to investigate enzymatic sonothrombolysis.

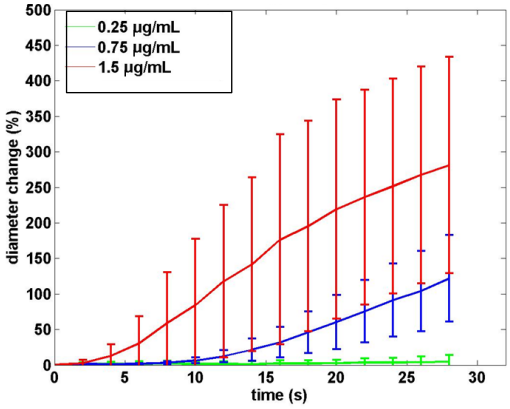


Figure A-5: effect of tPA concentration on thrombolysis (no US) in the acousto-fluidic chamber. FITC-labelled clots were exposed to 3 different concentrations of tPA for 30 minutes. Changes in channel diameter was measured from confocal images (n = 4). Error bars represent standard deviation from the mean.

A.3.3. Effect of ultrasound and microbubbles

Next, the feasibility of performing microbubble-enhanced enzymatic sonothrombolysis in this setup was examined. Figure A-6 indicates approximately 2-fold acceleration with the use of ultrasound and microbubbles: at 28 minutes, lysis was 121.9 ± 61.1% in the control group, and 227.3 ± 74.8 in the treatment group.

Real-time monitoring of enzymatic sonothrombolysis at the microscopic scale was therefore achieved. The next section examines the possible mechanisms involved accelerating lysis rates.

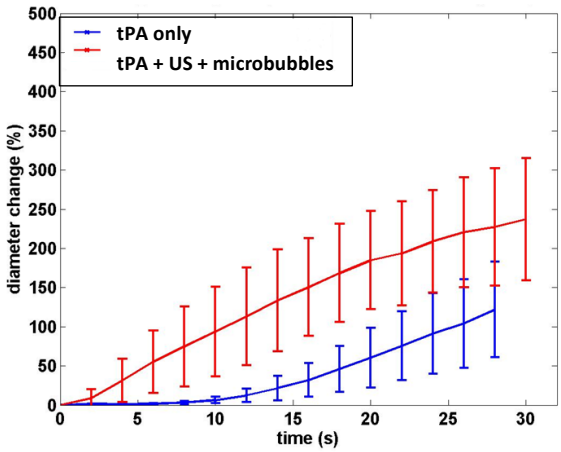


Figure A-6: Effect of ultrasound and microbubbles on clot lysis in the acousto-fluidic chamber: diameter change over time with and without ultrasound and microbubbles (red and blue lines respectively). FITC-labelled clots were exposed for 30 minutes to 0.75 µg/mL tPA, 963 kHz ultrasound with a maximum peak rarefactional pressure of 250 kPa, a pulse repetition frequency of 1 Hz and a duty cycle of 0.05%. Changes in channel diameter was measured from confocal images (n = 4). Error bars represent standard deviation from the mean.

A.3.4. Mechanisms

A.3.4.a) Thermal effects

Thermal variations in the channel were monitored over 30 minutes of treatment with ultrasound and microbubbles. Temperature remained remarkably stable, with variations within ± 0.06 °C from the initial temperature. Thermal effects were therefore ruled out as a mechanism for sonothrombolysis in this setup.

A.3.4.b) Cavitation

Acoustic emissions in the channel were monitored. With US only (Figure A-7 a.), the frequency content of the signal in the channel was similar to the signal in the water-filled chamber (Figure A-3 b.): the excitation frequency and the first two harmonics were detected. With US and microbubbles (Figure A-7 b.), the signal contained multiple harmonics. It may also contain ultraharmonics, although their intensity was close to the noise floor.

This indicates that acoustic cavitation occurs in the experimental setup; it is a mechanism candidate for sonothrombolysis.

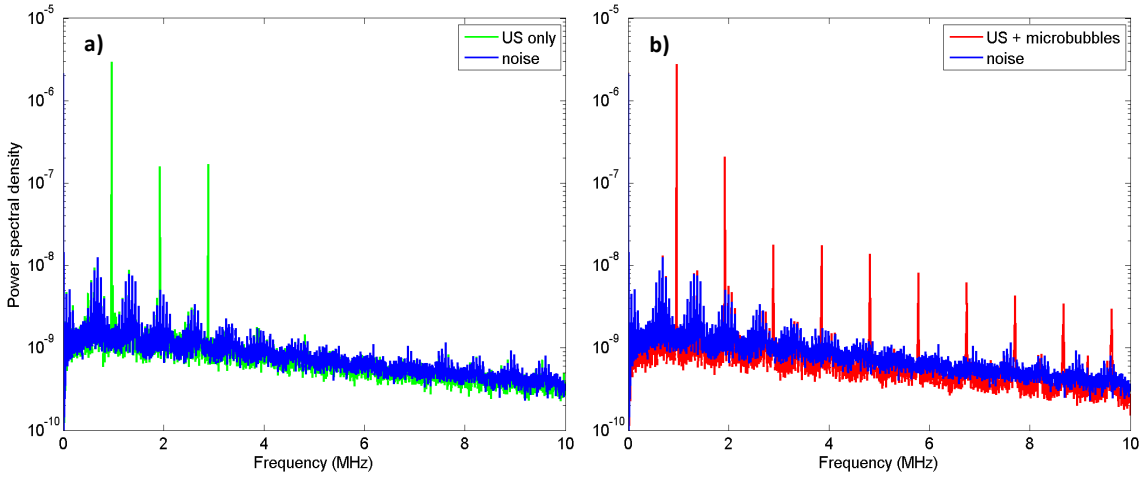


Figure A-7: Spectral content of the acoustic emissions in the channel during ultrasound exposure: a) without microbubbles; b) with microbubbles. Plasma clots were exposed for 30 minutes to 963 kHz ultrasound with a maximum peak rarefactional pressure of 250 kPa, a pulse repetition frequency of 1 Hz and a duty cycle of 0.05%. Emissions were acquired over the whole duration of treatment with a fibre optic hydrophone inserted into the channel. Averaging was carried out in the frequency domain after applying a Fast Fourier Transform.

A.3.4.c) Acoustic streaming

Acoustic streaming in the channel was monitored with fluorescent beads as flow tracers in PBS (no microbubbles). The beads remained stationary as the ultrasound was turned on. This rules out acoustic streaming as a mechanism for sonothrombolysis in this setup.

A.3.4.d) Acoustic radiation force

Acoustic radiation force in the channel was investigated: microbubble movement in the channel was monitored by brightfield microscopy (Figure A-8). During the first pulse, microbubbles coalesced and translated towards the channel wall. The clusters persisted and underwent repeated translations in the subsequent pulses.

Acoustic radiation force on the microbubbles was therefore clearly observed. As these preliminary observations were carried out in agarose clot phantoms, it was not possible to observe the effect of these microbubble movements on the clot itself.

A.3.4.e) Microstreaming

Microstreaming due to microbubble oscillations was observed using fluorescent microscopic beads as flow markers. Figure A-9 clearly shows vigorous streaming patterns in the channel.

Due to the low frame rate of the camera (30 frames/second), these preliminary experiments were carried out with continuous wave ultrasound. In further work, it is hoped that quantification of fluid velocity can be carried out in pulsed mode using high-speed fluorescence imaging.

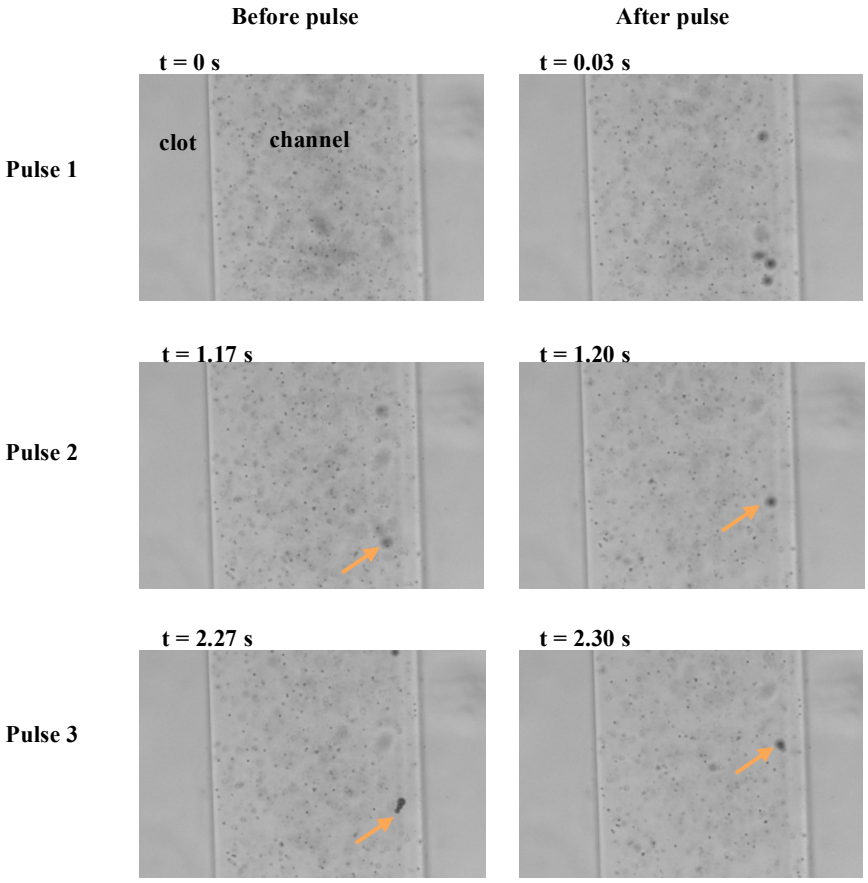


Figure A-8: Example of microbubble coalescence, persistance and translation under acoustic radiation forces. Agarose clot phantoms were exposed to 963 kHz ultrasound with a maximum peak rarefactional pressure of 250 kPa, a pulse repetition frequency of 1 Hz and a duty cycle of 0.05%. The contents of the channel (Sonovue and fluorescent beads in PBS, in the absence of flow) were imaged before and after three consecutive pulses by brightfield microscopy.

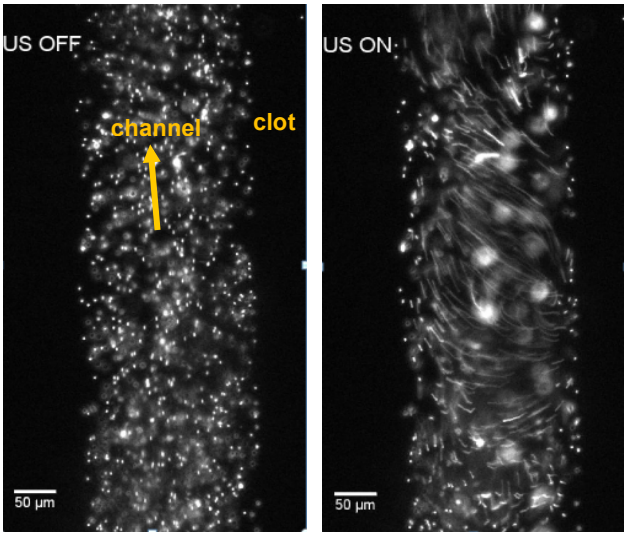


Figure A-9: Example of microstreaming in the channel. Agarose clot phantoms were exposed to 963 kHz continuous wave ultrasound with a maximum peak rarefactional pressure of 250 kPa. The contents of the channel (Sonovue and fluorescent beads in PBS, in the absence of flow) were imaged during exposure with fluorescence microscopy

A.3.4.f) Drug transport

The effect of ultrasound and microbubbles on tPA transport into the clot was investigated using a fluorescently labelled drug model (Figure A-10). The addition of ultrasound and microbubbles did not have any effect on the penetration depth of the drug model.

This experiment, however, only investigates unconstrained drug diffusion into the clot: the model drug used does not bind to fibrin fibres as tPA does [278]. In addition, diffusion was more rapid in this experiment than in the sonothrombolysis experiments, because the concentration of model drug was increased to facilitate imaging.

Further experiments are therefore required to confirm these preliminary findings.

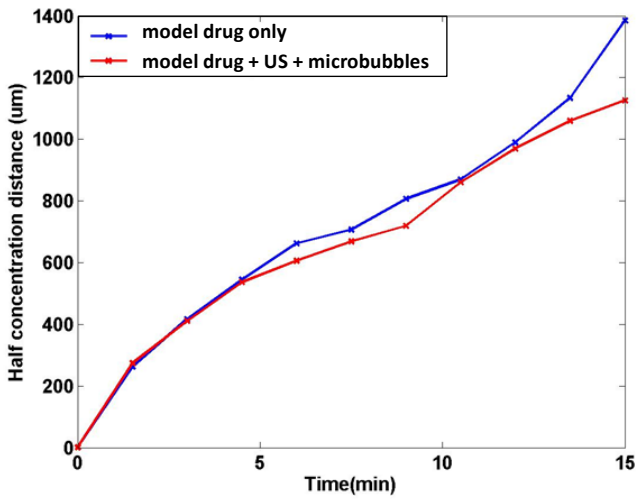


Figure A-10: Example of model drug penetration into the clot, with and without sonothrombolysis (red and blue line respectively, n = 1). FITC-labelled plasma clots were exposed for 15 minutes to 963 kHz ultrasound with a maximum peak rarefactional pressure of 250 kPa, a pulse repetition frequency of 1 Hz and a duty cycle of 0.05%. Diffusion of TRITC-labelled BSA into the clot was monitored by confocal imaging. The half concentration distance, defined as the distance at which TRITC intensity is half the average intensity in the channel, was computed.

APPENDIX B

Effect of ultrasound on the structure of fibrin: fluorescence lifetime imaging

In this study, fibrin structure is investigated with viscosity-sensitive molecular probes. This chapter outlines the main methods and results.

The contribution of Marketa Kubankova, who chose the molecular rotors, operated the microscope, and analyzed the lifetime data, is gratefully acknowledged.

B.1. Rationale

B.1.1. Objectives

Although the changes in fibrin fibre structure are very well documented in the context of clotting [294]–[296] and drug-induced thrombolysis [292], there is little literature on this question in the context of ultrasound-induced thrombolysis. In a study published in 1997, Braaten *et al*. performed scanning electron microscopy on fibrin gels after exposure to continuous wave 1 MHz ultrasound. In non-crosslinked gels, fibre diameter decreased by an average of 27% and fibre density per unit area increased by an average of 65% during ultrasound exposure, with no discernible evidence of fibre breakdown. Although the spread of the results was large, they were statistically significant. These modifications were reversible, and clot structure returned to baseline within 15 minutes after exposure. On the other hand, no changes were observed in highly cross-linked gels. The authors

concluded that ultrasound reversibly disaggregates non-crosslinked fibrin fibres, most likely by loosening the interaction between protofibrils [277].

The aim of the present study is to further examine the molecular interactions responsible for changes in network arrangement during ultrasound-mediated thrombolysis. To probe the changes in structure of the fibrin fibres at the microscopic level, we have investigated the use of fluorescence lifetime imaging microscopy (FLIM). This approach relies on fluorophores with a fluorescence lifetime that is sensitive to the viscosity of their immediate environment ("molecular rotors"), making them valuable sensors of molecular structure.

B.1.2. Study design

In practice, the study must comprise two stages. At first, a suitable dye is chosen from the pool of known molecular rotors. This can be done by measuring the lifetime of each rotor before and after clotting has occurred. A change in lifetime indicates that the rotor is sensitive to the presence of fibres in the sample.

As a second step, the effect of ultrasound is investigated by comparing the fluorescence lifetime before and after exposure of a clot sample to ultrasound, for instance with an ultrasonic bath.

B.2. Methods

B.2.1. Clot models

The study explores three clot models of increasing simplicity:

- **whole blood clots**, which are very close in composition to in-vivo clots.
- **plasma clots**, a simplified model of whole blood clots that removes some of the practical difficulties associated with the presence of red blood cells
- **fibrin clots**, a model widely used in the literature [264], [293] that reduces a blood clot to its most basic component, a cross-linked fibrin network.

B.2.2. Imaging protocol

Immediately after preparation, the samples were placed on the microscope in a temperature-controlled stage at 37°C (E200, Lauda GmbH, Germany). Clotting was then initiated in the sample and fluorescence lifetime images were acquired at x630 magnification with an oil-immersion lens

During image acquisition, the photons were binned over the entire 256x256 pixel image into 256 bins, so that each bin had a minimum of 700 photon counts. Each image was thus associated with a single fluorescent decay trace. The trace was then analysed off-line by the "phasor approach" [297] in purpose-written Matlab software [298]. The method involves applying a Fourier transformation to the fluorescence decay trace and plotting its real and imaginary coordinates (G and S respectively) on a two-dimensional plot. For monoexponential decays, these coordinates lie on a semicircle of diameter 1 and centre (0.5;0); for multiexponential decays, they lie inside this "universal circle". In this representation, fluorescent lifetime thus increases with decreasing G and increasing S.

B.2.3. Molecular rotors

Table B-1summarizes the molecular rotors and their optical characteristics.

The molecular rotors were initially introduced into the clot solution as free molecules dissolved in DMSO. As this approach did not yield the expected results (no change in lifetime during clotting), it was hypothesised that a great number of dye molecules were located in pores of the network, away from the fibres, therefore sensing no change in their surroundings. To increase the proportion of molecules located on or near the fibres, molecular rotors were then attached directly to the fibrinogen monomers using NHS ester chemistry.

Dye name	Name of molecule	Excitation wavelength for 2-photon imaging (nm)	Acquisition wavelength (nm)
$DiSC_2(3)$	3,3′-Diethylthiacarbocyanine iodide	1000	600-700
BC10	Bodipy-based rotor 1	1000	600-700
B++	Bodipy-based rotor 2	1000	600-700
Sq5	Squaraine 5	840	600-790
ThT	Thioflavin T	840	480-700
KR	Kiton Red	1000	600-700
Cy3-NHs	Sulfo-Cyanine3 N-hydroxysuccinimide ester	1000	600-700
Bodipy-NHs	Bodipy-N-hydroxysuccinimide ester	1000	600-700

Table B-1: Characteristics of molecular rotors

B.2.4. Experimental groups

The experiments performed are summarized in Table B-2

	Whole blood	Plasma	Fibrin
Free dye	$DiSC_2(3)$ BC10 B++ Sq5 ThT KR	$DiSC_2(3)$ BC10 B++ Sq5 ThT KR	$DiSC_2(3)$ BC10 B++ Sq5 ThT KR
Bound dye	Cy3-NHS (pH6.5) Cy3-NHS (pH 8.1) Bodipy-NHS (pH 8.1) Bodipy-NHS (pH 6.5)	Cy3-NHS (pH6.5) Cy3-NHS (pH 8.1) Bodipy-NHS (pH 8.1) Bodipy-NHS (pH 6.5)	Cy3-NHS (pH6.5)

Table B-2: Experimental groups

B.3. Results

The first step of the investigation was to identify a molecular rotor that is sensitive to changes in clot fibre structure. Fluorescence lifetimes were monitored during clotting for 6 free dyes and 2 fibrin-conjugated dyes, in 3 different clot models (whole blood-, plasma- and fibrin-based).

B.3.1. Preliminary experiments

Autofluorescence

In the conditions of image acquisition, blood and plasma autofluorescence did not interfere with the measurements (data not shown).

Function of dye conjugates

Fibrin conjugation has not affected the ability of the rotors to function as a viscosity sensor. As expected, fluorescent lifetimes of the rotor are similar in water and in blood, and they increase with increasing glycerol content. (data not shown)

Dies in solvent

Presence of proteins in the biological solvents (blood or plasma) did not significantly affect rotor function (data not shown).

B.3.2. Free dye

The six molecular rotors were each aliquoted to a well, for a final concentration of 0.75 μL/mL for $DiSC_2(3)$, Sq5, KR, and B++, and 1.25 μL/mL for BC10 and ThT.

Lifetime measurements during clotting were carried out in 3 distinct clot models, with 6 different molecular rotors in each model. No significant and repeatable change was observed (data not shown). A new approach was adopted, directly conjugating the molecular rotors to the fibrinogen monomers so as to achieve co-localisation of the fibrin fibres and the viscosity sensors.

B.3.3. Labelled fibrinogen monomers

In this approach, four types of fibrin-conjugated molecular rotors were investigated. Figure B-1shows examples of clot samples formed with the labelled fibrinogen monomers. This confirms that the fibrinogen was successfully labelled, and that after clotting most of the molecular rotors were localized in or near the fibres.

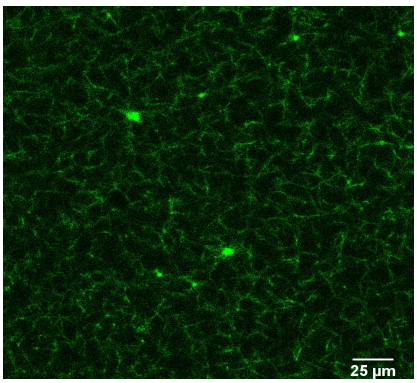


Figure B-1: Confocal images of fibrin network in human blood with conjugated dyes: (c) Bodipy-NHS prepared at pH 6.5.

As in the previous section, fluorescence lifetime was monitored during coagulation. Figure B-2 and Figure B-3 show the phasor diagrams of the conjugated rotors in whole blood clots and in plasma clots respectively. For Bodipy conjugates in whole blood, images were taken at multiple locations in the clot before and after clotting. In all other cases, a single image was taken at the same positon before and after.

For all molecular rotors (with the exception of Bodipy prepared at pH 6.5 and used in plasma clots), small changes in lifetime were observed in both clot models. The differences were however not judged sufficient to qualify the conjugates as useful sensors of fibre structure.

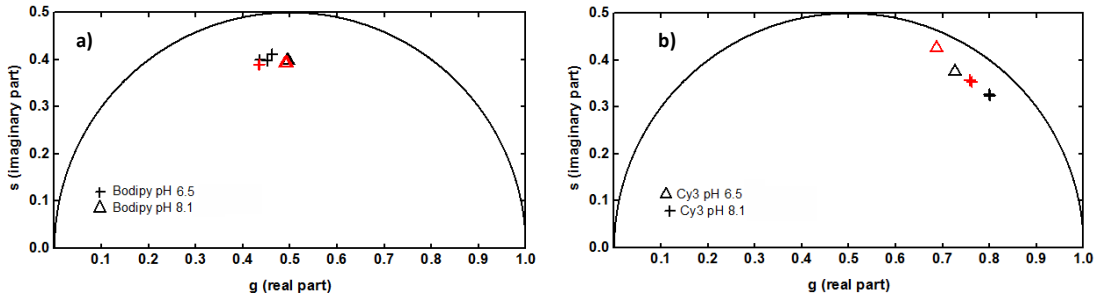


Figure B-2 : Phasor plot of fibrin-conjugated dyes in plasma before and after clotting (black and red markers respectively): a) Bodipy-NHS; b) Cy3-NHS

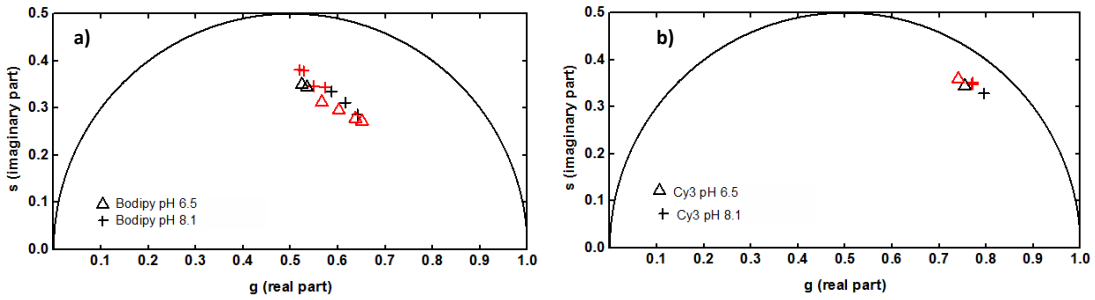


Figure B-3: Phasor plot of fibrin-conjugated dyes in whole blood before and after clotting (black and red markers respectively): a) Bodipy-NHS; b) Cy3-NHS

B.4. Conclusion

Fluorescence lifetime imaging with viscosity-sensitive molecular rotors is an attractive method to probe molecular structures in real-time. Possible applications include sonothrombolysis, where the effect of ultrasound on fibrin networks is not fully understood.

A suitable molecular rotor was sought by observing fluorescence lifetime changes during coagulation, where drastic transformations in structure occur: fibrinogen polymerizes into fibrils which then assemble into fibres. However, no suitable rotor could be identified. The technique is therefore not appropriate for investigating the changes in fibrin structure during ultrasound exposure. In Appendix C, another technique is examined: spectral imaging with polarity-sensitive fluorescent probes.

APPENDIX C

Effect of ultrasound on the structure of fibrin: spectral imaging

This appendix describes the rationale and protocol for using polarity-sensitive dyes to probe the effect of ultrasound exposure on fibrin structure. The results are shown and discussed in Chapter 5.

C.1. Rationale

The objective of this preliminary study was to investigate the effect of ultrasound on fibrin structure.

With scanning electron microscopy, Braaten *et al.* noted reversible changes in non-cross-linked fibre gels during exposure to ultrasound. Specifically, a shift was observed towards a denser network composed of thinner fibres [277]. Chernysh *et al*. reached similar conclusions using turbidity measurements; using deconvolution microscopy and recovery after photo-bleaching, the authors also reported real-time observation on the spatial organisation of the fibrin network [265]. However, the molecular mechanisms responsible for these changes are largely unknown, and real-time spatial information is necessary to probe the structure of individual fibrin fibres during and after ultrasound exposure.

Confocal imaging with environment sensitive probes is a promising approach to investigate the molecular structure of fibrin polymers. Polarity sensitive fluorescent probes

are frequently used to quantify lipid packing in artificial and biological membranes such as liposomes, giant unilamellar vesicles, or live cells [279], [280], [299]. These dyes are sensitive to the order of their immediate environment and experience a shift in emission spectrum between ordered and disordered phases (red-shift in the disordered phase). Among the possible probes, Di-4-AN(F)EPPTEA (FE)10, was chosen for this study because of its high photostability, which makes it suitable for confocal imaging [279].

C.2. Protocol

C.2.1. Materials

Phosphate-buffered saline (PBS), fibrinogen from bovine plasma, calcium chloride dehydrate and thrombin from bovine plasma were purchased from Sigma Aldrich Corporation, St Louis, MO, USA. Thrombin was dissolved at a concentration of 100 NIH units/mL in TNE buffer (0.15 mol/L NaCl and 0.01 mol/L Tris-HCl, adjusted to pH 7.4). The FE dye was obtained from Dr Sezgin, from the Weatherall Institute of Molecular Medicine at the University of Oxford.

C.2.2. Methods

Non-cross-linked, unretracted clots were prepared in 8-well chamber slides. In each well, 165µL of clot solution were prepared with fibrinogen, calcium chloride and thrombin in PBS at a final concentration of 9.9×10^{-3} mol/L, 2.4×10^{-2} mol/L and 1.15 NIH units/mL respectively. The clots were incubated for 10 minutes at 37°C, then covered in FE dye, at 5:1000 volume dilution in PBS. The dye solution was incubated with the clots for a further 10 minutes at room temperature, with regular mixing to enhance dye penetration. The clots were then washed in PBS three times.

[10] FE is a derivative of Di-4-ANEPPDHQ, a probe designed initially as a voltage-sensitive dye. It was developed by Kwiatek *et al.*[302].

The clots were imaged by confocal microscopy before and immediately after exposure to ultrasound.

Confocal microscopy was carried out with a Zeiss LSM/FCS setup with 488 nm laser excitation. Spectral lambda imaging between was performed in the 509-684 nm wavelength range with the GaAsP detector . The wavelength interval for each step was set to 8.3 nm.

Ultrasound treatment consisted in a 60 second exposure to 22.5 kHz ultrasound, applied with an ultrasonic cell disruptor (Microson XL, Misonix Inc., Farmingdale, NY, USA) operating at level 2.

The contribution of Dr Erdinc Sezgin to the design and preparation of the experiment is gratefully acknowledged.

APPENDIX D

Transcranial sound field characterisation

D.1. Objectives

The aim of this study was to investigate the sound field created in the hippocampus by exposure to 0.5 MHz focused ultrasound through the temporal bone window.

This investigation was carried out as part of a feasibility study for ultrasound stimulation of the hippocampus, with clinical applications in neural modulation and memory enhancement.

The hippocampus is constituted by two symmetrical regions located in the medial temporal lobes, close to the posterior cerebral artery and a few centimetres posterior to the middle cerebral artery.

D.2. Methods

D.2.1. Experimental methods

The experiments were carried out in a tank of degassed, deionised water maintained at 37°C with an immersion heater (Grant Instruments, Shepreth, UK). The ultrasound exposure was provided by 0.5 MHz transducer (Sonic Concepts, Bothell, WA, USA) in continuous wave mode. The pressure field was mapped with a fibre optic hydrophone (Precision Acoustics, Dorchester, UK) mounted on a computer-controlled three-axis

translation system (Precision Acoustics), centred at the focus of the transducer in the free field.

A half skull from a human cadaver (sagittal cut) was placed between the HIFU transducer and the hydrophone, with the temporal bone in front of the transducer. The skull was positioned so that the hippocampus region, as indicated by markers in the internal bone structure, coincided with the fibre optic hydrophone (Figure D-1). The region of incidence of the ultrasound beam on the temporal bone was verified using a 532 nm laser pointer.

Before the experiment, the skull was degassed in a vacuum chamber filled with deionized water for 24h to minimise its gas content.

D.2.2. Numerical simulation

The three dimensional structure of the skull was acquired from CT scans. It was then used to simulate the transcranial field by a finite elements method in the PZFlex software (Weidlinger Associates Inc, New York, NY, USA). The contribution of Dr Shan Qiao in the numerical simulation is gratefully acknowledged.

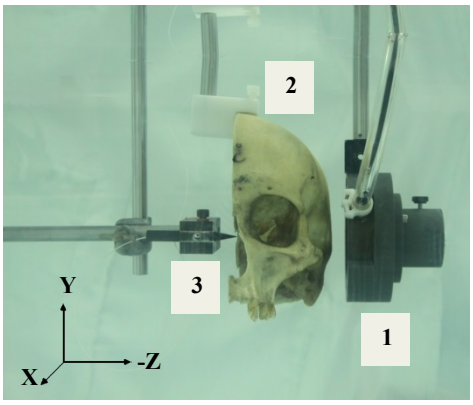


Figure D-1: images of the experimental setup: front view of the 0.5 MHz HIFU transducer (1), the human half skull with a sagittal section (2), and the fibre optic hydrophone (3), with orientation of the axes.

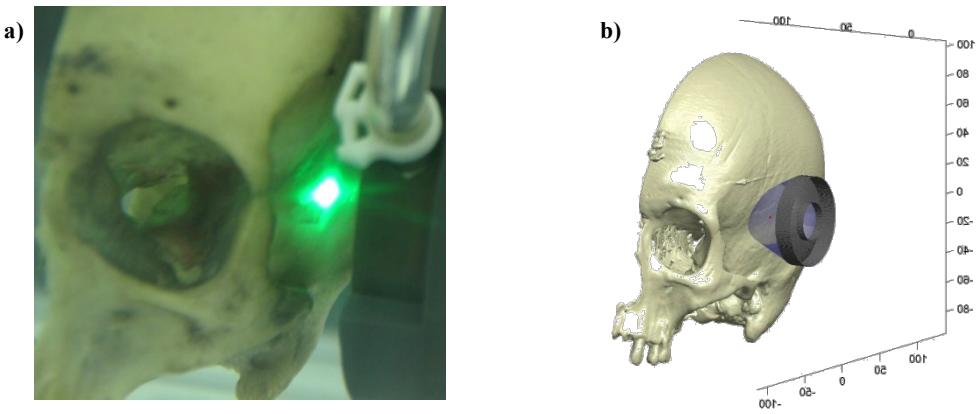


Figure D-2: experimental and numerical alignment of the transducer: a) side view of the experimental apparatus, with laser beam (green) used for skull positioning; b) numerical alignment of the skull with the transducer.

D.3. Results and discussion

Good agreement was achieved in the positioning of the skull between the numerical model and the experiments (Figure D-2).

The presence of the skull was responsible for considerable loss in pressure compared to the free field (-60%, see Figure D-3) In addition, substantial aberrations were noted in the axial and transaxial planes, including a shift of the main peak by 1 mm in the axial direction and a distortion in the side lobes. Qualitatively, the shapes of the measured and simulated ultrasound fields were also in close agreement.

These observations (distortion of the field and loss in pressure) are further discussed in Chapter 5.

D.4. Conclusion

Successful transcranial insonation of the hippocampus was achieved through the temporal bone, with distortions of the field and a 65% loss in pressure at the focus. Transcranial insonation of the middle cerebral artery is expected to yield similar observations.

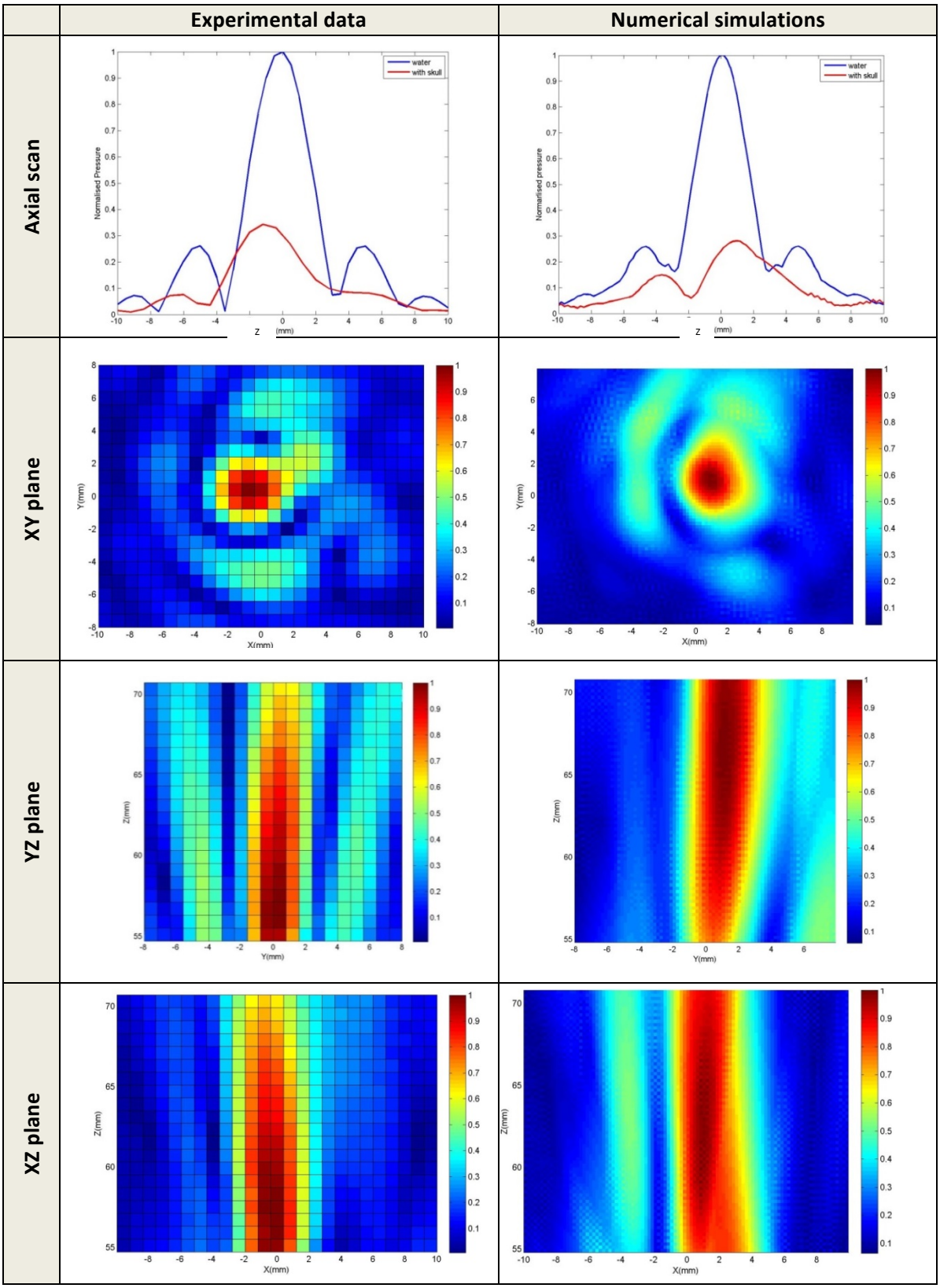


Figure D-3: Experimental and numerical characterisation of the ultrasound field created in the hippocampus by transcranial insonation through the temporal bone window at 0.5 MHz. Top pane: axial scan (Z direction), in the presence of the skull (in red) compared to the free field (in blue). Second pane: transaxial plane (XY). Bottom two panes: axial planes (YZ and XZ).

References

[1] A. V. Alexandrov, C. A. Molina, J. C. Grotta, et al., "Ultrasound-Enhanced Systemic Thrombolysis for Acute Ischemic Stroke," *N. Engl. J. Med.*, vol. 351, pp. 2170–8, 2004.

[2] C. a. Molina, A. D. Barreto, G. Tsivgoulis, et al., "Transcranial ultrasound in clinical sonothrombolysis (TUCSON) trial," *Ann. Neurol.*, vol. 66, no. 1, pp. 28–38, 2009.

[3] D. Cosgrove and C. Harvey, "Clinical uses of microbubbles in diagnosis and treatment," *Med. Biol. Eng. Comput.*, vol. 47, no. 8, pp. 813–826, 2009.

[4] J. R. Lindner, "Microbubbles in medical imaging: current applications and future directions.," *Nat. Rev. Drug Discov.*, vol. 3, no. 6, pp. 527–532, 2004.

[5] K. Ferrara, R. Pollard, and M. Borden, "Ultrasound microbubble contrast agents: fundamentals and application to gene and drug delivery.," *Annu. Rev. Biomed. Eng.*, vol. 9, pp. 415–447, 2007.

[6] T. Truelsen, S. Begg, and C. Mathers, "The global burden of cerebrovascular disease," 2001.

[7] V. L. Feigin, C. M. M. Lawes, D. a Bennett, et al., "Review Stroke epidemiology : a review of population- based studies of incidence , prevalence, and case-fatality in the late 20th century," vol. 2, no. January, pp. 43–53, 2003.

[8] J. H. Rha and J. L. Saver, "The impact of recanalization on ischemic stroke outcome: A meta-analysis," *Stroke*, vol. 38, no. 3, pp. 967–973, 2007.

[9] National Institute for Health and Care Excellence, "Stroke and transient ischaemic attack in over 16s : diagnosis and initial management," 2008.

[10] US Food and Drug Aministration, "Alteplase Product Approval Information - Licensing Action 6/18/96," *Sba*. 1996.

[11] American College of Emergency Physicians & American Academy of Neurology, "Clinical policy: Use of intravenous tPA for the management of acute ischemic stroke in the emergency department," *Ann. Emerg. Med.*, vol. 61, no. 2, pp. 225–243, 2013.

[12] NINDS rt-PA Stroke Study Group, "Tissue plasminogen activator for acute ischemic stroke. The National Institute of Neurological Disorders and Stroke rt-PA Stroke Study Group.," *N. Engl. J. Med.*, vol. 333, no. 24, pp. 1581–7, 1995.

[13] P. Barber, J. Zhang, A. Demchuk, et al., "Why are stroke patients excluded from TPA therapy? An analysis of patient eligibility.," *Neurology*, vol. 56, no. 8, pp. 1015–1020, 2001.

[14] California Acute Stroke Pilot Registry Investigators, "Prioritizing interventions to improve rates of thrombolysis for ischemic stroke.," *Neurology*, vol. 64, no. 4, pp. 654–659, 2005.

[15] F. Xie, J. Lof, C. Everbach, et al., "Treatment of Acute Intravascular Thrombi With Diagnostic Ultrasound and Intravenous Microbubbles," *JACC Cardiovasc. Imaging*, vol. 2, no. 4, pp. 511–518, 2009.

[16] S. Kutty, J. Wu, J. M. Hammel, et al., "Microbubble Mediated Thrombus Dissolution with Diagnostic Ultrasound for the Treatment of Chronic Venous Thrombi," *PLoS One*, vol. 7, no. 12, 2012.

[17] W. C. Culp, T. R. Porter, F. Xie, et al., "Microbubble potentiated ultrasound as a method of declotting thrombosed dialysis grafts: Experimental study in dogs," *Cardiovasc. Intervent. Radiol.*, vol. 24, no. 6, pp. 407–412, 2001.

[18] G. Trübestein, C. Engel, F. Etze, et al., "Thrombolysis by ultrasound.," *Clin. Sci. Mol. Meidicine . Suppl.*, vol. 3, pp. 697–698, 1976.

[19] K. Tachibana and S. Tachibana, "Albumin microbubble echo-contrast material as an enhancer for ultrasound accelerated thrombolysis.," *Circulation*, vol. 92, no. 5, pp. 1148–1150, 1995.

[20] C. W. Francis, P. T. Önundarson, E. L. Carstensen, et al., "Enhancement of fibrinolysis in vitro by ultrasound," *J. Clin. Invest.*, vol. 90, no. 5, pp. 2063–2068, 1992.

[21] W. C. Culp, R. Flores, A. T. Brown, et al., "Successful microbubble sonothrombolysis without tissue-type plasminogen activator in a rabbit model of acute ischemic stroke," *Stroke*, vol. 42, no. 8, pp. 2280–2285, 2011.

[22] J. E. Leeman, J. S. Kim, F. T. H. Yu, et al., "Effect of Acoustic Conditions on Microbubble-Mediated Microvascular Sonothrombolysis," *Ultrasound Med. Biol.*, vol. 38, no. 9, pp. 1589–1598, 2012.

[23] S. Datta, C. C. Coussios, A. Y. Ammi, et al., "Ultrasound-Enhanced Thrombolysis Using Definity® as a Cavitation Nucleation Agent," *Ultrasound Med. Biol.*, vol. 34, no. 9, pp. 1421–1433, 2008.

[24] F. Perren, J. Loulidi, D. Poglia, et al., "Microbubble potentiated transcranial duplex ultrasound enhances IV thrombolysis in acute stroke," *J. Thromb. Thrombolysis*, vol. 25, no. 2,

pp. 219–223, 2008.

[25] C. A. Molina, M. Ribo, M. Rubiera, et al., "Microbubble administration accelerates clot lysis during continuous 2-MHz ultrasound monitoring in stroke patients treated with intravenous tissue plasminogen activator," *Stroke*, vol. 37, no. 2, pp. 425–429, 2006.

[26] A. Alonso, C. E. Dempfle, A. Della Martina, et al., "In vivo clot lysis of human thrombus with intravenous abciximab immunobubbles and ultrasound," *Thromb. Res.*, vol. 124, no. 1, pp. 70–74, 2009.

[27] F. Xie, J. Lof, T. Matsunaga, et al., "Diagnostic ultrasound combined with glycoprotein IIb/IIIa-targeted microbubbles improves microvascular recovery after acute coronary thrombotic occlusions," *Circulation*, vol. 119, no. 10, pp. 1378–1385, 2009.

[28] Y. Wu, E. C. Unger, T. P. McCreery, et al., "Binding and lysing of blood clots using MRX-408," *Invest Radiol*, vol. 33, no. 12, pp. 880–885, 1998.

[29] A. Alonso, A. Della Martina, M. Stroick, et al., "Molecular imaging of human thrombus with novel abciximab immunobubbles and ultrasound," *Stroke*, vol. 38, no. 5, pp. 1508–1514, 2007.

[30] M. J. Martin, E. M. L. Chung, A. H. Goodall, et al., "Enhanced detection of thromboemboli with the use of targeted microbubbles," *Stroke*, vol. 38, no. 10, pp. 2726–2732, 2007.

[31] M. de Saint Victor, C. Crake, C.-C. Coussios, et al., "Properties, characteristics and applications of microbubbles for sonothrombolysis.," *Expert Opin. Drug Deliv.*, vol. 11, no. 2, pp. 187–209, 2014.

[32] P. Cintas, F. Nguyen, B. Boneu, et al., "Enhancement of enzymatic fibrinolysis with 2-MHz ultrasound and microbubbles," *J. Thromb. Haemost.*, vol. 2, no. 7, pp. 1163–1166, 2004.

[33] A. F. Prokop, A. Soltani, and R. Roy, "Cavitational Mechanisms in Ultrasound-Accelerated Fibrinolysis," *Ultrasound Med. Biol.*, vol. 33, no. 6, pp. 924–933, 2007.

[34] T. R. Porter, R. F. LeVeen, R. Fox, et al., "Thrombolytic enhancement with perfluorocarbon-exposed sonicated dextrose albumin microbubbles," *Am. Heart J.*, vol. 132, no. 5, pp. 964–968, 1996.

[35] J. T. Sutton, N. M. Ivancevich, S. R. Perrin, et al., "Clot Retraction Affects the Extent of Ultrasound-Enhanced Thrombolysis in an Ex Vivo Porcine Thrombosis Model," *Ultrasound Med. Biol.*, vol. 39, no. 5, pp. 813–824, 2013.

[36] I. Kondo, K. Mizushige, T. Ueda, et al., "Histological observations and the process of ultrasound contrast agent enhancement of tissue plasminogen activator thrombolysis with ultrasound exposure.," *Jpn. Circ. J.*, vol. 63, no. 6, pp. 478–484, 1999.

[37] B. Petit, E. Gaud, D. Colevret, et al., "In Vitro Sonothrombolysis of Human Blood Clots with BR38 Microbubbles," *Ultrasound Med. Biol.*, vol. 38, no. 7, pp. 1222–1233, 2012.

[38] T. R. Porter, D. Kricsfeld, J. Lof, et al., "Effectiveness of transcranial and transthoracic ultrasound and microbubbles in dissolving intravascular thrombi.," *J. Ultrasound Med.*, vol. 20, no. 12, pp. 1313–1325; quiz 1326, 2001.

[39] W. T. Shi, J. E. Powers, A. L. Klibanov, et al., "In vitro investigation of thrombosis dissolution with microbubble-induced continuous acoustic activities," *Proc. - IEEE Ultrason. Symp.*, pp. 1985–1988, 2007.

[40] A. T. Brown, R. Flores, E. Hamilton, et al., "Microbubbles Improve Sonothrombolysis In Vitro and Decrease Hemorrhage In Vivo in a Rabbit Stroke Model," *Invest. Radiol.*, vol. 46, no. 3, pp. 202–207, 2011.

[41] M. Nedelmann, N. Ritschel, S. Doenges, et al., "Combined contrast-enhanced ultrasound and rt-PA treatment is safe and improves impaired microcirculation after reperfusion of middle cerebral artery occlusion.," *J. Cereb. Blood Flow Metab.*, vol. 30, no. 10, pp. 1712–1720, 2010.

[42] J. J. Pacella, J. Brands, F. G. Schnatz, et al., "Treatment of microvascular micro-embolization using microbubbles and long-tone-burst ultrasound: An invivo study," *Ultrasound Med. Biol.*, vol. 41, no. 2, pp. 456–464, 2015.

[43] M. Saqqur, G. Tsivgoulis, F. Nicoli, et al., "The Role of Sonolysis and Sonothrombolysis in Acute Ischemic Stroke: A Systematic Review and Meta-analysis of Randomized Controlled Trials and Case-Control Studies.," *J. Neuroimaging*, pp. 1–12, 2013.

[44] A. Viguier, R. Petit, M. Rigal, et al., "Continuous monitoring of middle cerebral artery recanalization with transcranial color-coded sonography and Levovist," *J. Thromb. Thrombolysis*, vol. 19, no. 1, pp. 55–59, 2005.

[45] A. V. Alexandrov, R. Mikulik, M. Ribo, et al., "A pilot randomized clinical safety study of sonothrombolysis augmentation with ultrasound-activated perflutren-lipid microspheres for acute ischemic stroke," *Stroke*, vol. 39, no. 5, pp. 1464–1469, 2008.

[46] M. Reinhard, C. A. Taschner, N. Horsch, et al., "Endovascular Treatment versus Sonothrombolysis for Acute Ischemic Stroke," *Cerebrovasc. Dis.*, vol. 40, no. 5–6, pp. 205–214, 2015.

[47] A. Nacu, C. Kvistad, N. Logallo, et al., "A pragmatic approach to sonothrombolysis in acute ischaemic stroke: the Norwegian randomised controlled sonothrombolysis in acute stroke study (NOR-SASS)," *BMC Neurol.*, 2015.

[48] E. Stride, "Physical principles of microbubbles for ultrasound imaging and therapy," *Cerebrovasc. Dis.*, vol. 27, no. SUPPL. 2, pp. 1–13, 2009.

[49] E. C. Everbach and C. W. Francis, "Cavitational mechanisms in ultrasound-accelerated thrombolysis at 1 MHz," *Ultrasound Med. Biol.*, vol. 26, no. 7, pp. 1153–1160, 2000.

[50] S. Datta, C. C. Coussios, L. E. McAdory, et al., "Correlation of cavitation with ultrasound enhancement of thrombolysis," *Ultrasound Med. Biol.*, vol. 32, no. 8, pp. 1257–1267, 2006.

[51] R. E. Apfel, "The Role of Impurities in Cavitation-Threshold Determination," *J. Acoust. Soc. Am.*, vol. 48, no. 5B, p. 1179, 1970.

[52] K. E. Hitchcock, N. M. Ivancevich, K. J. Haworth, et al., "Ultrasound-Enhanced rt-PA Thrombolysis in an ex vivo Porcine Carotid Artery Model," *Ultrasound Med. Biol.*, vol. 37, no. 8, pp. 1240–1251, 2011.

[53] J. S. Kim, J. E. Leeman, L. Kagemann, et al., "Volumetric quantification of in vitro sonothrombolysis with microbubbles using high-resolution optical coherence tomography.," *J. Biomed. Opt.*, vol. 17, no. 7, p. 070502, 2012.

[54] D. V Sakharov, R. T. Hekkenberg, and D. C. Rijken, "Acceleration of Fibrinolysis by High-frequency Ultrasound," *Thromb. Res.*, vol. 100, no. 4, pp. 333–340, 2000.

[55] S. Pfaffenberger, B. Devcic-Kuhar, K. El-Rabadi, et al., "2MHz ultrasound enhances t-PA-mediated thrombolysis: Comparison of continuous versus pulsed ultrasound and standing versus travelling acoustic waves," *Thromb. Haemost.*, vol. 89, no. 3, pp. 583–589, 2003.

[56] C. K. Holland, S. S. Vaidya, S. Datta, et al., "Ultrasound-enhanced tissue plasminogen activator thrombolysis in an in vitro porcine clot model," *Thromb. Res.*, vol. 121, no. 5, pp. 663–673, 2008.

[57] H. L. Weiss, P. Selvaraj, K. Okita, et al., "Mechanical clot damage from cavitation during sonothrombolysis.," *J. Acoust. Soc. Am.*, vol. 133, no. 5, pp. 3159–75, 2013.

[58] J. H. Hwang, J. Tu, A. A. Brayman, et al., "Correlation between inertial cavitation dose and endothelial cell damage in vivo," *Ultrasound Med. Biol.*, vol. 32, no. 10, pp. 1611–1619, 2006.

[59] M. A. Yenari, J. Palmer, P. Bracci, et al., "Thrombolysis with tissue plasminogen activator (tPA) is temperature dependent," *Thromb. Res.*, vol. 77, no. 5, pp. 475–481, 1995.

[60] A. Blinc, C. W. Francis, J. L. Trudnowski, et al., "Characterization of ultrasound-potentiated fibrinolysis in vitro.," *Blood*, vol. 81, no. 10, pp. 2636–2643, 1993.

[61] J. Eggers, I. R. König, B. Koch, et al., "Sonothrombolysis with transcranial color-coded sonography and recombinant tissue-type plasminogen activator in acute middle cerebral artery main stem occlusion: Results from a randomized study," *Stroke*, vol. 39, no. 5, pp. 1470–1475, 2008.

[62] D. Skoloudik, M. Bar, O. Skoda, et al., "Safety and Efficacy of the Sonographic Acceleration of the Middle Cerebral Artery Recanalization: Results of the pilot Thrombotripsy Study," *Ultrasound Med. Biol.*, vol. 34, no. 11, pp. 1775–1782, 2008.

[63] A. Soltani, K. R. Volz, and D. R. Hansmann, "Effect of modulated ultrasound parameters on ultrasound-induced thrombolysis.," *Phys. Med. Biol.*, vol. 53, no. 23, pp. 6837–6847, 2008.

[64] Y. H. Chuang, P. W. Cheng, and P. C. Li, "Combining radiation force with cavitation for enhanced sonothrombolysis," *IEEE Trans. Ultrason. Ferroelectr. Freq. Control*, vol. 60, no. 1, pp. 97–104, 2013.

[65] C. Acconcia, B. Y. C. Leung, K. Hynynen, et al., "Interactions between ultrasound stimulated microbubbles and fibrin clots," *Appl. Phys. Lett.*, vol. 103, 2013.

[66] V. N. Suchkova, R. B. Baggs, S. K. Sahni, et al., "Ultrasound improves tissue perfusion in ischemic tissue through a nitric oxide dependent mechanism," *Thromb. Haemost.*, vol. 88, no. 5, pp. 865–870, 2002.

[67] C. M. Davis, A. Y. Ammi, N. J. Alkayed, et al., "Ultrasound stimulates formation and release of vasoactive compounds in brain endothelial cells," *Am. J. Physiol. - Hear. Circ. Physiol.*, vol. 309, no. 4, pp. H583–H591, 2015.

[68] M. Rubiera, M. Ribo, R. Delgado-Mederos, et al., "Do Bubble Characteristics Affect Recanalization in Stroke Patients Treated with Microbubble-Enhanced Sonothrombolysis?," *Ultrasound Med. Biol.*, vol. 34, no. 10, pp. 1573–1577, 2008.

[69] F. Xie, J. M. Tsutsui, J. Lof, et al., "Effectiveness of lipid microbubbles and ultrasound in declotting thrombosis," *Ultrasound Med. Biol.*, vol. 31, no. 7, pp. 979–985, 2005.

[70] V. Nahirnyak, T. D. Mast, and C. K. Holland, "Ultrasound-Induced Thermal Elevation in Clotted Blood and Cranial Bone," *Ultrasound Med. Biol.*, vol. 33, no. 8, pp. 1285–1295, 2007.

[71] F. J. Fry and J. E. Barger, "Acoustical properties of

the human skull.," *J. Acoust. Soc. Am.*, vol. 63, no. 5, pp. 1576–1590, 1978.

[72] A. Y. Ammi, T. D. Mast, I. H. Huang, et al., "Characterization of Ultrasound Propagation Through Ex-vivo Human Temporal Bone," *Ultrasound Med. Biol.*, vol. 34, no. 10, pp. 1578–1589, 2008.

[73] G. T. Clement, J. Sun, T. Giesecke, et al., "A hemisphere array for non-invasive ultrasound brain therapy and surgery.," *Phys. Med. Biol.*, vol. 45, no. 12, pp. 3707–19, 2000.

[74] C. Baron, J. F. Aubry, M. Tanter, et al., "Simulation of Intracranial Acoustic Fields in Clinical Trials of Sonothrombolysis," *Ultrasound Med. Biol.*, vol. 35, no. 7, pp. 1148–1158, 2009.

[75] M. J. Borrelli, W. D. O'Brien, E. Hamilton, et al., "Influences of microbubble diameter and ultrasonic parameters on in vitro sonothrombolysis efficacy," *J. Vasc. Interv. Radiol.*, vol. 23, no. 12, pp. 1677–1684, 2012.

[76] J. Owen, B. Zhou, P. Rademeyer, et al., "Understanding the structure and mechanism of formation of a new magnetic microbubble formulation.," *Theranostics*, vol. 2, no. 12, pp. 1127–1139, 2012.

[77] A. OK-Saracco, P. Aspelin, K. Leifland, et al., "Bolus Compared with Continuous Infusion of Microbubble Contrast Agent Using Real-Time Contrast Harmonic Imaging Ultrasound in Breast Tumors," *Acta radiol.*, vol. 50, no. 8, pp. 854–859, 2009.

[78] M. Okada, C. W. Hoffmann, K. J. Wolf, et al., "Bolus versus continuous infusion of microbubble contrast agent for liver US: initial experience.," *Radiology*, vol. 237, no. 3, pp. 1063–7, 2005.

[79] J. M. Correas, P. N. Burns, X. Lai, et al., "Infusion versus bolus of an ultrasound contrast agent: in vivo dose-response measurements of BR1.," *Invest. Radiol.*, vol. 35, no. 1, pp. 72–79, 2000.

[80] K. Wei, R. Jayaweera, S. Firoozan, et al., "Quantification of myocardial blood flow with ultrasound-induced destruction of microbubbles administered as a constant venous infusion.," *Circulation*, vol. 97, no. 5, pp. 473–483, 1998.

[81] F. Xie, J. Slikkerveer, S. Gao, et al., "Coronary and microvascular thrombolysis with guided diagnostic ultrasound and microbubbles in acute ST segment elevation myocardial infarction.," *J. Am. Soc. Echocardiogr.*, vol. 24, no. 12, pp. 1400–8, 2011.

[82] European Medical Agency, "Sonovue: Summary of Product Characteristics.," 2006.

[83] D. Bokor, J. B. Chambers, P. J. Rees, et al., "Clinical safety of SonoVue, a new contrast agent for ultrasound imaging, in healthy volunteers and in patients with chronic obstructive pulmonary disease.," *Invest Radiol*, vol. 36, no. 2, pp. 104–109, 2001.

[84] P. Grayburn, J. L. Weiss, T. C. Hack, et al., "Phase III multicenter trial comparing the efficacy of 2% dodecafluoropentane emulsion (EchoGen) and sonicated 5% human albumin (Albunex) as ultrasound contrast agents in patients with suboptimal echocardiograms," *J. Am. Coll. Cardiol.*, vol. 32, no. 1, pp. 230–236, 1998.

[85] C. Wright, K. Hynynen, and D. Goertz, "In Vitro and In Vivo High Intensity Focused Ultrasound Thrombolysis," *Invest. Radiol.*, vol. 47, no. 4, pp. 217–225, 2012.

[86] A. D. Maxwell, C. A. Cain, A. P. Duryea, et al., "Noninvasive Thrombolysis Using Pulsed Ultrasound Cavitation Therapy - Histotripsy," *Ultrasound Med. Biol.*, vol. 35, no. 12, pp. 1982–1994, 2009.

[87] M. Ariani, M. C. Fishbein, J. S. Chae, et al., "Dissolution of peripheral arterial thrombi by ultrasound.," *Circulation*, vol. 84, no. 4, pp. 1680–1688, 1991.

[88] D. M. Kent, J. Hinchey, L. L. Price, et al., "In acute ischemic stroke, are asymptomatic intracranial hemorrhages clinically innocuous?," *Stroke*, vol. 35, no. 5. pp. 1141–1146, 2004.

[89] The NINDS t-PA Stroke Study Group, "Intracerebral Hemorrhage After Intravenous t-PA Therapy for Ischemic Stroke," *Stroke*, vol. 28, no. 11, pp. 2109–2118, 1997.

[90] X. Wang, K. Tsuji, S.-R. Lee, et al., "Mechanisms of hemorrhagic transformation after tissue plasminogen activator reperfusion therapy for ischemic stroke.," *Stroke.*, vol. 35, no. 11 Suppl 1, pp. 2726–2730, 2004.

[91] M. Daffertshofer, A. Gass, P. Ringleb, et al., "Transcranial low-frequency ultrasound-mediated thrombolysis in brain ischemia: Increased risk of hemorrhage with combined ultrasound and tissue plasminogen activator - Results of a phase II clinical trial," *Stroke*, vol. 36, no. 7, pp. 1441–1446, 2005.

[92] W. M. Clark, G. W. Albers, K. P. Madden, et al., "The rtPA (Alteplase) 0- to 6-Hour Acute Stroke Trial, Part A (A0276g) : Results of a Double-Blind, Placebo-Controlled, Multicenter Study," *Stroke*, vol. 31, no. 4, pp. 811–816, 2000.

[93] R. E. Apfel and C. K. Holland, "Gauging the likelihood of cavitation from short-pulse, low-duty cycle diagnostic ultrasound," *Ultrasound Med. Biol.*, vol. 17, no. 2, pp. 179–185, 1991.

[94] J. Sponer, "Dependence of the cavitation threshold on the ultrasonic frequency," *Czechoslov. J. Phys.*,

vol. 40, no. 10, pp. 1123–1132, 1990.

[95] M. Reinhard, A. Hetzel, S. Krüger, et al., "Blood-brain barrier disruption by low-frequency ultrasound," *Stroke*, vol. 37, no. 6, pp. 1546–1548, 2006.

[96] Z. Wang, M. a. Moehring, A. H. Voie, et al., "In Vitro Evaluation of Dual Mode Ultrasonic Thrombolysis Method for Transcranial Application with an Occlusive Thrombosis Model," *Ultrasound Med. Biol.*, vol. 34, no. 1, pp. 96–102, 2008.

[97] S. Meairs, R. Kern, and A. Alonso, "Why and how do microbubbles enhance the effectiveness of diagnostic and therapeutic interventions in cerebrovascular disease?," *Curr Pharm Des*, vol. 18, no. 15, pp. 2223–2235, 2012.

[98] W. S. Chen, A. A. Brayman, T. J. Matula, et al., "The pulse length-dependence of inertial cavitation dose and hemolysis," *Ultrasound Med. Biol.*, vol. 29, no. 5, pp. 739–748, 2003.

[99] J. M. Meunier, C. K. Holland, C. J. Lindsell, et al., "Duty Cycle Dependence of Ultrasound Enhanced Thrombolysis in a Human Clot Model," *Ultrasound Med. Biol.*, vol. 33, no. 4, pp. 576–583, 2007.

[100] V. Frenkel, J. Oberoi, M. J. Stone, et al., "Pulsed high-intensity focused ultrasound enhances thrombolysis in an in vitro model.," *Radiology*, vol. 239, no. 1, pp. 86–93, 2006.

[101] J. Tu, T. J. Matula, A. A. Brayman, et al., "Inertial cavitation dose produced in ex vivo rabbit ear arteries with Optison by 1-MHz pulsed ultrasound," *Ultrasound Med. Biol.*, vol. 32, no. 2, pp. 281–288, 2006.

[102] X. Chen, J. Wang, J. J. Pacella, et al., "Dynamic Behavior of Microbubbles during Long Ultrasound Tone-Burst Excitation: Mechanistic Insights into Ultrasound-Microbubble Mediated Therapeutics Using High-Speed Imaging and Cavitation Detection.," *Ultrasound Med. Biol.*, vol. 42, no. 2, pp. 528–38, 2016.

[103] S. Schäfer, S. Kliner, L. Klinghammer, et al., "Influence of ultrasound operating parameters on ultrasound-induced thrombolysis in vitro," *Ultrasound Med. Biol.*, vol. 31, no. 6, pp. 841–847, 2005.

[104] J. E. Chomas, P. Dayton, J. Alien, et al., "Mechanisms of contrast agent destruction," *IEEE Trans. Ultrason. Ferroelectr. Freq. Control*, vol. 48, no. 1, pp. 232–248, 2001.

[105] C. C. Church, "Frequency, pulse length, and the mechanical index," *Acoust. Res. Lett. Online*, vol. 6, no. 3, p. 162, 2005.

[106] W. D. O'Brien, "Ultrasound-biophysics mechanisms," *Progress in Biophysics and Molecular Biology*, vol. 93, no. 1–3. pp. 212–255, 2007.

[107] J. B. Fowlkes and L. a Crum, "Cavitation threshold measurements for microsecond length pulses of ultrasound.," *J. Acoust. Soc. Am.*, vol. 83, no. 6, pp. 2190–2201, 1988.

[108] S. D. Tiukinhoy-Laing, S. Huang, M. Klegerman, et al., "Ultrasound-facilitated thrombolysis using tissue-plasminogen activator-loaded echogenic liposomes," *Thromb. Res.*, vol. 119, no. 6, pp. 777–784, 2007.

[109] D. Smith, S. Vaidya, J. Kopechek, et al., "Ultrasound-Triggered Release of Recombinant Tissue-Type Plasminogen Activator from Echogenic Liposomes," *Ultrasound Med. Biol.*, vol. 36, no. 1, pp. 145–157, 2010.

[110] L. A. Crum and G. M. Hansen, "Growth of air bubbles in tissue by rectified diffusion.," *Phys. Med. Biol.*, vol. 27, no. 3, pp. 413–417, 1982.

[111] C. C. Church and W. D. O'Brien, "Evaluation of the Threshold for Lung Hemorrhage by Diagnostic Ultrasound and a Proposed New Safety Index," *Ultrasound Med. Biol.*, vol. 33, no. 5, pp. 810–818, 2007.

[112] M. Ribo, C. A. Molina, B. Alvarez, et al., "Intra-arterial administration of microbubbles and continuous 2-MHz ultrasound insonation to enhance intra-arterial thrombolysis," *J. Neuroimaging*, vol. 20, no. 3, pp. 224–227, 2010.

[113] K. Mizushige, I. Kondo, K. Ohmori, et al., "Enhancement of ultrasound-accelerated thrombolysis by echo contrast agents: Dependence on microbubble structure," *Ultrasound Med. Biol.*, vol. 25, no. 9, pp. 1431–1437, 1999.

[114] M. R. Dhond, T. T. Nguyen, C. Dolan, et al., "Ultrasound-enhanced thrombolysis at 20 kHz with air-filled and perfluorocarbon-filled contrast bispheres," *J. Am. Soc. Echocardiogr.*, vol. 13, no. 11, pp. 1025–1029, 2000.

[115] M. Postema, "Optically Observed Microbubble Coalescence and Collapse," in *IEEE Ultrasonics Symposium*, 2002, pp. 1949–1952.

[116] M. A. Borden, D. E. Kruse, C. F. Caskey, et al., "Influence of lipid shell physicochemical properties on ultrasound-induced microbubble destruction," *IEEE Trans. Ultrason. Ferroelectr. Freq. Control*, vol. 52, no. 11, pp. 1992–2002, 2005.

[117] L. Dinia, M. Rubiera, M. Ribo, et al., "Reperfusion after stroke sonothrombolysis with microbubbles may predict intracranial bleeding.," *Neurology*, vol. 73, no. 10, pp. 775–780, 2009.

[118] J. Pagola, M. Ribo, J. Alvarez-Sabín, et al., "Timing of recanalization after microbubble-enhanced intravenous thrombolysis in basilar artery

occlusion," *Stroke*, vol. 38, no. 11, pp. 2931–2934, 2007.

[119] J. Slikkerveer, S. a. Kleijn, Y. Appelman, et al., "Ultrasound enhanced prehospital thrombolysis using microbubbles infusion in patients with acute st elevation myocardial infarction: Pilot of the sonolysis study," *Ultrasound Med. Biol.*, vol. 38, no. 2, pp. 247–252, 2012.

[120] D. Sanak, R. Herzig, D. Skoloudik, et al., "The safety and efficacy of continuous transcranial duplex doppler monitoring of middle cerebral artery occlusion in acute stroke patients: Comparison of TCDD and thrombolysis in MCA recanalization," *J. Neuroimaging*, vol. 20, no. 1, pp. 58–63, 2010.

[121] T. Nishioka, H. Luo, M. C. Fishbein, et al., "Dissolution of thrombotic arterial occlusion by high intensity, low frequency ultrasound and dodecafluoropentane emulsion: An in vitro and in vivo study," *J. Am. Coll. Cardiol.*, vol. 30, no. 2, pp. 561–568, 1997.

[122] R. Flores, L. J. Hennings, J. D. Lowery, et al., "Microbubble-augmented ultrasound sonothrombolysis decreases intracranial hemorrhage in a rabbit model of acute ischemic stroke.," *Invest. Radiol.*, vol. 46, no. 7, pp. 419–24, 2011.

[123] J. M. Tsutsui, F. Xie, and J. Johanning, "Ultrasound Guided by Diagnostic Ultrasound and Intravenous Microbubbles," *J. ultrasound Med.*, vol. 25, pp. 1161–1168, 2006.

[124] W. C. Culp, T. R. Porter, T. C. McCowan, et al., "Microbubble-augmented ultrasound declotting of thrombosed arteriovenous dialysis grafts in dogs," *J Vasc Interv Radiol*, vol. 14, no. 3, pp. 343–347, 2003.

[125] W. C. Culp, T. R. Porter, J. Lowery, et al., "Intracranial clot lysis with intravenous microbubbles and transcranial ultrasound in swine," *Stroke*, vol. 35, no. 10, pp. 2407–2411, 2004.

[126] Y. Birnbaum, H. Luo, T. Nagai, et al., "Noninvasive in vivo clot dissolution without a thrombolytic drug: recanalization of thrombosed iliofemoral arteries by transcutaneous ultrasound combined with intravenous infusion of microbubbles.," *Circulation*, vol. 97, no. 2, pp. 130–134, 1998.

[127] X. B. Zhou, H. Qin, J. Li, et al., "Platelet-targeted microbubbles inhibit re-occlusion after thrombolysis with transcutaneous ultrasound and microbubbles," *Ultrasonics*, vol. 51, no. 3, pp. 270–274, 2011.

[128] M. Fatar, M. Stroick, M. Griebe, et al., "Effect of Combined Ultrasound and Microbubbles Treatment in an Experimental Model of Cerebral Ischemia," *Ultrasound Med. Biol.*, vol. 34, no. 9, pp. 1414–1420, 2008.

[129] M. Stroick, A. Alonso, M. Fatar, et al., "Effects of simultaneous application of ultrasound and microbubbles on intracerebral hemorrhage in an animal model," *Ultrasound Med. Biol.*, vol. 32, no. 9, pp. 1377–1382, 2006.

[130] A. Moumouh, L. Barentin, F. Tranquart, et al., "Fibrinolytic Effects of Transparietal Ultrasound Associated with Intravenous Infusion of an Ultrasound Contrast Agent: Study of a Rat Model of Acute Cerebral Stroke," *Ultrasound Med. Biol.*, vol. 36, no. 1, pp. 51–57, 2010.

[131] W. S. Liu, Z. Z. Huang, X. W. Wang, et al., "Effects of microbubbles on transcranial Doppler ultrasound-assisted intracranial urokinase thrombolysis," *Thromb. Res.*, vol. 130, no. 3, pp. 547–551, 2012.

[132] S. T. Laing, M. R. Moody, H. Kim, et al., "Thrombolytic efficacy of tissue plasminogen activator-loaded echogenic liposomes in a rabbit thrombus model," *Thromb. Res.*, vol. 130, no. 4, pp. 629–635, 2012.

[133] S. Kutty, F. Xie, S. Gao, et al., "Sonothrombolysis of intra-catheter aged venous thrombi using microbubble enhancement and guided three-dimensional ultrasound pulses," *J. Am. Soc. Echocardiogr.*, vol. 23, no. 9, pp. 1001–1006, 2010.

[134] T. Holscher, R. Raman, K. Ernström, et al., "In vitro sonothrombolysis with duplex ultrasound: first results using a simplified model.," *Cerebrovasc. Dis.*, vol. 28, no. 4, pp. 365–70, 2009.

[135] M. D. Torno, M. D. Kaminski, Y. Xie, et al., "Improvement of in vitro thrombolysis employing magnetically-guided microspheres," *Thromb. Res.*, vol. 121, no. 6, pp. 799–811, 2008.

[136] W. S. Chen, A. A. Brayman, T. J. Matula, et al., "Inertial cavitation dose and hemolysis produced in vitro with or without Optison," *Ultrasound Med. Biol.*, vol. 29, no. 5, pp. 725–737, 2003.

[137] A. Soltani, R. Singhal, M. Obtera, et al., "Potentiating intra-arterial sonothrombolysis for acute ischemic stroke by the addition of the ultrasound contrast agents (Optison & SonoVue)," *J. Thromb. Thrombolysis*, vol. 31, no. 1, pp. 71–84, 2011.

[138] A. Becker, E. Marxer, J. Brüßler, et al., "Ultrasound active nanoscaled lipid formulations for thrombus lysis," *Eur. J. Pharm. Biopharm.*, vol. 77, no. 3, pp. 424–429, 2011.

[139] Y.-H. Chuang, P.-W. Cheng, S.-C. Chen, et al.,

"Effects of ultrasound-induced inertial cavitation on enzymatic thrombolysis.," *Ultrason. Imaging*, vol. 32, no. 2, pp. 81–90, 2010.

[140] S. C. Chen, J. L. Ruan, P. W. Cheng, et al., "In vitro evaluation of ultrasound-assisted thrombolysis using targeted ultrasound contrast agents," *Ultrason. Imaging*, pp. 235–246, 2009.

[141] G. J. Shaw, J. M. Meunier, S. L. Huang, et al., "Ultrasound-enhanced thrombolysis with tPA-loaded echogenic liposomes," *Thromb. Res.*, vol. 124, no. 3, pp. 306–310, 2009.

[142] X. Hua, P. Liu, Y. H. Gao, et al., "Construction of thrombus-targeted microbubbles carrying tissue plasminogen activator and their in vitro thrombolysis efficacy: A primary research," *J. Thromb. Thrombolysis*, vol. 30, no. 1, pp. 29–35, 2010.

[143] H. Jin, H. Tan, L. Zhao, et al., "Ultrasound-triggered thrombolysis using urokinase-loaded nanogels," *Int. J. Pharm.*, vol. 434, no. 1–2, pp. 384–390, 2012.

[144] S. T. Ren, H. Zhang, Y. W. Wang, et al., "The Preparation of a New Self-Made Microbubble-Loading Urokinase and Its Thrombolysis Combined with Low-Frequency Ultrasound In Vitro," *Ultrasound Med. Biol.*, vol. 37, no. 11, pp. 1828–1837, 2011.

[145] D. L. Miller and R. A. Gies, "Enhancement of ultrasonically-induced hemolysis by perfluorocarbon- based compared to air-based echo-contrast agents," *Ultrasound Med. Biol.*, vol. 24, no. 2, pp. 285–292, 1998.

[146] M. W. Miller, E. C. Everbach, C. Cox, et al., "A comparison of the hemolytic potential of Optison and Albunex in whole human blood in vitro: Acoustic pressure, ultrasound frequency, donor and passive cavitation detection considerations," *Ultrasound Med. Biol.*, vol. 27, no. 5, pp. 709–721, 2001.

[147] P. S. Sidhu, P. L. Allan, F. Cattin, et al., "Diagnostic efficacy of SonoVue®, a second generation contrast agent, in the assessment of extracranial carotid or peripheral arteries using colour and spectral Doppler ultrasound: A multicentre study," *Br. J. Radiol.*, vol. 79, no. 937, pp. 44–51, 2006.

[148] J. Romagnuolo, B. Hoffman, S. Vela, et al., "Accuracy of contrast-enhanced harmonic EUS with a second-generation perflutren lipid microsphere contrast agent (with video)," *Gastrointest. Endosc.*, vol. 73, no. 1, pp. 52–63, 2011.

[149] X. Wang, C. E. Hagemeyer, J. D. Hohmann, et al., "Novel single-chain antibody-targeted microbubbles for molecular ultrasound imaging of thrombosis: Validation of a unique noninvasive method for rapid and sensitive detection of thrombi and monitoring of success or failure of thrombolysis in mice," *Circulation*, vol. 125, no. 25, pp. 3117–3126, 2012.

[150] A. Della Martina, E. Allémann, T. Bettinger, et al., "Grafting of abciximab to a microbubble-based ultrasound contrast agent for targeting to platelets expressing GP IIb/IIIa - Characterization and in vitro testing," *Eur. J. Pharm. Biopharm.*, vol. 68, no. 3, pp. 555–564, 2008.

[151] P. Schumann, J. P. Christiansen, R. M. Quigley, et al., "Targeted-microbubble binding selectively to GPIIb IIIa receptors of platelet thrombi.," *Invest. Radiol.*, vol. 37, no. 11, pp. 587–593, 2002.

[152] E. C. Unger, T. P. McCreery, R. H. Sweitzer, et al., "In vitro studies of a new thrombus-specific ultrasound contrast agent.," *Am. J. Cardiol.*, vol. 81, no. 12A, p. 58G–61G, 1998.

[153] W. M. Xu, M. Feng, H. Y. Zhao, et al., "Preparation of thrombosis-targeted lipid microbubbles and determination of rabbit carotid artery thrombosis by microbubbles ultrasonogaphy," *J. Huazhong Univ. Sci. Technol. - Med. Sci.*, vol. 33, no. 1, pp. 146–152, 2013.

[154] P. Dayton, A. Klibanov, G. Brandenburger, et al., "Acoustic radiation force in vivo: A mechanism to assist targeting of microbubbles," *Ultrasound Med. Biol.*, vol. 25, no. 8, pp. 1195–1201, 1999.

[155] J. J. Rychak, A. L. Klibanov, K. F. Ley, et al., "Enhanced Targeting of Ultrasound Contrast Agents Using Acoustic Radiation Force," *Ultrasound Med. Biol.*, vol. 33, no. 7, pp. 1132–1139, 2007.

[156] S. Zhao, M. Borden, S. H. Bloch, et al., "Radiation-force assisted targeting facilitates ultrasonic molecular imaging," vol. 3, no. 3, pp. 135–148, 2004.

[157] P. Rademeyer, "A new technique for microbubble characterisation and the implications to contrast enhanced ultrasound," University of Oxford, 2015.

[158] A. Senyei, K. Widder, and G. Czerlinski, "Magnetic guidance of drug-carrying microspheres," *J. Appl. Phys.*, vol. 49, no. 6, pp. 3578–3583, 1978.

[159] S. Lübbe, C. Bergemann, H. Riess, et al., "Clinical experiences with magnetic drug targeting: a phase I study with 4'-epidoxorubicin in 14 patients with advanced solid tumors.," *Cancer Res.*, vol. 56, no. 20, pp. 4686–4693, 1996.

[160] A. N. Rusetski and E. K. Ruuge, "Magnetic fluid as a possible drug carrier for thrombosis treatment," *J. Magn. Magn. Mater.*, vol. 85, no. 1–3, pp. 299–302, 1990.

[161] E. Stride, C. Porter, A. G. Prieto, et al., "Enhancement of Microbubble Mediated Gene Delivery by Simultaneous Exposure to Ultrasonic and Magnetic Fields," *Ultrasound Med. Biol.*, vol. 35, no. 5, pp. 861–868, 2009.

[162] H. Mulvana, R. J. Eckersley, R. Browning, et al., "Enhanced gene transfection in vivo using magnetic localisation of ultrasound contrast agents: Preliminary results," *2010 IEEE Int. Ultrason. Symp.*, pp. 670–673, 2010.

[163] H. Mannell, J. Pircher, T. Räthel, et al., "Targeted endothelial gene delivery by ultrasonic destruction of magnetic microbubbles carrying lentiviral vectors," *Pharm. Res.*, vol. 29, no. 5, pp. 1282–1294, 2012.

[164] S. Huth, J. Lausier, S. W. Gersting, et al., "Insights into the mechanism of magnetofection using PEI-based magnetofectins for gene transfer," *J. Gene Med.*, vol. 6, no. 8, pp. 923–936, 2004.

[165] S. C. McBain, H. H. P. Yiu, and J. Dobson, "Magnetic nanoparticles for gene and drug delivery," *International Journal of Nanomedicine*, vol. 3, no. 2. pp. 169–180, 2008.

[166] C. Crake, M. de Saint Victor, C. Coviello, et al., "Passive acoustic mapping of magnetic microbubbles in an in vitro flow model.," in *21st International Congress on Acoustics, Journal of the Acoustical Society of America*, 2013.

[167] Q. Cao, X. Han, and L. Li, "Enhancement of the efficiency of magnetic targeting for drug delivery: Development and evaluation of magnet system," *J. Magn. Magn. Mater.*, vol. 323, no. 15, pp. 1919–1924, 2011.

[168] S. Nishijima, F. Mishima, Y. Tabata, et al., "Research and Development of Magnetic Drug Delivery System Using Bulk High Temperature Superconducting Magnet," *IEEE Trans. Appl. Supercond.*, vol. 19, no. 3, pp. 2257–2260, 2009.

[169] J. O. Mangual, S. Li, H. J. Ploehn, et al., "Biodegradable nanocomposite magnetite stent for implant-assisted magnetic drug targeting," *J. Magn. Magn. Mater.*, vol. 322, no. 20, pp. 3094–3100, 2010.

[170] N. Pei, Z. Huang, W. Ma, et al., "In vitro study of deep capture of paramagnetic particle for targeting therapeutics," *J. Magn. Magn. Mater.*, vol. 321, no. 18, pp. 2911–2915, 2009.

[171] S. Takeda, F. Mishima, S. Fujimoto, et al., "Development of magnetically targeted drug delivery system using superconducting magnet," *J. Magn. Magn. Mater.*, vol. 311, no. 1, pp. 367–371, 2007.

[172] B. Shapiro, "Towards dynamic control of magnetic fields to focus magnetic carriers to targets deep inside the body," *J. Magn. Magn. Mater.*, vol. 321, no. 10, pp. 1594–1599, 2009.

[173] S. C. McBain, U. Griesenbach, S. Xenariou, et al., "Magnetic nanoparticles as gene delivery agents: enhanced transfection in the presence of oscillating magnet arrays.," *Nanotechnology*, vol. 19, no. 40, p. 405102, 2008.

[174] D. B. Baruah, R. N. Dash, M. R. Chaudhari, et al., "Plasminogen activators: A comparison," *Vascul. Pharmacol.*, vol. 44, no. 1, pp. 1–9, 2006.

[175] I. Lentacker, S. C. De Smedt, and N. N. Sanders, "Drug loaded microbubble design for ultrasound triggered delivery," *Soft Matter*, vol. 5, no. 11, p. 2161, 2009.

[176] E. C. Unger, T. Porter, W. Culp, et al., "Therapeutic applications of lipid-coated microbubbles," *Advanced Drug Delivery Reviews*, vol. 56, no. 9. pp. 1291–1314, 2004.

[177] S. S. Margossian, H. S. Slayter, E. Kaczmarek, et al., "Physical characterization of recombinant tissue plasminogen activator.," *Biochim. Biophys. Acta*, vol. 1163, no. 3, pp. 250–6, 1993.

[178] Y. Mu, L. Li, and G. Ayoufu, "Experimental study of the preparation of targeted microbubble contrast agents carrying urokinase and RGDS," *Ultrasonics*, vol. 49, no. 8, pp. 676–681, 2009.

[179] J. L. M. Heeremans, R. Prevost, M. E. A. Bekkers, et al., "Thrombolytic treatment with tissue-type plasminogen activator (t-PA) containing liposomes in rabbits: A comparison with free t-PA," *Thromb. Haemost.*, vol. 73, no. 3, pp. 488–494, 1995.

[180] I. Lentacker, B. Geers, J. Demeester, et al., "Design and evaluation of doxorubicin-containing microbubbles for ultrasound-triggered doxorubicin delivery: cytotoxicity and mechanisms involved.," *Mol. Ther.*, vol. 18, no. 1, pp. 101–108, 2010.

[181] S. D. Tiukinhoy-Laing, K. Buchanan, D. Parikh, et al., "Fibrin targeting of tissue plasminogen activator-loaded echogenic liposomes.," *J. Drug Target.*, vol. 15, no. 2, pp. 109–114, 2007.

[182] M. D. Kaminski, Y. Xie, C. J. Mertz, et al., "Encapsulation and release of plasminogen activator from biodegradable magnetic microcarriers," *Eur. J. Pharm. Sci.*, vol. 35, no. 1–2, pp. 96–103, 2008.

[183] D. Pajek, A. Burgess, Y. Huang, et al., "High-Intensity Focused Ultrasound Sonothrombolysis: The Use of Perfluorocarbon Droplets to Achieve Clot Lysis at Reduced Acoustic Power," *Ultrasound Med. Biol.*, vol. 40, no. 9, pp. 2151–2161, 2014.

[184] N. Rapoport, K. H. Nam, R. Gupta, et al., "Ultrasound-mediated tumor imaging and nanotherapy using drug loaded, block copolymer

stabilized perfluorocarbon nanoemulsions," in *Journal of Controlled Release*, 2011, vol. 153, no. 1, pp. 4–15.

[185] J. Y. Lee, D. Carugo, C. Crake, et al., "Nanoparticle-Loaded Protein-Polymer Nanodroplets for Improved Stability and Conversion Efficiency in Ultrasound Imaging and Drug Delivery," *Adv. Mater.*, vol. 27, no. 37, pp. 5484–5492, 2015.

[186] R. Kern, A. Diels, J. Pettenpohl, et al., "Real-time ultrasound brain perfusion imaging with analysis of microbubble replenishment in acute MCA stroke.," *J. Cereb. Blood Flow Metab.*, vol. 31, no. 8, pp. 1716–1724, 2011.

[187] S. H. Rezkalla and R. A. Kloner, "No-reflow phenomenon," *Circulation*, vol. 105, no. 5, pp. 656–662, 2002.

[188] J. L. Anderson, "Why does thrombolysis fail? Breaking through the reperfusion ceiling," *Am. J. Cardiol.*, vol. 80, no. 12, p. 1588–&, 1997.

[189] D. M. Wootton and D. N. Ku, "Fluid mechanics of vascular systems, diseases, and thrombosis.," *Annu. Rev. Biomed. Eng.*, vol. 1, pp. 299–329, 1999.

[190] H. Snow, "Conway Review Lecture 2001 Atheroma and the mechanics of blood flow in arteries," *Ir. J. Med. Sci.*, vol. 171, no. 3, pp. 165–169, 2001.

[191] M. Tehrani and J. Yoon, "A Novel Scheme for Nanoparticle Steering in Blood Vessels Using a Functionalized Magnetic Field," *IEEE Trans. Biomed. Eng.*, vol. 62, no. 1, pp. 303–313, 2015.

[192] E. M. Cherry and J. K. Eaton, "A comprehensive model of magnetic particle motion during magnetic drug targeting," *Int. J. Multiph. Flow*, vol. 59, pp. 173–185, 2014.

[193] J. Owen, P. Rademeyer, D. Chung, et al., "Magnetic targeting of microbubbles against physiologically relevant flow conditions," *Interface Focus*, vol. 5, no. 5, p. 20150001, Oct. 2015.

[194] J. H. Chesebro, G. Knatterud, R. Roberts, et al., "Thrombolysis in Myocardial Infarction (TIMI) Trial, Phase I: A comparison between intravenous tissue plasminogen activator and intravenous streptokinase. Clinical findings through hospital discharge.," *Circulation*, vol. 76, no. 1, pp. 142–154, 1987.

[195] Y. C. Fung, *Biomechanics: Circulation*, 2nd ed. Springer-Verlag New York, 1997.

[196] T. F. Sherman, "On connecting large vessels to small. The meaning of Murray's law.," *J. Gen. Physiol.*, vol. 78, no. 4, pp. 431–453, 1981.

[197] S. Chikazumi, *Physics of Ferromagnetism*, vol. 1, no. 11. 1997.

[198] M. E. Young, P. A. Carroad, and R. L. Bell, "Estimation of diffusion coefficients of proteins," *Biotechnol. Bioeng.*, vol. 22, no. 5, pp. 947–955, 1980.

[199] L. C. Barnsley, D. Carugo, J. Owen, et al., "Halbach arrays consisting of cubic elements optimised for high field gradients in magnetic drug targeting applications," *Phys. Med. Biol.*, vol. 60, no. 21, pp. 8303–8327, 2015.

[200] M. T. Tyn and T. W. Gusek, "Prediction of diffusion coefficients of proteins," *Biotechnol. Bioeng.*, vol. 35, no. 4, pp. 327–338, 1990.

[201] L. Mullin, R. Gessner, J. Kwan, et al., "Effect of anesthesia carrier gas on in vivo circulation times of ultrasound microbubble contrast agents in rats," *Contrast Media Mol. Imaging*, vol. 6, no. 3, pp. 126–131, 2011.

[202] T. B. Jones, *Electromechanics of particles*. Cambridge University Press, 1995.

[203] Y. H. Ghallab and W. Badawy, *Lab-on-a-chip: Techniques, Circuits, and Biomedical Applications*. Boston, MA: Artech House, 2010.

[204] C. P. Bean and J. D. Livingston, "Superparamagnetism," *J. Appl. Phys.*, vol. 30, no. 4, pp. S120–S129, 1959.

[205] L. C. Barnsley, D. Carugo, and E. Stride, "Optimized shapes of magnetic arrays for drug targeting applications," *J. Phys. D. Appl. Phys.*, vol. in press, 2015.

[206] D. Carugo, J. Y. Lee, A. Pora, et al., "Facile and cost-effective production of microscale PDMS architectures using a combined micromilling-replica moulding (μMi-REM) technique.," *Biomed. Microdevices*, vol. 18, no. 1, 2016.

[207] ELVESYS Microfluidic Innovation Center, "Syringe pumps and microfluidics," 2015. [Online]. Available: http://www.elveflow.com/microfluidic-tutorials/microfluidic-reviews-and-tutorials/syringe-pumps-and-microfluidics/. [Accessed: 01-Feb-2015].

[208] J. Owen, "Magnetic Microbubbles: investigation and design of new formulations for targeted therapy," University of Oxford, 2014.

[209] C. Sennoga, V. Mahue, J. Loughran, et al., "On sizing and counting of microbubbles using optical microscopy," *Ultrasound Med. Biol.*, vol. 36, no. 12, pp. 2093–2096, 2010.

[210] H. Mulvana, R. J. Eckersley, M. X. Tang, et al., "Theoretical and Experimental Characterisation of Magnetic Microbubbles," *Ultrasound Med. Biol.*, vol. 38, no. 5, pp. 864–875, 2012.

[211] D. Carugo, "Development of microfluidic systems

for therapeutic applications," University of Southampton, 2012.

[212] B. Verhaagen, C. Boutsioukis, C. P. Sleutel, et al., "Irrigant transport into dental microchannels," *Microfluid. Nanofluidics*, vol. 16, pp. 1165–1177, Oct. 2013.

[213] K. Svanes and B. W. Zweifach, "Variations in small blood vessel hematocrits produced in hypothermic rats by micro-occlusion," *Microvasc. Res.*, vol. 1, no. 2, pp. 210–220, 1968.

[214] M. Kersaudy-Kerhoas and E. Sollier, "Micro-scale blood plasma separation: from acoustophoresis to egg-beaters.," *Lab Chip*, vol. 13, no. 17, pp. 3323–46, 2013.

[215] R. D. Jaeggi, R. Sandoz, and C. S. Effenhauser, "Microfluidic depletion of red blood cells from whole blood in high-aspect-ratio microchannels," *Microfluid. Nanofluidics*, vol. 3, no. 1, pp. 47–53, 2007.

[216] H. W. Hou, A. A. S. Bhagat, W. C. Lee, et al., "Microfluidic devices for blood fractionation," *Micromachines*, vol. 2, no. 3, pp. 319–343, 2011.

[217] M. Sinclair, J. Lee, A. Schuster, et al., "Microsphere skimming in the porcine coronary arteries: Implications for flow quantification.," *Microvasc. Res.*, vol. 100, pp. 59–70, 2015.

[218] M. J. Borrelli, W. D. O'Brien, E. Hamilton, et al., "Influences of microbubble diameter and ultrasonic parameters on in vitro sonothrombolysis efficacy," *J. Vasc. Interv. Radiol.*, vol. 23, no. 12, pp. 1677–1684, 2012.

[219] J. Owen, P. Grove, P. Rademeyer, et al., "The influence of blood on targeted microbubbles," *J. R. Soc. Interface*, vol. 11, 2014.

[220] D. Jones, *Diffusion MRI: Theory, Methods, and Applications*. Oxford University Press, 2010.

[221] J. F. Schenck, "Safety of strong, static magnetic fields," *Journal of Magnetic Resonance Imaging*, vol. 12, no. 1. pp. 2–19, 2000.

[222] J. S. Stroud, S. a Berger, and D. Saloner, "Numerical analysis of flow through a severely stenotic carotid artery bifurcation.," *J. Biomech. Eng.*, vol. 124, no. 1, pp. 9–20, 2002.

[223] S. A. Berger and L.-D. Jou, "Flows in Stenotic Vessels," *Annu. Rev. Fluid Mech.*, vol. 32, no. 1, pp. 347–382, 2000.

[224] M. J. Borrelli, W. D. O'Brien, E. Hamilton, et al., "Influences of microbubble diameter and ultrasonic parameters on in vitro sonothrombolysis efficacy," *J. Vasc. Interv. Radiol.*, vol. 23, no. 12, pp. 1677–1684, 2012.

[225] P. Cintas, A. P. Le Traon, and V. Larrue, "High rate of recanalization of middle cerebral artery occlusion during 2-MHz transcranial color-coded doppler continuous monitoring without thrombolytic drug," *Stroke*, vol. 33, no. 2, pp. 626–628, 2002.

[226] J. M. Serrador, P. a Picot, B. K. Rutt, et al., "MRI measures of middle cerebral artery diameter in conscious humans during simulated orthostasis.," *Stroke.*, vol. 31, no. 7, pp. 1672–1678, 2000.

[227] M. Demchuk, W. S. Burgin, I. Christou, et al., "Thrombolysis in Brain Ischemia (TIBI) Transcranial Doppler Flow Grades Predict Clinical Severity, Early Recovery, and Mortality in Patients Treated With Intravenous Tissue Plasminogen Activator," *Stroke*, vol. 32, no. 1, pp. 89–93, 2001.

[228] T. Ogata, K. Kimura, M. Nakajima, et al., "Transcranial color-coded real-time sonographic criteria for occlusion of the middle cerebral artery in acute ischemic stroke.," *AJNR. Am. J. Neuroradiol.*, vol. 25, no. 10, pp. 1680–4, 2004.

[229] G. Vilahur, T. Padro, and L. Badimon, "Atherosclerosis and thrombosis: Insights from large animal models," *Journal of Biomedicine and Biotechnology*. pp. 1–12, 2011.

[230] R. Engel-Herbert and T. Hesjedal, "Calculation of the magnetic stray field of a uniaxial magnetic domain," *J. Appl. Phys.*, vol. 97, no. 7, 2005.

[231] N. Hockham, C. C. Coussios, and M. Arora, "A real-time controller for sustaining thermally relevant acoustic cavitation during ultrasound therapy," *IEEE Trans. Ultrason. Ferroelectr. Freq. Control*, vol. 57, no. 12, pp. 2685–2694, 2010.

[232] M. Nedelmann, C. Brandt, F. Schneider, et al., "Ultrasound-induced blood clot dissolution without a thrombolytic drug is more effective with lower frequencies," *Cerebrovasc. Dis.*, vol. 20, no. 1, pp. 18–22, 2005.

[233] M. Nedelmann, P. Reuter, M. Walberer, et al., "Detrimental effects of 60 kHz sonothrombolysis in rats with middle cerebral artery occlusion.," *Ultrasound Med. Biol.*, vol. 34, no. 12, pp. 2019–2027, 2008.

[234] S. M. Graham, R. Carlisle, J. J. Choi, et al., "Inertial cavitation to non-invasively trigger and monitor intratumoral release of drug from intravenously delivered liposomes," *J. Control. Release*, vol. 178, pp. 101–107, 2014.

[235] P. Morris, A. Hurrell, A. Shaw, et al., "A Fabry-Perot fiber-optic ultrasonic hydrophone for the simultaneous measurement of temperature and acoustic pressure.," *J. Acoust. Soc. Am.*, vol. 125, no. 6, pp. 3611–3622, 2009.

[236] J. Y. Chueh, A. K. Wakhloo, G. H. Hendricks, et al., "Mechanical characterization of thromboemboli in acute ischemic stroke and laboratory embolus

analogs," *Am. J. Neuroradiol.*, vol. 32, no. 7, pp. 1237–1244, 2011.

[237] J. J. Rychak, A. L. Klibanov, and J. A. Hossack, "Acoustic radiation force enhances targeted delivery of ultrasound contrast microbubbles: In vitro verification," *IEEE Trans. Ultrason. Ferroelectr. Freq. Control*, vol. 52, no. 3, pp. 421–432, 2005.

[238] N. de Jong, A. Bouakaz, and P. Frinking, "Basic acoustic properties of microbubbles.," *Echocardiography*, vol. 19, no. 3, pp. 229–40, 2002.

[239] U. O. Häfeli, K. Gilmour, A. Zhou, et al., "Modeling of magnetic bandages for drug targeting: Button vs. Halbach arrays," *J. Magn. Magn. Mater.*, vol. 311, no. 1 SPEC. ISS., pp. 323–329, 2007.

[240] B. Petit, Y. Bohren, E. Gaud, et al., "Sonothrombolysis: The Contribution of Stable and Inertial Cavitation to Clot Lysis," *Ultrasound Med. Biol.*, vol. 41, no. 5, pp. 1402–1410, 2015.

[241] J. Oliver, D. Webb, and D. Newby, "Stimulated tissue plasminogen activator release as a marker of endothelial function in humans.," *Arterioscler. Thromb. Vasc. Biol.*, vol. 25, pp. 219–223, 2005.

[242] V. J. Marder, D. J. Chute, S. Starkman, et al., "Analysis of thrombi retrieved from cerebral arteries of patients with acute ischemic stroke," *Stroke*, vol. 37, no. 8, pp. 2086–2093, 2006.

[243] H. Mulvana, S. Cochran, and M. Hill, "Ultrasound assisted particle and cell manipulation on-chip," *Adv. Drug Deliv. Rev.*, vol. 65, no. 11–12, pp. 1600–1610, 2013.

[244] G. J. Jaffe, G. D. Green, and G. Abrams, "Stability of recombinant tissue plasminogen activator," *Am. J. Ophtalmol.*, vol. 108, pp. 90–91, 1989.

[245] A. Alkatheri, "Stability of recombinant tissue plasminogen activator at -30 C over one year," *Pharmaceuticals*, vol. 6, no. 1, pp. 25–31, 2013.

[246] C. Longstaff, C. Thelwell, S. C. Williams, et al., "The interplay between tissue plasminogen activator domains and fibrin structures in the regulation of fibrinolysis: Kinetic and microscopic studies," *Blood*, vol. 117, no. 2, pp. 661–668, 2011.

[247] D. C. Rijken, M. Hoylaerts, and D. Collen, "Fibrinolytic Properties of One-chain and Two-chain Human Extrinsic (Tissue-type) Plasminogen Activator," *J. Biol. Chem.*, vol. 257, no. 6, pp. 2920–2925, 1982.

[248] M. Mleczko, S. M. Dicker, S. P. Wrenn, et al., "Influence of Microbubble Shell Chemistry on the Destruction Threshold of Ultrasound Contrast Agent Microbubbles," in *Acoustical Imaging*, vol. 31, 2012, pp. 91–101.

[249] K. B. Bader, G. Bouchoux, T. Peng, et al., "Thrombolytic efficacy and enzymatic activity of rt-PA-loaded echogenic liposomes," *J. Thromb. Thrombolysis*, pp. 144–155, 2015.

[250] F. Bajd and I. Serša, "Mathematical modeling of blood clot fragmentation during flow-mediated thrombolysis," *Biophys. J.*, vol. 104, no. 5, pp. 1181–1190, 2013.

[251] S. Pfaffenberger, B. Devcic-Kuhar, C. Kollmann, et al., "Can a commercial diagnostic ultrasound device accelerate thrombolysis?: An in vitro skull model," *Stroke*, vol. 36, no. 1, pp. 124–128, 2005.

[252] G. Bouchoux, T. A. Shivashankar, , Ravishankar Abruzzo, and C. K. Holland, "In silico study of low-frequency transcranial ultrasound fields in acute ischemic stroke patients," *Ultrasound Med. Biol.*, vol. 40, no. 6, pp. 1154–66, 2014.

[253] J. J. Choi and C.-C. Coussios, "Spatiotemporal evolution of cavitation dynamics exhibited by flowing microbubbles during ultrasound exposure.," *J. Acoust. Soc. Am.*, vol. 132, no. 5, pp. 3538–49, 2012.

[254] E. Lyka, C. Coviello, R. Kozick, et al., "A sum-of-harmonics time-domain method to distinguish harmonic and broadband signals during passive acoustic mapping of ultrasound therapies," in *Journal of the Acoustical Society of America*, 2015, p. 2399.

[255] A. A. Jarquin-Valdivia, J. McCartney, D. Palestrant, et al., "The thickness of the temporal squama and its implication for transcranial sonography.," *J. Neuroimaging*, vol. 14, no. 2, pp. 139–142, 2004.

[256] T. Itoh, M. Matsumoto, N. Handa, et al., "Rate of successful recording of blood flow signals in the middle cerebral artery using transcranial Doppler sonography," *Stroke*, vol. 24, no. 8, pp. 1192–1195, 1993.

[257] D. N. White, J. M. Clark, and M. N. White, "Studies in ultrasonic echoencephalography. VII. General principles of recording information in ultrasonic B- and C-scanning and the effects of scatter, reflection and refraction by cadaver skull on this information.," *Med. Biol. Eng.*, vol. 5, pp. 3–14, 1967.

[258] M. Gyöngy and C.-C. Coussios, "Passive cavitation mapping for localization and tracking of bubble dynamics.," *J. Acoust. Soc. Am.*, vol. 128, no. 4, pp. EL175–L180, 2010.

[259] M. Gyöngy and C. C. Coussios, "Passive spatial mapping of inertial cavitation during HIFU exposure," *IEEE Trans. Biomed. Eng.*, vol. 57, no. 1, pp. 48–56, 2010.

[260] C. Crake, R. Carlisle, J. Owen, et al., "In vivo

biodistribution of fluorescently tagged magnetic microbubbles for cavitation enhancement with real time passive acoustic mapping," in *J. Acoust. Soc. Am*, 2015, p. 1845.

[261] R. M. Jones, M. A. O'Reilly, and K. Hynynen, "Transcranial passive acoustic mapping with hemispherical sparse arrays using CT-based skull-specific aberration corrections: a simulation study," *Phys. Med. Biol.*, vol. 58, no. 14, pp. 4981–5005, 2013.

[262] B. Rifai, C. D. Arvanitis, M. Bazan-Peregrino, et al., "Cavitation-enhanced delivery of macromolecules into an obstructed vessel.," *J. Acoust. Soc. Am.*, vol. 128, no. 5, pp. EL310–L315, 2010.

[263] S. Xu, Y. Zong, Y. Feng, et al., "Dependence of pulsed focused ultrasound induced thrombolysis on duty cycle and cavitation bubble size distribution," *Ultrason. Sonochem.*, vol. 22, pp. 160–166, 2015.

[264] C. Acconcia, B. Y. C. Leung, A. Manjunath, et al., "Interactions between Individual Ultrasound-Stimulated Microbubbles and Fibrin Clots," *Ultrasound Med. Biol.*, vol. 40, no. 9, pp. 2134–2150, 2014.

[265] I. N. Chernysh, C. E. Everbach, P. K. Purohit, et al., "Molecular mechanisms of the effect of ultrasound on the fibrinolysis of clots," *J. Thromb. Haemost.*, vol. 13, no. 4, pp. 601–609, 2015.

[266] K. B. Bader, M. J. Gruber, and C. K. Holland, "Shaken and Stirred: Mechanisms of Ultrasound-Enhanced Thrombolysis," *Ultrasound Med. Biol.*, vol. 41, no. 1, pp. 187–196, 2015.

[267] W. Francis, A. Blinc, and S. Lee, "Ultrasound Accelerates Tissue Plasminogen Transport of Recombinant Activator Into Clots," vol. 21, no. 3, pp. 419–424, 1995.

[268] B. Devcic-Kuhar, S. Pfaffenberger, L. Gherardini, et al., "Ultrasound affects distribution of plasminogen and tissue-type plasminogen activator in whole blood clots in vitro," *Thromb. Haemost.*, vol. 92, no. 5, pp. 980–985, 2004.

[269] V. Nahirnyak, S. W. Yoon, and C. K. Holland, "Acousto-mechanical properties of clotted blood," *J. Acoust. Soc. Am.*, vol. 119, no. 6, pp. 3766–3722, 2006.

[270] M. M. Calor-Filho and J. C. Machado, "Measurement of the ultrasonic attenuation coefficient of human blood plasma during clotting in the frequency range of 8 to 22 MHz," *Ultrasound Med. Biol.*, vol. 32, no. 7, pp. 1055–1064, 2006.

[271] S. Elder, "Cavitation Microstreaming," *J. Acoust. Soc. Am.*, vol. 31, no. 1, pp. 54–65, 1959.

[272] A. Prosperetti, "Bubble phenomena in sound fields: part two," *Ultrasonics*, no. May, pp. 115–124, 1984.

[273] D. E. Goertz, "An overview of the influence of therapeutic ultrasound exposures on the vasculature: High intensity ultrasound and microbubble-mediated bioeffects.," *Int. J. Hyperthermia*, vol. 31, no. 2, pp. 134–144, 2015.

[274] A. Soltani and C. Soliday, "Effect of ultrasound on enzymatic activity of selected plasminogen activators," *Thromb. Res.*, vol. 119, no. 2, pp. 223–228, 2007.

[275] B. M. Härdig, H. W. Persson, and S. B. Olsson, "Low-energy ultrasound exposure of the streptokinase molecule may enhance but also attenuate its fibrinolytic properties," *Thromb. Res.*, vol. 117, no. 6, pp. 713–720, 2006.

[276] F. Siddiqi, A. Blinc, J. Braaten, et al., "Ultrasound increases flow through fibrin gels," *Thromb. Haemost.*, vol. 73, no. 3, pp. 495–498, 1995.

[277] J. Braaten, R. Goss, and C. W. Francis, "Ultrasound reversibly disaggregates fibrin fibers," *Thromb. Haemost.*, no. 78, pp. 1063–8, 1997.

[278] F. Siddiqi, T. M. Odrljin, P. J. Fay, et al., "Binding of tissue-plasminogen activator to fibrin: effect of ultrasound.," *Blood*, vol. 91, no. 6, pp. 2019–2025, 1998.

[279] E. Sezgin, T. Sadowski, and K. Simons, "Measuring lipid packing of model and cellular membranes with environment sensitive probes," *Langmuir*, vol. 30, no. 27, pp. 8160–8166, 2014.

[280] E. Sezgin, D. Waithe, J. Bernardino De La Serna, et al., "Spectral imaging to measure heterogeneity in membrane lipid packing," *ChemPhysChem*, vol. 16, no. 7, pp. 1387–1394, 2015.

[281] G. J. Shaw, A. Dhamija, N. Bavani, et al., "Arrhenius temperature dependence of in vitro tissue plasminogen activator thrombolysis.," *Phys. Med. Biol.*, vol. 52, no. 11, pp. 2953–2967, 2007.

[282] J. Reith, H. S. Jørgensen, P. M. Pedersen, et al., "Body temperature in acute stroke: Relation to stroke severity, infarct size, mortality, and outcome," *Lancet*, vol. 347, no. 8999, pp. 422–425, 1996.

[283] H. Minamisawa, M. L. Smith, and B. K. Siesjö, "The effect of mild hyperthermia and hypothermia on brain damage following 5, 10, and 15 minutes of forebrain ischemia.," *Ann. Neurol.*, vol. 28, no. 1, pp. 26–33, 1990.

[284] M. D. Hammer and D. W. Krieger, "Hypothermia for acute ischemic stroke: not just another neuroprotectant.," *Neurologist*, vol. 9, no. 6, pp. 280–9, 2003.

[285] J. B. Casals, N. C. G. Pieri, M. L. T. Feitosa, et al.,

"The use of animal models for stroke research: A review," *Comparative Medicine*, vol. 61, no. 4. pp. 305–313, 2011.

[286] R. C. Becker, "Textbook of Coronary Thrombosis and Thrombolysis," in *Developments in Cardiovascular Medicine*, vol. 193, R. C. Becker, Ed. Springer Science & Business Media, 1997.

[287] F. Xie, S. Gao, J. Wu, et al., "Diagnostic Ultrasound Induced Inertial Cavitation to Non-Invasively Restore Coronary and Microvascular Flow in Acute Myocardial Infarction," *PLoS One*, vol. 8, no. 7, pp. 1–7, 2013.

[288] J. K. Leach, E. a. O'Rear, E. Patterson, et al., "Accelerated thrombolysis in a rabbit model of carotid artery thrombosis with liposome-encapsulated and microencapsulated streptokinase," *Thromb. Haemost.*, vol. 90, no. 1, pp. 64–70, 2003.

[289] S. T. Laing, M. Moody, B. Smulevitz, et al., "Ultrasound-enhanced thrombolytic effect of tissue plasminogen activator-loaded echogenic liposomes in an in vivo rabbit aorta thrombus model-brief report," *Arterioscler. Thromb. Vasc. Biol.*, vol. 31, no. 6, pp. 1357–1359, 2011.

[290] C. Crake, M. D. Saint Victor, J. Owen, et al., "Passive acoustic mapping of magnetic microbubbles for cavitation enhancement and localization.," *Phys. Med. Biol.*, vol. 60, no. 2, pp. 785–806, 2015.

[291] E. Bor-Seng-Shu, R. De Carvalho Nogueira, E. G. Figueiredo, et al., "Sonothrombolysis for acute ischemic stroke: a systematic review of randomized controlled trials," *Neurosurg. Focus*, vol. 32, no. 1, p. E5, 2012.

[292] D. V. Sakharov, J. F. Nagelkerkel, and D. C. Rijken, "Rearrangements of the fibrin network and spatial distribution of fibrinolytic components during plasma clot lysis: Study with confocal microscopy," *J. Biol. Chem.*, vol. 271, no. 4, pp. 2133–2138, 1996.

[293] J. P. Collet, D. Park, C. Lesty, et al., "Influence of fibrin network conformation and fibrin fiber diameter on fibrinolysis speed: dynamic and structural approaches by confocal microscopy.," *Arterioscler. Thromb. Vasc. Biol.*, vol. 20, no. 5, pp. 1354–1361, 2000.

[294] J. W. Weisel, G. N. Phillips, and C. Cohen, "The structure of fibrinogen and fibrin: II. Architecture of the fibrin clot.," *Ann. N. Y. Acad. Sci.*, vol. 408, pp. 367–379, 1983.

[295] J. W. Weisel, G. N. Phillips, and C. Cohen, "A model from electron microscopy for the molecular structure of fibrinogen and fibrin.," *Nature*, vol. 289, no. 5795, pp. 263–267, 1981.

[296] I. N. Chernysh, J. W. Weisel, and W. Dc, "Dynamic imaging of fibrin network formation correlated with other measures of polymerization Plenary paper Dynamic imaging of fibrin network formation correlated with other measures of polymerization," *Blood*, vol. 111, no. 10, pp. 4854–4861, 2011.

[297] M. a Digman, V. R. Caiolfa, M. Zamai, et al., "The phasor approach to fluorescence lifetime imaging analysis.," *Biophys. J.*, vol. 94, no. 2, pp. L14–L16, 2008.

[298] A. J. Thompson, T. W. Herling, M. Kubánková, et al., "Molecular Rotors Provide Insights into Microscopic Structural Changes During Protein Aggregation," *J. Phys. Chem. B*, vol. 119, no. 32, pp. 10170–10179, 2015.

[299] D. M. Owen, A. Magenau, A. Majumdar, et al., "Imaging membrane lipid order in whole, living vertebrate organisms.," *Biophys. J.*, vol. 99, no. 1, 2010.

[300] I. Leibacher, S. Schatzer, and J. Dual, "Impedance matched channel walls in acoustofluidic systems.," *Lab Chip*, vol. 14, no. 3, pp. 463–70, 2014.

[301] A. C. Lendrum, D. S. Fraser, W. Slidders, et al., "Studies on the character and staining of fibrin," *J. Clin. Pathol.*, vol. 15, no. 5, pp. 401–413, 1962.

[302] J. M. Kwiatek, D. M. Owen, A. Abu-Siniyeh, et al., "Characterization of a New Series of Fluorescent Probes for Imaging Membrane Order," *PLoS One*, vol. 8, no. 2, pp. 1–7, 2013.